Continuum modeling of the coupled transport of mass, energy, and momentum in paperboard.

Askfelt, Henrik

2016

Document Version:
Other version

Department of Construction Sciences
Solid Mechanics

ISRN LUTFD2/TFHF-16/1057-SE(1-174)
ISBN (PRINTED VERSION) 978-91-7753-008-4
ISBN (ELECTRONIC VERSION) 978-91-7753-009-1

Continuum modeling of the coupled transport of mass, energy, and momentum in paperboard

Doctoral Dissertation by

Henrik Askfelt

Printed by Media-Tryck AB, Lund, Sweden
For information, adress:
Division of Solid Mechanics, Lund University, Box 118, SE-221 00 Lund, Sweden
Homepage: http://www.solid.lth.se

To Benjamin Askfelt

Preface

The presented thesis is the result of my Ph.D. studies. The studies has been conducted at the Division of Solid Mechanics at Lund University between 2011 and 2016 and has been sponsored by Tetra Pak AB. First of all I would like to express my gratitude to some of the people whom have contributed to the completion of this thesis. I would like thank my main supervisor Prof. Matti Ristinmaa and my co–supervisors Prof. Niels Saabye Ottosen and Adj. Prof. Johan Tryding for their guidance, their great support, and their encouragement during my studies. I am also very grateful for all the support I have received from Stora Enso AB in Karlstad, regarding both knowledge and facilities. I have received much assistance in my experimental work, for which I am grateful; Ph.D. Jonas Engqvist from Lund University, Dan Enochsson and Per Johansson from Tetra Pak AB, Ph.D. Junis Amini, Claes Åkerblom, and Ann–Kristin Wallentinsson from Stora Enso AB, and Anne–Marie Olsson from Innventia AB. I would like to thank all of my colleagues from the Division of Solid Mechanics, both former and present, whom have given me a great environment to work in. I feel obligated to give a special thank you to Marcus Alexandersson with whom I have spent countless hours discussing concepts of mixture theories and how these relate to physics. A thank you should also be given to my long–term friends outside of work who have helped me to distract my thoughts from work and keep me sane. I express my deepest gratitude to my family whose love and support is unprecedented. Without your help this work would not have been possible. Thank you! Finally, and most importantly, I thank my son, Benjamin, for being exactly the person that he is. Thank you!

Lund, September 2016

Henrik Askfelt

Abstract

This thesis investigates the coupling between moisture, heat, and deformation in paperboard. The presented investigations are primarily conducted via macroscale continuum modeling but experimental characterisations are also made. The continuum modeling is presented in a mixture theory framework where the paperboard is considered as a porous media composed of three immiscible phases; a network of cellulose fibers, liquid water bound in or to the fibers, and moist air. The motion of each phase is described and the interactions of mass, energy and momentum between the three phases are also considered. Emphasis in the current work is to derive a thermodynamically consistent model and all constitutive relations are derived with consideration to the Clausius–Duhem inequality. The derived continuum model is used in numerical investigations to study the response of slow, long time processes such as storing of paperboard rolls as well as rapid processes where the board is exposed to significant temperature changes and mechanical loads during a short period of time.

The thesis begins with an introduction where some of the characteristic properties of paperboard are described and the basic concepts of the hybrid mixture theory framework are explained. The main part of the thesis is then composed of four papers, A, B, C, and D. In Paper A, a model describing the transport of mass and heat in paperboard is developed. The model considers slow transport processes and assumes the fiber network to be incompressible. Special focus of Paper A is to develop a model that is able to describe the static and dynamic sorption properties of paperboard. The derived model is used to predict the evolution of the moisture and heat distributions in paperboard rolls in climates with a varying relative humidity. In Papers B and C, the model derived in Paper A is further developed to handle rapid processes where significant temperature changes are expected. Furthermore, in Papers B and C, the assumption of an incompressible fiber network is abandoned and an orthotropic stress–strain response with an advanced yield surface is incorporated in a large strain setting. The model is then used to predict the response of paperboard during a transversal sealing process. In Paper D, experimental investigations are made on the in–plane permeability and on the static and dynamic sorption properties of paperboard. The results from these investigations are then used together with the model developed in Paper B and C to analyse the physics behind a blister test.

Sammanfattning

Kartong är ett material som används flitigt inom förpackningsindustrin. En anledning till att kartong har blivit ett populärt förpackningsmaterial är att det är ett styvt material i förhållande till sin densitet. Denna egenskap medför att förpackningar tillverkade i kartong är lätta och kan bära hög belastning. En annan anledning att kartong används framför andra förpackningsmaterial, så som exempelvis plast, är miljöaspekten som blir allt mer viktig. Kartong är dessutom ett material som är förhållandevis billigt att producera vilket är viktigt att begrunda för förpackningsindustrin då enorma kvantiteter förpackningar produceras varje dag.

Under tillverkningsprocessen av kartong sprejas en fiber-lösning på en duk som sedan avvattnas och torkas. På grund av gravitationskrafter och en hastighetsskillnad mellan flödet på fibermassan och duken får fibrerna i kartongen en ordnad porös struktur. Denna struktur medför att transporten av massa, energi och rörelsemängd i kartong är riktningsberoende. De olika transportprosesserna är dessutom kopplade och kunskapen gällande hur kartong reagerar på olika externa belastningar är ej fullständig. De existerande kunskapsluckorna leder till att utvecklingsprosessen av nya förpackningar förlängs, till tillfälliga produktionsstopp och i vissa fall till problem med de producerade förpackningarna.

Som ett steg mot att fylla de befintliga kunskapsluckorna ligger fokus i detta arbete på kopplingen mellan de olika transportprocesserna i kartong. Den teoretiska modellen som beskriver kartongen har satts upp på makroskalan i ett ramverk benämnt blandningsteorier. I detta ramverk anses kartongen kunna beskrivas som en superposition av tre faser; ett fibernätverk, vatten bundet i och på fibrerna samt fuktig luft i porutrymmet. Varje fas har en specifik rörelse och kan utbyta massa, rörelsemängd, och energi med de andra faserna.

Fyra artiklar, A, B, C och D, är sammanbundna i denna avhandling. I samtliga artiklar används blandningsteorier för att modellera kartong. I artikel A presenteras en modell som beskriver värmetransporten och fukttransporten i kartong under långsamma förlopp. Modell används sedan för att prediktera hur fuktdistributionen och värmedistributionen ändras i kartongrullar under förvaring i klimat med varierande relativ fuktighet. I artiklarna B och C utökas modellen så att modellen kan hantera snabba förlopp och även beskriva stora plastiska deformationer av fibernätverket. Den utökade modellen används sedan för att prediktera hur kartong beter sig under en transversell försegling. Slutligen i artikel D presenteras experiment där i-planet permeabiliteten och den statiska och dynamiska sorptionen i kartong undersöks. Resultaten från dessa experiment används sedan tillsammans med modellen framtagen i artiklarna B och C för att analysera ett blister test.

List of appended papers

This doctoral thesis is based on the following manuscripts:

Paper A
Marcus Alexandersson, Henrik Askfelt, and Matti Ristinmaa (2016)
Triphasic model of heat and moisture transport with internal mass exchange in paperboard.
Transport in Porous Media, 112 (2016) 381–408

Paper B
Henrik Askfelt, Marcus Alexandersson, and Matti Ristinmaa (2016)
Transient transport of heat, mass, and momentum in paperboard including dynamic phase change of water.
International Journal of Engineering Science, 109 (2016) 54-72

Paper C
Henrik Askfelt and Matti Ristinmaa
Response of moist paperboard during rapid compression and heating
Accepted for publication in Applied Mathematical Modelling

Paper D
Henrik Askfelt and Matti Ristinmaa
Experimental and numerical analysis of adhesion failure in moist packaging material during excessive heating.
To be submitted for publication

Own Contribution The author of this thesis has taken a shared responsibility for the preparation and writing of Paper A and the main responsibility for the preparation and writing of papers B, C, and D. In all papers, the development of the model and the analyses of the results have been conducted in collaborations with the co-authors. The numerical implementations in papers B, C, and D have been made by the author. The experimental measurements in Paper D have been carried out by the main author.

Contents

Nomenclature

Table 1: Latin symbols

Notation	Description
A_α	Inner part of the specific Helmholtz free energy of phase α (J/kg)
A_{α_j}	Specific Helmholtz free energy of constituent α_j (J/kg)
a_w	Water activity (-)
$b, b_\alpha, b_{\alpha_j}$	External source of entropy (J/kg/K/s)
$\mathbf{b}, \mathbf{b}_\alpha, \mathbf{b}_{\alpha_j}$	Specific body force vector (N/kg)
$\mathbf{d}, \mathbf{d}_\alpha, \mathbf{d}_{\alpha_j}$	Rate of deformation tensor (1/s)
D, D^E	Dissipation (J/m^3/s)
$e^*_\alpha, e^*_\alpha, e_{\alpha_j}$	Specific total internal energy (J/kg)
e, e_α	Inner part of the specific internal energy (J/kg)
$\hat{e}^\beta_\alpha, \hat{e}^\beta_{\alpha_j}$	Rate of mass transfer per unit mass density (1/s)
$\mathbf{F}_\alpha$	Deformation gradient of phase α (-)
ΔH_{ads}	Enthalpy of adsorption (J/kg)
$\hat{\mathbf{i}}_{\alpha_j}$	Rate of momentum transfer per unit mass density (N/kg)
J_α	Determinant of the deformation gradient of phase α (-)
$\mathbf{l}_\alpha$	Spatial velocity gradient of phase α (1/s)
$m, m_\alpha, m_{\alpha_j}$	Mass (kg)
m_{dry}	Dry mass (kg)
n_α	Volume fraction (-)
N_α	Number of phases (-)
N_{α_j}	Number of constituents in phase α (-)
$p^{eq}_{g_v}$	Water vapor pressure at equilibrium (Pa)
$p^{sat}_{g_v}$	Saturated water vapor pressure (Pa)
$\mathbf{q}, \mathbf{q}_\alpha, \mathbf{q}_{\alpha_j}$	Heat flux vector (J/m^2/s)
$Q, Q_\alpha, Q_{\alpha_j}$	External source of energy (J/kg/s)
$\hat{Q}^\beta_\alpha, \hat{Q}^\beta_{\alpha_j}, \hat{Q}_{\alpha_j}$	Rate of energy interaction (J/kg/s)
$\hat{r}_{\alpha_j}$	Rate of mass transfer per unit mass density (1/s)
t	Time (s)
$\hat{\mathbf{T}}^\beta_\alpha, \hat{\mathbf{T}}^\beta_{\alpha_j}$	Rate of momentum transfer (N/kg)
$v, v_\alpha, v_{\alpha_j}$	Volume (m^3)
$\mathbf{v}, \mathbf{v}_\alpha, \mathbf{v}_{\alpha_j}$	Mass averaged velocity (m/s)
$\mathbf{v}_{\alpha,\beta}$	Seepage velocity (m/s)
W	Moisture ratio (-)
$\mathbf{w}_\alpha, \mathbf{w}_{\alpha j}$	Diffusion velocity (m/s)
$\mathbf{x}$	Spatial position (m)
$\mathbf{X}_\alpha$	Material position related to phase α (m)

Table 2: Greek symbols

Notation	Description
$\eta, \eta_\alpha, \eta_{\alpha_j}$	Inner part of the specific entropy (J/kg/K)
η_{α_j}	Specific entropy of constituent α_j (J/kg/K)
θ	Absolute temperature (K)
λ_i	Lagrangian multipliers (J/kg)
λ_α^θ	Thermal conductivity of phase α (W/m/K)
$\Lambda, \Lambda_\alpha, \Lambda_{\alpha_j}$	Entropy production (J/kg/K/s)
$\rho, \rho_\alpha, \rho_{\alpha_j}$	Intrinsic Density (kg/m^3)
$\boldsymbol{\sigma}, \boldsymbol{\sigma}_\alpha, \boldsymbol{\sigma}_{\alpha_j}$	Cauchy stress tensor (Pa)
$\boldsymbol{\varphi}, \boldsymbol{\varphi}_\alpha, \boldsymbol{\varphi}_{\alpha_j}$	Entropy flux (J/m^2/K/s)
$\boldsymbol{\chi}_\alpha$	Mapping of the motion of phase α
$\boldsymbol{\omega}_\alpha, \boldsymbol{\omega}_s^e, \boldsymbol{\omega}_s^p$ (m)	Spin tensor (1/s)
Ω	Spatial configuration (m^3)
Ω_α^0	Material configuration of phase α (m^3)

Table 3: Abbreviations

Abbreviation	Full text
CD	Cross machine direction in paperboard
HMC	Hygroscopic moisture content
HMT	Hybrid mixture theory
MD	Machine direction in paperboard
RVE	Representative volume element
ZD	Out–of–plane direction in paperboard

1 Introduction

For the packaging industry, delivering package solutions for food products, protection of the integrity of a package is of the highest priority. The package material typically has a layered structure in the out–of–plane direction, cf., Figure 1. Paperboard oc-

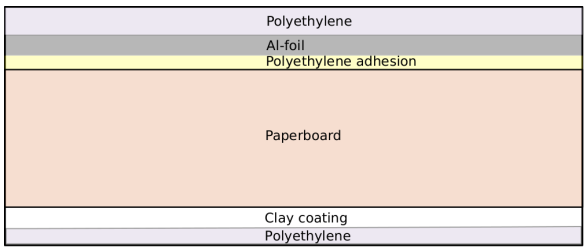

Figure 1: A simplified illustration of the set–up of layers in the aseptic package material.

cupies the largest part of the package material and carries the main stiffness of the package. Paperboard allows transport of gas and liquid and, therefore, paperboard alone does not serve as a barrier protecting food products from ambient climates. For this reason a thin layer of polyethylene is attached on the inside of the paperboard, i.e., closer to the food product. Considering food products that should be stored in rough ambient climates and for long periods of time, the additional polyethylene layer will not suffice and a thin layer of aluminium is inserted between the polyethylene and the paperboard. The Al–foil protects the food product against light and reduces the transport of gas and liquid from the ambient climate even more.

Printing on a food package is typically performed on the paperboard. However, in order to make the surface of the board smoother and improve the printing quality it is not uncommon to add a clay coating on the outer side of the paperboard. Finally as an additional protection from the ambient climate a thin layer of polyethylene is attached outside the clay coating.

In order to be able to guarantee the integrity of a food package knowledge about the different components of the package material and how they interact are of great importance. As a step towards an increased knowledge in this area the current thesis treats the response of moist paperboard. In particular, the couplings between moisture, heat and deformation in paperboard are investigated. Modeling of the clay coating, the polyethylene, or the aluminium are not considered in this work. However, the properties of these layers are considered when assigning boundary conditions for the numerical simulations.

2 Characteristic properties of paperboard

2.1 General

Paperboard is a porous medium whose main components are; a network of cellulose fibers, liquid water, and moist air. As an illustration of the porous nature of paper-

board an x–ray tomograph image of the cross section of a paperboard is included in Figure 2(b). The cellulose fibers have a high length to width ratio, the typical length and width of the fibers are (1–5 mm), and (20–50 μm), respectively. As may be seen from the tomograph image in Figure 2(b), the cellulose fibers are not solid but contain a cavity. This cavity is referred to as lumen and the thickness of the surrounding fiber wall is (2–8 μm), see also Baggerud (2004). During the manufacturing process of paperboard, a pulp suspension of water and 0.1-1% fibers is sprayed on to a moving web which is then dewatered, compressed, and dried, see Baggerud (2004). Due to the gravitational forces as well as a speed difference between the suspension flow and the web, the structure of the fiber network tend to be ordered and paperboard is considered to be an orthotropic material. The orthotropic nature of paperboard introduces direction–dependent transports of mass, momentum, and energy. The characteristic directions in paperboard are; Machine Direction (MD), Cross machine Direction (CD), and out-of-plane direction (ZD), cf. Figure 2(a).

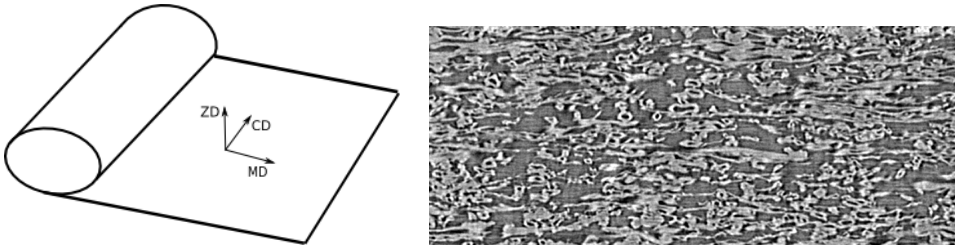

(a) (b)

Figure 2: **a**) Illustration of the characteristic directions of paperboard, **b**) Image of of a cross–section of paperboard taken with the x–ray tomograph at the 4D–imaging lab, Lund University.

2.2 Moisture interaction

Liquid water may be located essentially anywhere in paperboard. Due to interactions with the cellulose fibers the energy of liquid water changes and depending on where in the paperboard the water is located the properties of the liquid water differ. Most of the liquid water that is located in the lumen, or in the inter–fiber pores, (0.5–10 μm), has the same properties as "free" liquid water, i.e., water that is not affected by the presence of a solid. However, the liquid water located in the intra–fiber pores (5–10^4 Å), may have very strong bond to the solid which reduces the energy of the water. In Papers A–D it is shown how the reduced energy affects the behaviour of the liquid water, e.g., the pressure of the liquid water and the heat of adsorption. An illustration of the possible locations of liquid water is provided in Figure 3.

The amount of liquid water in paperboard is here characterised by the moisture ratio W which is defined by

$$W = \frac{m - m_{dry}}{m_{dry}} \tag{1}$$

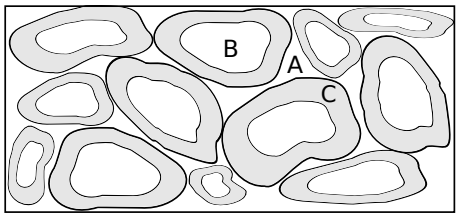

Figure 3: Illustration of the possible locations of water in paperboard; A) inter–fiber pores, B) lumen, and C) intra–fiber pores.

Here m is the mass of the paperboard and m_{dry} is the mass of the paperboard when it is completely dry. It may be noted that the moisture ratio is equivalent to the dry basis moisture content, which is another quantity commonly used to characterise the amount of moisture in paperboard and other porous media. The energy level of the liquid water inside the board is defined by the water activity a_w which describes the escaping tendency of the water, or how tightly the water is bound. The water activity is defined by the ratio between the equilibrium vapor pressure and the saturation vapor pressure, i.e.,

$$a_w = \frac{p_{g_v}^{eq}}{p_{g_v}^{sat}}, \tag{2}$$

see also Bénet et al. (2012). The limiting values of the water activity are 0 and 1, where $a_w \to 0_+$ indicates that the moisture ratio goes to zero and the bounding forces of the last water are very high. The upper limit value $a_w = 1$ indicates that the moisture ratio is so high that some of the water may be considered as "free" liquid water. Typically, the water activity in a porous media is represented by sorption isotherms. In Petterson and Stenström (2000) a review is presented where isotherms frequently used for paperboard are discussed. The format of the sorption isotherm will have a direct implication on the heat of adsorption and considering this aspect it is argued, in Petterson and Stenström (2000), that the isotherm suggested by Heikkilä 1993 is best suited for calculations on paper. The Heikkilä isotherm is given by the following format

$$a_w = 1 - \exp(a^a W^{a^b} + a^c(\theta - 273.15)W^{a^d}) \tag{3}$$

where a^a, a^b, a^c, and a^d are constants that may be calibrated against experimental sorption isotherms. A typical isotherm of the format in (3) is plotted in 4(a). The affect on the enthalpy of adsorption is discussed in Papers A and B and the typical effect from an isotherm of the format in (3) is shown in Figure 4(b). From this figure it is evident that the energy needed to remove water increases significantly for lower moisture ratios.

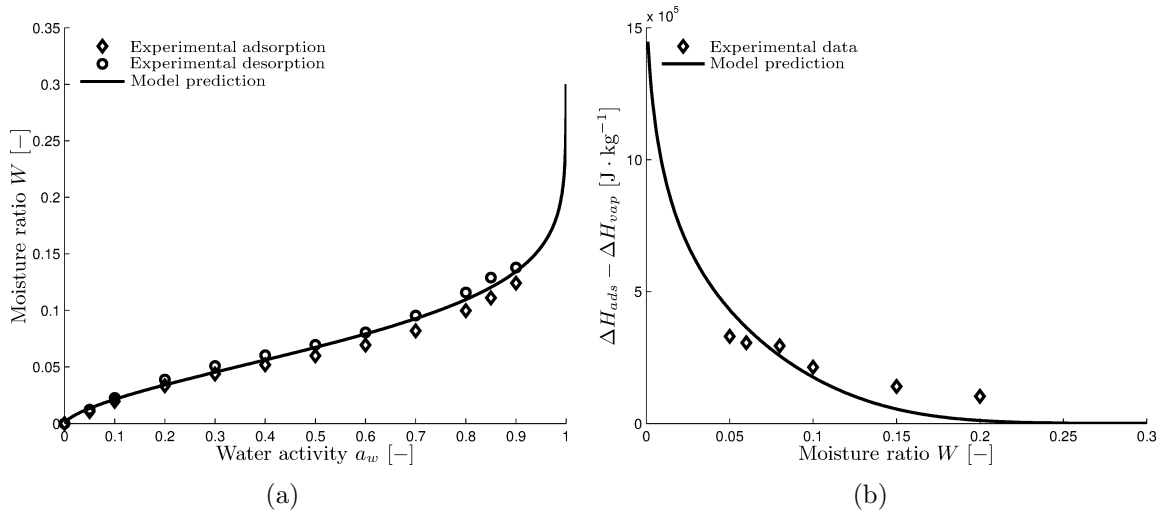

Figure 4: a) Typical sorption isotherm of the format provided in (3) **b**) Change in the enthalpy of adsorption due to soild–liquid interactions.

The sorption isotherm measured during adsorption typically renders lower values of moisture ratios compared to the sorption isotherms measured during desorption, see Figure 4(a). This property is common for porous media and is known as hysteresis. Hysteresis effects are not considered in the present thesis and the reader is referred to e.g., Venkateswaran (1970) for more information on the subject.

The distribution of moisture inside a paperboard will influence the boards ability to transport liquid water, dry air, and vapor. Constitutive relations describing the liquid water seepage are derived in Papers A and B, alternative formats may also be found in e.g., Eriksson et al. (2006); Bennethum (2012). However, in Papers A–D, moisture ratios below the hygroscopic moisture content (HMC) are considered and all liquid water is assumed to be bound in or to the fibers, see also Baggerud (2004). This motivates the assumption that the liquid water has the same motion as the fiber network and that the liquid water seepage can be approximated as zero. Note that, this does not imply a constant moisture distribution since the moisture distribution could change due to e.g., sorption.

In Papers A and D, the inter–fiber gas seepage is assumed to be a linear laminar flow described by Darcy's law. In Papers B and C, more significant pressure gradients are expected and the inter–fiber gas seepage is modeled as nonlinear laminar flow described by Forchheimer's equation, see also e.g., Hassanizadeh and Gray (1987); Bennethum and Giorgi (1997); Market (2005); Landervik and Larsson (2007). The permeability tensor describes the seepage flow resistance and is in Papers A–D described by an orthotropic function that depends on the current ratio of air in the board. The paperboard is assumed to be composed of a fiber network, liquid water, and moist air and the ratio of moist air is influenced by the ratio of liquid water in the board. Also the inter–fiber diffusivity tensor, which describes the resistance of vapor diffusion, is in all papers described by an orthotropic function that depends on the current ratio of air in the board.

Furthermore, the distribution of moisture inside paperboard will influence mechan-

ical properties of paperboard, e.g., the elastic modulus and the yield surface of the board and the hygro–expansion of the fibers. These effects are not considered in the present thesis and the interested reader is referred to Rigdahl et al. (1984); Linvill and Östlund (2014); Linvill (2015); Salmén and Olsson (2016), and Östlund (2006); Bosco et al. (2015a,b,c), respectively, for more information on these subjects.

2.3 Heat interaction

Due to the layered structure in the out–of–plane direction of paperboard, the thermal conductivity of paperboard is typically modeled with a series flow, a parallel flow, or a combination of the two, see also Karlsson and Stenström (2005); Baggerud (2004). In Paper A the thermal conductivity of paperboard is modeled as a series flow in ZD and as a parallel flow in CD, while in Papers C and D the thermal conductivity is modeled as a parallel combination of a series flow and a parallel flow, see Figure 5.

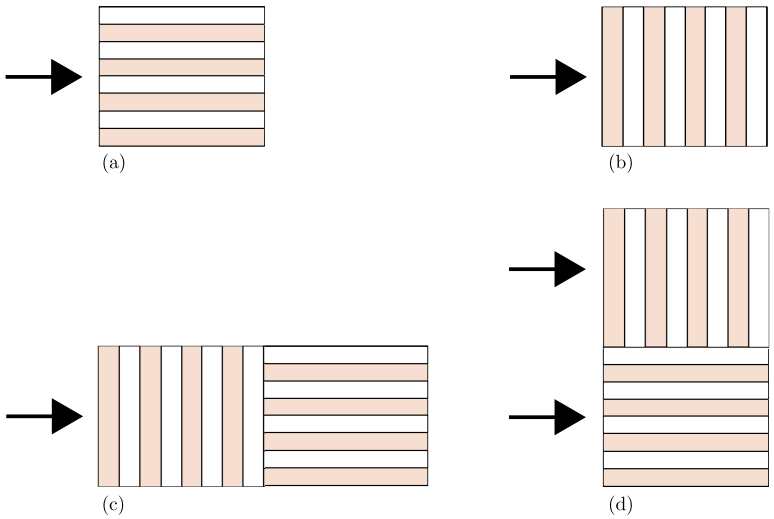

Figure 5: Illustration of the different thermal conductivity flow types **a**) parallel flow, **b**) series flow, **c**) series combination of a series flow and a parallel flow, and **d**) parallel combination of a series flow and a parallel flow. The black arrows indicate the direction of the conductive heat flow.

The thermal conductivities of liquid water and moist air are both functions of the absolute temperature whereas the thermal conductivity of cellulose fibers usually is considered to be independent of the absolute temperature, see also Baggerud (2004); Lucisano (2002); Lavrykov and Ramarao (2012). Assuming a parallel combination of a series flow and a parallel flow, the thermal conductivity of paperboard in the out–of–plane direction is plotted as a function of the absolute temperature in Figure 6(a). As a comparison the thermal conductivities of liquid water, cellulose, and moist air are also included in this figure. From Figure 6(a) it is noticed that moist paper should have a higher thermal conductivity and that the moist air inside the paperboard acts as an isolator. This reasoning agrees well with Figure 6(a) where the in–plane and out–of–plane thermal conductivities of paperboard are plotted as functions of the sheet

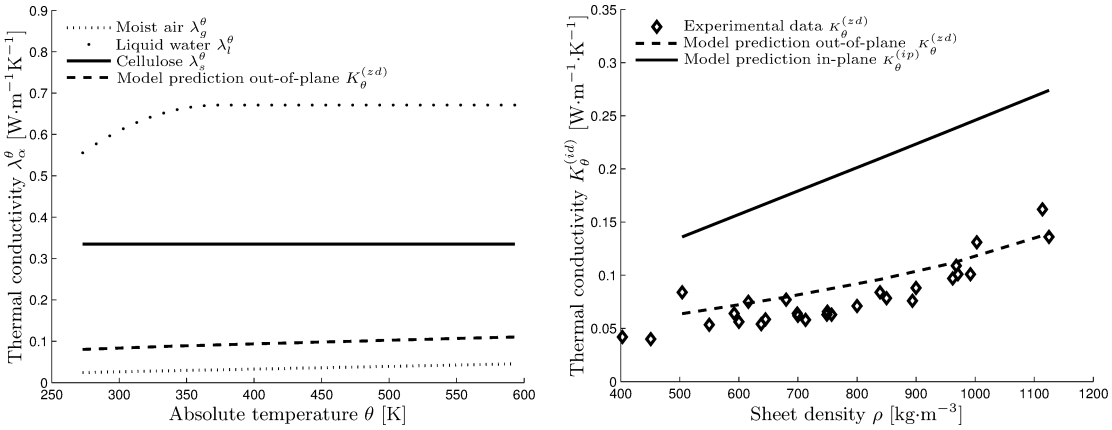

Figure 6: **a**) Model prediction of the temperature dependency of the thermal conductivity, λ_α^θ, of each phase compared with the out-of-plane thermal conductivity of paperboard with porosity $\phi = 0.53$ and $W = 0.1$, **b**) Thermal conductivity of paperboard as a function of the sheet density.

density. A more elaborate description of the thermal conductivity of paperboard is included in Paper C, where convective and diffusive heat fluxes also are discussed.

The ability to accumulate heat in paperboard is determined by the specific heat of the board. The specific heat of paperboard is in Papers A–D described as the sum of the specific heats of the components of the paperboard weighted by the bulk densities of the components. This implies that the specific heat of paperboard will increase with a higher moisture ratio and decrease with a higher porosity. In Papers B–D, the specific heat of the fiber network and the specific heat of the moist air are both modeled as functions of the absolute temperature.

In Papers A, C and D, the dynamic viscosities of both the moist air and the liquid water are modeled as functions of the absolute temperature, this effect will influence the mass transport processes within the board. As indicated in equation (3), the sorption between the bound water and the water vapor as well as the enthalpy of adsorption associated with this transformation are processes that depend on the temperature distribution.

Other properties that are influenced by the temperature distribution includes the stiffness and the yield surface of paperboard. These dependencies are not considered in the present thesis and the reader is referred to the work in Salmén and Back (1977); Wallmeier et al. (2015) for more information about these subjects.

2.4 Mechanical properties

It is well known that the mechanical response of paperboard is orthotropic, see e.g., Stenberg (2002); Xia et al. (2002); M. Nygårds et al. (2009); Borgqvist (2016). As an illustration of the magnitude of the anisotropy, experimental data from uniaxial tension and compression tests in the in–plane directions MD, CD, and the out–of–plane direction ZD, provided in Borgqvist (2016), are shown in Figure 7. Comparing the uniaxial tensile tests in Figures 7(a) and 7(c), it is observed that there is a significant

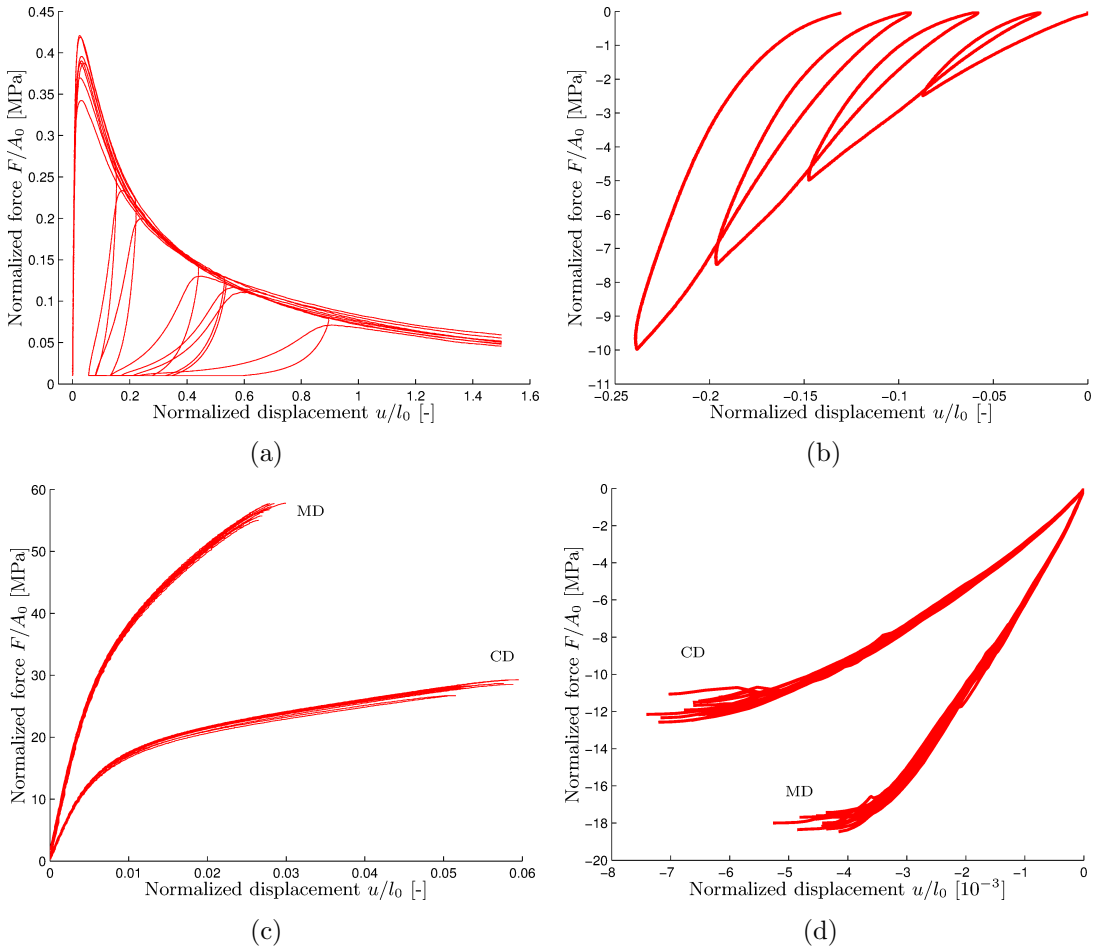

Figure 7: Mechanical response of paperboard from experimental data provided in Borgqvist (2016) **a**) uniaxial cyclic tension in ZD, **b**) uniaxial cyclic compression in ZD, **c**) uniaxial tension in MD and CD, and **d**) uniaxial compression in MD and CD. The experiments are performed in 50% relative humidity and 296.15 K. The initial cross section area and the initial span–length of each test are denoted A_0 and l_0 respectively.

difference in the load the paper is able to carry in the different directions. Considering both the compression and tensile tests for the in–plane directions MD and CD, it is seen that the paperboard has a higher stiffness and a higher tensile strength, but a lower failure strain in MD, compared to CD. The stress–strain curves provided in Figure 7 describe the macroscale response of paperboard. For an investigation of the relation between the macroscopic response of paperboard and the microscopic properties of paperboard, e.g., stress–strain response of the cellulose fibers, the bond strength, the compliance of bond regions, and the bond intensity the reader is referred to Borodulina et al. (2012).

The stress–strain response of paperboard is not the focus of the present work and the viscous effects are neglected. In the present work the macroscale continuum model suggested in Borgqvist et al. (2014, 2015) is adopted for modeling of the stress–strain response of the fiber network. This model is thermodynamically consistent,

the calibration is fairly simple, and it has been shown to provide reliable results in complex load situations such as, creasing, folding, and short span compression, see Borgqvist et al. (2015, 2016). Additionally the model suggested by Borgqvist, views the paperboard as a continuum and the model is based on the macroscale, which are two necessary aspects when incorporating the model in the mixture theory framework. An approach for including the Borgqvist model in the mixture theory framework is provided in Papers B and C.

As discussed in the two previous Subsections 2.2 and 2.3, the mechanical stress–strain response depends on the moisture and temperature distribution of the board. In the same manner the moisture and temperature distributions depend on the deformations of the board. The plastic deformations of paperboard are dissipative and will generate heat, see e.g., Hyll et al. (2012). As an example of how the deformation of paperboard affects the moisture distribution it is shown in Paper C how a rapid compression of paperboard will affect the gas pressure which in turn will influence the sorption behaviour.

3 Mixture theory

Depending on the scale paperboard is modeled on, paperboard may be considered as a heterogeneous or a homogeneous material, see also Mäkelä and Östlund (2003). In the presented thesis a hybrid mixture theory, HMT, approach is adopted and paperboard is viewed as a homogeneous continuum on the macroscale. The basic idea of mixture theories is to view a body as a mixture of different phases and constituents. The different components of the mixture are then allowed individual motions and to interact with each other. These features have made mixture theories a powerful framework to work with when modeling multiphysical processes.

Extensive reviews of the historic development of mixture theories are found in Atkin and Crane (1976); Bowen (1976); de Boer and Ehlers (1988); de Boer (1992); Rajagopal and Tao (1995); de Boer (2000). In the present work the hybrid mixture theory, HMT, framework is adopted. This framework is described in Achanta et al. (1994) as "essentially classical mixture theory applied to macroscale averaged balance laws for phases and interfaces". The HMT framework was first proposed as a two scale model in Hassanizadeh and Gray (1979a,b, 1980) and was later developed to a three scale model in Bennethum (1994); Bennethum and Cushman (1996a,b).

3.1 Kinematics framework

An extensive overview of the kinematics concerning the theory of mixtures is provided in Bowen (1976), and in this section only a brief presentation is given.

Each spatial point $\mathbf{x}$ in the mixture is viewed as a superposition of N_α immiscible phases denoted $()_\alpha$. Each phase is considered to be separate continuum defined as a homogeneous mixture of N_{α_j} miscible constituents denoted $()_{\alpha_j}$. Each constituent is also considered to be separate continuum. In Hassanizadeh and Gray (1990); Bennethum and Cushman (1996a) it is shown how the interfaces between the phases also

may be treated as separate continuum. However, in the presented work the thermodynamic properties of the interfaces are only considered implicitly via the constitutive relations that describe the interactions between the phases.

Let $\mathbf{X}_\alpha$ denote the material coordinates of phase α in reference configuration Ω_α^0. The nonlinear mapping functions $\boldsymbol{\chi}_\alpha : \Omega_\alpha^0 \times t \to \Omega \subset \mathbb{R}^3$ from the different reference configurations to the spatial configuration Ω are given by

$$\mathbf{x} = \boldsymbol{\chi}_\alpha(\mathbf{X}_\alpha, t) \tag{4}$$

where t denotes the current time. The deformation gradients, $\mathbf{F}_\alpha$, associated with the mappings between the material configurations Ω_α^0 and the spatial configuration Ω are defined by

$$\mathbf{F}_\alpha = \frac{\partial \boldsymbol{\chi}_\alpha(\mathbf{X}_\alpha, t)}{\partial \mathbf{X}_\alpha} \tag{5}$$

In order to ensure that these mappings are continuous bijective, the Jacobians are assumed to be greater than zero, i.e., $J_\alpha = \det(\mathbf{F}_\alpha) > 0$. The spatial velocity gradients $\mathbf{l}_\alpha$ are additively split into two parts, the symmetric rate of deformation tensors $\mathbf{d}_\alpha$ and the skew-symmetric spin tensors $\boldsymbol{\omega}_\alpha$ i.e.,

$$\mathbf{l}_\alpha = \frac{D_\alpha(\mathbf{F}_\alpha)}{Dt}\mathbf{F}_\alpha^{-1}, \qquad \mathbf{d}_\alpha = \frac{1}{2}(\mathbf{l}_\alpha + \mathbf{l}_\alpha^T), \qquad \boldsymbol{\omega}_\alpha = \frac{1}{2}(\mathbf{l}_\alpha - \mathbf{l}_\alpha^T) \tag{6}$$

Here $D_\alpha(\bullet)/Dt$ denote the material time derivative with respect to the motion of phase α, which is related to the spatial time derivative $\partial(\bullet)/\partial t$ as follows

$$D_\alpha(\bullet)/Dt = \partial(\bullet)/\partial t + \mathbf{v}_\alpha \cdot \nabla(\bullet) \tag{7}$$

The volume and the mass of a representative volume element, (RVE), of the mixture are denoted v and m and are related to their phase and constituent counterparts via

$$m = \sum_\alpha m_\alpha, \qquad m_\alpha = \sum_j m_{\alpha_j}, \qquad v = \sum_\alpha v_\alpha \tag{8}$$

All constituents of phase α are considered miscible and associated with the volume of phase α, i.e., $v_{\alpha_j} = v_\alpha \; \forall \; j$.

The macroscale balance laws assumed in hybrid mixture theory are derived through averaging of microscale balance laws. During the averaging from micro- to macroscale a new variable, the volume fraction n_α, appears naturally, as

$$n_\alpha = \frac{v_\alpha}{v}, \tag{9}$$

Throughout this work, quantities multiplied by volume fractions are denoted with a bar, i.e., $\bar{(\bullet)} = n_\alpha(\bullet)$. The intrinsic densities $\rho, \rho_\alpha, \rho_{\alpha_j}$ and the bulk densities $\bar{\rho}_\alpha, \bar{\rho}_{\alpha_j}$ are given by

$$\rho = m/v, \qquad \rho_\alpha = \frac{m_\alpha}{v_\alpha}, \qquad \rho_{\alpha_j} = \frac{m_{\alpha_j}}{v_\alpha}, \qquad \bar{\rho}_\alpha = n_\alpha \rho_\alpha, \qquad \bar{\rho}_{\alpha_j} = n_\alpha \rho_{\alpha_j} \tag{10}$$

With the densities defined in (10) the intensive format of (8) follows, i.e.,

$$\rho = \sum_{\alpha} \bar{\rho}_{\alpha}, \qquad \rho_{\alpha} = \sum_{j} \rho_{\alpha_j}, \qquad \sum_{\alpha} n_{\alpha} = 1 \tag{11}$$

The mass averaged velocities, $\mathbf{v}$, and, $\mathbf{v}_{\alpha}$, are defined as the weighted summations of the phase velocities, $\mathbf{v}_{\alpha}$, and constituent velocities, $\mathbf{v}_{\alpha_j}$, respectively, i.e.,

$$\mathbf{v} = \frac{1}{\rho} \sum_{\alpha} \bar{\rho}_{\alpha} \mathbf{v}_{\alpha} \qquad \mathbf{v}_{\alpha} = \frac{1}{\bar{\rho}_{\alpha}} \sum_{j} \bar{\rho}_{\alpha_j} \mathbf{v}_{\alpha_j} \tag{12}$$

Furthermore, definitions of diffusion velocities $\mathbf{w}_{\alpha}, \mathbf{w}_{\alpha_j}$ and a relative velocity $\mathbf{v}_{\alpha,\beta}$ are introduced by

$$\mathbf{w}_{\alpha} = \mathbf{v}_{\alpha} - \mathbf{v}, \qquad \mathbf{w}_{\alpha_j} = \mathbf{v}_{\alpha_j} - \mathbf{v}_{\alpha}, \qquad \mathbf{v}_{\alpha,\beta} = \mathbf{v}_{\alpha} - \mathbf{v}_{\beta} \tag{13}$$

As a consequence of (12) the diffusion velocities are restricted by the following summations

$$\sum_{j} \rho_{\alpha_j} \mathbf{w}_{\alpha_j} = \mathbf{0}, \qquad \sum_{\alpha} \bar{\rho}_{\alpha} \mathbf{w}_{\alpha} = \mathbf{0} \tag{14}$$

3.2 Macroscale balance laws

In this subsection the balance laws adopted in the HMT framework are listed. For a more elaborate description of the balance laws and the interpretations of the containing variables the reader is referred to Hassanizadeh and Gray (1979a,b, 1980); Bennethum (1994); Bennethum and Cushman (1996a,b).

Classical continuum formats of the balance of mass, the balance of linear momentum, the balance of energy, and the entropy production of the mixture are given by

$$\frac{D(\rho)}{Dt} + \rho \nabla \cdot (\mathbf{v}) = 0 \tag{15a}$$

$$\rho \frac{D(\mathbf{v})}{Dt} - \nabla \cdot (\boldsymbol{\sigma}) - \rho \mathbf{b} = \mathbf{0} \tag{15b}$$

$$\rho \frac{D(e^*)}{Dt} - \boldsymbol{\sigma} : \mathbf{d} + \nabla \cdot (\mathbf{q}) + \rho Q = 0 \tag{15c}$$

$$\rho \frac{D(\eta)}{Dt} + \nabla \cdot (\boldsymbol{\varphi}) - \rho \Lambda - \rho b = 0 \tag{15d}$$

Here e^* denotes the total internal energy, $\boldsymbol{\sigma}$ the Cauchy stress tensor, $\mathbf{b}$ the body force vector, $\mathbf{q}$ the heat flux, Q the external source of energy, Λ the entropy production, η the entropy, $\boldsymbol{\varphi}$ the entropy flux, and b the external source of entropy of the mixture.

Each phase and each constituent is viewed as a separate continuum governed by balance laws corresponding to (15), but specific for the considered component. The

balance of mass, the balance of linear momentum, the balance of energy, and the entropy production of phase α are given by

$$\frac{D_\alpha(\bar{\rho}_\alpha)}{Dt} + \bar{\rho}_\alpha \nabla \cdot (\mathbf{v}_\alpha) = \sum_{\beta \neq \alpha} \bar{\rho}_\alpha \hat{e}_\alpha^\beta \tag{16a}$$

$$\bar{\rho}_\alpha \frac{D_\alpha(\mathbf{v}_\alpha)}{Dt} - \nabla \cdot (\bar{\boldsymbol{\sigma}}_\alpha) - \bar{\rho}_\alpha \mathbf{b}_\alpha = \sum_{\beta \neq \alpha} \bar{\rho}_\alpha \hat{\mathbf{T}}_\alpha^\beta \tag{16b}$$

$$\bar{\rho}_\alpha \frac{D_\alpha(e_\alpha^*)}{Dt} - \bar{\boldsymbol{\sigma}}_\alpha : \mathbf{d}_\alpha + \nabla \cdot (\bar{\mathbf{q}}_\alpha) + \bar{\rho}_\alpha Q_\alpha = \sum_{\beta \neq \alpha} \bar{\rho}_\alpha \hat{Q}_\alpha^\beta \tag{16c}$$

$$\bar{\rho}_\alpha \frac{D_\alpha(\eta_\alpha)}{Dt} + \nabla \cdot (\bar{\boldsymbol{\varphi}}_\alpha) - \bar{\rho}_\alpha b_\alpha - \bar{\rho}_\alpha \Lambda_\alpha = \sum_{\beta \neq \alpha} \bar{\rho}_\alpha \hat{\eta}_\alpha^\beta \tag{16d}$$

Here e_α^* denotes the total internal energy, $\boldsymbol{\sigma}_\alpha$ the Cauchy stress tensor, $\mathbf{b}_\alpha$ the body force vector, $\mathbf{q}_\alpha$ the heat flux, Q_α the external source of energy, Λ_α the entropy production, η_α the entropy, $\boldsymbol{\varphi}_\alpha$ the entropy flux, and b_α the external source of entropy of phase α. Furthermore $\hat{e}_\alpha^\beta$ describes the rate of mass gain in phase α from phase β, $\hat{\mathbf{T}}_\alpha^\beta$ describes the rate of linear momentum gain in phase α from phase β, $\hat{Q}_\alpha^\beta$ describes the rate of energy gain in phase α from phase β, and $\hat{\eta}_\alpha^\beta$ describes the rate of entropy gain in phase α from phase β.

The balance of mass, the balance of linear momentum, the balance of energy, and the entropy production of constituent α_j are given by

$$\frac{D_{\alpha_j}(\bar{\rho}_{\alpha_j})}{Dt} + \bar{\rho}_{\alpha_j} \nabla \cdot (\mathbf{v}_{\alpha_j}) = \bar{\rho}_{\alpha_j} \hat{r}_{\alpha_j} + \sum_{\beta \neq \alpha} \bar{\rho}_{\alpha_j} \hat{e}_{\alpha_j}^\beta \tag{17a}$$

$$\bar{\rho}_{\alpha_j} \frac{D_{\alpha_j}(\mathbf{v}_{\alpha_j})}{Dt} - \nabla \cdot (\bar{\boldsymbol{\sigma}}_{\alpha_j}) - \bar{\rho}_{\alpha_j} \mathbf{b}_{\alpha_j} = \bar{\rho}_{\alpha_j} \hat{\mathbf{i}}_{\alpha_j} + \sum_{\beta \neq \alpha} \bar{\rho}_{\alpha_j} \hat{\mathbf{T}}_{\alpha_j}^\beta \tag{17b}$$

$$\bar{\rho}_{\alpha_j} \frac{D_{\alpha_j}(e_{\alpha_j})}{Dt} - \bar{\boldsymbol{\sigma}}_{\alpha_j} : \mathbf{d}_{\alpha_j} + \nabla \cdot (\bar{\mathbf{q}}_{\alpha_j}) + \bar{\rho}_{\alpha_j} Q_{\alpha_j} = \bar{\rho}_{\alpha_j} \hat{Q}_{\alpha_j} + \sum_{\beta \neq \alpha} \bar{\rho}_{\alpha_j} \hat{Q}_{\alpha_j}^\beta \tag{17c}$$

$$\bar{\rho}_{\alpha_j} \frac{D_{\alpha_j}(\eta_{\alpha_j})}{Dt} + \nabla \cdot (\bar{\boldsymbol{\varphi}}_{\alpha_j}) - \bar{\rho}_{\alpha_j} b_{\alpha_j} - \bar{\rho}_{\alpha_j} \Lambda_{\alpha_j} = \sum_{\beta \neq \alpha} \bar{\rho}_{\alpha_j} \hat{\eta}_{\alpha_j}^\beta + \bar{\rho}_{\alpha_j} \hat{\eta}_{\alpha_j} \tag{17d}$$

where e_{α_j} denotes the internal energy, $\boldsymbol{\sigma}_{\alpha_j}$ the Cauchy stress tensor, $\mathbf{b}_{\alpha_j}$ the body force vector, $\mathbf{q}_{\alpha_j}$ the heat flux, Q_{α_j} the external source of energy, Λ_{α_j} the entropy production, η_{α_j} the entropy, $\boldsymbol{\varphi}_{\alpha_j}$ the entropy flux, and b_{α_j} the external source of entropy of constituent α_j. Furthermore $\hat{e}_{\alpha_j}^\beta$ describes the rate of mass gain in constituent α_j from phase β, $\hat{r}_{\alpha_j}$ describes the rate of mass gain in constituent α_j from other constituents in phase α, $\hat{\mathbf{T}}_{\alpha_j}^\beta$ describes the rate of linear momentum gain in constituent α_j from phase β, $\hat{\mathbf{i}}_{\alpha_j}$ describes the rate of linear momentum gain in constituent α_j from other constituents in phase α, $\hat{Q}_{\alpha_j}^\beta$ describes the rate of energy gain in constituent α_j from phase β, $\hat{Q}_{\alpha_j}$ describes the rate of energy gain in constituent α_j from

other constituents in phase α, $\hat{\eta}^{\beta}_{\alpha_j}$ describes the rate of entropy gain in constituent α_j from phase β, and $\hat{\eta}_{\alpha_j}$ describes the rate of entropy gain in constituent α_j from other constituents in phase α.

In order for (15a), (16a), and (17a) to be compatible the following constraints and definitions are imposed

$$\sum_j \rho_{\alpha_j} \hat{r}_{\alpha_j} = 0, \qquad \sum_\alpha \sum_{\beta \neq \alpha} \bar{\rho}_\alpha \hat{e}^{\beta}_{\alpha} = 0, \qquad \rho_\alpha \hat{e}^{\beta}_{\alpha} = \sum_j \rho_{\alpha_j} \hat{e}^{\beta}_{\alpha_j} \tag{18}$$

In order for (15b), (16b), and (17b) to be compatible the following constraints and definitions are imposed

$$\boldsymbol{\sigma}_\alpha = \sum_j \boldsymbol{\sigma}_{\alpha_j} - \rho_{\alpha_j} \mathbf{w}_{\alpha_j} \otimes \mathbf{w}_{\alpha_j} \tag{19a}$$

$$\boldsymbol{\sigma} = \sum_\alpha \bar{\boldsymbol{\sigma}}_\alpha - \bar{\rho}_{\alpha_j} \mathbf{w}_\alpha \otimes \mathbf{w}_\alpha \tag{19b}$$

$$\rho_\alpha \mathbf{b}_\alpha = \sum_j \rho_{\alpha_j} \mathbf{b}_{\alpha_j} \tag{19c}$$

$$\rho \mathbf{b} = \sum_\alpha \bar{\rho}_\alpha \mathbf{b}_\alpha \tag{19d}$$

$$\sum_j \rho_{\alpha_j} \hat{\mathbf{i}}_{\alpha_j} + \rho_{\alpha_j} \hat{r}_{\alpha_j} \mathbf{w}_{\alpha_j} = \mathbf{0} \tag{19e}$$

$$\rho_\alpha \hat{\mathbf{T}}^{\beta}_{\alpha} = \sum_j \rho_{\alpha_j} \hat{\mathbf{T}}^{\beta}_{\alpha_j} + \rho_{\alpha_j} \hat{e}^{\beta}_{\alpha_j} \mathbf{w}_{\alpha_j} \tag{19f}$$

$$\sum_\alpha \sum_{\beta \neq \alpha} \bar{\rho}_\alpha \hat{\mathbf{T}}^{\beta}_{\alpha} + \bar{\rho}_\alpha \hat{e}^{\beta}_{\alpha} \mathbf{w}_\alpha = \mathbf{0} \tag{19g}$$

The total internal energy e^* of the mixture and the total internal energy e^*_α of phase α are defined as

$$e^* = e + \frac{1}{\rho} \sum_\alpha \frac{1}{2} \bar{\rho}_\alpha \mathbf{w}_\alpha \cdot \mathbf{w}_\alpha, \qquad e^*_\alpha = e_\alpha + \frac{1}{\rho_\alpha} \sum_j \frac{1}{2} \rho_{\alpha_j} \mathbf{w}_{\alpha_j} \cdot \mathbf{w}_{\alpha_j} \tag{20}$$

where e and e_α denote the inner parts or the thermal parts of the internal energies of the mixture and of phase α, respectively, and are defined by

$$e = \frac{1}{\rho} \sum_\alpha \bar{\rho}_\alpha e_\alpha, \qquad e_\alpha = \frac{1}{\rho_\alpha} \sum_j \rho_{\alpha_j} e_{\alpha_j} \tag{21}$$

In order for (15c), (16c), and (17c) to be compatible, the following constraints and definitions are imposed

$$\sum_j \left[\rho_{\alpha_j} \hat{Q}_{\alpha_j} + \rho_{\alpha_j} \hat{\mathbf{i}}_{\alpha_j} \cdot \mathbf{w}_{\alpha_j} + \rho_{\alpha_j} \hat{r}_{\alpha_j} (e_{\alpha_j} + \frac{1}{2} \mathbf{w}_{\alpha_j} \cdot \mathbf{w}_{\alpha_j}) \right] = 0 \tag{22a}$$

$$\hat{Q}_\alpha^\beta = \frac{1}{\rho_\alpha}\sum_j \left[\rho_{\alpha_j}\hat{Q}_{\alpha_j}^\beta + \rho_{\alpha_j}\hat{\mathbf{T}}_{\alpha_j}^\beta \cdot \mathbf{w}_{\alpha_j} + \rho_{\alpha_j}\hat{e}_{\alpha_j}^\beta(e_{\alpha_j} - e_\alpha^*\frac{1}{2}\mathbf{w}_{\alpha_j}\cdot\mathbf{w}_{\alpha_j})\right] \tag{22b}$$

$$\sum_\alpha\sum_{\beta\neq\alpha}\left[\bar{\rho}_\alpha\hat{Q}_\alpha^\beta + \bar{\rho}_\alpha\hat{\mathbf{T}}_\alpha^\beta\cdot\mathbf{w}_\alpha + \bar{\rho}_\alpha\hat{e}_\alpha^\beta(e_\alpha^* + \frac{1}{2}\mathbf{w}_\alpha\cdot\mathbf{w}_\alpha)\right] = 0 \tag{22c}$$

$$\mathbf{q}_\alpha = \sum_j\left[\mathbf{q}_{\alpha_j} - \boldsymbol{\sigma}_{\alpha_j}\cdot\mathbf{w}_{\alpha_j} + \rho_{\alpha_j}\mathbf{w}_{\alpha_j}(e_{\alpha_j} + \frac{1}{2}\mathbf{w}_{\alpha_j}\cdot\mathbf{w}_{\alpha_j})\right] \tag{22d}$$

$$\mathbf{q} = \sum_\alpha\left[\bar{\mathbf{q}}_\alpha - \bar{\boldsymbol{\sigma}}_\alpha\cdot\mathbf{w}_\alpha + \bar{\rho}_\alpha\mathbf{w}_\alpha(e_\alpha + \frac{1}{2}\mathbf{w}_\alpha\cdot\mathbf{w}_\alpha)\right] \tag{22e}$$

$$Q_\alpha = \frac{1}{\rho_\alpha}\sum_j\left[\rho_{\alpha_j}Q_{\alpha_j} + \rho_{\alpha_j}\mathbf{b}_{\alpha_j}\cdot\mathbf{w}_{\alpha_j})\right] \tag{22f}$$

$$Q = \frac{1}{\rho}\sum_\alpha\left[\bar{\rho}_\alpha Q_\alpha + \bar{\rho}_\alpha\mathbf{b}_\alpha\cdot\mathbf{w}_\alpha)\right] \tag{22g}$$

The inner part of the entropy of the mixture η and the inner part of the entropy of phase α η_α are defined by

$$\eta = \frac{1}{\rho}\sum_\alpha\bar{\rho}_\alpha\eta_\alpha, \qquad \eta_\alpha = \frac{1}{\rho_\alpha}\sum_j\rho_{\alpha_j}\eta_{\alpha_j} \tag{23}$$

In the same manner the inner part of the entropy production of the mixture Λ and the inner part of the entropy of phase α Λ_α are defined by

$$\Lambda = \frac{1}{\rho}\sum_\alpha\bar{\rho}_\alpha\Lambda_\alpha, \qquad \Lambda_\alpha = \frac{1}{\rho_\alpha}\sum_j\rho_{\alpha_j}\Lambda_{\alpha_j} \tag{24}$$

Finally, in order for (15d), (16d), and (17d) to be compatible the following constraints and definitions are imposed

$$\boldsymbol{\varphi}_\alpha = \sum_j\left[\boldsymbol{\varphi}_{\alpha_j} - \rho_{\alpha_j}\eta_{\alpha_j}\mathbf{w}_{\alpha_j}\right] \tag{25a}$$

$$\boldsymbol{\varphi} = \sum_\alpha\left[\bar{\boldsymbol{\varphi}}_\alpha - \bar{\rho}_\alpha\eta_\alpha\mathbf{w}_\alpha\right] \tag{25b}$$

$$b_\alpha = \frac{1}{\rho_\alpha}\sum_j\rho_{\alpha_j}b_{\alpha_j} \tag{25c}$$

$$b = \frac{1}{\rho}\sum_\alpha\bar{\rho}_\alpha b_\alpha \tag{25d}$$

$$\hat{\eta}_\alpha^\beta = \frac{1}{\rho_\alpha}\sum_j\left[\rho_{\alpha_j}\hat{\eta}_{\alpha_j}^\beta + \rho_{\alpha_j}e_{\alpha_j}^\beta(\eta_{\alpha_j} - \eta_\alpha)\right] \tag{25e}$$

$$\sum_\alpha\sum_{\beta\neq\alpha}\left[\bar{\rho}_\alpha\hat{\eta}_\alpha^\beta + \bar{\rho}_\alpha\hat{e}_\alpha^\beta\eta_\alpha\right] = 0 \tag{25f}$$

$$\sum_j \left[\rho_{\alpha_j}\hat{\eta}_{\alpha_j} + \rho_{\alpha_j}\hat{r}_{\alpha_j}\eta_{\alpha_j}\right] = 0 \tag{25g}$$

It should be noted that when stating the balance equations in this section it was assumed that all components were microscopically non–polar which reduces the balance of angular momentum to the restriction of symmetric Cauchy stress tensors, see also Hassanizadeh and Gray (1979b). For consideration of polar components see e.g., Ehlers and Volk (1999).

3.3 Independent and dependent variables

Depending on what phenomena a model is suppose to capture, a model could be set up on the mixture level, on the phase level, or on the constituent level. Considering a model set up on the constituent level the system of equations will be made up of $6{\cdot}N_\alpha \cdot N_{\alpha_j}$ governing equations (17), where each phase is considered to be made up of the same number of constituents, i.e., N_{α_j}. The unknown variables appearing in these equations are collected in a set $\mathcal{U}$ given by

$$\begin{aligned}\mathcal{U} = \{&n_\alpha, \rho_{\alpha_j}, \mathbf{v}_{\alpha_j}, \mathbf{b}_{\alpha_j}, e_{\alpha_j}, \boldsymbol{\sigma}_{\alpha_j}, \mathbf{q}_{\alpha_j}, Q_{\alpha_j}, \Lambda_{\alpha_j}, \eta_{\alpha_j}, \boldsymbol{\varphi}_{\alpha_j}, b_{\alpha_j} \\ &\hat{e}^\beta_{\alpha_j}, \hat{r}_{\alpha_j}, \hat{\mathbf{T}}^\beta_{\alpha_j}, \hat{\mathbf{i}}_{\alpha_j}, \hat{Q}^\beta_{\alpha_j}, \hat{Q}_{\alpha_j}, \hat{\eta}^\beta_{\alpha_j}, \hat{\eta}_{\alpha_j}\}\end{aligned} \tag{26}$$

As shown in the proceeding subsections these variables are constrained, however the number of unknown still exceeds the number of equations. For this reason a subset of $\mathcal{U}$ is considered as independent variables, i.e., variables that can not be described by other independent variables, while the variables in the remaining subset are considered dependent, or constitutive variables, which are fully defined by the independent variables. In a closed systems of equations, the number of independent variables should be equal to the number of governing equations and constitutive relations should be provided for all constitutive variables.

3.4 Constitutive relations

Derivation of suitable formats of the constitutive relations is not trivial and in attempt to ease this work the following two assumptions are commonly made.

1) Entropy flux proportional to the heat flux

The entropy fluxes and the external sources of entropy are assumed to be proportional to the heat fluxes and the external heat sources, respectively, see also Coleman and Noll (1963); Hassanizadeh and Gray (1979b); Bennethum (1994), i.e.,

$$b_{\alpha_j} = \frac{Q_{\alpha_j}}{\theta_{\alpha_j}}, \qquad \boldsymbol{\varphi}_{\alpha_j} = \frac{\mathbf{q}_{\alpha_j}}{\theta_{\alpha_j}} \tag{27}$$

2) Local thermal equilibrium

For any given time t and any spatial point $\mathbf{x}$ the same absolute temperature is assumed for all phases and constituents, i.e.,

$$\theta_{\alpha_j}(t,\mathbf{x}) = \theta_{\alpha}(t,\mathbf{x}) = \theta(t,\mathbf{x}) \tag{28}$$

This assumption is commonly referred to as the assumption of a, local thermal equilibrium, and should not be confused with the assumption of an isothermal state.

3.4.1 Dissipation inequality

In order to derive a thermodynamically consistent model the Clausius-Duhem inequality is considered for the mixture, i.e.,

$$\rho\Lambda = \sum_{\alpha}\sum_{j} \bar{\rho}_{\alpha_j}\Lambda_{\alpha_j} \geq 0 \tag{29}$$

The Clausius-Duhem inequality is a statement of the second law of thermodynamics and should hold for all parts of the body and for all times, see also Coleman and Noll (1963). The absolute temperature θ is always greater to or equal to zero and the dissipated energy from the system is defined by

$$D = \theta\rho\Lambda = \sum_{\alpha}\sum_{j} \theta\bar{\rho}_{\alpha_j}\Lambda_{\alpha_j} \geq 0 \tag{30}$$

Insertion of (17d), (17c), and (27) into (30) and making use of the constraints in Subsection 3.2 the dissipation inequality may be rewritten as

$$\begin{aligned}
D = \sum_{\alpha} \Bigg\{ & -\bar{\rho}_{\alpha}\left(\frac{D_{\alpha}(A_{\alpha})}{Dt} + \eta_{\alpha}\frac{D_{\alpha}(\theta)}{Dt}\right) \\
& - \frac{\nabla(\theta)}{\theta}\cdot\left[\bar{\mathbf{q}}_{\alpha} + \sum_{j}\left(\bar{\boldsymbol{\sigma}}_{\alpha_j}\cdot\mathbf{w}_{\alpha_j} - \bar{\rho}_{\alpha_j}\mathbf{w}_{\alpha_j}(A_{\alpha_j} + \frac{1}{2}\mathbf{w}_{\alpha_j}\cdot\mathbf{w}_{\alpha_j})\right)\right] \\
& + \left(\bar{\boldsymbol{\sigma}}_{\alpha} + \sum_{j}\bar{\rho}_{\alpha_j}\mathbf{w}_{\alpha_j}\otimes\mathbf{w}_{\alpha_j}\right) : \mathbf{d}_{\alpha} \\
& + \sum_{j}\left(\bar{\boldsymbol{\sigma}}_{\alpha_j} - \bar{\rho}_{\alpha_j}A_{\alpha_j}\mathbf{I}\right) : (\nabla\otimes\mathbf{w}_{\alpha_j}) \\
& - \sum_{j}\left(\nabla(A_{\alpha_j}\bar{\rho}_{\alpha_j}) + \sum_{\beta\neq\alpha}\bar{\rho}_{\alpha_j}(\hat{\mathbf{T}}^{\beta}_{\alpha_j} + \hat{\mathbf{i}}_{\alpha_j})\right)\cdot\mathbf{w}_{\alpha_j} \\
& - \sum_{\beta\neq\alpha}\bar{\rho}_{\alpha}\left(\hat{\mathbf{T}}^{\beta}_{\alpha}\cdot\mathbf{w}_{\alpha} + \hat{e}^{\beta}_{\alpha}(A_{\alpha} + \frac{1}{2}\mathbf{w}_{\alpha}\cdot\mathbf{w}_{\alpha})\right) \\
& - \sum_{j}\sum_{\beta\neq\alpha}[\bar{\rho}_{\alpha_j}\hat{e}^{\beta}_{\alpha_j} + \bar{\rho}_{\alpha_j}\hat{r}_{\alpha_j}]\frac{1}{2}\mathbf{w}_{\alpha_j}\cdot\mathbf{w}_{\alpha_j}\Bigg\} \geq 0
\end{aligned} \tag{31}$$

In this expression the Helmholtz potential A_{α_j} of constituent α_j and the inner part of the Helmholtz potential A_α of phase α were introduced as

$$A_{\alpha_j} = e_{\alpha_j} - \theta\eta_{\alpha_j}, \qquad A_\alpha = \frac{1}{\rho}\sum_j \rho_j A_{\alpha_j} \tag{32}$$

In order to guarantee that the constitutive relations do not contradict any of the balance laws, Liu's Lagrange multiplier method is adopted, Liu (1972). Adopting the Liu's Lagrange multiplier method the balance laws may be weakly enforced through an expansion of the dissipation inequality, according to

$$D^E = D + \sum_i \lambda_i r_i \geq 0 \tag{33}$$

where λ_i denotes a Lagrange multiplier that is energy conjugated with restriction r_i. Deriving a thermodynamically consistent model, all constitutive relations must be chosen such that the expanded dissipation inequality (33) is unconditionally fulfilled. This is not very restrictive and the optional constitutive relations are still many. Having a structured procedure for how to exploit the dissipation inequality is therefore of great assistance when suggesting suitable constitutive relations. The procedure adopted in the present thesis follows that presented in e.g., Sullivan (2013).

3.5 Adopting a HMT approach to model paperboard

A crucial step, when adopting a HMT framework to model a multiphysical process, is the decomposition of the mixture into phases and constituents. This choice is not trivial and will depend on microscopic structure of the material, and also on what processes the model should be able to capture. Considering paperboard, a fairly general decomposition is shown in Figure 8.

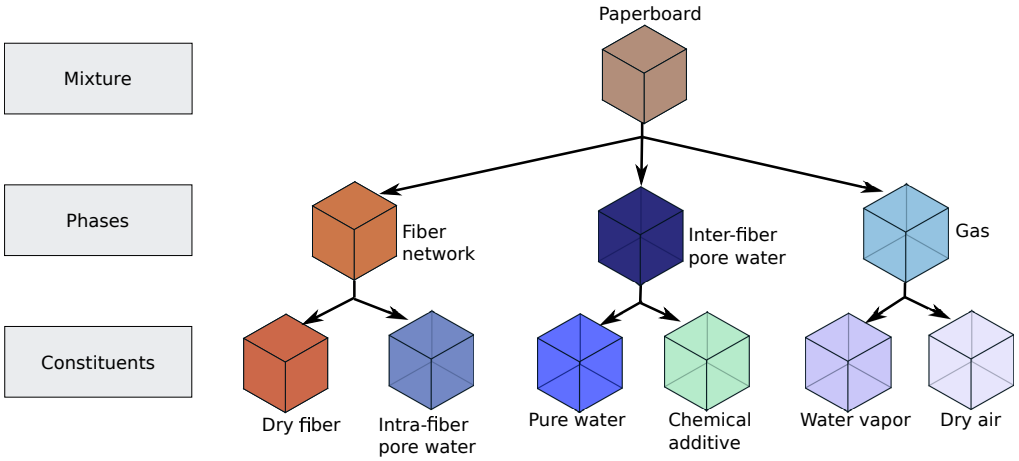

Figure 8: Illustration of an optional two scale decomposition of paperboard.

With the decomposition in Figure 8 it would be possible to model the difference in energy levels between the intra–fiber water and the water in the lumen and the inter–fiber pores that was discussed in Subsection 2.2. Furthermore the sorption properties

could be separated into adsorbtion/desorption (mass exchange between the intra–fiber pore water and the water vapor), evaporation/condensation (mass exchange between the pure water in the inter–fiber pores and the water vapor) and absorbtion (mass exchange between the intra–fiber pore water and pure water in the inter–fiber pores). The effect of chemical additives in the inter–fiber pore water could also be investigated.

In the presented thesis, the effect of chemical additives is not investigated and this constituent is not included. Furthermore, the presented thesis treats moisture ratios below the HMC and all liquid water is considered to be bound in or to the fibers. The liquid water may still be viewed as a a combination of the intra–fiber pore water and the inter–fiber pore water as suggested in Figure 8, however to simplify the model the liquid water may also be viewed as a separate phase describing the averaged properties of both these components. In Papers A–D the simplified approach is adopted and the decomposition of paperboard assumed in all papers is depicted in Figure 9.

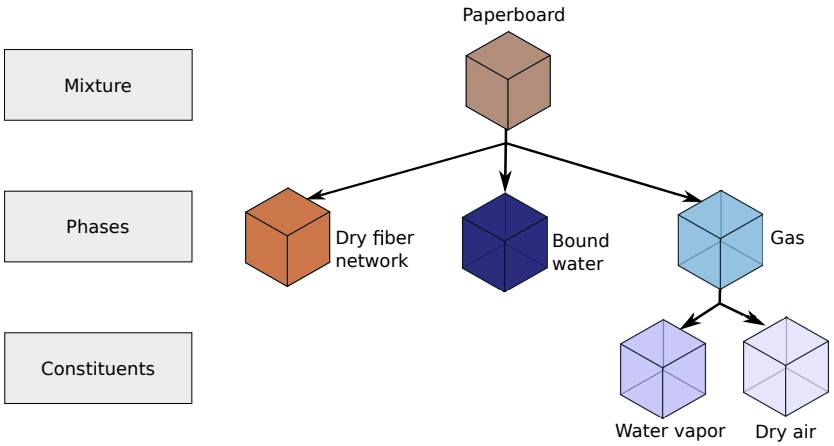

Figure 9: Decomposition of paperboard assumed in the present thesis.

The benefits of choosing the decomposition in Figure 9 compared to that in Figure 8 is that the system of equations governing the response of the paperboard is reduced significantly. However, evidently the fewer components also limits the processes the model is able to describe. A consequence of the simplified decomposition is that no separation is made between the adsorption/desorption and the condensation/evaporation i.e., in Papers A–D the mass exchange between the bound water and the water vapor describes the average of both the adsorption/desorption and the condensation/evaporation.

4 Numerical examples

In order to illustrate the benefits of modeling paperboard in a HMT framework, the derived models have been used to predict the response of paperboard during three different loading conditions.

4.1 Storing of paperboard rolls

The properties of paperboard are highly affected by moisture, see Section 2.2. For the packaging industry it is therefore very important to know and control the moisture ratio of the paperboard used in production. In Paper A, the transports of mass and energy are investigated for paperboard rolls during storing in a climate with a varying relative humidity. The geometry of the assumed paperboard roll is shown in Figure 10(a) and due to the rotational symmetry of the roll the computational domain is reduced to the 2D plane shown in Figure 10(b).

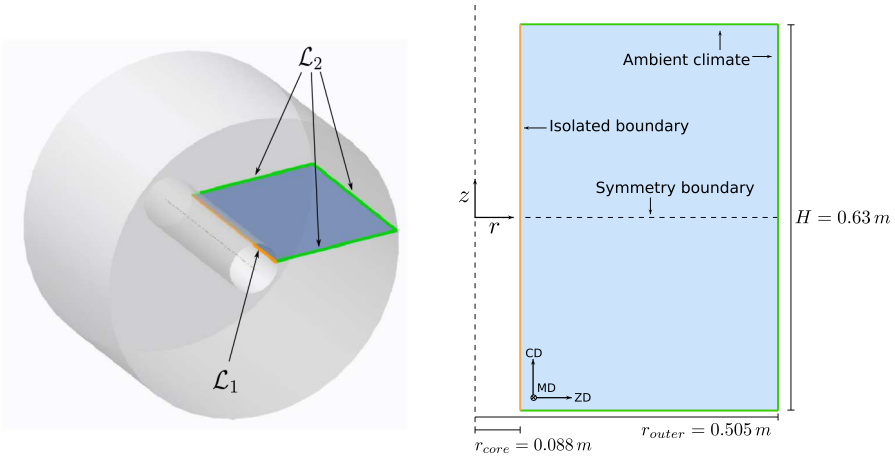

(a) (b)

Figure 10: Graphic representation of the modeled section of a paperboard roll

Initially the roll is assumed to be in equilibrium with the ambient climate and when the simulation starts the relative humidity of the ambient climate is ramped up from 50% to 80%. The predicted moisture distributions in the radial and axial directions are shown in Figures 11(a) and 11(b), respectively.

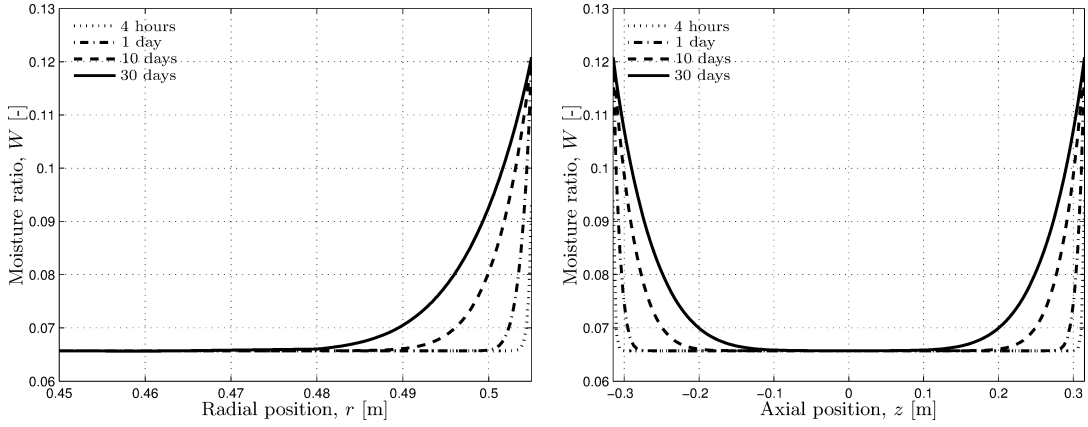

(a) (b)

Figure 11: **a**) Simulated moisture profile in radial direction at $z = 0$ and **b**) axial moisture profile at $r = r_{core}$, at different times for a paperbaord roll subjected to a relative humidity ramp 50% to 80%

From Figure 11 it is observed that the paperboard roll has obtained a non–homogeneous moisture distribution. This information is important since this will imply that the different layers paperboard from the roll will have different properties.

In Figure 12(a) the development of the local relative humidity inside the board is shown. It is noticed that the moisture ratio does not follow the sorption isotherm which means that the mass exchange between the bound water and the water vapor is dynamic. The driving force of the mass exchange is shown in 12(b), where it is observed that the driving force increase as the ambient relative humidity increase and then decrease when the ambient relative humidity is held constant.

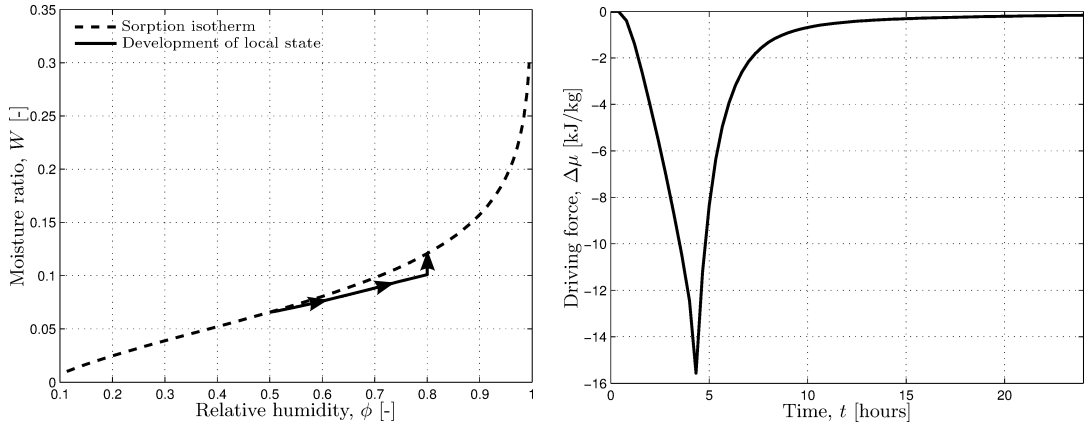

(a) (b)

Figure 12: **a**) Development of local relative humidity at the boundary at $z = 0, r = r_{outer}$ and **b**) chemical potential difference plotted against time, at the same position for a paperboard roll subjected to a relative humidity ramp 50% to 80%

4.2 Transversal sealing

In Paper C, numerical simulations of the transversal sealing of a food package are considered. This is a complex process and the simulated sealing presented in Paper C is simplified. In the simplified sealing, focus is on investigating the response of moist paperboard during a simultaneous compression and heating. The idealized sealing considered is depicted in Figure 13(a). Due to the symmetry the computational domain is reduced to the area enclosed by the dashed lines.

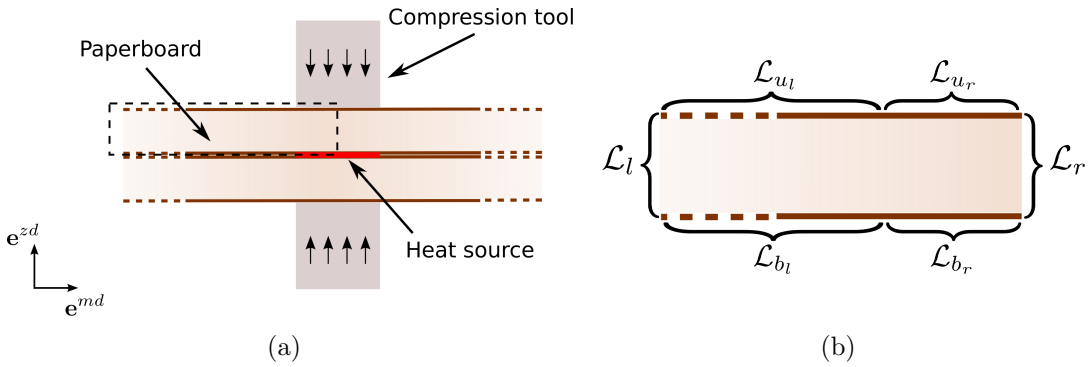

(a) (b)

Figure 13: **a**) Illustration of the problem setup where the dashed lines indicate the computational domain, **b**) labeling of the boundary decomposition of the computational domain.

The boundary conditions considered during the simulations are given by; symmetry conditions on $\mathcal{L}_{b_l}, \mathcal{L}_{b_r}$, and $\mathcal{L}_r$, constant primary variables on $\mathcal{L}_l$, Newton cooling and no mass flux through $\mathcal{L}_{u_l}$ and $\mathcal{L}_{u_r}$. Furthermore the temperature on $\mathcal{L}_{b_r}$ is ramped up from 298.15 K to 548.15 K and $\mathcal{L}_{u_r}$ is compressed 40% of the boards initial thickness. Different simulation times and initial moisture ratios are considered. The distributions of the absolute temperature, the water vapor pressure, the out–of–plane stresses, and the volume specific change in liquid mass for a simulation with the initial moisture ratio $W^0 = 0.1$ and the total simulation time $t = 0.1$ s are shown in Figure 14.

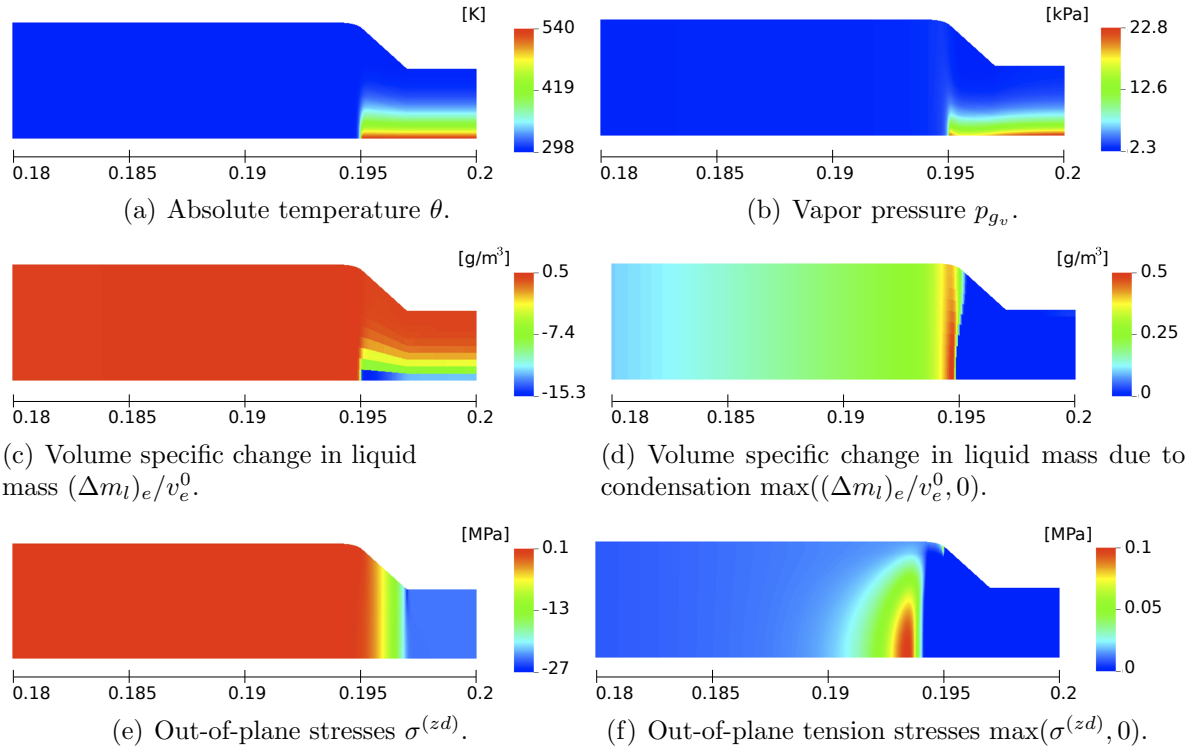

(a) Absolute temperature θ.

(b) Vapor pressure p_{g_v}.

(c) Volume specific change in liquid mass $(\Delta m_l)_e / v_e^0$.

(d) Volume specific change in liquid mass due to condensation $\max((\Delta m_l)_e / v_e^0, 0)$.

(e) Out-of-plane stresses $\sigma^{(zd)}$.

(f) Out-of-plane tension stresses $\max(\sigma^{(zd)}, 0)$.

Figure 14: Predicted distributions in a board with the initial moisture ratio $W^0 = 0.1$ after a local compression of 40% and heating of 250 K in 0.1 seconds.

The results obtained from the idealized sealing simulations show that the simultaneous heating and compression of the paperboard will result in a non–homogeneous moisture distribution. From Figures 14(c) and 14(d) it is observed that the drying area is very local and that it is followed by an condensation front where the moisture ratio actually is increased. The compression of the board results in out–of–plane compression stresses, see Figure 14(e), however it will also contribute to an increased gas pressure. In Figure 14(f) it is observed that the combined effect of the compression, the increased temperature, and the drying will actually result in out–of–plane tension stresses that are in the same order of magnitude as the out–of–plane failure stress of paperboard.

4.3 Blister test

In Paper D, numerical and experimental investigations of a blister test are made. The blister test is a non–standardized test method to test the quality of aseptic package materials. The main idea of a blister test is to expose an aseptic package material with hot air jet and measure the time until the package material experiences an internal failure. The internal failure will cause the surface of the package material to elevate. An illustration of the experimental set up of a blister test is shown in Figure 15.

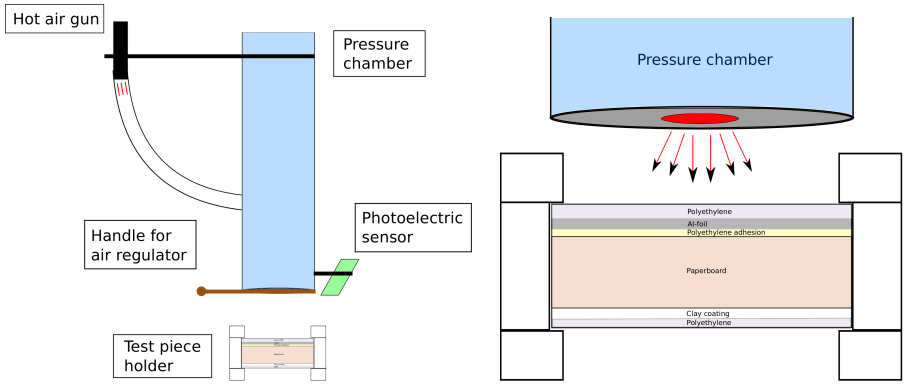

Figure 15: **a**) Illustration of the experimental blister test setup **b**) Zoom in on the test piece holder.

Simulation results of the evolution of the out–of–plane stress distributions are shown in Figure 16. Three different ambient climates were investigated where the board initially was in equilibrium with the ambient climate. In these simulations the package material was described as a layered structure with paperboard as the main component. On top of the paperboard one layer of LDPE and one layer of aluminium were added. The focus in Paper D was, however, on the response of the paperboard and the purpose of the LDPE and aluminium layers was merely to provide more realistic boundary conditions for the paperboard. The stress levels in these layers are therefore not of interest in this work and these layer have been given the value zero in Figure 16.

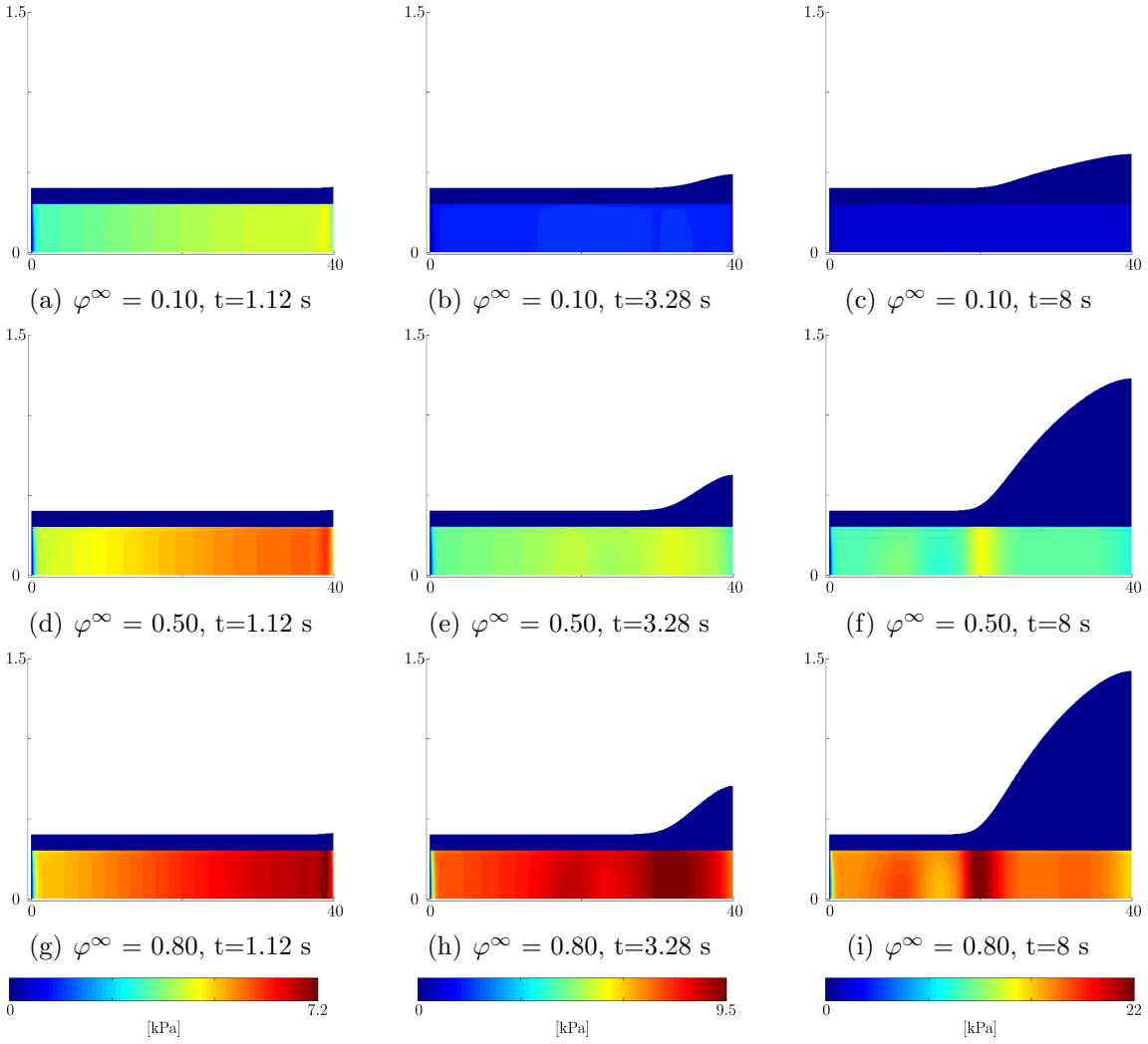

Figure 16: Predicted distributions of the out–of–plane stresses $\sigma^{(zd)} = \mathbf{e}^{(zd)} \cdot \boldsymbol{\sigma} \cdot \mathbf{e}^{(zd)}$ for **a**)-**c**) RH=10, **d**)-**f**) RH=50, and **g**)-**i**) RH=80. The md and zd axis are shown in mm.

The out–of–plane tension stresses observed in Figure 16 are a consequence of an increased gas pressure inside the paperboard. The pressure increase partly stems from the explicit dependence on temperature in the ideal gas law, but is also highly influenced by the mass exchange between the bound water and the water vapor. In Figure 16, it is observed that the hight of the blisters differs depending on the initial moisture ratio of the board. The difference in heights is a consequence of different rates of mass exchange between bound water and water vapor as well as the difference in saturation. Considering the magnitude of the out–of–plane tension stress distributions in Figure 16 it is concluded that the paperboard will experience an elastic stress–strain response during the blister test.

5 Future work

The model presented in this thesis is derived in a hybrid mixture theory framework. One of the benefits of adopting a mixture theory framework is that it provides constitutive relations for several complex physical phenomena within the paperboard. However, a consequence of introducing these constitutive relations is that the calibration of the model becomes tedious. Many of the processes are coupled and the process of calibration is not always trivial. In the authors opinion, the main focus of future work should be aimed towards calibration of the provided model.

Another area that also should be considered in the future work is to include the explicit dependencies of moisture and heat in the stress–strain response. In addition the viscous nature of paperboard should also be included in the stress–strain response.

6 Summary of the papers

Paper A: In Paper A, a model describing the transport of moisture and heat in paperboard is developed. The model is derived in a hybrid mixture theory framework and considers the board to be composed of three immiscible phases; a network of cellulose fibers, liquid water bound in or to the fibers, and moist air in the inter–fiber pores. The model considers the dynamic mass exchange between the bound water and the water vapor and assumes that the transport processes are relatively slow. In Paper A it is also shown how the derived model may be used to predict the evolutions of the moisture and heat distributions in paperboard rolls during storing in climates with a varying relative humidity.

Paper B: In Paper B, the response of moist paperboard exposed to significant temperature and pressure changes during a short period of time is investigated. In such an environment considerable gas pressure gradients are expected and the inter–fiber gas seepage is considered as nonlinear laminar flow. The model derived in Paper A, is therefore extended to incorporate nonlinear transport processes. In Paper B, the model presented in Paper A is also modified to include plastic deformations in a large strain setting.

Paper C: The system of equations derived in Paper B is, in Paper C, closed by providing explicit formats for all constitutive relations. All constitutive relations are considered to be orthotropic and depend on the current ratios of moisture and air in the board. In Paper C it is also shown how an advanced orthotropic elasto–plastic stress–strain model may be included in the generic framework derived in Paper B. The complete model presented in Paper C is used to simulate the response of moist paperboard during a transversal sealing process.

Paper D: In Paper D, experimental investigations are made of the static and dynamic desorption as well as the in–plane permeability. The model developed in Papers A, B, and C is adopted and the in–plane permeability as well as the static and dynamic sorption properties are recalibrated. The model is used to analyse the response of paperboard during a blister test. The blister test is also investigated experimentally. The analyses of the model and the experimental investigations are compared and it is concluded that the initiation of a blister is caused primarily due to melting of the polyethylene adhesion while expansion of the blister is primarily governed by the moisture distribution in the board.

References

E. Baggerud, Modelling of Mass and Heat Transport in Paper, Ph.D. thesis, Lund University, 2004.

J. C. Bénet, A. Ramirez-Martinez, F. Ouedraogo, F. Cherblanc, Measurment of chemical potential of a liquid in porous media, Journal of Porous Media 15 (2012) 1019–1029.

M. Petterson, S. Stenström, Experimental evaluation of electric infrared dryers, Tappi Journal 83 (2000) 89–106.

A. Venkateswaran, Sorption of aqueous and nonaqueous media by wood and cellulose, Chemical Reviews 70 (1970) 619–637.

J. Eriksson, S. Ormarsson, H. Petersson, Finite-element analysis of coupled nonlinear heat and moisture transport in wood, Numerical Heat Transfer, Part A : Applications 50 (2006) 851–864.

L. S. Bennethum, Macroscopic Flow Potentials in Swelling Porous Media, Transport in Porous Media 94 (2012) 47–68.

S. M. Hassanizadeh, W. G. Gray, High Velocity Flow in Porous Media, Transport in Porous Media 2 (1987) 521–531.

L. S. Bennethum, T. Giorgi, Generalized Forchheimer Equation for Two-Phase Flow Based on Hybrid Mixture Theory, Transport in Porous Media 26 (1997) 261–275.

B. Market, Porous Media Viscoelasticity with Application to Polymeric Foams, Ph.D. thesis, Universitat Stuttgart, 2005.

M. Landervik, R. Larsson, Pore-gas interaction in foams at finite deformation using staggered solution techniques, Computer methods in applied mechanics and engineering 197 (2007) 148–159.

M. Rigdahl, H. Andersson, L. Salmen, H. Hollmark, The Influence of Moisture on the Stiffness of Paper in Terms of Network Mechanics, Fibre Science and Technology 20 (1984) 1–11.

E. Linvill, S. Östlund, The Combined Effect of Moisture and Temperature on the Mechanical Response of Paper, Experimental Mechanics 54 (2014) 1329–1341.

E. Linvill, Development of Finite Element Models for 3D Forming Processes of Paper and Paperboard, 2015.

L. Salmén, A. M. Olsson, Physical properties of cellulosic materials related to moisture changes, Wood Science and Technology 50 (2016) 81–89.

M. Östlund, Modeling the Influence of Drying Conditions on the Stress Buildup During Drying of Paperboard, Journal of Engineering Materials and Technology 128 (2006) 495–502.

E. Bosco, R. H. J. Peerlings, M. G. D. Geers, Predicting hygro-elastic properties of paper sheets based on an idealized model of the underlying fibrous network, International Journal of Solids and Structures (2015a) 43–52.

E. Bosco, M. V. Bastawrous, R. H. J. Peerlings, J. P. M. Hoefnagels, M. G. D. Geers, Bridging network properties to effective hygro-expansivity of paper: experiments and modelling, Philosophical Magazine 95 (2015b) 3385–3401.

E. Bosco, R. H. J. Peerlings, M. G. D. Geers, Explaining irreversible hygroscopic strains in paper: a multi-scale modelling study on the role of fibre activation and micro-compressions, Mechanics of Materials 91 (2015c) 76–94.

M. Karlsson, S. Stenström, Static and Dynamic Modeling of Carboard Drying Part 1: Theoretical Model, Drying Technology 23 (2005) 143–163.

M. F. C. Lucisano, On Heat and Paper: From Hot Pressing To Impuls Technology, Ph.D. thesis, Royal Institute of Technology Stockholm, 2002.

S. A. Lavrykov, B. V. Ramarao, Thermal Properties of Copy Paper Sheets, Drying Technology 30 (2012) 197–311.

N. L. Salmén, E. L. Back, Simple stress-strain measurements on dry papers from 25° C to 250 ° C, Svensk Papperstidning 80 (1977) 178–183.

M. Wallmeier, E. Linvill, M. Hauptmann, J. P. Majschak, S. Östlund, Explicit FEM analysis of the deep drawing of paperboard, Mechanics of Materials 89 (2015) 202–215.

N. Stenberg, On the Out-of-Plane Mechanical Behaviour of Paper Materials, Ph.D. thesis, Royal Institute of Technology Stockholm, 2002.

Q. S. Xia, M. C. Boyce, D. M. Parks, A constitutive model for the anisotropic elastic-plastic deformation of paper and paperboard, International Journal of Solids and Structures 39 (2002) 4053–4071.

M. Nygårds, M. Just, J. Tryding, Experimental and numerical studies of creasing of paperboard, International journal of solids and structures 46 (2009) 2493–2505.

E. Borgqvist, Continuum modeling of the mechanical response of paper-based materials, Ph.D. thesis, Lund University, 2016.

S. Borodulina, A. Kulachenko, S. Galland, M. Nygårds, Stress-strain curve of paper revisited, Nordic Pulp an Paper Research Journal 27 (2012) 318–328.

E. Borgqvist, T. Lindström, J. Tryding, M. Wallin, M. Ristinmaa, Distortional hardening plasticity model for paperboard, International Journal of Solids and Structures 51 (2014) 2411–2423.

E. Borgqvist, M. Wallin, M. Ristinmaa, J. Tryding, An anisotropic in-plane and out-of-plane elasto-plastic continuum model for paperboard, Composite Structures 126 (2015) 184–195.

E. Borgqvist, M. Wallin, J. Tryding, M. Ristinmaa, E. Tudisco, Localized Deformation in Compression and Folding of Paperboard, Packaging Technology and Science 29 (2016) 397–414, ISSN 1099-1522.

C. Hyll, H. Vomhoff, M. Nygårds, Analysis of the plastic and elastic energy during the deformation and rupture of paper sample using thermography, Nordic Pulp an Paper Research Journal 27 (2012) 329–334.

P. Mäkelä, S. Östlund, Orthotropic elastic-plastic material model for paper materials, International journal of solids and structures 40 (2003) 5599–5620.

R. J. Atkin, R. E. Crane, Continuum Theories of Mixtures: Basic Theory and Historical Development, The Quarterly Journal of Mechanics and Applied Mathematics 29.

R. M. Bowen, Part I - Theory of Mixtures, in: A. C. Eringen (Ed.), Continuum Physics, Academic Press, 1–127, 1976.

R. de Boer, W. Ehlers, A Historical Review of the Formulation of Porous Media Theories, Acta Mechanica 74 (1988) 1–8.

R. de Boer, Development of Porous Media Theories - A Brief Historical Review, Tranport in Porous Media 94 (1992) 155–164.

K. R. Rajagopal, L. Tao, Mechanics of mixtures , World Scientific, 1995.

R. de Boer, Theory of Porous Media Highlights in Historical Development and Current State, Springer-Verlag Berlin Heidelberg, 2000.

S. Achanta, J. H. Cushman, M. R. Okos, On multicomponent, multiphase thermomechanics with interfaces, Int. J Engng Sci 32 (1994) 1717–1738.

M. Hassanizadeh, W. G. Gray, General conservation equations for multi-phase systems: 1. Averaging procedure, Advances in Water Resources 2 (1979a) 131–144.

M. Hassanizadeh, W. G. Gray, General conservation equations for multi-phase systems: 2. Mass, momenta, energy, and entropy equations Averaging procedure, Advances in Water Resources 2 (1979b) 191–203.

M. Hassanizadeh, W. G. Gray, General conservation equations for multi-phase systems: 3. Constitutive theory for porous media flow, Advances in Water Resources 32 (1980) 25–40.

L. S. Bennethum, Multiscale, hybrid mixture theory for swelling systems with interfaces, Ph.D. thesis, Purdue University, 1994.

L. S. Bennethum, J. H. Cushman, Multiscale, hybrid mixture theory for swelling systems-I: Balance Laws, International Journal of Engineering Science 34 (1996a) 125–145.

L. S. Bennethum, J. H. Cushman, Multiscale, hybrid mixture theory for swelling systems-II: Constitutive theory, International Journal of Engineering Science 34 (1996b) 147–169.

S. M. Hassanizadeh, W. G. Gray, Mechanics and thermodynamics of multiphase flow in porous media including interphase boundaries, Advances in Water Resources 13 (4) (1990) 169–186.

W. Ehlers, W. Volk, Localization Phenomena in Liquid-Saturated and Empty Porous Solids, Transport in Porous Media 34 (1999) 159–177.

B. D. Coleman, W. Noll, The thermodynamics of elastic materials with heat conduction and viscosity, Archive for Rational Mechanics and Analysis 13 (1) (1963) 167–178, ISSN 1432-0673.

I. S. Liu, Method of Lagrange multipliers for exploitation of the entropy principle, Archive for Rational Mechanics and Analysis 46 (1972) 131–141.

E. R. Sullivan, Heat and moisture transport in unsaturated porous media: acoupled model in terms of chemical potential, Ph.D. thesis, 2013.

Paper A

Marcus Alexandersson, Henrik Askfelt, and Matti Ristinmaa

Triphasic model of heat and moisture transport with internal mass exchange in paperboard.

Transport in Porous Media, 112 (2016) 381–408

Triphasic Model of Heat and Moisture Transport with Internal Mass Exchange in Paperboard.

Marcus Alexandersson[a], Henrik Askfelt[a], and Matti Ristinmaa[a]

[a] Division of Solid Mechanics, Lund University

P.O. Box 118, S-221 00 Lund, Sweden

Abstract

Mixture theory is used to derive a triphasic model to describe processes in paperboard consisting of solid fiber, bound water and gas. The gas is viewed as a miscible mix of the two constituents dry air and water vapor. The governing equations are mass conservation laws for bound water, dry air, water vapor and mixture energy balance. Constitutive relations are found by exploiting the macroscale dissipation inequality. Resulting constitutive equations include Fickian diffusion of water vapor and dry air, Darcian flow for gas and Fourier heat conduction for the mixture. Mass exchange between bound water and water vapor due to adsorption/desorption is driven by the difference in chemical potential. The interaction function is based on equilibrium considerations for the bound water–water vapor system. From the description of the sorption isotherm, expressions for net isosteric heat and free energy related to water–fiber interaction are derived. The resulting thermodynamically consistent model is used to simulate moisture and heat dynamics for paperboard rolls. Simulation results are presented for a paperboard roll with anisotropic material properties subjected to a change in ambient relative humidity from 50% to 80%.

Nomenclature

Latin Symbols

a_w	Water activity (-).
a^{dir}	Parameter for intrinsic permeability in material direction *dir* (-).
A	Sorption isotherm parameter (J/mol).
A_α, A_{α_j}	Specific Helmholtz free energy (J/kg).
$\boldsymbol{b}_\alpha$, $\boldsymbol{b}_{\alpha_j}$	Specific body force (N/kg).
B	Sorption isotherm parameter (-).
c^v_α, $c^v_{\alpha_j}$	Isochoric heat capacity (J/kg-K).
C	Sorption isotherm parameter (J/kg).
$\boldsymbol{d}_\alpha$	Rate of deformation (1/s).
D, D^*, D^{n_1}, D^{n_2}, D^d	Rate of energy dissipation per unit volume (W/m^3).
$\boldsymbol{D}_{\alpha_j}$	Diffusivity tensor (s).
$\hat{e}^\beta_\alpha$, $\hat{e}^\beta_{\alpha_j}$	Rate parameter for mass gain from phase β (1/s).
$\hat{E}_{\alpha_j}$	Rate parameter for energy gain from other constituents in α (J/kg-s).
f	Specific free energy related to water–fiber interaction (J/kg).
G_α	Specific Gibbs free energy (J/kg).
h_α, h_{α_j}	Specific enthalpy (J/kg).
H	Roll width (m).
$\hat{\boldsymbol{i}}_{\alpha_j}$	Rate of gain of linear momentum (m/s^2).
$\boldsymbol{I}$	Identity matrix (-).
$\boldsymbol{K}$	Thermal conductivity tensor (W/m-K).
$\boldsymbol{K}^p_{\beta,\alpha}$	Intrinsic permeability tensor (m^3-s/kg).
k_{ser}, k_{par}, k_α	Thermal conductivity (W/m-K).
$\mathcal{L}_i$	Boundary segment i (m).
M_{g_j}	Molar mass (kg/mol).
dm, dm_α, dm_{α_j}	Mass of component in REV (kg).
$\bar{\boldsymbol{n}}$	Outward normal (-).
n_α	Volume fraction (-).
p_α, p_{α_j}	Pressure (N/m^2)
$p^{eq}_{g_v}$	Equilibrium vapor pressure (N/m^2).
$p^{sat}_{g_v}$	Saturation vapor pressure (N/m^2).
$q^n_{g_v}, q^n_{g_a}$	Boundary combined mass flux (kg/m^2-s)
q^n_θ	Boundary heat flux (W/m^2)
$\boldsymbol{q}_\alpha$, $\boldsymbol{q}_{\alpha_j}$	Heat flux (W/m^2).
$\tilde{\boldsymbol{q}}$	Combined heat flux (W/m^2).
$\hat{Q}^\beta_{\alpha_j}$	Rate parameter for energy gain from phase β (W/kg).

r	Spatial coordinate (m).
r_α, r_{α_j}	External heat source (W/kg).
$\hat{r}_{\alpha_j}$	Rate of mass gain from other constituents in α (1/s).
r_{core}, r_{outer}	Paperboard roll radius (m).
R	Universal gas constant (J/mol-K).
$\hat{\boldsymbol{T}}_\alpha^\beta$, $\hat{\boldsymbol{T}}_{\alpha_j}^\beta$	Rate parameter for gain of linear momentum from phase β (m/s^2).
t, t_r	Time (s).
u_α, u_{α_j}	Specific internal energy (J/kg).
dv, dv_α	Volume of components in REV (m^3).
$\boldsymbol{v}$, $\boldsymbol{v}_\alpha$, $\boldsymbol{v}_{\alpha_j}$	Velocity (m/s).
$\boldsymbol{v}^{\beta,\alpha}$	Velocity of β relative to α (m/s).
$\boldsymbol{w}_\alpha$, $\boldsymbol{w}_{\alpha_j}$	Diffusive velocity (m/s).
W	Moisture ratio (-).
z	Spatial coordinate (m).

Greek Symbols

ζ	Rate coefficient for mass transfer (kg-s/m^5).
η_α, η_{α_j}	Specific entropy (J/kg-K).
θ	Absolute temperature (K).
$\lambda_\alpha, \lambda_{\alpha_j}$	Lagrangian multiplier (J/kg).
$\boldsymbol{\Lambda}_w$	Lagrangian multiplier (J/kg).
μ_α, μ_{α_j}	Specific chemical potential (J/kg).
$\bar{\mu}_\alpha$, $\bar{\mu}_{\alpha_j}$	Dynamic viscosity (Pa-s)
ρ, ρ_α, ρ_{α_j}	Intrinsic density (kg/m^3).
$\boldsymbol{\sigma}_\alpha$, $\boldsymbol{\sigma}_{\alpha_j}$	Stress (N/m^2).
$\hat{\boldsymbol{\tau}}_\alpha$, $\hat{\boldsymbol{\tau}}_{\alpha_j}$	Total rate of gain of linear momentum per unit volume (N/m^3).
ϕ	Relative humidity (-).
ω_i	Arbitrary weight function (-).
Ω_s	Solid phase domain (m^2).
$\partial\Omega_s$	Boundary of solid phase domain (m).

Superscripts and Subscripts

$(\bullet)^o$	State without interactions.
$(\bullet)^*$	Fixed reference state.
$(\bullet)_\alpha$	Property of phase α.
$(\bullet)_{\alpha_j}$	Property of constituent j in phase α.
$(\bullet)_\infty$	Property of ambient atmosphere
$(\bullet)_0$	Property at initial state

1 Introduction

Due to its relatively low cost and accessibility paperboard has numerous engineering applications including the use as base material in food containers. Chemically and mechanically treated wood fibres are the main components in paperboard. Self bonding of the fibers upon water removal in manufacturing creates a porous fiber network. The nature of the wood fibers results in a high affinity towards water. Interactions between water molecules and fibers effect the structure, strength and stiffness of the fiber network. Changes in mechanical properties influence the processability of the board. Spatial variations of moisture and temperature throughout a board result in locally different response to load and may compromise the package quality. Too low moisture increases risk of crack formation and too high moisture effects creasing and folding operations negatively.

At normal atmospheric conditions the pores are filled with moist air and no continuous water phase is present. In the hygroscopic region water molecules are tightly bonded to the fibers. The high degree of interaction changes the physical properties of water and the hygroscopic water behaves different from free water (Baggerud, 2004). Equilibrium moisture sorption isotherms relate the amount of equilibrium hygroscopic water (moisture) to the relative humidity and temperature of the surrounding. Adsorbing water to fibers releases heat greater than the heat released if the vapor would condense but not interact with fibers. The heat above the latent heat is referred to as net isosteric heat of sorption.

Paperboard is considered to be orthotropic where the symmetry directions are machine direction (MD), cross–machine direction (CD) and thickness direction (ZD). Board manufacturing results in fiber orientation predominantly in the plane MD–CD where fiber alignment is favored in MD causing a high degree of anisotropy.

Paper and paperboard models including diffusional transport of vapor and liquid as well as sorption dynamics in an isothermal setting are found in works by Bandyopadhyay et al. (2000, 2002). Simultaneous heat and mass transport during sorption in paper sheets has been addressed by Foss et al. (2003) and Zapata et al. (2013). Karlsson and Stenström (2005) developed models for coupled heat and moisture problems for paperboard drying applications. Baggerud (2004) and Östlund (2006) extended the paper drying models to include out of plane shrinkage.

Models for thermo–hydro–mechanical problems in other porous media applications including mass exchange have been derived by numerous authors, e.g., Graf (2008); Schrefler (2002); Sullivan (2013); Jussila (2007) developed general thermodynamically consistent models with focus on geological materials and applications. Ristinmaa et al. (2011) presented a mixture theory based thermoelasto–plastic model including flow and mass exchange with aim towards biomechanical, concrete and wood type materials.

In this work hybrid mixture theory (HMT) is adopted to model features of the porous nature of paperboard. The theory was developed by Achanta et al. (1994), Bennethum and Cushman (1996a,b) Hassanizadeh and Gray (1979a,b) where, instead of upscaling constitutive relations to macroscale, constitutive relations are obtained directly by exploiting the macroscale entropy inequality, in the sense of Coleman

and Noll (1963). HMT has been successfully used to model coupled deformation and transport processes in a variety of materials and processes including: swelling biopolymers for drug delivery (Weinstein et al., 2008), drying of foods (Takhar, 2011, 2014), (Bensal et al., 2014) and clay soils (Bennethum et al., 1997).

The aim of the present paper is to create a thermodynamically consistent model including fluid flow and sorption effects in a fibrous material. A purely macroscopic approach excluding microscopic features is presented in this work. The triphasic description of paperboard includes fiber, bound water and gas, where the gas is considered to be a miscible mix of water vapor and dry air. The phase interfaces are not explicitly accounted for but will be implicitly included in the constitutive relations related to the interaction between phases. Constitutive relations derived in the model resemble the classical results where Fick's law is used for intraphase diffusion, Darcy's law for gas seepage and Fourier's law for heat conduction. The anisotropic transport properties are accounted for in the constitutive relations for diffusion, seepage and heat conduction.

The triphasic paperboard model is used to analyse the response of a roll exerted to different ambient climates, defined by gas pressure, relative humidity and temperature. Moisture penetration, temperature variation and sorption dynamics are investigated for a paperboard roll subjected to a change in ambient relative humidity.

2 Preliminaries

In mixture theory, when up–scaling from micro to macro scale, information about the geometrical configuration is replaced by the macroscopic quantity: volume fraction. Let α denote phases and α_j denote constituents j in phase α. The volume fraction of a phase α is then denoted by n_α and defined as

$$n_\alpha = \frac{dv_\alpha}{dv}, \tag{1}$$

where dv_α is the volume of phase α and dv is the elemental volume of the representative elementary volume (REV). The volume fractions are constrained by the relationship

$$\sum_\alpha n_\alpha = 1, \tag{2}$$

which states that all phases together occupy the whole REV. The constituents of a phase are assumed to be miscible, hence they are associated with the same volume as the phase. The intrinsic density of a component is defined as the mass of the component in the REV divided by the volume it occupies of the REV. The following definitions are used

$$\rho = \frac{dm}{dv}, \quad \rho_\alpha = \frac{dm_\alpha}{dv_\alpha}, \quad \rho_{\alpha_j} = \frac{dm_{\alpha_j}}{dv_\alpha}, \tag{3}$$

where dm, dm_α and dm_{α_j} are the mass of REV, mass of phase α in REV and mass of constituent j in REV, respectively. As a consequence the following relations hold

$$\rho_\alpha = \sum_j \rho_{\alpha_j}, \quad \rho = \sum_\alpha n_\alpha \rho_\alpha. \tag{4}$$

Let $\boldsymbol{v}_{\alpha_j}$ denote the velocity of constituent j in phase α relative to some frame of reference. The velocity of phase α relative to the same reference frame is given as the mass averaged velocity of its constituents. Equivalently the barycentric velocity of the combination of all phases is introduced, i.e.,

$$\boldsymbol{v} = \frac{1}{\rho}\sum_{\alpha} n_\alpha \rho_\alpha \boldsymbol{v}_\alpha, \quad \boldsymbol{v}_\alpha = \frac{1}{\rho_\alpha}\sum_{j} \rho_{\alpha_j}\boldsymbol{v}_{\alpha_j}. \tag{5}$$

It is advantageous to separate the species diffusion and seepage. For this purpose relative velocities are introduced as

$$\boldsymbol{w}_\alpha = \boldsymbol{v}_\alpha - \boldsymbol{v}, \quad \boldsymbol{w}_{\alpha_j} = \boldsymbol{v}_{\alpha_j} - \boldsymbol{v}_\alpha, \quad \boldsymbol{v}^{\alpha,\beta} = \boldsymbol{v}_\alpha - \boldsymbol{v}_\beta, \quad \beta \neq \alpha, \tag{6}$$

where $\boldsymbol{w}_{\alpha_j}, \boldsymbol{w}_\alpha$ are termed diffusion velocities and $\boldsymbol{v}^{\alpha,\beta}$ is termed seepage velocity. As a consequence of the velocity definitions the following relations must hold

$$\sum_j \rho_{\alpha_j}\boldsymbol{w}_{\alpha_j} = \boldsymbol{0}, \quad \sum_\alpha \rho_\alpha \boldsymbol{w}_\alpha = \boldsymbol{0}. \tag{7}$$

The material time derivative with respect to a phase and the material time derivative with respect to a constituent are defined as

$$\frac{D_\alpha(\bullet)}{Dt} = \frac{\partial(\bullet)}{\partial t} + \boldsymbol{v}_\alpha \cdot \nabla(\bullet), \quad \frac{D_{\alpha_j}(\bullet)}{Dt} = \frac{\partial(\bullet)}{\partial t} + \boldsymbol{v}_{\alpha_j} \cdot \nabla(\bullet), \tag{8}$$

where $(\bullet)$ is any scalar or tensorial quantity.

2.1 General equations

Each component of the mixture is associated with a corresponding set of field equations. The available field equations are balances of mass, linear momentum and energy, (cf. Bennethum and Cushman, 1996a, 2002a,b). For constituents the following field equations are assumed

$$\frac{D_{\alpha_j}(n_\alpha \rho_{\alpha_j})}{Dt} + n_\alpha \rho_{\alpha_j} \nabla \cdot \boldsymbol{v}_{\alpha_j} = \sum_{\beta \neq \alpha} n_\alpha \rho_{\alpha_j} \hat{e}^\beta_{\alpha_j} + n_\alpha \rho_{\alpha_j} \hat{r}_{\alpha_j}, \tag{9}$$

$$n_\alpha \rho_{\alpha_j} \frac{D_{\alpha_j}(\boldsymbol{v}_{\alpha_j})}{Dt} = \nabla \cdot (n_\alpha \boldsymbol{\sigma}_{\alpha_j}) + n_\alpha \rho_{\alpha_j} \boldsymbol{b}_{\alpha_j} + \sum_{\beta \neq \alpha} n_\alpha \rho_\alpha \hat{\boldsymbol{T}}^\beta_{\alpha_j} + n_\alpha \rho_{\alpha_j} \hat{\boldsymbol{i}}_{\alpha_j}, \tag{10}$$

$$\begin{aligned} n_\alpha \rho_{\alpha_j} \frac{D_{\alpha_j}(u_{\alpha_j})}{Dt} &= n_\alpha \boldsymbol{\sigma}_{\alpha_j} : \nabla(\boldsymbol{v}_{\alpha_j}) - \nabla \cdot (n_\alpha \boldsymbol{q}_{\alpha_j}) + n_\alpha \rho_{\alpha_j} r_{\alpha_j} \\ &\quad + \sum_{\beta \neq \alpha} n_\alpha \rho_{\alpha_j} \hat{Q}^\beta_{\alpha_j} + n_\alpha \rho_{\alpha_j} \hat{E}_{\alpha_j}, \end{aligned} \tag{11}$$

where $\boldsymbol{\sigma}_{\alpha_j}$ is the constituent Cauchy stress tensor and $n_\alpha \rho_{\alpha_j} \boldsymbol{b}_{\alpha_j}$ is the body force vector acting on the constituent. Balance of angular momentum is omitted assuming the material is non–polar (Hassanizadeh and Gray, 1979b). In the balance of energy

u_{α_j} is the specific internal energy, $\boldsymbol{q}_{\alpha_j}$ is the partial heat flux vector and r_{α_j} the external heat source of constituent j. The quantities with hat denote interaction terms, specifically $n_\alpha \rho_{\alpha_j} \hat{e}^\beta_{\alpha_j}$ is the rate of mass gain of constituent j in α from β, i.e it represents the inter–phase mass transfer. The term $n_\alpha \rho_{\alpha_j} \hat{r}_{\alpha_j}$ is the rate of mass gain of constituent j in α from all other constituents in the same phase (intra–phase mass transfer). The mass gain of phase α from β is defined as

$$\sum_{\beta \neq \alpha} n_\alpha \rho_\alpha \hat{e}^\beta_\alpha = \sum_j \sum_{\beta \neq \alpha} n_\alpha \rho_{\alpha_j} \hat{e}^\beta_{\alpha_j}. \tag{12}$$

The rate of gain of linear momentum from interaction with other constituents in the same phase is given by $n_\alpha \rho_{\alpha_j} \hat{\boldsymbol{i}}_{\alpha_j}$ and $n_\alpha \rho_{\alpha_j} \hat{\boldsymbol{T}}^\beta_{\alpha_j}$ is the rate of gain of linear momentum from interaction with the constituent of phase β. The gain of linear momentum for interaction between phases, the body force acting on a phase and the phase stress are defined by (cf. Bennethum and Cushman, 1996a)

$$n_\alpha \rho_\alpha \hat{\boldsymbol{T}}^\beta_\alpha = \sum_j n_\alpha \rho_{\alpha_j} (\hat{\boldsymbol{T}}^\beta_{\alpha_j} + \hat{e}^\beta_{\alpha_j} \boldsymbol{w}_{\alpha_j}), \tag{13}$$

$$n_\alpha \rho_\alpha \boldsymbol{b}_\alpha = \sum_j n_\alpha \rho_{\alpha_j} \boldsymbol{b}_{\alpha_j}, \tag{14}$$

$$n_\alpha \boldsymbol{\sigma}_\alpha = \sum_j (n_\alpha \boldsymbol{\sigma}_{\alpha_j} - n_\alpha \rho_{\alpha_j} \boldsymbol{w}_{\alpha_j} \otimes \boldsymbol{w}_{\alpha_j}). \tag{15}$$

The two remaining quantities with a hat present in the balance of energy are, $n_\alpha \rho_{\alpha_j} \hat{E}_{\alpha_j}$ is the rate of energy gain from other constituents in α, and $n_\alpha \rho_{\alpha_j} \hat{Q}^\beta_{\alpha_j}$ is the rate of gain of energy of constituent j in phase α from phase β. With the above definitions the balances of mass and linear momentum for phases are given as

$$\frac{D_\alpha (n_\alpha \rho_\alpha)}{Dt} + n_\alpha \rho_\alpha \nabla \cdot \boldsymbol{v}_\alpha = \sum_{\beta \neq \alpha} n_\alpha \rho_\alpha \hat{e}^\beta_\alpha, \tag{16}$$

$$n_\alpha \rho_\alpha \frac{D_\alpha (\boldsymbol{v}_\alpha)}{Dt} = \nabla \cdot (n_\alpha \boldsymbol{\sigma}_\alpha) + n_\alpha \rho_\alpha \boldsymbol{b}_\alpha + \sum_{\beta \neq \alpha} n_\alpha \rho_\alpha \hat{\boldsymbol{T}}^\beta_\alpha. \tag{17}$$

The natural primary variable associated with the balance of mass is the density, for the linear momentum balance the velocity and for the energy equation the temperature. The extra unknowns must be addressed by additional constitutive assumptions in order to close the system of equations. The dissipation inequality for a multiphase system with constituents has been derived by Bennethum and Cushman (2002b) by combining the entropy inequality and the energy equation and introducing the Helmholtz free energy. The format of the inequality presented here disregards

electrostatic effects (cf. Ristinmaa et al., 2011)

$$
\begin{aligned}
D = \sum_{\alpha} \Big\{ & - n_\alpha \rho_\alpha \Big(\frac{D_\alpha(A_\alpha)}{Dt} + \eta_\alpha \frac{D_\alpha(\theta)}{Dt} \Big) - \Big[n_\alpha \boldsymbol{q}_\alpha + \sum_j \big[n_\alpha \boldsymbol{\sigma}_{\alpha_j} \cdot \boldsymbol{w}_{\alpha_j} \\
& - n_\alpha \rho_{\alpha_j} \boldsymbol{w}_{\alpha_j} \frac{1}{2} \boldsymbol{w}_{\alpha_j} \cdot \boldsymbol{w}_{\alpha_j} - n_\alpha \rho_{\alpha_j} A_{\alpha_j} \boldsymbol{w}_{\alpha_j} \big] \Big] \cdot \frac{1}{\theta} \nabla(\theta) \\
& + (n_\alpha \boldsymbol{\sigma}_\alpha + \sum_j n_\alpha \rho_{\alpha_j} \boldsymbol{w}_{\alpha_j} \otimes \boldsymbol{w}_{\alpha_j}) : \boldsymbol{d}_\alpha \\
& + \sum_j (n_\alpha \boldsymbol{\sigma}_{\alpha_j} - n_\alpha \rho_{\alpha_j} A_{\alpha_j} \boldsymbol{I}) : (\nabla \otimes \boldsymbol{w}_{\alpha_j}) \\
& + \sum_j \Big[- \nabla(n_\alpha \rho_{\alpha_j} A_{\alpha_j}) - n_\alpha \rho_{\alpha_j} \hat{\boldsymbol{i}}_{\alpha_j} - \sum_{\beta \neq \alpha} n_\alpha \rho_{\alpha_j} \hat{\boldsymbol{T}}^{\beta}_{\alpha_j} \Big] \cdot \boldsymbol{w}_{\alpha_j} \\
& - \sum_j \big[n_\alpha \rho_{\alpha_j} \hat{r}_\alpha + \sum_{\beta \neq \alpha} n_\alpha \rho_{\alpha_j} \hat{e}^{\beta}_{\alpha_j} \big] \frac{1}{2} \boldsymbol{w}_{\alpha_j} \cdot \boldsymbol{w}_{\alpha_j} \\
& - \sum_{\beta \neq \alpha} n_\alpha \rho_\alpha \hat{e}^{\beta}_{\alpha} (A_\alpha + \frac{1}{2} \boldsymbol{w}_\alpha \cdot \boldsymbol{w}_\alpha) - \sum_{\beta \neq \alpha} n_\alpha \rho_\alpha \hat{\boldsymbol{T}}^{\beta}_{\alpha} \boldsymbol{w}_\alpha \Big\} \geq 0,
\end{aligned}
\tag{18}
$$

where the rate of deformation $\boldsymbol{d}_\alpha$ is the symmetric part of $\nabla(\boldsymbol{v}_\alpha)$ and $\boldsymbol{q}_\alpha$ the phase heat flux. In the above inequality it is assumed that local thermal equilibrium prevails, meaning that for a spatial point all phases and constituents have the same temperature θ. The introduction of the specific Helmholtz free energy is made by means of Legendre transformation, i.e.,

$$
A_{\alpha_j} = u_{\alpha_j} - \eta_{\alpha_j} \theta, \tag{19}
$$

where η_{α_j} denotes the entropy of constituent j in phase α. Moreover the specific Helmholtz free energy and entropy for a phase are defined by

$$
n_\alpha \rho_\alpha A_\alpha = \sum_j n_\alpha \rho_{\alpha_j} A_{\alpha_j} \,, \quad n_\alpha \rho_\alpha \eta_\alpha = \sum_j n_\alpha \rho_{\alpha_j} \eta_{\alpha_j}. \tag{20}
$$

3 Triphasic model with mass exchange

The phases considered are solid (s), bound water (l), and gas (g). Fig. 1 illustrates how the paperboard is separated into phases which are smeared out and superimposed at macroscale to form a continuum. Of particular interest is the transport of water molecules which motivates us to further separate the gas into a water vapor (g_v) and dry air (g_a), i.e., gas is a homogeneous mixture of water vapor and dry air, hence both constituents are considered to simultaneously occupy the total gas volume of the REV. For this purpose let us define

$$
\alpha = \{s, l, g\}, \quad g_j = \{g_v, g_a\}. \tag{21}
$$

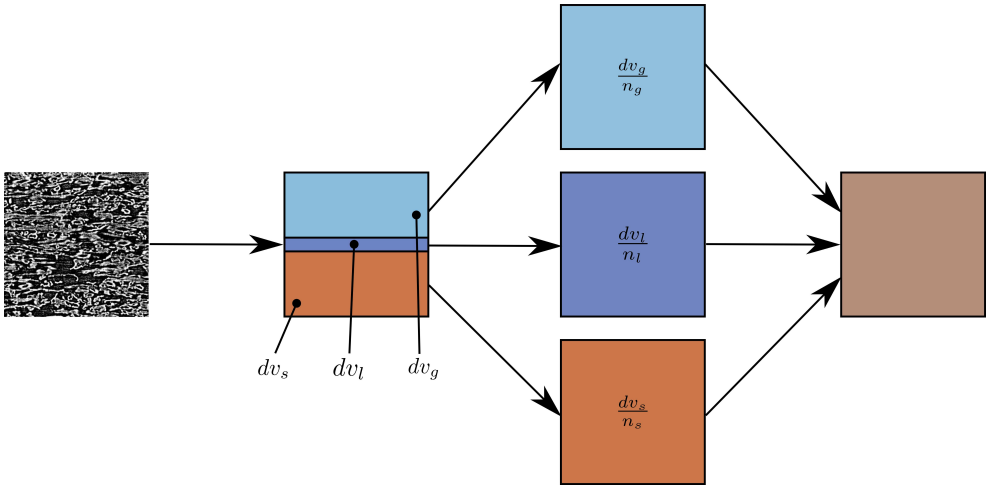

Figure 1: Schematic representation of separation of the REV into phases that are smeared out by means of volume averaging and at the macroscale are viewed as superimposed phases to create a mixture continuum

The focus of this work is on the transport phenomena within paperboard where the moisture contents are relatively low (below the fiber saturation point). At low moisture contents the water–fiber interactions are strong and the bound water phase (l) will thus have properties different from water outside the material. The diffusive vapor and moisture transport as well as heat transport through convection and conduction in paperboard rolls in storage are considered slow. The slow nature of the processes motivates certain simplifications. It is assumed that inertial terms are negligible compared to other terms in the linear momentum balance equations. The influence of gravitational forces on the transport are considered negligible. No chemical reactions take place within the gas phase and mass is only exchanged between bound water and its vapor, the solid fiber and dry air components are assumed inert. Moisture sorption hysteresis is for simplicity not considered in this work. The solid fiber will serve as a frame of reference to which the motions of the other species are compared. Solid deformation is of minor importance in the application considered in this work. Therefore the solid is assumed rigid and incompressible. The bound water is assumed intrinsically incompressible, which together with (2) are used as closure conditions. Furthermore the pores are assumed to be continuously connected.

Based on the expected physical behavior of the system the Helmholtz free energy functions are postulated to have the following dependencies

$$A_s = A_s(\theta), \tag{22a}$$
$$A_l = A_l(\theta, n_l) = A_l^o(\theta) + f(\theta, n_l), \tag{22b}$$
$$A_{g_v} = A_{g_v}(\theta, \rho_{g_v}), \tag{22c}$$
$$A_{g_a} = A_{g_a}(\theta, \rho_{g_a}), \tag{22d}$$

where the bound water free energy is additively split into a non–interacting part A_l^o and a water–fiber interaction f. Incorporation of dependency on bound water volume fraction (n_l) indicates that the specific water potential is influenced by the amount of

water present (cf. Fremond and Nicolas, 1990; Jussila, 2007). The function f is related to the influence of sorption as it accounts for the change in free energy due to water–fiber interaction. In absence of hysteresis the sorption isotherm yield a unique relation between the moisture ratio, temperature and humidity at equilibrium. It is therefore motivated to assume that the equilibrium interface surface areas are functions of the same state variables as the sorption isotherm. Consequently the effect the interfaces have on the system can be considered lumped into the interaction part f of the bound water potential. It is assumed that neither the solid nor the gas are influenced by the presence of other phases. For later purposes let $\hat{m}_v$ denote the rate of evaporation defined as

$$\hat{m}_v = n_g \rho_{g_v} \hat{e}^l_{g_v} = -n_l \rho_l \hat{e}^g_l \tag{23}$$

and $\hat{\boldsymbol{\tau}}_{g_v}, \hat{\boldsymbol{\tau}}_{g_a}, \hat{\boldsymbol{\tau}}_g, \hat{\boldsymbol{\tau}}_l$ denote total momentum transfer

$$\hat{\boldsymbol{\tau}}_{g_v} = n_g \rho_{g_v} [\hat{\boldsymbol{i}}_{g_v} + (\hat{\boldsymbol{T}}^s_{g_v} + \hat{\boldsymbol{T}}^l_{g_v})], \tag{24a}$$

$$\hat{\boldsymbol{\tau}}_{g_a} = n_g \rho_{g_v} [\hat{\boldsymbol{i}}_{g_a} + (\hat{\boldsymbol{T}}^s_{g_a} + \hat{\boldsymbol{T}}^l_{g_a})], \tag{24b}$$

$$\hat{\boldsymbol{\tau}}_g = n_g \rho_g (\hat{\boldsymbol{T}}^s_g + \hat{\boldsymbol{T}}^l_g), \tag{24c}$$

$$\hat{\boldsymbol{\tau}}_l = n_l \rho_l (\hat{\boldsymbol{T}}^s_l + \hat{\boldsymbol{T}}^g_l). \tag{24d}$$

The combined heat flux $\tilde{\boldsymbol{q}}$ is defined as

$$\tilde{\boldsymbol{q}} = \sum_\alpha n_\alpha \boldsymbol{q}_\alpha. \tag{25}$$

3.1 Dissipation inequality for triphasic paperboard

The dissipation inequality (18) is modified to incorporate the interdependency of variables by adding balances of mass for the mixture species (9), (16) and the gradient of condition (7) (cf. Bennethum et al., 2000) by means of Liu's Lagrange multiplier method (Liu, 1972). The mass balances are written to follow the solid phase (note that the material time derivative of the solid phase is identical to the partial derivative with respect to time since the solid phase velocity is assumed to be zero). The expanded dissipation inequality is given by

$$\begin{aligned}
D^* = D &+ \lambda_l \Big\{ \rho_l \frac{D_s(n_l)}{Dt} + n_l \rho_l \boldsymbol{I} : \boldsymbol{d}_l + \rho_l \nabla(n_l) \cdot \boldsymbol{v}^{l,s} + \hat{m}_v \Big\} \\
&+ \lambda_{g_v} \Big\{ n_g \frac{D_s(\rho_{g_v})}{Dt} - \rho_{g_v} \frac{D_s(n_l)}{Dt} + \nabla(n_g \rho_{g_v}) \cdot \boldsymbol{w}_{g_v} + \nabla(n_g \rho_{g_v}) \cdot \boldsymbol{v}^{g,s} \\
&\qquad + n_g \rho_{g_v} \boldsymbol{I} : \boldsymbol{d}_g + n_g \rho_{g_v} \nabla \otimes \boldsymbol{w}_{g_v} - \hat{m}_v \Big\} \\
&+ \lambda_{g_a} \Big\{ n_g \frac{D_s(\rho_{g_a})}{Dt} - \rho_{g_a} \frac{D_s(n_l)}{Dt} + \nabla(n_g \rho_{g_a}) \cdot \boldsymbol{w}_{g_a} + \nabla(n_g \rho_{g_a}) \cdot \boldsymbol{v}^{g,s} \\
&\qquad + n_g \rho_{g_a} \boldsymbol{I} : \boldsymbol{d}_g + n_g \rho_{g_a} \nabla \otimes \boldsymbol{w}_{g_a} \Big\} \\
&+ \boldsymbol{\Lambda}_w : \Big\{ \nabla(n_g \rho_{g_v}) \otimes \boldsymbol{w}_{g_v} + n_g \rho_{g_v} \nabla \otimes \boldsymbol{w}_{g_v} + \nabla(n_g \rho_{g_a}) \otimes \boldsymbol{w}_{g_a} \\
&\qquad + n_g \rho_{g_a} \nabla \otimes \boldsymbol{w}_{g_a} \Big\} \geq 0.
\end{aligned} \tag{26}$$

Further, the expanded dissipation (D^*) is separated into three parts

$$D^* = D^{n_1} + D^{n_2} + D^d \geq 0, \tag{27}$$

where it is assumed that each part fulfills the inequality. In D^{n_1} and D^{n_2} each curly bracket is independent of the corresponding coefficient, hence to unconditionally satisfy the dissipation inequality the expressions inside curly brackets must be zero. The first part D^{n_1} is given as

$$\begin{aligned} D^{n_1} = \frac{D_s(\theta)}{Dt}\Big\{ &- n_s\rho_s\Big(\frac{\partial A_s}{\partial\theta} + \eta_s\Big) - n_l\rho_l\Big(\frac{\partial A_l}{\partial\theta} + \eta_l\Big) - n_g\rho_{g_v}\Big(\frac{\partial A_{g_v}}{\partial\theta} + \eta_{g_v}\Big) \\ &- n_g\rho_{g_a}\Big(\frac{\partial A_{g_a}}{\partial\theta} + \eta_{g_a}\Big)\Big\} = 0. \end{aligned} \tag{28}$$

It is assumed that each parenthesis is zero which provides definitions of the entropies of each phase and constituent, i.e.,

$$\eta_s = -\frac{\partial A_s}{\partial\theta}, \quad \eta_l = -\frac{\partial A_l}{\partial\theta}, \quad \eta_{g_v} = -\frac{\partial A_{g_v}}{\partial\theta}, \quad \eta_{g_a} = -\frac{\partial A_{g_a}}{\partial\theta}. \tag{29}$$

The second part D^{n_2} of (27) is given by

$$\begin{aligned} D^{n_2} = &\boldsymbol{d}_g : \Big\{n_g\boldsymbol{\sigma}_g + n_g\rho_{g_v}\lambda_{g_v}\boldsymbol{I} + n_g\rho_{g_a}\lambda_{g_a}\boldsymbol{I} + n_g\rho_{g_v}\boldsymbol{w}_{g_v}\otimes\boldsymbol{w}_{g_v} + n_g\rho_{g_a}\boldsymbol{w}_{g_a}\otimes\boldsymbol{w}_{g_a}\Big\} \\ &+ \boldsymbol{d}_l : \Big\{n_l\boldsymbol{\sigma}_l + n_l\rho_l\lambda_l\boldsymbol{I}\Big\} \\ &+ \nabla\otimes\boldsymbol{w}_{g_v} : \Big\{n_g\boldsymbol{\sigma}_{g_v} - n_g\rho_{g_v}A_{g_v}\boldsymbol{I} + n_g\rho_{g_v}\lambda_{g_v}\boldsymbol{I} + \boldsymbol{\Lambda}_w n_g\rho_{g_v}\Big\} \\ &+ \nabla\otimes\boldsymbol{w}_{g_a} : \Big\{n_g\boldsymbol{\sigma}_{g_a} - n_g\rho_{g_a}A_{g_a}\boldsymbol{I} + n_g\rho_{g_a}\lambda_{g_a}\boldsymbol{I} + \boldsymbol{\Lambda}_w n_g\rho_{g_a}\Big\} \\ &+ \frac{D_s(\rho_{g_v})}{Dt}\Big\{n_g\lambda_{g_v} - n_g\rho_g\frac{\partial A_g}{\partial\rho_{g_v}}\Big\} \\ &+ \frac{D_s(\rho_{g_a})}{Dt}\Big\{n_g\lambda_{g_a} - n_g\rho_g\frac{\partial A_g}{\partial\rho_{g_a}}\Big\} \\ &+ \frac{D_s(n_l)}{Dt}\Big\{\rho_l\lambda_l - \rho_{g_v}\lambda_{g_v} - \rho_{g_a}\lambda_{g_a} - n_l\rho_l\frac{\partial A_l}{\partial n_l}\Big\} = 0. \end{aligned} \tag{30}$$

From the assumption that each curly bracket is independent of its coefficient the expressions inside curly brackets are zero. Elimination of the Lagrangian multipliers and using (15), (20), provides the constitutive relations for the pressures (for more details, see Appendix A)

$$p_{g_v} = (\rho_{g_v})^2\frac{\partial A_{g_v}}{\partial\rho_{g_v}}, \quad p_{g_a} = (\rho_{g_a})^2\frac{\partial A_{g_a}}{\partial\rho_{g_a}}, \quad p_g = p_{g_v} + p_{g_a}, \quad p_l = p_g + n_l\rho_l\frac{\partial A_l}{\partial n_l}, \tag{31}$$

where phase and constituent stresses are $\boldsymbol{\sigma}_\alpha = -p_\alpha \boldsymbol{I},\ \boldsymbol{\sigma}_{\alpha_j} = -p_{\alpha_j}\boldsymbol{I}$. The third part D^d of (27) is given by

$$
\begin{aligned}
D^d = -\frac{1}{\theta}\nabla(\theta)\cdot\Big\{&\tilde{\boldsymbol{q}} + n_g\boldsymbol{\sigma}_{g_v}\cdot\boldsymbol{w}_{g_v} + n_g\boldsymbol{\sigma}_{g_a}\cdot\boldsymbol{w}_{g_a} - n_g\rho_{g_v}\boldsymbol{w}_{g_v}(A_{g_v} + \frac{1}{2}\boldsymbol{w}_{g_v}\cdot\boldsymbol{w}_{g_v}) \\
&- n_g\rho_{g_a}\boldsymbol{w}_{g_a}(A_{g_a} + \frac{1}{2}\boldsymbol{w}_{g_a}\cdot\boldsymbol{w}_{g_a})\Big\} \\
&- \boldsymbol{w}_{g_v}\cdot\Big\{\nabla(n_g\rho_{g_v}A_{g_v}) + \hat{\boldsymbol{\tau}}_{g_v} - \lambda_{g_v}\nabla(n_g\rho_{g_v}) - \boldsymbol{\Lambda}_w\cdot\nabla(n_g\rho_{g_v})\Big\} \\
&- \boldsymbol{w}_{g_a}\cdot\Big\{\nabla(n_g\rho_{g_a}A_{g_a}) + \hat{\boldsymbol{\tau}}_{g_a} - \lambda_{g_a}\nabla(n_g\rho_{g_a}) - \boldsymbol{\Lambda}_w\cdot\nabla(n_g\rho_{g_a})\Big\} \\
&+ \boldsymbol{v}^{l,s}\cdot\Big\{-n_l\rho_l\nabla(A_l) - n_l\rho_l\eta_l\nabla(\theta) - \hat{\boldsymbol{\tau}}_l + \lambda_l\rho_l\nabla(n_l)\Big\} \\
&+ \boldsymbol{v}^{g,s}\cdot\Big\{-n_g\rho_g\nabla(A_g) - n_g\rho_g\eta_g\nabla(\theta) - \hat{\boldsymbol{\tau}}_g + \lambda_{g_v}\nabla(n_g\rho_{g_v}) + \lambda_{g_a}\nabla(n_g\rho_{g_a})\Big\} \\
&- \hat{m}_v\Big\{A_g + \lambda_{g_v} - A_l - \lambda_l - \frac{1}{2}\Big(\boldsymbol{w}_{g_v}\cdot\boldsymbol{w}_{g_v} + \boldsymbol{v}^{l,s}\cdot\boldsymbol{v}^{l,s} - \boldsymbol{v}^{g,s}\cdot\boldsymbol{v}^{g,s}\Big)\Big\} \geq 0. \qquad (32)
\end{aligned}
$$

Assuming the contribution from energy transport via diffusive mass flux to be negligible, the combined heat flux may be written as

$$\tilde{\boldsymbol{q}} = -\boldsymbol{K}\cdot\nabla(\theta), \qquad (33)$$

where the thermal conductivity tensor $\boldsymbol{K}$ is positive definite, which ensure that the first term of (32) is non–negative.

Elimination of the interaction terms $\hat{\boldsymbol{\tau}}_l$, $\hat{\boldsymbol{\tau}}_g$, $\hat{\boldsymbol{\tau}}_{g_v}$, $\hat{\boldsymbol{\tau}}_{g_a}$ in brackets two to five is done by means of linear momentum equations (10), (17) and definitions (24), which then is used to derive the following relations (details are found in Appendix B)

$$\boldsymbol{v}^{g,s} = -\frac{\boldsymbol{K}^p_{g,s}}{\bar{\mu}_g}\cdot[n_g\nabla(p_g) - n_g\rho_g\boldsymbol{b}_g], \qquad (34a)$$

$$\boldsymbol{v}^{l,s} = -\frac{\boldsymbol{K}^p_{l,s}}{\bar{\mu}_l}\cdot[n_l\nabla(p_l) + n_l\rho_l\frac{\partial A_l}{\partial n_l}\nabla(n_l) - n_l\rho_l\boldsymbol{b}_l], \qquad (34b)$$

$$\boldsymbol{w}_{g_v} = -\boldsymbol{D}_{g_v}\cdot[\nabla(\mu_{g_v}) - \boldsymbol{b}_{g_v}], \qquad (34c)$$

$$\boldsymbol{w}_{g_a} = -\boldsymbol{D}_{g_a}\cdot[\nabla(\mu_{g_a}) - \boldsymbol{b}_{g_a}], \qquad (34d)$$

where $\boldsymbol{K}^p_{g,s}$, $\boldsymbol{K}^p_{l,s}$, $\boldsymbol{D}_{g_v}$ and $\boldsymbol{D}_{g_a}$ are positive definite tensors, $\bar{\mu}_g$ and $\bar{\mu}_l$ are respectively the dynamic viscosity of gas and bound water. Furthermore the chemical potentials are given as

$$\mu_{g_v} = A_{g_v} + \frac{p_{g_v}}{\rho_{g_v}}, \quad \mu_{g_a} = A_{g_a} + \frac{p_{g_a}}{\rho_{g_a}}, \quad \mu_l = A_l + \frac{p_l}{\rho_l}. \qquad (35)$$

Relations (34a,b) and (34c,d) are recognized as Darcy type laws for seepage flow and Fick type laws for diffusive flux, respectively. Assuming the quadratic velocity terms in the last bracket of (32) to be negligible we obtain a relation for mass transfer between bound water and water vapor as

$$\hat{m}_v = \zeta[\mu_l - \mu_{g_v}], \qquad (36)$$

where ζ is a non–negative scalar.

3.2 Reduced set of balance equations

With the aim to model moisture and temperature distribution the general governing equations are reduced to four simplified governing equations namely, water vapor mass balance, dry air mass balance, bound water mass balance and energy balance (see Appendix C):

Water vapor mass balance

$$n_g \frac{D_s(\rho_{g_v})}{Dt} - \rho_{g_v} \frac{D_s(n_l)}{Dt} + \nabla \cdot (n_g \rho_{g_v} \boldsymbol{w}_{g_v}) + \nabla \cdot (n_g \rho_{g_v} \boldsymbol{v}^{g,s}) - \hat{m}_v = 0, \tag{37}$$

Dry air mass balance

$$n_g \frac{D_s(\rho_{g_a})}{Dt} - \rho_{g_a} \frac{D_s(n_l)}{Dt} - \nabla \cdot (n_g \rho_{g_v} \boldsymbol{w}_{g_v}) + \nabla \cdot (n_g \rho_{g_a} \boldsymbol{v}^{g,s}) = 0, \tag{38}$$

Bound water mass balance

$$\rho_l \frac{D_s(n_l)}{Dt} + \hat{m}_v = 0, \tag{39}$$

Energy balance

$$\begin{aligned}
&(n_s \rho_s \frac{\partial u_s}{\partial \theta} + n_l \rho_l \frac{\partial u_l}{\partial \theta} + n_g \rho_{g_v} \frac{\partial u_{g_v}}{\partial \theta} + n_g \rho_{g_a} \frac{\partial u_{g_a}}{\partial \theta}) \frac{D_s(\theta)}{Dt} + n_g u_{g_v} \frac{D_s(\rho_{g_v})}{Dt} \\
&+ n_g u_{g_a} \frac{D_s(\rho_{g_a})}{Dt} - (\rho_{g_v} u_{g_v} + \rho_{g_a} u_{g_a} - \rho_l u_l - n_l \rho_l \frac{\partial u_l}{\partial n_l}) \frac{D_s(n_l)}{Dt} \\
&+ \nabla \cdot (\tilde{\boldsymbol{q}} + n_g (\rho_{g_v} u_{g_v} + p_{g_v} + \rho_{g_a} u_{g_a} + p_{g_a}) \boldsymbol{v}^{g,s}) = 0,
\end{aligned} \tag{40}$$

where the material derivative of the solid phase is equivalent to the partial derivative since the solid phase velocity is assumed to be zero. In the above formulation the bound water is assumed to be bonded to the solid fiber such that its motion is negligible.

4 Modelling processes in paperboard

The Helmholtz free energy function for the solid A_s is postulated to be able to model storage of heat at a constant heat capacity. The bound water energy is chosen to model incompressible water, with constant heat capacity, extended with a water–fiber interaction term. For the gas species the format is chosen to capture that of a perfect gas (ideal gas with constant heat capacity). To solve the system for the unknowns

$\theta, \rho_{g_v}, \rho_{g_a}, n_l$ the following functional forms of Helmholtz free energy are used

$$A_s(\theta) = -c_s^v[\theta \ln\big(\frac{\theta}{\theta^*}\big) - (\theta - \theta^*)] - \eta_s^*\theta + u_s^*, \tag{41a}$$

$$A_l(\theta, n_l) = -c_l^v[\theta \ln\big(\frac{\theta}{\theta^*}\big) - (\theta - \theta^*)] + f(\theta, n_l) - \eta_l^*\theta + u_l^*, \tag{41b}$$

$$A_{g_v}(\theta, \rho_{g_v}) = -c_{g_v}^v[\theta \ln\big(\frac{\theta}{\theta^*}\big) - (\theta - \theta^*)] + \frac{R\theta}{M_{g_v}} \ln\big(\frac{\rho_{g_v}}{\rho_{g_v}^*}\big) - \eta_{g_v}^*\theta + u_{g_v}^*, \tag{41c}$$

$$A_{g_a}(\theta, \rho_{g_a}) = -c_{g_a}^v[\theta \ln\big(\frac{\theta}{\theta^*}\big) - (\theta - \theta^*)] + \frac{R\theta}{M_{g_a}} \ln\big(\frac{\rho_{g_a}}{\rho_{g_a}^*}\big) - \eta_{g_a}^*\theta + u_{g_a}^*, \tag{41d}$$

where $c_{\alpha_j}^v$ and c_α^v are isochoric heat capacities, M_{g_j} is the molar mass of constituent α_j and R is the universal gas constant. Quantities denoted with the superscript $(\bullet)^*$ denote a reference state. The reference state is chosen as a state at 25°C and 1 atm pressure in equilibrium without any water–fiber interactions. Corresponding reference densities are obtained from the ideal gas law

$$p_{g_j} = \rho_{g_j} \frac{R\theta}{M_{g_j}}, \tag{42}$$

which follows from (31). The parameter u_s^* does not enter the equations and may be chosen arbitrarily. Table 1 specify the given reference state. The necessary constitutive relations to close the system of equations are summarized in Table 2. The constitutive parameters are found in Table 3 and Table 4.

The permeability tensor is orthotropic and fitted to experimental data using a Kozeny–Carman type model (Masoodi and Pillai, 2010)

$$K_{g,s}^{p,dir} = K_0^{dir} \Big(\frac{n_g}{n_g^0}\Big)^{a^{dir}} \frac{(1 - n_g^0)}{(1 - n_g)}, \tag{43}$$

where the superscript *dir* indicates which material direction the intrinsic permeability is taken (MD,CD or ZD). The gas viscosity $\bar{\mu}_g$ is estimated in the same sense as in Pont et al. (2011) by weighting of constituent viscosities

$$\bar{\mu}_g = \bar{\mu}_{g_v} + (\bar{\mu}_{g_a} - \bar{\mu}_{g_v})(p_{g_a}/p_g)^{0.608}. \tag{44}$$

In machine direction (MD) and in cross–machine direction (CD) the thermal conductivity is approximated by k_{par} and in thickness direction (ZD) by k_{ser}, where

$$k_{par} = n_l k_l + n_s k_s + n_g k_g, \quad k_{ser} = \frac{1}{n_l/k_l + n_s/k_s + n_g/k_g}. \tag{45}$$

A combined serial and parallel description has also been used to model paperboard (e.g. Karlsson and Stenström, 2005; Baggerud, 2004).

The remaining part to be specified is the function $f(\theta, n_l)$ in the Helmholtz free energy for the bound water. It will be shown that the choice of f is directly coupled to the sorption isotherm and the net isosteric heat of sorption.

Table 1: Reference state, 25°C and 1 *atm* gas pressure (Cengel and Boles, 2007)

Parameter	Unit	Value
Absolute temperature (θ^*)	K	298.15
Pressure – vapor ($p^*_{g_v}$)	Pa	3.169×10^3
Pressure – bound water (p^*_l)	Pa	1.013×10^5
Entropy – vapor ($\eta^*_{g_v}$)	J/kg-K	8.557×10^3
Entropy – dry air ($\eta^*_{g_a}$)	J/kg-K	6.866×10^3
Entropy – bound water (η^*_l)	J/kg-K	3.672×10^2
Internal energy – vapor ($u^*_{g_v} = h^*_{g_v} - R\theta^*/M_{g_v}$)	J/kg	2.409×10^6
Internal energy – dry air ($u^*_{g_a} = h^*_{g_a} - R\theta^*/M_{g_a}$)	J/kg	2.130×10^5
Internal energy – bound water ($u^*_l = h^*_l - p^*_l/\rho_l$)	J/kg	1.047×10^5

Table 2: Constitutive relations

Quantity	Relation	Equation
Diffusive velocity – vapor ($\boldsymbol{w}_{g_v}$)	$\boldsymbol{w}_{g_v} = -\boldsymbol{D}_{g_v} \cdot \nabla(\mu_{g_v})$	Eq.(34c)
Seepage velocity – gas ($\boldsymbol{v}^{g,s}$)	$\boldsymbol{v}^{g,s} = -\frac{\boldsymbol{K}^p_{g,s}}{\bar{\mu}_g} \cdot n_g \nabla(p_g)$	Eq.(34a)
Heat flux ($\tilde{\boldsymbol{q}}$)	$\tilde{\boldsymbol{q}} = -\boldsymbol{K} \cdot \nabla(\theta)$	Eq.(33)
Rate of mass gain of vapor ($\hat{m}_v$)	$\hat{m}_v = \zeta \frac{R\theta}{M_{g_v}} \ln(\frac{p^{sat}_{g_v} a_w}{p_{g_v}})$	Eq.(36)
Volume fraction – gas (n_g)	$n_g = 1 - n_l - n_s$	Eq.(2)
Gas pressure (p_g)	$p_g = p_{g_v} + p_{g_a}$	Eq.(15)
Pressure – constituent (p_{α_j})	$p_{\alpha_j} = \rho_{\alpha_j} \frac{R\theta}{M_{\alpha_j}}, \quad \alpha_j = \{g_v, g_a\}$	Eq. (42)
Chemical potential – vapor (μ_{g_v})	$\mu_{g_v} = A_{g_v} + \frac{p_{g_v}}{\rho_{g_v}}$	Eq.(35)
Internal energy – constituent (u_{α_j})	$u_{\alpha_j} = A_{\alpha_j} + \eta_{\alpha_j}\theta, \quad \alpha_j = \{g_v, g_a\}$	Eq.(19)
Internal energy – phase (u_α)	$u_\alpha = A_\alpha + \eta_\alpha \theta, \quad \alpha = \{s, l\}$	Eq. (19)+(20)
Entropy – constituent (η_{α_j})	$\eta_{\alpha_j} = -\frac{\partial A_{\alpha_j}}{\partial \theta}, \quad \alpha_j = \{g_v, g_a\}$	Eq.(29)
Internal energy – phase (η_α)	$\eta_\alpha = -\frac{\partial A_\alpha}{\partial \theta}, \quad \alpha = \{s, l\}$	Eq.(29)

4.1 Mass transfer between bound water and water vapor

The equilibrium vapor pressure of water inside the porous medium is lower than the corresponding vapor pressure over a flat interface due to the interaction. The ratio of equilibrium vapor pressure inside the porous media ($p^{eq}_{g_v}$) and that over a flat liquid

Table 3: Constitutive parameters and constants

Parameter	Unit	Value
Heat capacity water (c_l^v)	J/kg-K	4.180×10^3
Heat capacity vapor ($c_{g_v}^v$)	J/kg-K	1.399×10^3
Heat capacity dry air ($c_{g_a}^v$)	J/kg-K	0.718×10^3
Heat capacity fiber (c_s^v)	J/kg-K	1.200×10^3
Universal gas constant (R)	J/mol-K	8.314
Molar mass water (M_{g_v})	kg/mol	1.802×10^{-2}
Molar mass dry air (M_{g_a})	kg/mol	2.896×10^{-2}
Liquid density (ρ_l)	kg/m^3	1.000×10^3
Fiber density (ρ_s)	kg/m^3	1.500×10^3
Vapor diffusivity ($\boldsymbol{D}_{g_v}$)	s	
-ZD component		$3.79 \times 10^{-10} \cdot \theta^{-1}$
-CD component		$2.09 \times 10^{-8} \cdot \theta^{-1}$
Gas permeability ($\boldsymbol{K}_{g,s}^p$)	m^2	
-ZD component		$6.759 \times 10^{-14} \cdot n_g^{4.18}/(1-n_g)$
-CD component		$6.183 \times 10^{-13} \cdot n_g^{2.20}/(1-n_g)$
Gas viscosity ($\bar{\mu}_g$)	Pa-s	$\bar{\mu}_{g_v} + (\bar{\mu}_{g_a} - \bar{\mu}_{g_v})(p_{g_a}/p_g)^{0.608}$
Vapor viscosity ($\bar{\mu}_{g_v}$)	Pa-s	$-7.92 \times 10^{-7} + 3.53 \times 10^{-8} \cdot \theta$
Dry air viscosity ($\bar{\mu}_{g_a}$)	Pa-s	$5.90{\times}10^{-6}{+}3.52{\times}10^{-8}{\cdot}\theta{+}2.2{\times}10^{-11}{\cdot}\theta^2$
Heat conductivity ($\boldsymbol{K}$)	W/m-K	
-ZD component		$1/(n_s/0.2 + n_l/0.6 + n_g/0.025)$
-CD component		$0.2 \cdot n_s + 0.6 \cdot n_l + 0.025 \cdot n_g$
Saturation vapor pressure ($p_{g_v}^{sat}$)	Pa	$3169 \cdot \exp(-5.03 \cdot \ln(\theta) - 6792/\theta + 51.43)$
Mass transfer rate coefficient (ζ)	kg-s/m^5	2.7×10^{-7}

surface ($p_{g_v}^{sat}$) is defined as the water activity

$$a_w = \frac{p_{g_v}^{eq}}{p_{g_v}^{sat}}. \tag{46}$$

In a dynamic case the local partial pressure is not equal to its saturation pressure and thus not directly related to the equilibrium activity a_w. The relation between activity, moisture and temperature is described by a sorption isotherm, which is in general

depending on the history, i.e, it has a hysteretic behavior. However, for simplicity this is omitted in this work, thus $a_w = a_w(\theta, n_l)$. The constitution of the macroscale activity a_w implicitly account for the presence of interfaces.

4.1.1 Determining sorption free energy from equilibrium requirements

In deriving (36) it is assumed that at equilibrium $\hat{m}_v = 0$. Consequently it is found that at equilibrium the chemical potential of water in adsorbed state and vapor state is identical $\mu_l = \mu_{g_v}$. Along the equilibrium path the change in potential must be identical, i.e, $d\mu_l = d\mu_{g_v}$. Integration from an equilibrium state corresponding to free water to an equilibrium state including water–fiber interaction at the same temperature yields

$$\mu_l - \mu_l^o = \mu_{g_v} - \mu_{g_v}^o. \tag{47}$$

Recalling definition (35) the chemical potential may be rewritten as

$$\mu_l - \mu_l^o = A_l - A_l^o + \frac{p_l - p_l^o}{\rho_l}. \tag{48}$$

Insertion of (22b) and (31), and using that at the flat interface the water pressure p_l^o is identical to the gas pressure p_g^o where $|p_g - p_g^o| \ll |n_l \, \frac{\partial f}{\partial n_l}|$, hence

$$\mu_l - \mu_l^o = \frac{\partial (n_l f)}{\partial n_l}. \tag{49}$$

The difference in chemical potential of the gas is obtained from Legendre transformation (35) which with utilization of the ideal gas law (42) and the definition of activity (46) provide

$$\mu_{g_v} - \mu_{g_v}^o = \frac{R\theta}{M_{g_v}} \ln(a_w). \tag{50}$$

Combining (47), (49), (50) provides a relation between f and the activity a_w

$$\frac{R\theta}{M_{g_v}} \ln(a_w) = \frac{\partial (n_l f)}{\partial n_l}. \tag{51}$$

4.1.2 Net isosteric heat of sorption

When water molecules transfer from a gaseous state to a bound state there is a release of energy. The heat recovered is referred to as latent heat of water. Adsorption to a surface is an exothermic reaction which due to the strong interaction releases more heat than pure condensation. The heat in excess of the latent heat is the net isosteric heat of adsorption $h_l^o - h_l$, where h_l is the enthalpy for water including interaction whilst h_l^o is the enthalpy of water without the presence of solid. The enthalpy is given by the Legendre transformation

$$h_l = G_l + \eta_l \theta, \tag{52}$$

where G_l is the specific Gibbs free energy of bound water. The bound water phase only has one constituent, thus $G_l = \mu_l$. Taking the difference of the current equilibrium

state and the reference state, recalling the relation for entropy (29), it is found that the net isosteric heat of adsorption is described by

$$h_l^o - h_l = \theta \frac{\partial f}{\partial \theta} - \frac{\partial (n_l f)}{\partial n_l}. \tag{53}$$

Physically it is required that $h_l^o - h_l$ is a positive quantity hence an arbitrary description of the isotherm cannot be used to guarantee this condition. As a consequence of the coupling the functional form of a_w determines the heat of sorption which limits the useful isotherm functions when combined heat and mass transport problems are addressed. This issue was discussed for isotherms for paper materials by Petterson and Stenström (2000). The net isosteric heat enters the energy balance (40) implicitly as internal energy u_l which is associated with h_l via Legendre transformation $u_l = h_l - p_l/\rho_l$. The requirement on u_l to obtain exothermic adsorption is addressed in Appendix D.

4.1.3 Specific choice of sorption isotherm

To describe the sorption isotherm a Chung–Pfost format is adopted, which is a model with two parameters including explicit temperature dependence (cf. Chirife and Iglesias, 1978). The model allows the general sigmoidal shape of the isotherm to be captured. The sorption isotherm is described by the function

$$a_w = \exp\big(-\frac{A}{R\theta}\exp(-BW)\big), \tag{54}$$

where A and B are model parameters. Chirife and Iglesias (1978) point out that A and B are in general temperature dependent. However, since the temperature changes considered here are small it is assumed that the temperature dependence of the parameters is negligible. The moisture ratio W is related to the bound water volume fraction via

$$W = \frac{n_l \rho_l}{n_s \rho_s}, \tag{55}$$

The function f is calculated from (51) for the specific choice of sorption isotherm a_w, and integration provides

$$f = \frac{1}{W}\Big(\frac{A}{BM_{g_v}}\exp(-BW) + C(\theta)\Big). \tag{56}$$

The quantity C is not present in a_w and regardless how it is chosen it will not effect the sorption isotherm, only the net isosteric heat of sorption. The net isosteric heat of sorption becomes

$$h_l^o - h_l = \frac{A}{M_{g_v}}\exp(-BW) + \frac{\theta}{W}\frac{\partial C}{\partial \theta}. \tag{57}$$

Model predictions in the region of interest are shown in Fig. 2(a) and 2(b). The model parameters are found in Table 4.

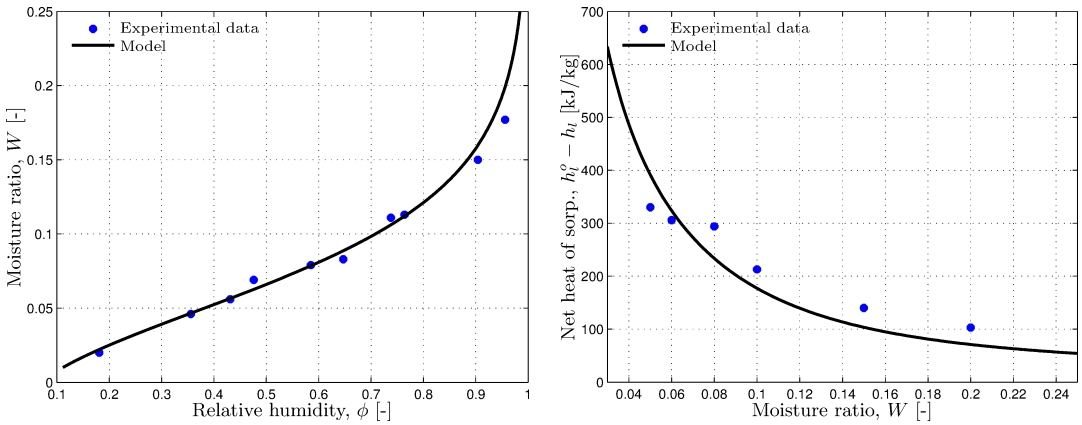

(a) (b)

Figure 2: **a** Adsorption isotherm fitted to experimental data for a Kraft paperboard and **b** isosteric heat fitted to experimental data for Kraft linerboard (Cleland et al., 2007)

Table 4: Sorption related properties

Parameter	Unit	Value	Equation
Sorption function (f)	J/kg	$\frac{1}{W}(\frac{A}{BM_{g_v}}\exp(-BW)+C)$	Eq.(56)
-Water activity (a_w)	-	$\exp(-\frac{A}{R\theta}\exp(-BW))$	Eq.(54)
-Net iso. heat of sorption ($h_l^o - h_l$)	J/kg	$\frac{A}{M_{g_v}}\exp(-BW)+\frac{\theta}{W}\frac{\partial C}{\partial \theta}$	Eq.(57)
- Model parameter A	J/mol	6.232×10^3	
- Model parameter B	-	20.56	
- Model parameter C	J/kg	$43.87\cdot\theta$	

4.2 Sorption kinetics

For water vapor considered as an ideal gas the chemical potential is given by

$$\mu_{g_v} = \mu_{g_v}^o + \frac{R\theta}{M_{g_v}} \ln \frac{p_{g_v}}{p_{g_v}^{sat}}. \tag{58}$$

The chemical potential at the state $\mu_{g_v}^o$ represents the chemical potential of vapor in equilibrium with liquid water over a flat interface at temperature θ. The bound water chemical potential in the porous medium is given by the chemical potential of the water vapor in equilibrium with the bound water, cf. eq.(47),

$$\mu_l = \mu_{g_v}(p_{g_v}^{eq}) = \mu_{g_v}^o + \frac{R\theta}{M_{g_v}} \ln \frac{p_{g_v}^{eq}}{p_{g_v}^{sat}}, \tag{59}$$

where μ_l was chosen to have the same reference state. Combining (36), (46), (58) and (59) provides an expression for the rate of mass exchange

$$\hat{m}_v = \zeta \frac{R\theta}{M_{g_v}} \ln \frac{p_{g_v}^{sat} a_w}{p_{g_v}}. \tag{60}$$

The driving force is the logarithmic deviation of the current vapor pressure from the vapor pressure at equilibrium in the presence of water–fiber interactions. A similar relation was derived in Bénet et al. (2009). It follows that $p_{g_v} > a_w p_{g_v}^{sat} \rightarrow \hat{m}_v < 0$ and $p_{g_v} < a_w p_{g_v}^{sat} \rightarrow \hat{m}_v > 0$.

The mass transfer relation is logarithmic and differs from the more common linear relation (first order reaction kinetics) (e.g. Foss et al., 2003; Zapata et al., 2013; Nyman et al., 2006). The coefficient ζ is estimated from an experiment using a laboratory paper sheet where it is assumed that the supply of vapor is sufficient such that the process dynamics is dominated by the rate of adsorption. A step change in relative humidity from 50% to 89%, with surrounding temperature of 23°C, induces a driving force for sorption. The heat transport is considered to be fast relative to the adsorption dynamics, thus the system is isothermal despite the release of adsorption heat. Fig. 3 displays experimental data and simulated model data obtained by use of (55), (39) and (60).

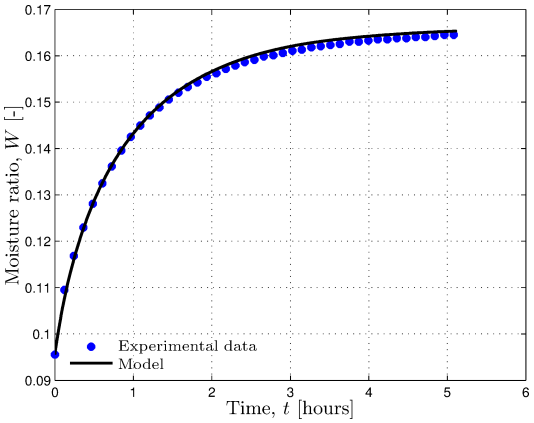

Figure 3: Dynamic adsorption measurements and simulation assuming homogeneous vapor and temperature fields for a relative humidity step from 50% to 89% at 23°C

5 Simulation of paperboard in storage

A finite element formulation is adopted for the coupled system of equations. The basis for the derivation of the finite element formulation is the weak formulation of the governing equations, which is obtained by multiplying (37)–(40) with arbitrary weight functions (ω_i) and integrating over the domain spanned by the solid phase (Ω_s)

as well as using the Gauss divergence theorem. The following is obtained

$$\int_{\Omega_s} \omega_{\rho_{g_v}} \Big(n_g \frac{D_s(\rho_{g_v})}{Dt} - \rho_{g_v} \frac{D_s(n_l)}{Dt} - \hat{m}_v \Big) r dS - \int_{\Omega_s} \nabla(\omega_{\rho_{g_v}}) \cdot n_g \rho_{g_v} [\boldsymbol{w}_{g_v} + \boldsymbol{v}^{g,s}] r dS + \int_{\partial\Omega_s} \omega_{\rho_{g_v}} q^n_{g_v} r d\mathcal{L} = 0, \tag{61a}$$

$$\int_{\Omega_s} \omega_{\rho_{g_a}} \Big(n_g \frac{D_s(\rho_{g_a})}{Dt} - \rho_{g_a} \frac{D_s(n_l)}{Dt} \Big) r dS - \int_{\Omega_s} \nabla(\omega_{\rho_{g_a}}) \cdot [-n_g \rho_{g_v} \boldsymbol{w}_{g_v} + n_g \rho_{g_a} \boldsymbol{v}^{g,s}] r dS + \int_{\partial\Omega_s} \omega_{\rho_{g_a}} q^n_{g_a} r d\mathcal{L} = 0, \tag{61b}$$

$$\int_{\Omega_s} \omega_{n_l} \Big(\rho_l \frac{D_s(n_l)}{Dt} + \hat{m}_v \Big) r dS = 0, \tag{61c}$$

$$\int_{\Omega_s} \omega_\theta \Big(\tilde{C} \frac{D_s(\theta)}{Dt} + n_g u_{g_v} \frac{D_s(\rho_{g_v})}{Dt} + n_g u_{g_a} \frac{D_s(\rho_{g_a})}{Dt} - \tilde{U} \frac{D_s(n_l)}{Dt} \Big) r dS - \int_{\Omega_s} \nabla(\omega_\theta) \cdot [\tilde{\boldsymbol{q}} + \tilde{H} \boldsymbol{v}^{g,s}] r dS + \int_{\partial\Omega_s} \omega_\theta q^n_\theta r d\mathcal{L} = 0, \tag{61d}$$

where $\partial\Omega_s$ is the boundary of Ω_s. The boundary flux terms are given by

$$q^n_{g_v} = \bar{\boldsymbol{n}} \cdot n_g \rho_{g_v} [\boldsymbol{w}_{g_v} + \boldsymbol{v}^{g,s}], \tag{62a}$$

$$q^n_{g_a} = \bar{\boldsymbol{n}} \cdot [-n_g \rho_{g_v} \boldsymbol{w}_{g_v} + n_g \rho_{g_a} \boldsymbol{v}^{g,s}], \tag{62b}$$

$$q^n_\theta = \bar{\boldsymbol{n}} \cdot [\tilde{\boldsymbol{q}} + \tilde{H} \boldsymbol{v}^{g,s}]. \tag{62c}$$

where $\bar{\boldsymbol{n}}$ is the outward normal to the boundary. Note that there is no flux term in the mass balance of bound water. Additionally the following notations were introduced: $\tilde{C} = n_s \rho_s \frac{\partial u_s}{\partial \theta} + n_l \rho_l \frac{\partial u_l}{\partial \theta} + n_g \rho_{g_v} \frac{\partial u_{g_v}}{\partial \theta} + n_g \rho_{g_a} \frac{\partial u_{g_a}}{\partial \theta}$, $\tilde{U} = \rho_{g_v} u_{g_v} + \rho_{g_a} u_{g_a} - \rho_l u_l - n_l \rho_l \frac{\partial u_l}{\partial n_l}$, $\tilde{H} = n_g(\rho_{g_v} u_{g_v} + p_{g_v} + \rho_{g_a} u_{g_a} + p_{g_a})$. Four–node isoparametric quadrilateral element with bilinear interpolations are used in the spatial discretization of all fields. The discrete problem is solved monolithically using a backward Euler time integration scheme with primary variables $\theta, \rho_{g_v}, \rho_{g_a}, n_l$.

The model is used to simulate the material response of a paperboard roll subjected to different ambient climates, which are characterized by surrounding temperature, relative humidity and gas pressure. The relative humidity ϕ is defined as

$$\phi = \frac{p_{g_v}}{p^{sat}_{g_v}}. \tag{63}$$

The geometry used in the simulation is shown in Fig. 4. The roll radii are $r_{core} = 0.088$ m, $r_{outer} = 0.505$ m and the width of the roll is $H = 0.63$ m. Solid volume fraction for the particular roll is set to $n_s = 0.48$. Cylinder coordinates are adopted and due to rotational symmetry a cross–section in the ZD–CD–plane is used as the computational domain.

Time dependent Dirichlet boundary conditions are used for the temperature, vapor density and dry air density on the boundary towards the ambient atmosphere. The inner boundary (core) is assumed to be isolated and impermeable such that all degrees

Table 5: Initial conditions for a paperboard roll and ambient climate

Parameter	Value
Initial ambient atmosphere	
Gas pressure ($p_{g0,\infty}$) (N/m^2)	1.013$\times$ 10^3
Relative humidity ($\phi_{0,\infty}$) (-)	0.5
Absolute temperature ($\theta_{0,\infty}$) (K)	298.15 (25°)
Initial conditions in roll	
Vapor density ($\rho_{g_v 0}$) (kg/m^3)	0.0115
Dry air density ($\rho_{g_a 0}$) (kg/m^3)	1.1653
Bound water volume fraction (n_{l0}) (-)	0.0473
Absolute temperature (θ_0) (K)	298.15 (25°)

of freedom have zero flux, i.e. Neumann conditions. A mesh 100 $\times$ 60 elements in r and z direction, respectively is used. The mesh density close to the external boundary is higher (80 elements in 0.025 m in r–direction and 55 elements in 0.065 m in z–direction).

Table 6: Boundary conditions for a paperboard roll subjected to a change in ambient relative humidity

Equation	$\mathcal{L}_1$	$\mathcal{L}_2$
Water vapor mass balance	$q^n_{g_v} = 0$	$\rho_{g_v}(t) = \frac{M_{g_v}}{R\theta_{0,\infty}} p^{sat}_{g_v}(\theta_{0,\infty})\phi_\infty(t)$
Dry air mass balance	$q^n_{g_a} = 0$	$\rho_{g_a}(t) = \frac{M_{g_a}}{R\theta_{0,\infty}} \big(p_{g0,\infty} - p^{sat}_{g_v}(\theta_{0,\infty})\phi_\infty(t)\big)$
Energy balance	$q^n_\theta = 0$	$\theta = \theta_{0,\infty}$

5.1 Paperboard roll response to change in ambient relative humidity

A gradual change in relative humidity from 50% to 80% is applied over a time of 4 hours (t_r) to the boundary such that the temperature and overall gas pressure of the surrounding are fixed at 25° C and 1 *atm*. Only the composition of the surrounding air is changed. Initially the body is in equilibrium with the surrounding state (initial state and boundary conditions are given in Table 5 and Table 6, respectively). The

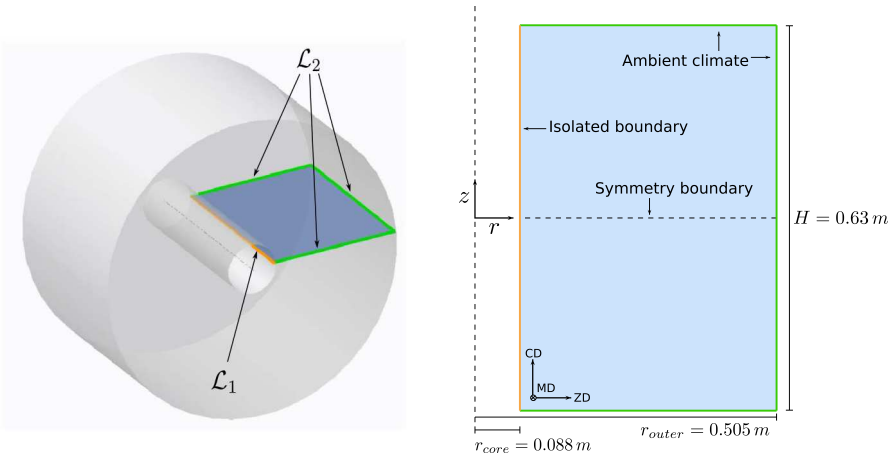

(a) (b)

Figure 4: Graphic representation of the modelled section of a paperboard roll

change in relative humidity with time is given by

$$\begin{cases} \phi_\infty(t) = \phi_{0,\infty} + [\phi_\infty(t = t_r) - \phi_{0,\infty}](t/t_r)^2, & t \leq t_r, \\ \phi_\infty(t) = \phi_\infty(t = t_r), & t > t_r, \end{cases} \tag{64}$$

where t_r is the time the ramp ends. A change in vapor concentration in the surrounding induces a driving force for diffusion and as the local vapor concentration is increased a driving force for sorption is created. The moisture penetration is significantly larger in the radial direction compared to the axial direction, cf. Fig. 5. This is an effect mainly attributed to the higher vapor diffusivity in the axial direction (CD). In the radial direction (ZD) the sorption kinetics is fast compared to the diffusion resulting in a small reaction region and steep moisture profile. The diffusivity is significantly faster in the transversal direction yielding a wider reaction region. However due to the large diffusion distances the problem is still diffusion dominated at the current rate of sorption determined by the constitutive coefficient ζ.

Initially the adsorption will take place close to the boundary. However when the boundary region approaches the equilibrium moisture content the reaction region propagates inwards. The width of this region is related to the ratio of diffusivity, diffusion distances and mass transfer coefficient. For high diffusivity relative to the mass transfer coefficient the region will penetrate deeply and sorption will take place throughout the body. Fig. 6 shows the development of the driving force $\Delta\mu = \mu_l - \mu_{g_v}$ in radial and axial direction. For fast sorption kinetics the profile will be steep and propagate slowly inwards as the vapor reacts locally until equilibrium is reached.

Although there is a release of heat due to sorption the final temperature is virtually the same and the sorption isotherms are thus almost the same for the initial and for the final state. The progression of the local relative humidity at the boundary node towards the surroundings at the symmetry line $z = 0$ towards equilibrium is illustrated in Fig. 7(a). It is apparent that the transfer stops upon reaching the equilibrium isotherm. For the same position it is seen that the driving force for mass transfer is

largest right after the ramp when the deviation from the isotherm is maximum and then approaches zero asymptotically with time Fig. 7(b).

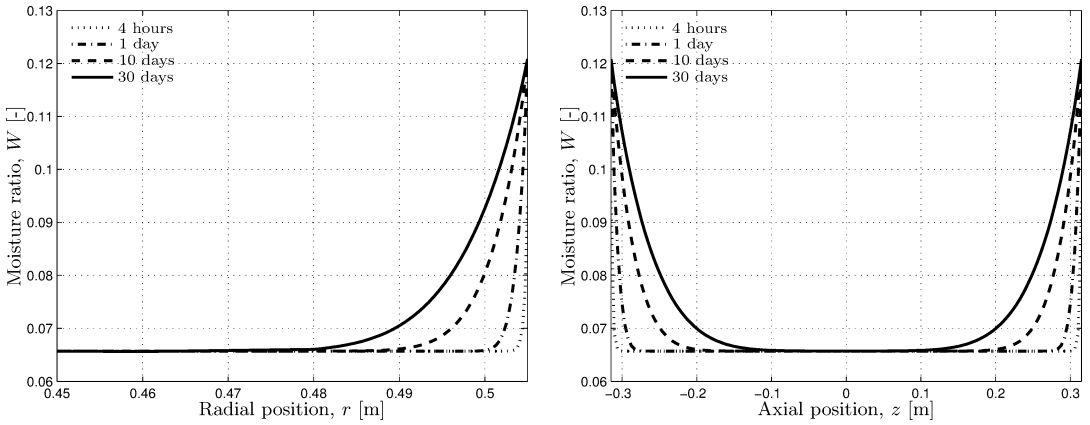

Figure 5: **a** Simulated moisture profile in radial direction at $z = 0$ and **b** axial moisture profile at $r = r_{core}$, at different times for a paperbaord roll subjected to a relative humidity ramp 50% to 80%

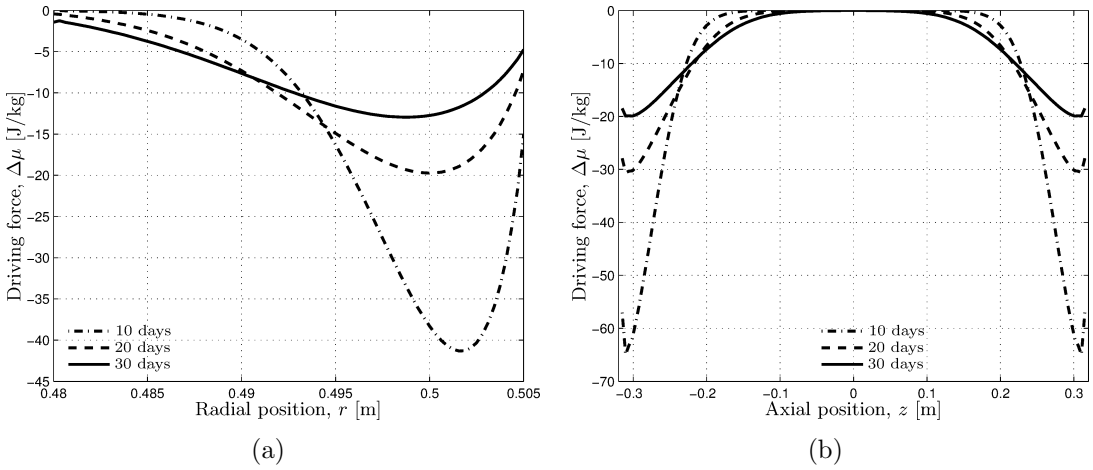

Figure 6: The difference in chemical potentials of bound water and vapor for different times in storage of a paperbaord roll subjected to a relative humidity change from 50% to 80%, **a** Radial direction at $z = 0$ and **b** Axial direction at $r = r_{core}$

6 Conclusions

In this work a macroscopic three phase model is derived to describe transport and mass exchange processes in paperboard. The phases considered are solid fiber, liquid water and pore gas. The gas phase comprises of dry air and water vapor. Governing equations are obtained through simplification of the general field equations: mass conservation, linear momentum and energy conservation, established in the hybrid

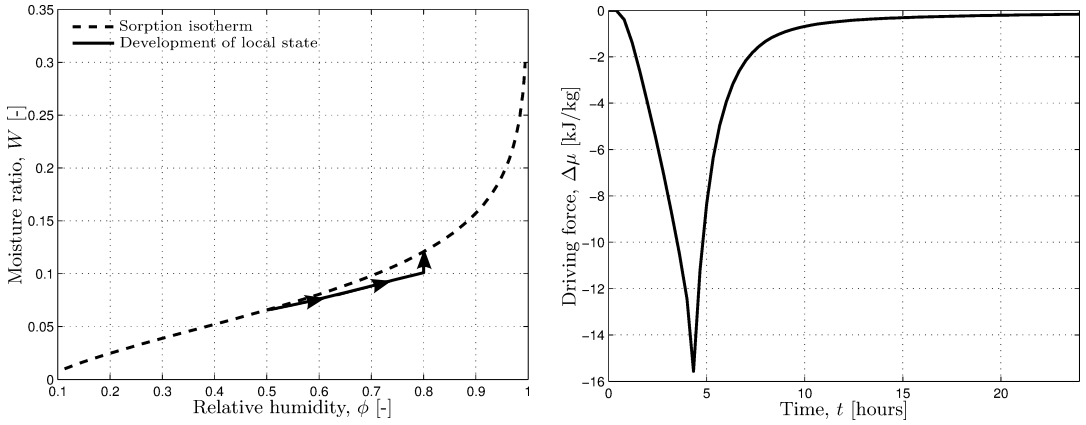

(a) (b)

Figure 7: **a** Development of local relative humidity at the boundary at $z = 0$ and **b** chemical potential difference plotted against time, at the same position for a paperboard roll subjected to a relative humidity ramp 50% to 80%

mixture theory framework (cf. Bennethum and Cushman, 1996a). The description of the system is based on appropriate choices of Helmholtz free energy expressions and systematic treatment of the dissipation inequality. Constitutive relations for fluid flow, diffusion, heat conduction and mass exchange between bound water and water vapor are obtained from the dissipation inequality. Fiber–water interaction is incorporated by the bound water free energy dependence on bound water volume fraction. A logarithmic mass transfer relation with the ratio of vapor pressure to equilibrium vapor pressure as driving force is derived from chemical potentials under the assumption that vapor behaves as an ideal gas. A Chung–Pfost type sorption isotherm, with assumed temperature independent model parameters, provides a satisfactory fit to experimental data for the activity and the net isosteric heat of sorption.

Utilizing the derived model it is possible to predict the transient response of a paperboard roll subjected to a change in the ambient atmosphere. Effects of anisotropy in transport parameters are readily observed on the moisture profile development governed mainly by diffusion and moisture sorption dynamics. Simulations also show that the driving force for sorption varies more in axial direction compared to radial direction due to anisotropy in transport parameters. The ratio of diffusivity to the kinetic mass transfer coefficient determines the width of the reaction region.

A Determining pressure relations

Assuming that the constitutive variables in curly brackets in (30) are not functions of its energy conjugated coefficient i.e., $\boldsymbol{d}_g$, $\boldsymbol{d}_l$, $\boldsymbol{\nabla} \otimes \boldsymbol{w}_{\boldsymbol{g_v}}$, $\boldsymbol{\nabla} \otimes \boldsymbol{w}_{\boldsymbol{g_a}}$, $\frac{D_s(\rho_{g_v})}{Dt}$, $\frac{D_s(\rho_{g_a})}{Dt}$ and $\frac{D_s(n_l)}{Dt}$, provide that the expressions inside the curly brackets are zero in order to

satisfy the dissipation inequality. Therefore it is possible to write

$$-p_g + \rho_{g_v}\lambda_{g_v} + \rho_{g_a}\lambda_{g_a} = 0, \tag{65a}$$

$$\lambda_l - \frac{p_l}{\rho_l} = 0, \tag{65b}$$

$$(-\frac{p_{g_v}}{\rho_{g_v}} - A_{g_v} + \lambda_{g_v})\boldsymbol{I} + \boldsymbol{\Lambda}_w = \mathbf{0}, \tag{65c}$$

$$(-\frac{p_{g_a}}{\rho_{g_a}} - A_{g_a} + \lambda_{g_a})\boldsymbol{I} + \boldsymbol{\Lambda}_w = \mathbf{0}, \tag{65d}$$

$$\lambda_{g_v} = \rho_g \frac{\partial A_g}{\partial \rho_{g_v}}, \tag{65e}$$

$$\lambda_{g_a} = \rho_g \frac{\partial A_g}{\partial \rho_{g_a}}, \tag{65f}$$

$$\rho_l\lambda_l - \rho_{g_v}\lambda_{g_v} - \rho_{g_a}\lambda_{g_a} - n_l\rho_l\frac{\partial A_l}{\partial n_l} = 0, \tag{65g}$$

where the deviatoric part of the fluid stress tensors as well as the second order terms are neglected. Inserting (65b), (65c), (65d) into the definition of phase stress (15) subjected to the same assumptions yield

$$\boldsymbol{\Lambda}_w = A_g\boldsymbol{I}. \tag{66}$$

Inserting (65e), (65f), (66) into (65c) and (65d) and utilizing that $\rho_g A_g(\theta, \rho_{g_v}, \rho_{g_a}) = \rho_{g_v}A_{g_v}(\theta, \rho_{g_v}) + \rho_{g_a}A_{g_a}(\theta, \rho_{g_a})$ enable us to write the partial pressures as

$$p_{g_v} = (\rho_{g_v})^2\frac{\partial A_{g_v}}{\partial \rho_{g_v}}, \quad p_{g_a} = (\rho_{g_a})^2\frac{\partial A_{g_a}}{\partial \rho_{g_a}}. \tag{67}$$

Combination of (65a), (65b) and (65g) result in

$$p_l = p_g + n_l\rho_l\frac{\partial A_l}{\partial n_l}. \tag{68}$$

B Derivations of expressions for seepage and diffusion velocities

Recall terms two to five in (32). Assuming that each term give non–negative dissipation the following is obtained

$$-\boldsymbol{w}_{g_v}\cdot\Big\{\nabla(n_g\rho_{g_v}A_{g_v}) + \hat{\boldsymbol{\tau}}_{g_v} - \lambda_{g_v}\nabla(n_g\rho_{g_v}) - \boldsymbol{\Lambda}_w\cdot\nabla(n_g\rho_{g_v})\Big\} \geq 0, \tag{69a}$$

$$-\boldsymbol{w}_{g_a}\cdot\Big\{\nabla(n_g\rho_{g_a}A_{g_a}) + \hat{\boldsymbol{\tau}}_{g_a} - \lambda_{g_a}\nabla(n_g\rho_{g_a}) - \boldsymbol{\Lambda}_w\cdot\nabla(n_g\rho_{g_a})\Big\} \geq 0, \tag{69b}$$

$$\boldsymbol{v}^{l,s}\cdot\Big\{-n_l\rho_l\nabla(A_l) - n_l\rho_l\eta_l\nabla(\theta) - \hat{\boldsymbol{\tau}}_l + \lambda_l\rho_l\nabla(n_l)\Big\} \geq 0, \tag{69c}$$

$$\boldsymbol{v}^{g,s}\cdot\Big\{-n_g\rho_g\nabla(A_g) - n_g\rho_g\eta_g\nabla(\theta) - \hat{\boldsymbol{\tau}}_g + \lambda_{g_v}\nabla(n_g\rho_{g_v}) + \lambda_{g_a}\nabla(n_g\rho_{g_a})\Big\} \geq 0. \tag{69d}$$

The linear momentum balances (10) and (17) written for the paperboard components with negligible inertial terms and non–deviatoric stresses are

$$-\nabla(n_g p_{g_v}) + \hat{\boldsymbol{\tau}}_{g_v} + n_g \rho_{g_v} \boldsymbol{b}_{g_v} = 0, \tag{70a}$$
$$-\nabla(n_g p_{g_a}) + \hat{\boldsymbol{\tau}}_{g_a} + n_g \rho_{g_a} \boldsymbol{b}_{g_a} = 0, \tag{70b}$$
$$-\nabla(n_g p_g) + \hat{\boldsymbol{\tau}}_g + n_g \rho_g \boldsymbol{b}_g = 0, \tag{70c}$$
$$-\nabla(n_l p_l) + \hat{\boldsymbol{\tau}}_l + n_l \rho_l \boldsymbol{b}_l = 0, \tag{70d}$$

where definitions (24) were used. Inserting (70c)–(70d) into (69c)–(69d) and expanding the gradients, recalling the dependencies of Helmholtz free energy in (41) and the definitions of entropy in (29) as well as equations (65b), (65e) and (65f), provide after simplifications

$$\boldsymbol{v}^{l,s} \cdot \Big\{ -n_l \rho_l \frac{\partial A_l}{\partial n_l} \nabla(n_l) - n_l \nabla(p_l) + n_l \rho_l \boldsymbol{b}_l \Big\} \geq 0, \tag{71a}$$
$$\boldsymbol{v}^{g,s} \cdot \Big\{ \big(\rho_{g_v} \rho_g \frac{\partial A_g}{\partial \rho_{g_v}} + \rho_{g_a} \rho_g \frac{\partial A_g}{\partial \rho_{g_a}} - p_g\big) \nabla(n_g) - n_g \nabla(p_g) + n_g \rho_g \boldsymbol{b}_g \Big\} \geq 0. \tag{71b}$$

From (65a) it is seen that the first term in (71b) vanish. One possible way to satisfy the dissipation inequality is

$$\boldsymbol{v}^{l,s} = -\frac{\boldsymbol{K}^p_{l,s}}{\bar{\mu}_l} \cdot [n_l \nabla(p_l) + n_l \rho_l \frac{\partial A_l}{\partial n_l} \nabla(n_l) - n_l \rho_l \boldsymbol{b}_l], \tag{72a}$$
$$\boldsymbol{v}^{g,s} = -\frac{\boldsymbol{K}^p_{g,s}}{\bar{\mu}_g} \cdot [n_g \nabla(p_g) - n_g \rho_g \boldsymbol{b}_g], \tag{72b}$$

where $\frac{\boldsymbol{K}^p_{l,s}}{\bar{\mu}_l}$ and $\frac{\boldsymbol{K}^p_{g,s}}{\bar{\mu}_g}$ are positive definite tensors. Insertion of (70a) and (70b) into (69a) and (69b) as

$$-\boldsymbol{w}_{g_v} \cdot \Big\{ \nabla(n_g \rho_{g_v} [A_{g_v} + \frac{p_{g_v}}{\rho_{g_v}}]) - n_g \rho_{g_v} \boldsymbol{b}_{g_v} - (\lambda_{g_v} \boldsymbol{I} + \boldsymbol{\Lambda}_w) \cdot \nabla(n_g \rho_{g_v}) \Big\} \geq 0, \tag{73a}$$
$$-\boldsymbol{w}_{g_a} \cdot \Big\{ \nabla(n_g \rho_{g_a} [A_{g_a} + \frac{p_{g_a}}{\rho_{g_a}}]) - n_g \rho_{g_a} \boldsymbol{b}_{g_a} - (\lambda_{g_a} \boldsymbol{I} + \boldsymbol{\Lambda}_w) \cdot \nabla(n_g \rho_{g_a}) \Big\} \geq 0. \tag{73b}$$

Insertion of (65c), (65d) and (66) into (73a) and (73b) result in

$$-\boldsymbol{w}_{g_v} \cdot \Big\{ n_g \rho_{g_v} \nabla(A_{g_v} + \frac{p_{g_v}}{\rho_{g_v}}) - n_g \rho_{g_v} \boldsymbol{b}_{g_v} \Big\} \geq 0, \tag{74a}$$
$$-\boldsymbol{w}_{g_a} \cdot \Big\{ n_g \rho_{g_a} \nabla(A_{g_a} + \frac{p_{g_a}}{\rho_{g_a}}) - n_g \rho_{g_a} \boldsymbol{b}_{g_a} \Big\} \geq 0. \tag{74b}$$

One possible way to satisfy the dissipation inequality is the choice

$$\boldsymbol{w}_{g_v} = -\boldsymbol{D}_{g_v} \cdot [\nabla(\mu_{g_v}) - \boldsymbol{b}_{g_v}], \tag{75a}$$
$$\boldsymbol{w}_{g_a} = -\boldsymbol{D}_{g_a} \cdot [\nabla(\mu_{g_a}) - \boldsymbol{b}_{g_a}], \tag{75b}$$

where $\mu_{g_v} = A_{g_v} + \frac{p_{g_v}}{\rho_{g_v}}$, $\mu_{g_a} = A_{g_a} + \frac{p_{g_a}}{\rho_{g_a}}$ and $\boldsymbol{D}_{g_v}$, $\boldsymbol{D}_{g_a}$ are positive definite tensors.

C Derivation of the energy balance

Combining the energy balances (11) for all component of the system (s, l, g_v, g_a) and eliminating the terms $n_\alpha \rho_{\alpha_j} \hat{E}_{\alpha_j}$ and $n_\alpha \rho_{\alpha_j} \hat{Q}^\beta_{\alpha_j}$ with summation constraints, that arise if the interfaces are assumed to not have any thermodynamic properties (e.g. no mass) (cf. Bennethum and Cushman, 1996a), provide

$$\begin{aligned} n_s\rho_s\frac{D_s(u_s)}{Dt} + n_l\rho_l\frac{D_s(u_l)}{Dt} + n_g\rho_{g_v}\frac{D_s(u_{g_a})}{Dt} + n_g\rho_{g_a}\frac{D_s(u_{g_a})}{Dt} = \\ - n_g\rho_{g_v}\nabla(u_{g_v})\cdot\boldsymbol{v}^{g,s} - n_g\rho_{g_a}\nabla(u_{g_v})\cdot\boldsymbol{v}^{g,s} + u_{g_v}\nabla\cdot(n_g\rho_{g_v}\boldsymbol{w}_{g_v}) + u_{g_a}\nabla\cdot(n_g\rho_{g_a}\boldsymbol{w}_{g_a}) \\ - \nabla\cdot(n_g p_g \boldsymbol{v}^{g,s}) - \nabla\cdot(\tilde{\boldsymbol{q}}) - \hat{m}_v(u_{g_v} - u_l). \end{aligned} \tag{76}$$

Here the material time derivative is taken to follow the solid phase. The bound water velocity ($\boldsymbol{v}^{l,s}$) and second order velocity terms are neglected. No external sources (r_{α_j}, r_α) are present and gravity is omitted. The terms involving diffusive velocities are eliminated with the help of the balances of mass for vapor (37) and dry air (38) and the rate of evaporation is eliminated using the bound water balance of mass (39)

$$u_{g_v}\nabla(n_g\rho_{g_v}\boldsymbol{w}_{g_v}) = -u_{g_v}\frac{D_s(n_g\rho_{g_v})}{Dt} + u_{g_v}\hat{m}_v - u_{g_v}\nabla\cdot(n_g\rho_{g_v}\boldsymbol{v}^{g,s}), \tag{77a}$$

$$u_{g_a}\nabla(n_g\rho_{g_a}\boldsymbol{w}_{g_a}) = -u_{g_a}\frac{D_s(n_g\rho_{g_a})}{Dt} - u_{g_a}\nabla\cdot(n_g\rho_{g_a}\boldsymbol{v}^{g,s}), \tag{77b}$$

$$u_l\hat{m}_v = -\rho_l u_l\frac{D_s(n_l)}{Dt}. \tag{77c}$$

Insertion of (77a), (77b) and (77c) into (76) result in

$$\begin{aligned} n_s\rho_s\frac{D_s(u_s)}{Dt} + n_l\rho_l\frac{D_s(u_l)}{Dt} + n_g\rho_{g_v}\frac{D_s(u_{g_a})}{Dt} + n_g\rho_{g_a}\frac{D_s(u_{g_a})}{Dt} + n_g u_{g_v}\frac{D_s(\rho_{g_v})}{Dt} \\ + n_g u_{g_a}\frac{D_s(\rho_{g_a})}{Dt} + \nabla\cdot(\hat{\boldsymbol{q}} + (n_g\rho_{g_v}u_{g_v} + n_g\rho_{g_a}u_{g_a} + n_g p_g)\boldsymbol{v}^{g,s}) \\ + \rho_l u_l\frac{D_s(n_l)}{Dt} + \rho_{g_v}u_{g_v}\frac{D_s(n_g)}{Dt} + \rho_{g_a}u_{g_a}\frac{D_s(n_g)}{Dt} = 0, \end{aligned} \tag{78}$$

For a rigid incompressible solid $n_s = n_s^0$ hence the time derivative of (2) becomes

$$\frac{D_s(n_g)}{Dt} = -\frac{D_s(n_g)}{Dt}. \tag{79}$$

Further, with Helmholtz free energies given by (41) the dependencies of the internal energies are

$$u_{g_v} = u_{g_v}(\theta), \quad u_{g_a} = u_{g_a}(\theta), \quad u_s = u_s(\theta), \quad u_l = u_l(\theta, n_l). \tag{80}$$

Utilizing the results from (79) and (80) the energy balance (78) may be written as

$$\begin{aligned} (n_s\rho_s\frac{\partial u_s}{\partial\theta} + n_l\rho_l\frac{\partial u_l}{\partial\theta} + n_g\rho_{g_v}\frac{\partial u_{g_v}}{\partial\theta} + n_g\rho_{g_a}\frac{\partial u_{g_a}}{\partial\theta})\frac{D_s(\theta)}{Dt} + n_g u_{g_v}\frac{D_s(\rho_{g_v})}{Dt} \\ + n_g u_{g_a}\frac{D_s(\rho_{g_a})}{Dt} - (\rho_{g_v}u_{g_v} + \rho_{g_a}u_{g_a} - \rho_l u_l - n_l\rho_l\frac{\partial u_l}{\partial n_l})\frac{D_s(n_l)}{Dt} \\ + \nabla\cdot(\tilde{\boldsymbol{q}} + n_g(\rho_{g_v}u_{g_v} + p_{g_v} + \rho_{g_a}u_{g_a} + p_{g_a})\boldsymbol{v}^{g,s}) = 0. \end{aligned} \tag{81}$$

D Requirement of exothermic adsorption

With insertion of the mass balances (37), (38), (39) the energy equation (40) may be written for a homogeneous state (the gradient terms disappear) as

$$\frac{\partial \theta}{\partial t} = -\frac{\tilde{u}}{\tilde{c}}\hat{m}_v, \tag{82}$$

where

$$\tilde{u} = (u_{g_v} - u_l^o) + (u_l^o - u_l) + W\frac{\partial (u_l^o - u_l)}{\partial W}, \tag{83}$$

$$\tilde{c} = n_s \rho_s c_s^v + n_l \rho_l c_l^v + n_g \rho_{g_v} c_{g_v}^v + n_g \rho_{g_a} c_{g_a}^v. \tag{84}$$

The first parenthesis is the internal energy change for evaporation of free water

$$u_{g_v} - u_l^o = (c_{g_v}^v - c_l^v)(\theta - \theta^*) + (u_{g_v}^* - u_l^*), \tag{85}$$

which is positive in the expected temperature range. The second term is related to the function f via Legendre transformations. For an adsorption process $\hat{m}_v < 0$ provide that the temperature will increase due to the reaction if $\tilde{u} > 0$.

The specific format of the internal energy of sorption is related to the choice of isotherm description. For a format of the sorption isotherm according to

$$a_w = \exp\Big(-\frac{A}{R\theta}\gamma(W)\Big), \tag{86}$$

the internal energy change associated with the solid–liquid interactions become

$$(u_l^o - u_l) + W\frac{\partial (u_l^o - u_l)}{\partial W} = \frac{1}{W}\frac{A}{R\theta}\gamma(W). \tag{87}$$

Specifically for the Chung–Pfost type isotherm $\gamma(W) = \exp(-BW)$, a sufficient condition for an exothermic adsorption is $A > 0$.

References

Achanta, S., Cushman, J., and Okos, M. R. (1994). On multicomponent, multiphase thermomechanics with interfaces. *International Journal of engineering science*, 32(11):1717–1738.

Baggerud, E. (2004). *Modelling of Mass and Heat Transport in Paper*. PhD thesis, Lund University.

Bandyopadhyay, A., Radhakrishnan, H., Ramarao, B. V., and Chatterjee, S. G. (2000). Moisture Sorption Response of Paper Subjected to Ramp Humidity Changes: Modeling and Experiments. *Industrial and Engineering Chemistry Research*, 39:219–226.

Bandyopadhyay, A., Ramarao, B. V., and Ramaswamy, S. (2002). Transient moisture diffusion through paperboard materials. *Colloids and Surfaces A: Physicochemical and Engineering Aspects*, 206:455–467.

Bénet, J.-C., Lozano, A.-L., Cherblanc, F., and Cousin, B. (2009). Phase Change of Water in a Hygroscopic Porous Medium. Phenomenological Relation and Experimental Analysis for Water in Soil. *Journal of Non-Equilibrium Thermodynamics*, 34(2):133–153.

Bennethum, L. S. and Cushman, J. H. (1996a). Multiscale, hybrid mixture theory for swelling systems. 1 Balance laws. *International Journal of Engineering Science*, 34(2):125–145.

Bennethum, L. S. and Cushman, J. H. (1996b). Multiscale, hybrid mixture theory for swelling systems. 2. Constitutive theory. *International Journal of Engineering Science*, 34(2):147–169.

Bennethum, L. S. and Cushman, J. H. (2002a). Multicomponent, multiphase thermodynamics of swelling porous media with electroquasistatics: I. Macroscale field equations. *Transport in Porous Media*, 47:309–336.

Bennethum, L. S. and Cushman, J. H. (2002b). Multicomponent, multiphase thermodynamics of swelling porous media with electroquasistatics: II. Constitutive theory. *Transport in Porous Media*, 47:337–362.

Bennethum, L. S., Murad, M., and Cushman, J. (1997). Modified Darcys Law Terzaghis Effective Stress Principle and Ficks Law for Swelling Clay Soils. *Computers and Geotechnics*, 20(3):245–266.

Bennethum, L. S., Murad, M. A., and Cushman, J. H. (2000). Macroscale thermodynamics and the chemical potential for swelling porous media. *Transport in Porous Media*, 39:187–225.

Bensal, H. S., Takhar, P. S., and Maneerote, J. (2014). Modeling multiscale transport mechanisms, phase changes and thermomechanics during frying. *Food Research International*, 62:709–717.

Cengel, Y. A. and Boles, M. A. (2007). *Thermodynamics: And Engineering Approach*. Wiley InterSciences, sixth edition edition.

Chirife, J. and Iglesias, H. A. (1978). Equations for fitting water sorption isotherms of foods: Part 1 - a review. *Journal of Food Technology*, 13:159–174.

Cleland, D. J., Bronlund, J. E., Tanner, D. J., Smale, N. J., Wang, J. F., Nevis, A. L., Elsten, T., Mackay, S. B., Mawson, A. J., and Merts, I. (2007). Refrigeration Load Due to Moisture Sorption From Food Packaging Materials (1210-RP). Technical report, Institute of Technology and Engineering.

Coleman, B. D. and Noll, W. (1963). The thermodynamics of elastic materials with heat conduction and viscosity. *Archive for Rational Thermodynamics and Analysis*, 13:167–178.

Foss, W. R., Bronkhorst, C. A., and Bennett, K. A. (2003). Simultaneous heat and mass transport in paper sheets during moisture sorption from humid air. *International Journal of Heat and Mass Transfer*, 46:2875–2886.

Fremond, M. and Nicolas, P. (1990). Macroscopic thermodynamics of porous media. *Continuum Mechanics and Thermodynamics*, 2:119–139.

Graf, T. (2008). *Mutliphasic Flow Processes in Deformable Porous Media under Consideration of Fluid Phase Transitions*. PhD thesis, Stuttgart University.

Hassanizadeh, S. M. and Gray, W. G. (1979a). General conservation equations for multiphase systems: 1. Averaging procedure. *Advances in Water Resources*, 2:131–144.

Hassanizadeh, S. M. and Gray, W. G. (1979b). General conservation equations for multiphase systems: 2. Mass, momenta, energy, and entropy equations. *Advances in Water Resources*, 2:191–208.

Jussila, P. (2007). *Thermomechanics of swelling unsaturated porous media: compacted bentonite clay in spent fuel disposal*. PhD thesis, Helsinki University of Technology.

Karlsson, M. and Stenström, S. (2005). Static and Dynamic Modeling of Cardboard Drying Part 1: Theoretical Model. *Drying Technology*, 23:143–163.

Liu, I.-S. (1972). Method of Lagrange multipliers for exploitation of the entropy principle. *Archive for Rational thermodynamics and analysis*, 46:131–141.

Masoodi, R. and Pillai, K. (2010). Darcy's Law-Based Model for Wicking in Paper-Like Swelling Porous Media. *AIChE Journal*, 56(9):2257–2267.

Nyman, U., Gustafsson, P. J., Johannesson, B., and Hägglund, R. (2006). A Numerical Method for Nonlinear Transient Moisture Flow in Celluosic Materials. *International Journal for Numerical Methods in Engineering*, 66:1859–1883.

Östlund, M. (2006). Modeling the influence of Drying Conditions on the Stress Buildup During Drying of Paperboard. *Journal of Engineering Materials and Technology*, 128:495–502.

Petterson, M. and Stenström, S. (2000). Experimental evaluation of electric infrared dryers. *Tappi Journal*, 83(8):89–106.

Pont, S. D., Meftah, F., and Schrefler, B. (2011). Modeling concrete under severe conditions as a multiphase material. *Nuclear Engineering and Design*, 241:562–572.

Ristinmaa, M., Ottosen, N. S., and Johannesson, B. (2011). Mixture theory for a thermoelasto-plastic porous solid considering fluid flow and internal mass exchange. *International Journal of Engineering Science*, 49:1185–1203.

Schrefler, B. A. (2002). Mechanics and thermodynamics of saturated/unsaturated porous materials and quantitative solutions. *Applied Mechanics Review: AMSE*, 55(46):351–388.

Sullivan, E. R. (2013). *Heat and moisture transport in unsaturated porous media: a coupled model in terms of chemical potential*. PhD thesis, University of Colorado.

Takhar, P. S. (2011). Hybrid mixture theory based moisture transport and stress development in corn kernels during drying: Coupled fluid transport and stress equations. *Journal of Food Engineering*, 105:663–670.

Takhar, P. S. (2014). Unsaturated fluid transport in swelling poroviscoelastic biopolymers. *Chemical Engineering Science*, 109:98–110.

Weinstein, T. F., Bennethum, L. S., and Cushman, J. H. (2008). Two-Scale, Three-Phase Theory for swelling drug deliver systems. Part 1: Constitutive theory. *Journal of Pharmaceutical Sciences*, 97(5):1878–1903.

Zapata, P., Fransen, M., Boonkkamp, J., and Saes, L. (2013). Coupled heat and moisture transport in paper with application to a warm print surface. *Applied Mathematical Modelling*, 37:7273–7286.

Paper B

Henrik Askfelt, Marcus Alexandersson, and Matti Ristinmaa

Transient transport of heat, mass, and momentum in paperboard including dynamic phase change of water.

International Journal of Engineering Science, 109 (2016) 54-72

Transient transport of heat, mass, and momentum in paperboard including dynamic phase change of water.

Henrik Askfelt[a], Marcus Alexandersson[a], and Matti Ristinmaa[a]

[a] Division of Solid Mechanics, Lund University

P.O. Box 118, S-221 00 Lund, Sweden

Abstract

A theory to describe deforming moist paperboard in environments where both temperature and pressure change significantly during a short period of time is presented. Paperboard is viewed as an orthotropic triphasic porous medium consisting of fibers, bound water and moist air. Furthermore, the moist air is considered as a mixture of two miscible gases, namely dry air and water vapor. A two–scale hybrid mixture theory is adopted in a large strain setting and balances of mass, linear momentum, and energy are presented on the macroscale. Constitutive relations are derived on the macroscale through exploitation of the dissipation inequality. Mass exchange between bound water and water vapor is included as a dynamic process. Mass transportation processes include chemical potential driven diffusion and nonlinear seepage flow. The elasto–plastic stress–strain response of the fiber network is described by assuming a multiplicative split of the deformation gradient associated with the motion of the fiber network. The dynamics related to the mass exchange between bound water and water vapor is illustrated by changes of pressure, relative humidity, moisture ratio, and rate of evaporation during rapid heating of a moist paperboard.

1 Introduction

Paperboard is a porous medium consisting of three species: fibers, air and water. Fibers contain a cavity, called lumen, and have the approximate dimensions: length (1–5 mm), width (20–50 μm), fiber wall thickness (2–8 μm), cf. Baggerud (2004). Due to the paperboard making process, the board possesses a layered structure in the thickness direction and in the plane of the board a majority of the fibres tend to be aligned in one direction. The fiber alignment causes the paperboard to behave as an orthotropic material with three characteristic directions, Machine Direction (MD) and Cross machine Direction (CD), in the plane which constitutes the board, and the out–of–plane direction (ZD) which is a normal to this plane, cf. Figure 1(a).

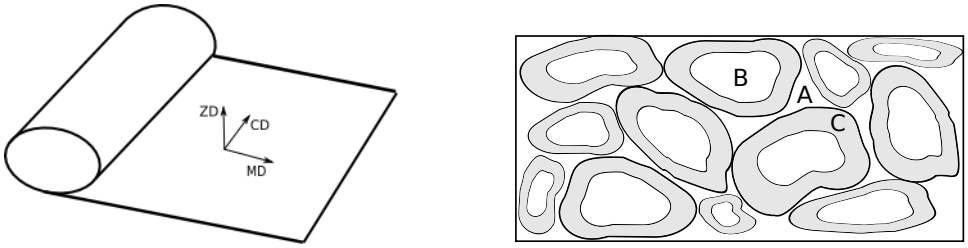

(a) (b)

Figure 1: **a** Illustration of the characteristic directions of paperboard and **b** illustration of the possible locations of water in paperboard A) inter–fiber pores, B) lumen, and C) intra–fiber pores.

Water may be present in the inter–fiber pores, (0.5–10 μm), in the lumen, or in the intra–fiber pores, (5–10^4 Å), which are located in the fiber walls cf. Figure 1(b). The properties of the liquid water differ depending on where the water is located. A majority of the water in the lumen and in the inter–fiber pores has the same properties as free water whereas water in the intra–fiber pores renders a reduced vapor pressure and an increased heat of adsorption due to interactions with fibers, cf. Baggerud (2004). The moisture distribution in a paperboard has a direct influence on the properties of the paperboard e.g. elastic modulus Rigdahl et al. (1984) and transport resistivities Karlsson and Stenström (2005); Linvill (2015). The moisture distribution in a paperboard also has indirect consequences e.g. an affect on the pressure in the inter–fiber pores during temperature changes and the heat development during evaporation and condensation.

Considering the food packaging industry, which uses paperboard as their main packaging material, paperboard is exposed to many extreme environments where the moisture induced changes on the paper properties are known to cause problems. To be able to avoid these problems a better understanding is needed of how the moisture distribution in a board will change in different environments and also of how a known moisture distribution will affect the properties of a board, both directly and indirectly. In order to fulfil this need, a model capturing the coupling between moisture, temperature and deformations in paperboard is required.

Considering isothermal conditions and constant moisture content the stress–strain

response of paperboard has been modelled in a large strain setting by e.g. Borgqvist et al. (2015); Xia et al. (2002); Harrysson and Ristinmaa (2008). In these works, to capture the locally evolving mechanical anisotropy of paperboard local characteristic directions, i.e. structural tensors, are introduced following the framework outlined in Spencer (1984); Boehler (1987).

Models addressing a transient moisture–temperature interaction, without considering the stress–strain response, have been described in e.g. Karlsson and Stenström (2005); Zapata et al. (2013); Alexandersson et al. (2016). In Zapata et al. (2013) paperboard is modelled as a two phase system. The evaporation is postulated to be a linear function of the sorption isotherm. The heat release from evaporation is addressed by including the isosteric heat in the balance of energy. In addition to the evaporation the moisture distribution is assumed to be affected by a Fickian inter–fiber vapor diffusion with a constant anisotropic diffusivity. In Karlsson and Stenström (2005) a thriphasic model is presented where the moisture distribution is determined by a combined mass flux (including both vapor diffusion and gas bulk flow), liquid water diffusion and evaporation. The evaporation is postulated to follow Stefans equation. The isosteric heat is included in the energy balance and the constitutive parameters describing the kinetics of the transportation phenomena are considered to depend on the composition of the board. Alexandersson et al. Alexandersson et al. (2016) adopts a hybrid mixture theory, HMT, and presents a model where the constitutive functions are derived in a thermodynamically consistent manner. The moisture distribution is determined by a combined mass flux in the inter–fiber pore space and evaporation. Adopting a HMT framework Alexandersson et al. Alexandersson et al. (2016) are able to derive general formats of the diffusion and the evaporation which are found to be driven by chemical potentials.

The aim of the presented article is to derive a model that is able to predict the response of deforming moist paperboard in environments where both temperature and pressure change significantly during a short period of time. The theory of mixtures is a class of methods that has been proven successful in describing this type of multi–physical problems. For the development of the theory of mixtures the reader is referred to Truesdell and Toupin (1960); Bowen (1976); Kelly (1964); Müller (1968); Green and Naghdi (1967); Ingram and Eringen (1967); Rajagopal and Tao (1995) and for extensive reviews of the historic development Bowen (1976); Rajagopal and Tao (1995); Atkin and Crane (1976); de Boer and Ehlers (1988); de Boer (1992, 2000).

A difficulty within the theory of mixtures is related to solving initial and boundary value problems. This stems from the fact that the mixture is viewed as a superposition of different continua and each continua is related to its own boundary/initial condition, whereas the considered problem usually only provides common boundary/initial conditions for the hole mixture. This aspect is considered in Rajagopal and Tao (1995); Rajagopal et al. (1986) and will not be further elaborated in the present paper. To illustrate the capabilities of the developed theory, numerical examples that considers the dynamics related to the mass exchange between the bound water and the water vapor during a rapid heating of paperboard are provided.

2 Preliminaries

The present section provides a brief presentation of the kinematics concerning the theory of mixtures, for a more extensive overview cf. Bowen (1976). Adopting a mixture theoretical approach each point in a body is viewed as a superposition of phases $()_\alpha$ where each phase is assumed to be composed of a number of miscible constituents $()_{\alpha_j}$. HMT also provides possibilities for including interfaces between phases, cf. e.g. Bennethum and Cushman (1996a); Hassanizadeh and Gray (1990), however, in the present study interfaces are only considered implicitly via constitutive relations. The motion of a phase is defined by a nonlinear map $\boldsymbol{\chi}_\alpha : \Omega_\alpha^0 \times T \rightarrow \Omega \subset \mathbb{R}^3$,

$$\mathbf{x} = \boldsymbol{\chi}_\alpha(\mathbf{X}_\alpha, t) \tag{1}$$

where $\mathbf{X}_\alpha$ denotes the location of phase α in the reference configuration Ω_α^0. The deformation gradient, $\mathbf{F}_\alpha$, associated with the motion of each phase is given by

$$\mathbf{F}_\alpha = \frac{\partial \boldsymbol{\chi}_\alpha(\mathbf{X}_\alpha, t)}{\partial \mathbf{X}_\alpha} \tag{2}$$

The spatial velocity gradient $\mathbf{l}_\alpha$ is additively split into a symmetric rate of deformation tensor $\mathbf{d}_\alpha$ and the skew–symmetric spin tensor $\boldsymbol{\omega}_\alpha$ according to

$$\mathbf{l}_\alpha = \frac{D_\alpha(\mathbf{F}_\alpha)}{Dt}\mathbf{F}_\alpha^{-1}, \qquad \mathbf{d}_\alpha = \frac{1}{2}(\mathbf{l}_\alpha + \mathbf{l}_\alpha^T), \qquad \boldsymbol{\omega}_\alpha = \frac{1}{2}(\mathbf{l}_\alpha - \mathbf{l}_\alpha^T) \tag{3}$$

Let v and m define the volume and mass of an RVE, (representative volume element), v and m are then related to their phase and constituent counterparts via

$$m = \sum_\alpha m_\alpha, \qquad m_\alpha = \sum_j m_{\alpha_j}, \qquad v = \sum_\alpha v_\alpha \tag{4}$$

All constituents are considered miscible meaning that all constituents α_j within a phase α are associated with the same volume as the phase, i.e $v_{\alpha_j} = v_\alpha \; \forall \; j$.

The macroscale balance laws assumed in mixture theory are derived through averaging of microscale balance laws Hassanizadeh and Gray (1979). During the averaging from micro to macroscale a new variable, volume fraction, appears naturally as

$$n_\alpha = \frac{v_\alpha}{v} \tag{5}$$

From the summation of phase volumes in (4) it is concluded that $\sum_\alpha n_\alpha = 1$ must be fulfilled, a constraint known as the saturation condition. Throughout the rest of this exposition, properties multiplied with a volume fraction are denoted with a bar, i.e., $\bar{(\bullet)} = n_\alpha(\bullet)$. As an example the intrinsic densities $\rho, \rho_\alpha, \rho_{\alpha_j}$ and bulk densities $\bar{\rho}_\alpha, \bar{\rho}_{\alpha_j}$ are given by

$$\rho = \frac{m}{v}, \qquad \rho_\alpha = \frac{m_\alpha}{v_\alpha}, \qquad \rho_{\alpha_j} = \frac{m_{\alpha_j}}{v_\alpha}, \qquad \bar{\rho}_\alpha = n_\alpha \rho_\alpha, \qquad \bar{\rho}_{\alpha_j} = n_\alpha \rho_{\alpha_j} \tag{6}$$

Mass averaged velocities $\mathbf{v}$ and $\mathbf{v}_\alpha$ are defined as weighted summations of phase velocities $\mathbf{v}_\alpha$ and constituent velocities $\mathbf{v}_{\alpha_j}$ respectively, i.e.

$$\mathbf{v} = \frac{1}{\rho}\sum_\alpha \bar{\rho}_\alpha \mathbf{v}_\alpha \qquad \mathbf{v}_\alpha = \frac{1}{\bar{\rho}_\alpha}\sum_j \bar{\rho}_{\alpha_j}\mathbf{v}_{\alpha_j} \tag{7}$$

Furthermore definitions for diffusion velocities $\mathbf{w}_\alpha, \mathbf{w}_{\alpha_j}$ and a relative velocity $\mathbf{v}_{\alpha,\beta}$ are introduced as

$$\mathbf{w}_\alpha = \mathbf{v}_\alpha - \mathbf{v}, \qquad \mathbf{w}_{\alpha_j} = \mathbf{v}_{\alpha_j} - \mathbf{v}_\alpha, \qquad \mathbf{v}_{\alpha,\beta} = \mathbf{v}_\alpha - \mathbf{v}_\beta \tag{8}$$

Combining the definitions of mass average velocities in (7) with (8), the following summation constraints for the diffusion velocities appear

$$\sum_\alpha \bar{\rho}_\alpha \mathbf{w}_\alpha = \mathbf{0}, \qquad \sum_j \bar{\rho}_{\alpha_j}\mathbf{w}_{\alpha_j} = \mathbf{0} \tag{9}$$

3 Balance laws

Paperboard is viewed as being composed of three phases, a solid phase $()_s$ representing the fiber network, a liquid phase $()_l$ representing bound water, and a gas phase $()_g$ representing moist air in the inter–fiber pores. The gas phase is viewed as a mixture of two miscible constituents, dry air $()_{g_d}$ and water vapor $()_{g_v}$. Macroscale balance laws provided in Bennethum (1994); Bowen (1982) are used as a starting point for derivation of a system of equations governing the response of paperboard. To obtain a format where the solid phase is the frame of reference, the material time derivatives following phase α and constituent α_j, $(j = d, v)$ are rewritten according to

$$\frac{D_\alpha(\bullet)}{Dt} = \frac{D_s(\bullet)}{Dt} + \mathbf{v}_{\alpha,s}\cdot\nabla(\bullet) \tag{10a}$$

$$\frac{D_{\alpha_j}(\bullet)}{Dt} = \frac{D_s(\bullet)}{Dt} + \mathbf{v}_{\alpha,s}\cdot\nabla(\bullet) + \mathbf{w}_{\alpha_j}\cdot\nabla(\bullet) \tag{10b}$$

where the nabla operator ∇ is defined as a spatial gradient operator. With transitions (10) the balance laws provided in Bennethum (1994) are presented for the assumed composition of phases and constituents.

Balance of mass

$$\frac{D_s(\bar{\rho}_s)}{Dt} + \bar{\rho}_s\nabla\cdot(\mathbf{v}_s) = \bar{\rho}_s(\hat{e}_s^l + \hat{e}_s^g) \tag{11a}$$

$$\frac{D_s(\bar{\rho}_l)}{Dt} + \nabla\cdot(\bar{\rho}_l\mathbf{v}_{l,s}) + \bar{\rho}_l\nabla\cdot(\mathbf{v}_s) = \bar{\rho}_l(\hat{e}_l^s + \hat{e}_l^g) \tag{11b}$$

$$\frac{D_s(\bar{\rho}_{g_j})}{Dt} + \nabla\cdot(\mathbf{J}_{g_j}) + \bar{\rho}_{g_j}\nabla\cdot(\mathbf{v}_s) = \bar{\rho}_{g_j}(\hat{e}_{g_j}^s + \hat{e}_{g_j}^l + \hat{r}_{g_j}) \tag{11c}$$

Here $\mathbf{J}_{g_j} = \bar{\rho}_{g_j}\mathbf{w}_{g_j} + \bar{\rho}_{g_j}\mathbf{v}_{g,s}$ denotes the combined mass flux of constituent g_j. Moreover, $\hat{e}^{\beta}_{g_j}$ accounts for the rate of mass transferred to constituent g_j from phase β and $\hat{r}_{g_j}$ the rate of mass transferred to constituent g_j from other constituents within the gas phase due to chemical reaction. The mass interaction terms are constrained via

$$\sum_{j=d,v} \rho_{g_j}\hat{r}_{g_j} = 0, \qquad \sum_{\alpha=s,l,g}\sum_{\beta\neq\alpha} \bar{\rho}_{\alpha}\hat{e}^{\beta}_{\alpha} = 0, \qquad \rho_g\hat{e}^{\beta}_{g} = \sum_{j=d,v} \rho_{g_j}\hat{e}^{\beta}_{g_j} \tag{12}$$

Balance of linear momentum

$$\bar{\rho}_s\frac{D_s(\mathbf{v}_s)}{Dt} - \nabla\cdot(\bar{\boldsymbol{\sigma}}_s) - \bar{\rho}_s\mathbf{b}_s = \bar{\rho}_s(\hat{\mathbf{T}}^{g}_{s} + \hat{\mathbf{T}}^{l}_{s}) \tag{13a}$$

$$\bar{\rho}_l\frac{D_s(\mathbf{v}_l)}{Dt} + \mathbf{v}_{l,s}\cdot\mathbf{d}_l - \nabla\cdot(\bar{\boldsymbol{\sigma}}_l) - \bar{\rho}_l\mathbf{b}_l = \bar{\rho}_l(\hat{\mathbf{T}}^{s}_{l} + \hat{\mathbf{T}}^{g}_{l}) \tag{13b}$$

$$\bar{\rho}_{g_j}\frac{D_s(\mathbf{v}_{g_j})}{Dt} + \mathbf{J}_{g_j}\cdot(\nabla\otimes\mathbf{v}_{g_j}) - \nabla\cdot(\bar{\boldsymbol{\sigma}}_{g_j}) - \bar{\rho}_{g_j}\mathbf{b}_{g_j} = \bar{\rho}_{g_j}\hat{\mathbf{i}}_{g_j} + \bar{\rho}_{g_j}(\hat{\mathbf{T}}^{s}_{g_j} + \hat{\mathbf{T}}^{l}_{g_j}) \tag{13c}$$

Here $\hat{\mathbf{i}}_{\alpha_j}, \hat{\mathbf{T}}^{\beta}_{\alpha_j}$ and $\hat{\mathbf{T}}^{\beta}_{\alpha}$ account for all momentum interactions between constituents within phase α, between constituent α_j and phase β, and between phase α and phase β, respectively. The momentum interaction terms are constrained via

$$\sum_{\alpha=s,l,g}\sum_{\beta\neq\alpha} \bar{\rho}_{\alpha}(\hat{\mathbf{T}}^{\beta}_{\alpha} + \hat{e}^{\beta}_{\alpha}\mathbf{v}_{\alpha}) = \mathbf{0}, \qquad \sum_{j=d,v} \rho_{g_j}(\hat{\mathbf{i}}_{g_j} + \hat{r}_{g_j}\mathbf{w}_{g_j}) = \mathbf{0} \tag{14}$$

where

$$\rho_g\hat{\mathbf{T}}^{\beta}_{g} = \sum_{j=d,v} \rho_{g_j}(\hat{\mathbf{T}}^{\beta}_{g_j} + \hat{e}^{\beta}_{g_j}\mathbf{w}_{g_j}) \tag{15}$$

Furthermore, in (13), $\mathbf{b}_{\alpha}, \mathbf{b}_{g_j}$ denote body forces and $\boldsymbol{\sigma}_{\alpha}, \boldsymbol{\sigma}_{g_j}$ the Cauchy stress tensors for specific phases and constituents, respectively. Summation rules for these quantities are given by

$$\rho_g\mathbf{b}_g = \sum_{j=d,v} \rho_{g_j}\mathbf{b}_{g_j}, \qquad \boldsymbol{\sigma}_g = \sum_{j=d,v} (\boldsymbol{\sigma}_{g_j} - \rho_{g_j}\mathbf{w}_{g_j}\otimes\mathbf{w}_{g_j}) \tag{16}$$

Balance of energy

Energy equations may be set up for each phase and constituent together with constraints on energy interaction variables. A local thermal equilibrium is assumed and, consequently, only one equation is needed to describe the transportation of energy. Performing a summation over the balance of energy equations of all phases and constituents present, making use of the constraints on energy interaction variables, presented in Bennethum (1994), and replacing all linear momentum interaction terms via

(13) will render the following format of the balance of energy of the mixture

$$\begin{aligned}\sum_{\alpha=s,l}\bar{\rho}_\alpha\frac{D_s(e_\alpha)}{Dt}+\sum_{j=v,d}\bar{\rho}_{g_j}\frac{D_s(e_{g_j})}{Dt}-e_l\nabla\cdot(\bar{\rho}_l\mathbf{v}_{l,s})-\sum_{j=v,d}e_{g_j}\nabla\cdot(\mathbf{J}_{g_j})-\boldsymbol{\sigma}:\mathbf{d}_s\\+\left(\bar{\rho}_l\frac{D_s(\mathbf{v}_l)}{Dt}+\mathbf{v}_{l,s}\cdot\mathbf{d}_l\right)\cdot\mathbf{v}_{l,s}\\+\sum_{j=v,d}\left(\bar{\rho}_{g_j}\frac{D_s(\mathbf{v}_{g_j})}{Dt}+\mathbf{J}_{g_j}\cdot(\nabla\otimes\mathbf{v}_{g_j})\right)\cdot\frac{\mathbf{J}_{g_j}}{\bar{\rho}_{g_j}}\\+\nabla\cdot(\mathbf{q})-\rho Q+\rho\mathbf{b}\cdot\mathbf{w}_s+\sum_{\alpha=s,l,g}\sum_{\beta\neq\alpha}\bar{\rho}_\alpha\hat{e}_\alpha^\beta(e_\alpha+\frac{1}{2}\mathbf{v}_{\alpha,s}\cdot\mathbf{v}_{\alpha,s})\\+\sum_{\beta=s,l}\sum_{j=v,d}\bar{\rho}_{g_j}\hat{e}_{g_j}^\beta(e_{g_j}-e_g+\mathbf{w}_{g_j}\cdot\mathbf{v}_{g,s}+\frac{1}{2}\mathbf{w}_{g_j}\cdot\mathbf{w}_{g_j})\\+\sum_{j=v,d}\bar{\rho}_{g_j}\hat{r}_{g_j}(e_{g_j}+\mathbf{w}_{g_j}\cdot\mathbf{v}_{g,s}+\frac{1}{2}\mathbf{w}_{g_j}\cdot\mathbf{w}_{g_j})=0\end{aligned}\tag{17}$$

where e_α and e_{α_j} denote the specific internal energies and Q an intrinsic heat source. Moreover, $\boldsymbol{\sigma}$ denotes the total Cauchy stress tensor, $\mathbf{b}$ the body force of the mixture, and $\mathbf{q}$ a combined heat flux vector which are defined as

$$\boldsymbol{\sigma}=\bar{\boldsymbol{\sigma}}_s+\bar{\boldsymbol{\sigma}}_l+\bar{\boldsymbol{\sigma}}_{g_d}+\bar{\boldsymbol{\sigma}}_{g_v}\tag{18a}$$

$$\begin{aligned}\mathbf{q}=\mathbf{q}^b+\sum_{j=d,v}[\bar{\boldsymbol{\sigma}}_{g_j}\cdot\mathbf{w}_{g_j}-\bar{\rho}_{g_j}\mathbf{w}_{g_j}(e_{g_j}+\frac{1}{2}\mathbf{w}_{g_j}\cdot\mathbf{w}_{g_j})]\\+(e_l\mathbf{I}-\frac{\boldsymbol{\sigma}_l}{\rho_l})\bar{\rho}_l\mathbf{v}_{l,s}+\sum_j(e_{g_j}\mathbf{I}-\frac{\boldsymbol{\sigma}_{g_j}}{\rho_{g_j}})\mathbf{J}_{g_j}\end{aligned}\tag{18b}$$

$$\rho\mathbf{b}=\sum_{\alpha=s,l,g}\bar{\rho}_\alpha\mathbf{b}_\alpha\tag{18c}$$

where $\mathbf{q}^b=\sum_{\alpha=s,l,g}\bar{\mathbf{q}}_\alpha$ and $\mathbf{I}$ denotes a second order identity tensor. The specific energy e_g and the heat flux $\mathbf{q}_g$ of the gas phase relate to their constituent counterparts via

$$\rho_g e_g=\sum_{j=d,v}\rho_{g_j}e_{g_j}+E_{g_j}^K\tag{19a}$$

$$\mathbf{q}_g=\sum_{j=d,v}[\mathbf{q}_{g_j}-\boldsymbol{\sigma}_{g_j}\cdot\mathbf{w}_{g_j}+\rho_{g_j}\mathbf{w}_{g_j}(e_{g_j}+\frac{1}{2}\mathbf{w}_{g_j}\cdot\mathbf{w}_{g_j}))]\tag{19b}$$

where $E_{g_j}^K=\rho_{g_j}\frac{1}{2}\mathbf{w}_{g_j}\cdot\mathbf{w}_{g_j}$ is related to the kinetic energy of constituent g_j.

4 Dissipation inequality

A thermodynamically consistent model is derived where macroscale constitutive relations are found through exploitation of the dissipation inequality. Following Bennethum and Cushman (1996b) the format of the macroscale dissipation inequality D

is given by

$$
\begin{aligned}
D = \sum_{\alpha} \Bigg\{ & -\bar{\rho}_{\alpha}\left(\frac{D_{\alpha}(A_{\alpha})}{Dt} + \eta_{\alpha}\frac{D_{\alpha}(\theta)}{Dt}\right) \\
& - \frac{\nabla(\theta)}{\theta}\cdot\left[\bar{\mathbf{q}}_{\alpha} + \sum_{j}\left(\bar{\boldsymbol{\sigma}}_{\alpha_j}\cdot\mathbf{w}_{\alpha_j} - \bar{\rho}_{\alpha_j}\mathbf{w}_{\alpha_j}(A_{\alpha_j} + \frac{1}{2}\mathbf{w}_{\alpha_j}\cdot\mathbf{w}_{\alpha_j})\right)\right] \\
& + \left(\bar{\boldsymbol{\sigma}}_{\alpha} + \sum_{j}\bar{\rho}_{\alpha_j}\mathbf{w}_{\alpha_j}\otimes\mathbf{w}_{\alpha_j}\right) : \mathbf{d}_{\alpha} \\
& + \sum_{j}\left(\bar{\boldsymbol{\sigma}}_{\alpha_j} - \bar{\rho}_{\alpha_j}A_{\alpha_j}\mathbf{I}\right) : (\nabla\otimes\mathbf{w}_{\alpha_j}) \\
& - \sum_{j}\left(\nabla(A_{\alpha_j}\bar{\rho}_{\alpha_j}) + \sum_{\beta\neq\alpha}\bar{\rho}_{\alpha_j}(\hat{\mathbf{T}}^{\beta}_{\alpha_j} + \hat{\mathbf{i}}_{\alpha_j})\right)\cdot\mathbf{w}_{\alpha_j} \\
& - \sum_{\beta\neq\alpha}\bar{\rho}_{\alpha}\left(\hat{\mathbf{T}}^{\beta}_{\alpha}\cdot\mathbf{w}_{\alpha} + \hat{e}^{\beta}_{\alpha}(A_{\alpha} + \frac{1}{2}\mathbf{w}_{\alpha}\cdot\mathbf{w}_{\alpha})\right) \\
& - \sum_{j}\sum_{\beta\neq\alpha}[\bar{\rho}_{\alpha_j}\hat{e}^{\beta}_{\alpha_j} + \bar{\rho}_{\alpha_j}\hat{r}_{\alpha_j}]\frac{1}{2}\mathbf{w}_{\alpha_j}\cdot\mathbf{w}_{\alpha_j}\Bigg\} \geq 0
\end{aligned}
\tag{20}
$$

where θ denotes the absolute temperature, A_{α_j} the Helmholtz potential of constituent α_j, and A_{α} the inner part of the Helmholtz potential of phase α, i.e.,

$$
\rho_{\alpha}A_{\alpha} = \sum_{j}\rho_{\alpha_j}A_{\alpha_j} \tag{21}
$$

5 Constitutive functions

To be able to predict significant inelastic deformations a multiplicative split of the deformation gradient of the solid phase is performed, i.e $\mathbf{F}_s = \mathbf{F}^e_s\mathbf{F}^p_s$ cf. Borgqvist et al. (2015); Harrysson and Ristinmaa (2008); Ristinmaa et al. (2011) for modelling of paperboard and Ehlers (1991, 1992) for porous media. Deformation caused by swelling is assumed negligible and the two deformation gradients appearing in the multiplicative split are associated with elastic deformations, $\mathbf{F}^e_s$, and plastic deformations, $\mathbf{F}^p_s$. From the multiplicative split of the deformation gradient follows an additive split of the spatial velocity gradient $\mathbf{l}_s$ according to

$$
\mathbf{l}_s = \mathbf{l}^e_s + \mathbf{l}^p_s, \qquad \mathbf{l}^e_s = \frac{D_s(\mathbf{F}^e_s)}{Dt}(\mathbf{F}^e_s)^{-1}, \qquad \mathbf{l}^p_s = \mathbf{F}^e_s\frac{D_s(\mathbf{F}^p_s)}{Dt}(\mathbf{F}^p_s)^{-1}(\mathbf{F}^e_s)^{-1} \tag{22}
$$

Both the elastic and the plastic part of the spatial velocity gradient are further split into symmetric $\mathbf{d}^e_s, \mathbf{d}^p_s$ and skew–symmetric parts $\boldsymbol{\omega}^e_s, \boldsymbol{\omega}^p_s$ according to (3). The intrinsic density of the solid phase is assumed constant, $\rho_s = \rho^0_s$, and the behaviour of the solid phase is here defined by the independent variables $\theta, \mathbf{F}^e_s$, and κ^k_s where $\{\kappa^1_s, .., \kappa^n_s\}$ denote (n) internal variables associated with the plastic response.

The amount of liquid water in the board is characterised by the moisture ratio $W = (m - m_{dry})/m_{dry}$ where m_{dry} denotes the dry weight of the board. Neglecting the mass of the gas phase the moisture ratio is approximated by

$$W = \frac{\bar{\rho}_l}{\bar{\rho}_s} \tag{23}$$

The moisture ratio is assumed to be within the maximum hygroscopic moisture content, HMC, which is defined as the equilibrium moisture content extrapolated to 100% relative humidity. Within the HMC region all water is considered bound, cf. Baggerud (2004), and the behaviour of the liquid water is here assumed to be defined by the independent variables ρ_l, θ, and W. Both gas constituents are assumed to behave as ideal gases and the behaviour of the gas constituents are considered to be defined by ρ_{gv}, ρ_{gd}, and θ.

Based on the above the dependencies of the Helmholtz potentials for the phases and constituents are given by

$$A_s(\theta, \mathbf{F}^e_s, \kappa^{(k)}_s), \qquad A_l(\theta, \rho_l, \frac{1}{W}), \qquad A_{g_j}(\theta, \rho_{g_j}) \tag{24}$$

Comparing with classical thermodynamics the free energies in (24) are given additional dependencies which introduce ambiguities in thermodynamic quantities such as pressure, entropy, chemical potential, etc. Gray and Miller (2007). For this purpose definitions of pressures and chemical potentials are included in A.

The only species assumed to be present in more than one phase is water and, assuming no chemical reactions to occur, mass will only be transformed through adsorption/desorption between the water vapor and the bound water, i.e.

$$\hat{e}^l_s = \hat{e}^g_s = \hat{e}^s_{gd} = \hat{e}^s_g = \hat{e}^s_l = \hat{e}^l_{g_d} = \hat{r}_{g_j} = 0, \tag{25a}$$

$$\bar{\rho}_l \hat{e}^g_l + \bar{\rho}_g \hat{e}^l_g = 0, \qquad \bar{\rho}_g \hat{e}^l_g = \bar{\rho}_{g_v} \hat{e}^l_{g_v} \tag{25b}$$

For convenience the notation of the rate of evaporation is changed such that $\hat{m} = \bar{\rho}_g \hat{e}^l_g$ is used throughout the rest of the text.

Ensuring that the derived constitutive functions do not contradict any of the balance laws, Liu's Lagrange multiplier method, Liu (1972), is adopted to enforce the balance of mass equations (11), cf. e.g. Bennethum and Cushman (1996b); Ristinmaa et al. (2011). Moreover, Liu's Lagrange multiplier method is also used to enforce the gradient of constraint (9) since it turns out that viewing the gradients of both diffusion velocities as independent variables results in appealing expressions for the constituent stress tensors, cf. e.g. Ristinmaa et al. (2011). Adopting Liu's Lagrange multiplier

the dissipation inequality is expanded into

$$
\begin{aligned}
D^E = D &+ \lambda_s \left(\rho_s \frac{D_s(n_s)}{Dt} + \bar{\rho}_s \mathbf{d}_s : \mathbf{I} \right) \\
&+ \lambda_l \left(\frac{D_s(\bar{\rho}_l)}{Dt} + \nabla(\bar{\rho}_l) \cdot \mathbf{v}_{l,s} + \bar{\rho}_l \mathbf{d}_l : \mathbf{I} + \hat{m} \right) \\
&+ \sum_{j=d,v} \lambda_{g_j} \left(\frac{D_s(\bar{\rho}_{g_j})}{Dt} + \nabla(\bar{\rho}_{g_j}) \cdot (\mathbf{v}_{g,s} + \mathbf{w}_{g_j}) \right. \\
&\left. + \bar{\rho}_{g_j} (\mathbf{I} : (\nabla \otimes \mathbf{w}_{g_j}) + \mathbf{I} : \mathbf{d}_g) \right) - \lambda_{g_v} \hat{m} \\
&+ \boldsymbol{\lambda}_g^w : \left(\sum_{j=d,v} \nabla \otimes (\bar{\rho}_{g_j} \mathbf{w}_{g_j}) \right) \geq 0
\end{aligned} \tag{26}
$$

where D is defined in (20) and $\lambda_s, \lambda_l, \lambda_{g_j}, \boldsymbol{\lambda}_w$ denote Lagrangian multipliers.

The expanded dissipation inequality in (26) is split into four addends

$$
D^E = D^z + D^s + D^y + D^p \geq 0 \tag{27}
$$

where $D^z + D^s + D^y$ defines the dissipation associated to transportation of mass, heat and elastic deformations and D^p defines the dissipation associated with plastic deformations of the fiber network.

5.1 Exploitation of D^z

The first addend appearing in (27), D^z, is defined by

$$
\begin{aligned}
D^z = &- \sum_{\alpha=s,l,g} \left[\bar{\rho}_\alpha \left(\frac{\partial(A_\alpha)}{\partial\theta} + \eta_\alpha \right) \left(\frac{D_s(\theta)}{Dt} + \nabla(\theta) \cdot \mathbf{v}_{\alpha,s} \right) \right] \\
&+ \left(\rho_s \lambda_s + \frac{n_l p_l^s}{n_s} - \sum_{j=d,v} \rho_{g_j} \lambda_{g_j} \right) \frac{D_s(n_s)}{Dt} \\
&+ \left(n_l \lambda_l - \bar{\rho}_l \frac{\partial A_l}{\partial \rho_l} - \frac{n_l p_l^s}{\rho_l} \right) \frac{D_s(\rho_l)}{Dt} \\
&+ \sum_{j=d,v} \left(\lambda_{g_j} n_g - \bar{\rho}_g \frac{\partial A_g}{\partial \rho_{g_j}} \right) \frac{D_s(\rho_{g_j})}{Dt} \geq 0
\end{aligned} \tag{28}
$$

where a liquid–solid interaction pressure p_l^s has been introduced as

$$
p_l^s = \rho_l W \frac{\partial A_l}{\partial W} \tag{29}
$$

The material time derivatives appearing in D^z may take any sign and in order for the dissipation inequality to be unconditionally fulfilled the following constitutive relations

appear

$$\eta_\alpha = -\frac{\partial A_\alpha}{\partial \theta}, \qquad \eta_{g_j} = -\frac{\partial A_{g_j}}{\partial \theta} \tag{30a}$$

$$\lambda_{g_j} = \rho_g \frac{\partial A_g}{\partial \rho_{g_j}}, \qquad \lambda_l \rho_l = p_l^t + p_l^s, \qquad \lambda_s \rho_s = p_g^t - \frac{n_l p_l^s}{n_s} \tag{30b}$$

The superscript $(\bullet)^t$ is used as a notation for the thermodynamic pressures (90) in order to distinguish these from the physical pressures (91). Relations (30a) are well known relations between Helmholtz free energy and the entropy. From (30b) it is found that the Lagrangian multipliers $\lambda_{g_j}, \lambda_l, \lambda_s$ are all related to pressures. For future calculations the expression for λ_{g_j} is rewritten by use of expressions (21), (24) and (90) as

$$\lambda_{g_j} = A_{g_j} + \frac{p_{g_j}^t}{\rho_{g_j}} - A_g \tag{31}$$

5.2 Exploitation of D^s

The second addend in (27) is further split into three parts $D^s = D^\sigma + D^t + D^\theta$ such that D^σ is exploited to find expressions for the stress tensors, D^t is exploited to find expressions for the linear momentum interaction terms and D^θ is exploited in order to find an expression for the heat flux.

Stress tensors

The dissipation related to the stress tensors, D^σ, is given by

$$\begin{aligned} D^\sigma = &\left(\bar{\boldsymbol{\sigma}}_s + \bar{\rho}_s \lambda_s \mathbf{I} - \bar{\boldsymbol{\sigma}}_s^{eff} \right) : \mathbf{d}_s + \left(\bar{\boldsymbol{\sigma}}_l + \bar{\rho}_l \lambda_l \mathbf{I} \right) : \mathbf{d}_l \\ &+ \left(\bar{\boldsymbol{\sigma}}_g + \sum_{j=d,v} \bar{\rho}_{g_j} \mathbf{w}_{g_j} \otimes \mathbf{w}_{g_j} + \sum_{j=d,v} \bar{\rho}_{g_j} \lambda_{g_j} \mathbf{I} \right) : \mathbf{d}_g \\ &+ \sum_{j=d,v} \left(\bar{\boldsymbol{\sigma}}_{g_j} - \bar{\rho}_{g_j} A_{g_j} \mathbf{I} + \bar{\rho}_{g_j} (\lambda_{g_j} \mathbf{I} + \boldsymbol{\lambda}_g^w) \right) : (\nabla \otimes \mathbf{w}_{g_j}) \geq 0 \end{aligned} \tag{32}$$

in which the effective Cauchy stress tensor $\bar{\boldsymbol{\sigma}}_s^{eff}$ of the solid phase is given by

$$\bar{\boldsymbol{\sigma}}_s^{eff} = J_s^{-1} \mathbf{P}_s^{eff} \mathbf{F}_s^{eT}, \qquad \mathbf{P}_s^{eff} = n_s^0 \rho_s^0 \frac{\partial A_s}{\partial \mathbf{F}_s^e} \tag{33}$$

Here $\mathbf{P}_s^{eff}$ defines the effective first Piola–Kirchhoff stress tensor of the solid phase and $J_s = \det(\mathbf{F}_s)$. Assuming all explicit viscous effects to be negligible, i.e., viscous effects are only considered implicitly via drag forces, the following expressions for the

stress tensors appear

$$\bar{\boldsymbol{\sigma}}_s = \bar{\boldsymbol{\sigma}}_{eff} - \lambda_s \bar{\rho}_s \mathbf{I} \tag{34a}$$

$$\bar{\boldsymbol{\sigma}}_l = -\lambda_l \bar{\rho}_l \mathbf{I} \tag{34b}$$

$$\bar{\boldsymbol{\sigma}}_g = -\sum_{j=d,v} (\bar{\rho}_{g_j} \mathbf{w}_{g_j} \otimes \mathbf{w}_{g_j} + n_g p^t_{g_j}) \tag{34c}$$

$$\bar{\boldsymbol{\sigma}}_{g_j} = -n_g p^t_{g_j} \mathbf{I} + \bar{\rho}_{g_j} (A_g \mathbf{I} - \boldsymbol{\lambda}^w_g) \tag{34d}$$

where expressions (34c) and (34d) are simplified through insertion of (31). Comparing (30b) and (34a) it is noted that $\lambda_s \rho_s$ appears as a pressure acting on the solid which is given as a weighted sum of the fluid pressures. Considering the definition of the physical pressure (91), expression (34b) states that the Lagrangian multiplier λ_l is proportional to the physical pressure of the liquid water

$$\rho_l \lambda_l = p_l \tag{35}$$

Comparing this expression with the second equality in (30b) it is observed that the physical pressure of the liquid water will change due to interaction with the solid according to

$$p_l = p^t_l + p^s_l \tag{36}$$

It is emphasised that p^s_l does not describe a particular phenomena, such as e.g. capillary pressure, but should instead be viewed as a macroscopic average of microscopic interactions between the fiber network and the liquid water. Making use of the summation of (16), (34c) and (34d) the Lagrangian multiplier $\boldsymbol{\lambda}^w_g$ is given by

$$\boldsymbol{\lambda}^w_g = A_g \mathbf{I} \tag{37}$$

which reduces expression (34d) to

$$\boldsymbol{\sigma}_{g_j} = -p^t_{g_j} \mathbf{I} \tag{38}$$

Considering the definition of the physical pressure (91) it is found that the thermodynamic pressure $p^t_{g_j}$ equals the physical pressure p_{g_j} for the gas constituents, i.e.

$$p_{g_j} = p^t_{g_j} \tag{39}$$

To sum up this subsection, the derived expressions of the stress tensors of all species and the total stress tensor $\boldsymbol{\sigma}$ are given by

$$\bar{\boldsymbol{\sigma}}_s = \bar{\boldsymbol{\sigma}}^{eff}_s - \sum_{j=d,v} (n_s p_{g_j} - n_l p^s_l) \mathbf{I} \tag{40a}$$

$$\bar{\boldsymbol{\sigma}}_l = -n_l (p^t_l + p^s_l) \mathbf{I} \tag{40b}$$

$$\bar{\boldsymbol{\sigma}}_{g_j} = -n_g p_{g_j} \mathbf{I} \tag{40c}$$

$$\boldsymbol{\sigma} = \bar{\boldsymbol{\sigma}}^{eff}_s - [n_l p^t_l + (1 - n_l) \sum_{j=d,v} p_{g_j}] \mathbf{I} \tag{40d}$$

The dissipation associated with the linear momentum interaction terms is provided in D^t which is given by

$$
\begin{aligned}
D^t =& \Bigg[- \nabla(A_{g_v}\bar{\rho}_{g_v}) + \nabla(\bar{\rho}_{g_v}) \cdot (\lambda_{g_v}\mathbf{I} + \boldsymbol{\lambda}_g^w) \\
&+ \left(\nabla(A_{g_d}\bar{\rho}_{g_d}) - \nabla(\bar{\rho}_{g_d}) \cdot (\lambda_{g_d}\mathbf{I} + \boldsymbol{\lambda}_g^w) \right) \frac{\rho_{g_v}}{\rho_{g_d}} + \hat{\boldsymbol{\tau}}_1 \Bigg] \cdot \mathbf{w}_{g_v} \\
&+ \left(\lambda_l \nabla(\bar{\rho}_l) - \bar{\rho}_l \nabla(\theta)(\frac{\partial A_l}{\partial \theta} + \eta_l) - \bar{\rho}_l \frac{\partial A_l}{\partial \rho_l} \nabla(\rho_l) - \bar{\rho}_l \frac{\partial A_l}{\partial W} \nabla(W) - \hat{\boldsymbol{\tau}}_2 \right) \cdot \mathbf{v}_{l,s} \\
&+ \sum_{j=d,v} \left(\lambda_{g_j} \nabla(\bar{\rho}_{g_j}) - \bar{\rho}_g (\frac{\partial A_g}{\partial \theta} + \eta_g) \nabla(\theta) - \bar{\rho}_g \frac{\partial A_g}{\partial \rho_{g_j}} \nabla(\rho_{g_j}) - \hat{\boldsymbol{\tau}}_3 \right) \cdot \mathbf{v}_{g,s} \geq 0 \quad (41)
\end{aligned}
$$

where the linear momentum interaction terms are collected into three parameters $\hat{\boldsymbol{\tau}}_1, \hat{\boldsymbol{\tau}}_2$ and $\hat{\boldsymbol{\tau}}_3$ as

$$
\begin{aligned}
\hat{\boldsymbol{\tau}}_1 &= \sum_{\beta=s,l} \bar{\rho}_{g_v} \left(\hat{\mathbf{T}}_{g_d}^{\beta} - \hat{\mathbf{T}}_{g_v}^{\beta} + \hat{\mathbf{i}}_{g_d} - \hat{\mathbf{i}}_{g_v} \right) \\
&= \nabla \cdot (\bar{\boldsymbol{\sigma}}_{g_v}) - \frac{\rho_{g_v}}{\rho_{g_d}} \nabla \cdot (\bar{\boldsymbol{\sigma}}_{g_d}) + \bar{\rho}_{g_v} (\mathbf{b}_{g_v} - \mathbf{b}_{g_d}) \quad (42a) \\
\hat{\boldsymbol{\tau}}_2 &= \sum_{\beta=s,g} \bar{\rho}_l \hat{\mathbf{T}}_l^{\beta} = -\nabla \cdot (\bar{\boldsymbol{\sigma}}_l) - \bar{\rho}_l \mathbf{b}_l \quad (42b) \\
\hat{\boldsymbol{\tau}}_3 &= \sum_{\beta=s,l} \sum_{j=d,v} \bar{\rho}_{g_j} \hat{\mathbf{T}}_{g_j}^{\beta} = - \sum_{j=d,v} \nabla \cdot (\bar{\boldsymbol{\sigma}}_{g_j}) - \bar{\rho}_g \mathbf{b}_g \quad (42c)
\end{aligned}
$$

To obtain the second equality signs in (42), linear momentum equations (13b) and (13c) are used together with definition (16a) and all fluid inertial terms are assumed negligible.

Inserting (30), (31), (35) and (37) together with summation (21) into (41) the following constitutive relations appear

$$
\begin{aligned}
\hat{\boldsymbol{\tau}}_1 =& - \nabla(\bar{\rho}_{g_d} A_{g_d}) \frac{\rho_{g_v}}{\rho_{g_d}} + (A_{g_d} + \frac{p_{g_d}}{\rho_{g_d}}) \nabla(\bar{\rho}_{g_d}) \frac{\rho_{g_v}}{\rho_{g_d}} \\
&+ \nabla(\bar{\rho}_{g_v} A_{g_v}) - (A_{g_v} + \frac{p_{g_v}}{\rho_{g_v}}) \nabla(\bar{\rho}_{g_v}) + \hat{\boldsymbol{\tau}}_1^{\pi} \quad (43a) \\
\hat{\boldsymbol{\tau}}_2 =& (p_l - p_l^s) \nabla(n_l) - \frac{W}{n_s} \nabla(n_s) + \hat{\boldsymbol{\tau}}_2^{\pi} \quad (43b) \\
\hat{\boldsymbol{\tau}}_3 =& \sum_{j=d,v} p_{g_j} \nabla(n_g) + \hat{\boldsymbol{\tau}}_3^{\pi} \quad (43c)
\end{aligned}
$$

where $\hat{\boldsymbol{\tau}}_i^{\pi}$ defines the dissipative part of $\hat{\boldsymbol{\tau}}_i$. For future reasoning, the momentum interactions $\hat{\boldsymbol{\tau}}_2$ and $\hat{\boldsymbol{\tau}}_3$ are interpreted as interfacial drag forces Hassanizadeh and Gray (1987); Bennethum and Giorgi (1997); Ehlers (1992).

Inter–fiber vapor diffusion

Expression (43a) may be rewritten as

$$\hat{\boldsymbol{\tau}}_1 = \nabla(n_g p_{g_d})\frac{\rho_{g_v}}{\rho_{g_d}} - \nabla(n_g p_{g_v}) + \bar{\rho}_{g_v}\nabla(A_{g_v} + \frac{p_{g_v}}{\rho_{g_v}} - A_{g_d} - \frac{p_{g_d}}{\rho_{g_d}}) + \hat{\boldsymbol{\tau}}_1^{\pi} \tag{44}$$

Considering the chemical potentials of the gas constituents, which are defined in (93),

$$\mu_{g_j} = A_{g_j} + \frac{p_{g_j}}{\rho_{g_j}} \tag{45}$$

allows equation (44) to be written as

$$\hat{\boldsymbol{\tau}}_1 = \nabla(n_g p_{g_d})\frac{\rho_{g_v}}{\rho_{g_d}} - \nabla(n_g p_{g_v}) + \bar{\rho}_{g_v}\nabla(\mu_{g_v} - \mu_{g_d}) + \hat{\boldsymbol{\tau}}_1^{\pi} \tag{46}$$

The nonequilibrium part of $\hat{\boldsymbol{\tau}}_1$ is assumed to be linear in $\mathbf{w}_{g_v}$, i.e.

$$\hat{\boldsymbol{\tau}}_1^{\pi} = \mathbf{R}_{g_v} \cdot \mathbf{w}_{g_v} \tag{47}$$

Enforcing $\mathbf{R}_{g_v}$ to be a positive definite second order tensor will together with (46) ensure that the first addend in (41) always is greater or equal to zero. Inserting (47) into (46) and setting this expression equal to (42a) the vapor diffusion in the inter–fiber pores is given by

$$-\frac{\mathbf{R}_{g_v}}{\bar{\rho}_{g_v}} \cdot \mathbf{w}_{g_v} = \nabla(\mu_{g_v} - \mu_{g_d}) + \mathbf{b}_{g_v} - \mathbf{b}_{g_d} \tag{48}$$

With this expression the inter–fiber dry air diffusion $\mathbf{w}_{g_d}$ is defined via (9).

Inter–fiber seepage

The present paper aims at predicting the response of paperboard in environments where significant temperature and pressure gradients may be present. The presence of significant pressure gradients increases the seepage velocities which in turn renders an increased bulk flow resistance. The increased bulk flow resistance is a consequence of an increase in the drag which is quadratic in the seepage velocity cf. Joseph et al. (1982). Expressions of the interfacial drag forces which are quadratic in the seepage velocity are derived in Srinivasan and Rajagopal (2014) using the hypothesis of maximization of the rate of entropy production and in Hassanizadeh and Gray (1987); Bennethum and Cushman (1996c) by assuming $\hat{\boldsymbol{\tau}}^{\pi}$ to consist of finite–order polynomials with coefficients allowed to depend on the invariants of the independent variables. Following the work of Hassanizadeh and Gray (1987); Bennethum and Cushman (1996c) the interfacial drag forces $\hat{\boldsymbol{\tau}}_2^{\pi}$ and $\hat{\boldsymbol{\tau}}_3^{\pi}$ are modelled by

$$\hat{\boldsymbol{\tau}}_2^{\pi} = -\mathbf{R}_{l,s} \cdot \mathbf{v}_{l,s} - \mathbf{F}_{l,s} \cdot \mathbf{v}_{l,s} \tag{49a}$$

$$\hat{\boldsymbol{\tau}}_3^{\pi} = -\mathbf{R}_{g,s} \cdot \mathbf{v}_{g,s} - \mathbf{F}_{g,s} \cdot \mathbf{v}_{g,s} \tag{49b}$$

where $\mathbf{R}_{l,s}$ and $\mathbf{R}_{g,s}$ are resistivity tensors related to small pressure heads (Darcy flow). The corrector tensors $\mathbf{F}_{l,s}$ and $\mathbf{F}_{g,s}$ compensate for the increased bulk flow resistance at higher pressure heads and are assumed to be defined as the resistivities $\mathbf{R}_{\alpha,s}$ scaled with the Forchheimer numbers $F_{o\alpha}$ according to

$$\mathbf{F}_{\alpha,s} = F_{o\alpha}\mathbf{R}_{\alpha,s}, \qquad F_{o\alpha} = \frac{\rho_\alpha \beta_{\alpha,s} k_{\alpha,s}}{\mu_\alpha^D}|\mathbf{v}_{\alpha,s}| \tag{50}$$

where μ_α^D denotes the dynamic viscosity, $\beta_{\alpha,s}$ [m^{-1}] is referred to as the Forchheimer correction coefficient, and $k_{\alpha,s}$ [m^2] the intrinsic permeability parameter. Enforcing $\mathbf{R}_{l,s}$ and $\mathbf{R}_{g,s}$ to be positive definite second order tensors will together with (43b) and (43c) ensure that the last two rows of D^t are greater or equal to zero. A Forchheimer type of equations, describing nonlinear anisotropic seepage flows, is retrieved by inserting (49) into (43b), (43c) and setting these expressions equal to (42b),(42c), i.e.

$$(1 + F_{ol})\mathbf{R}_{l,s} \cdot \mathbf{v}_{l,s} = -n_l \nabla(p_l) - p_l^s \nabla(n_l) - \frac{W}{n_s}\nabla(n_s) + \bar{\rho}_l \mathbf{b}_l \tag{51a}$$

$$(1 + F_{og})\mathbf{R}_{g,s} \cdot \mathbf{v}_{g,s} = -n_g \nabla(p_{g_v} + p_{g_d}) + \bar{\rho}_g \mathbf{b}_g \tag{51b}$$

The hydraulic pressure drop and the body forces appearing in (51) are both included in the standard Darcy law. The term $p_l^s \nabla(n_l)$ appearing in the liquid–solid seepage drives bound water to flow from regions with more water towards regions with less water, Bennethum et al. (1997).

Heat flux

The last addend of D^s relates to dissipation associated with conductive heat flux and is given by

$$D^\theta = -\frac{\nabla(\theta)}{\theta} \cdot \left[\mathbf{q}^b + \sum_{j=d,v}\left(\bar{\boldsymbol{\sigma}}_{g_j} \cdot \mathbf{w}_{g_j} - \mathbf{w}_{g_j}(\bar{\rho}_{g_j} A_{g_j} + \bar{E}_{g_j}^K)\right)\right] \geq 0 \tag{52}$$

From this the following constitutive relation appear

$$\mathbf{q}^b = -\sum_{j=d,v}\left[\bar{\boldsymbol{\sigma}}_{g_j} \cdot \mathbf{w}_{g_j} - \mathbf{w}_{g_j}(\bar{\rho}_{g_j} A_{g_j} + \bar{E}_{g_j}^K)\right] + (\mathbf{q}^b)^\pi \tag{53}$$

Assuming $(\mathbf{q}^b)^\pi$ to be linear in $\nabla(\theta)$ will render a Fourier type of relation for the heat flux as

$$(\mathbf{q}^b)^\pi = -\mathbf{K}_\theta \cdot \nabla(\theta) \tag{54}$$

where $\mathbf{K}_\theta$ defines an effective conductivity tensor which accounts for the thermal resistivities of all phases. Enforcing $\mathbf{K}_\theta$ to be a positive definite second order tensor, expressions (53) and (54) ensure that $D^\theta \geq 0$. Inserting (53) and (54) in (18b) the total heat flux $\mathbf{q}$ is expressed as

$$\mathbf{q} = \mathbf{q}^{conv} + \mathbf{q}^{cond} + \mathbf{q}^{diff} \tag{55}$$

where $\mathbf{q}^{conv}$ denotes the convective heat flux related to energy transported via seepage flows, $\mathbf{q}^{diff}$ denotes the diffusive heat flux related to the energy transported via mass diffusion within the gas phase and $\mathbf{q}^{cond}$ denotes the conductive heat flux related to energy transport via molecular interaction. The partial heat fluxes are given by

$$\mathbf{q}^{conv} = \bar{\rho}_l h_l \mathbf{v}_{l,s} + \sum_{j=d,v} \bar{\rho}_{g_j} h_{g_j} \mathbf{v}_{g,s} \tag{56a}$$

$$\mathbf{q}^{cond} = -\mathbf{K}_\theta \cdot \nabla(\theta) \tag{56b}$$

$$\mathbf{q}^{diff} = \sum_{j=d,v} \bar{\rho}_{g_j} \mu_{g_j} \mathbf{w}_{g_j} \tag{56c}$$

A similar expression for the diffusive heat flux is found in Grasley et al. (2011). In the expression of the convective heat flux, h_l and h_{g_j} denote the fluid enthalpies which are defined by

$$h_l = A_l + \eta_l \theta + \frac{p_l}{\rho_l}, \qquad h_{g_j} = A_{g_j} + \eta_{g_j} \theta + \frac{p_{g_j}}{\rho_{g_j}} \tag{57}$$

5.3 Exploitation of D^y

The dissipation associated with evaporation/condensation and the evolution of the liquid volume fraction is collected in D^y and takes the following format

$$\begin{aligned} D^y =& (A_l + \lambda_l - A_g - \lambda_{g_v} - \Delta_v^{\hat{m}})\hat{m} \\ &+ \left(\rho_l \lambda_l - \rho_l W \frac{\partial A_l}{\partial W} - \sum_{j=d,v} \rho_{g_j} \lambda_{g_j} \right) \frac{D_s(n_l)}{Dt} \geq 0 \end{aligned} \tag{58}$$

Here all second order velocity terms appearing as energy conjugated with the rate of evaporation are lumped together in $\Delta_v^{\hat{m}}$.

Evaporation/condensation

The rate of evaporation is assumed to be linear in its energy conjugated term. From (58) it follows that

$$\hat{m} = k_{\hat{m}} (A_l + \lambda_l - A_g - \lambda_{g_v} - \Delta_v^{\hat{m}}) \tag{59}$$

where $k_{\hat{m}}$ defines an internal mass transfer coefficient whose inverse relates to both the resistance for water to evaporate/condensate and the internal area. Enforcing $k_{\hat{m}} \geq 0$ ensures that the first row in D^y is greater or equal to zero. Inserting the derived expression for the Lagrangian multipliers defined in (30b) and (31), neglecting all second order velocity terms, and making use of the definitions of the chemical potentials (93), the rate of evaporation is given by

$$\hat{m} = k_{\hat{m}} (\mu_l - \mu_{g_v}) \tag{60}$$

Standard expressions for these chemical potentials are found in e.g. J.C. Bénet et al. (2012); DeVoe (2012),

$$\mu_l = \mu_l^f + R_{g_v}\theta \ln(a_w) \tag{61a}$$

$$\mu_{g_v} = \mu_{g_v}^0(\theta) + R_{g_v}\theta \ln(\frac{p_{g_v}}{p^0}) \tag{61b}$$

where $\mu_{g_v}^0$ denotes the chemical potential of the water vapor measured at the standard pressure p^0 =1 atm, and μ_l^f denotes the chemical potential of "free" liquid water, cf. Grasley et al. (2011), at an equilibrium state where water is in equilibrium with a vapor saturated gas phase, i.e.

$$\mu_l^f = \mu_{g_v}(\theta, p_{g_v}^{sat}) \tag{62}$$

The terminology "free" is here used to indicate a state where the liquid water is not affected by interactions with a solid. Interactions between fibers and liquid water reduces the energy of the water and within the HMC–region this is quantified with the water activity. The water activity indicates how tightly water is bound to a solid and is defined by $a_w = \frac{p_{g_v}^{eq}}{p_{g_v}^{sat}}$, cf. J.C. Bénet et al. (2012), where $p_{g_v}^{eq}$ denotes the equilibrium vapor pressure inside the porous media and $p_{g_v}^{sat}$ the saturated vapor pressure. Furthermore R_{g_v} denotes the specific gas constant of water vapor. If the expressions of chemical potentials in (61) are inserted into (60) it is found that the rate of evaporation is driven by the ratio between the equilibrium vapor pressure $a_w p_{g_v}^{sat}$ inside the board and the current vapor pressure p_{g_v} inside the board according to

$$\hat{m} = k_{\hat{m}} R_{g_v}\theta \ln(\frac{a_w p_{g_v}^{sat}}{p_{g_v}}) \tag{63}$$

Standard expressions for chemical potentials in (61) are used together with the definitions of the chemical potentials (92) and (93) to render a relation between Helmholtz free energy A_l of the bound water and the free energy A_l^f of water in a "free" state. This results in

$$A_l^f(\theta, \rho_l) = \mu_l^f - \frac{p_l^t}{\rho_l} \tag{64a}$$

$$A_l(\theta, \rho_l, \frac{1}{W}) = \mu_l - \frac{p_l^t + p_l^s}{\rho_l} \tag{64b}$$

$$A_l = A_l^f - \frac{p_l^s}{\rho_l} + R_{g_v}\theta \ln(a_w) \tag{64c}$$

Using (29) to replace the liquid–solid interaction pressure in (64c) renders a differential equation in A_l. The following expression for Helmholtz free energy of the liquid water is then obtained

$$A_l(\theta, \rho_l, \frac{1}{W}) = A_l^f(\theta, \rho_l) + \frac{R_{g_v}\theta}{W}\int \ln(a_w) dW + \frac{1}{W}C(\theta) \tag{65}$$

Here $C(\theta)$ denotes an arbitrary function which is defined through knowledge about A_l at specific moisture ratios.

Evolution of n_l

All balance of mass equations may be considered to have two primary variables, a volume fraction and an intrinsic density. This is known as the closure problem and arises as a consequence of loosing microscopic information during the averaging taking place when macroscopic balance laws are derived cf. e.g. Bennethum and Cushman (1996b). Two common approaches to treat this problem is to either derive a constitutive function for the evolution of the volume fraction, Bowen (1982); Bennethum et al. (2000, 1997) or to consider the intrinsic density to be constant, Hassanizadeh (1986); Ehlers (1992). In the present paper the intrinsic density of the solid is assumed constant and a constitutive law is proposed for the evolution of the liquid volume fraction which is assumed to be linear in its energy conjugated term. From (58) it follows that

$$\frac{D_s(n_l)}{Dt} = r_{n_l}\left(p_l - \sum_{j=d,v} p_{g_j} - p_l^s\right) \tag{66}$$

Enforcing $r_{n_l} \geq 0$ ensures that the second row of D^y is greater or equal to zero. Defining $k_{n_l} = r_{n_l}^{-1}$ allows expression (66) to be rearranged into a dynamic expression for the liquid–solid interaction pressure as

$$p_l^s = p_l - \sum_{j=d,v} p_{g_j} - k_{n_l}\frac{D_s(n_l)}{Dt} \tag{67}$$

The above relation reveals that the interaction pressure is affected by the rate of which the liquid volume fraction changes. This is similar to the common relation where the dynamic part of the interaction pressure is given by the time derivative of the saturation cf. e.g. Hassanizadeh and Gray (1990). Comparing (67) with (36) it is found that the thermodynamic pressures of the fluids relate via

$$p_l^t = \sum_{j=d,v} p_{g_j} + k_{n_l}\frac{D_s(n_l)}{Dt} \tag{68}$$

At an equilibrium state where $\frac{D_s(n_l)}{Dt} = 0$ and $p_g = \sum_{j=d,v} p_{g_j}$, relations (67) and (68) reduces into

$$p_l^s = p_l - p_g \tag{69a}$$

$$p_l^t = \sum_{j=d,v} p_{g_j} \tag{69b}$$

The first relation (69a) states that the liquid–solid interaction pressure equals a pressure jump between the liquid phase and the gas phase at equilibrium. It should, however, be emphasized that the pressures used in this article are postulated on the macroscale implying that the terminology pressure jump is not used as a interface property but as a notion of the difference in the macroscopic pressures. The second relation (69b) implies that the thermodynamic pressure of the liquid phase equals the sum of the thermodynamic pressures of the gas constituents at equilibrium, i.e. Dalton's law.

5.4 Exploitation of D^p

The remaining addend D^p of the dissipation inequality is related to plastic deformations of the fibrous network and is given by

$$D^p = \bar{\boldsymbol{\sigma}}_s^{eff} : \mathbf{d}_s^p - \sum_{k=1}^{n} \frac{1}{J_s} \bar{K}_s^{(k)} \frac{D_s(\kappa_s^{(k)})}{Dt} \geq 0 \tag{70}$$

The hardening parameters, $\bar{K}_s^{(k)}$, are introduced as

$$\bar{K}_s^{(k)} = n_s^0 \rho_s^0 \frac{\partial A_s}{\partial \kappa_s^{(k)}} \tag{71}$$

where n_s^0 and ρ_s^0 denotes the initial solid volume fraction and intrinsic density respectively. To obtain a plastic evolution described with respect to the effective Kirchhoff stress tensor, $\bar{\boldsymbol{\tau}}_s^{eff} = J_s \bar{\boldsymbol{\sigma}}_s^{eff}$, D^p is multiplied with $J_s > 0$,

$$D^p J_s = \bar{\boldsymbol{\tau}}_s^{eff} : \mathbf{d}_s^p - \sum_{k=1}^{n} \bar{K}_s^{(k)} \frac{D_s(\kappa_s^{(k)})}{Dt} \geq 0 \tag{72}$$

Expression (72) motivates a yield surface defined by $f(\bar{\boldsymbol{\tau}}_s^{eff}, \mathbf{n}^{(k)}, \bar{K}_s^{(k)})$ where $\mathbf{n}^{(k)}$ define director vectors which allows for an anisotropic plastic response, cf. Spencer (1984); Boehler (1987). Assuming associated plasticity, evolution laws for the plastic rate of deformation $\mathbf{d}_s^p$ and for the internal variables $\kappa_s^{(k)}$ are given by

$$\mathbf{d}_s^p = \dot{\lambda}_p \frac{\partial f}{\partial \bar{\boldsymbol{\tau}}_s^{eff}}, \qquad \frac{D_s(\kappa_s^{(k)})}{Dt} = -\dot{\lambda}_p \frac{\partial f}{\partial \bar{K}_s^{(k)}} \tag{73}$$

Here $\dot{\lambda}_p$ is a Lagrangian multiplier fulfilling the Kuhn–Tucker conditions, $\dot{\lambda}_p \geq 0,\ \dot{\lambda}_p f = 0$ and for elastic responses $\dot{\lambda}_p = 0$.

6 Summarizing the derived model

In this section the balance equations presented in section 3 and the constitutive relations derived in section 5 are summarized into a closed set of equations. The retrieved system of equations is considered to govern the response of a deforming moist paperboard in environments where both temperature and pressure may change significantly during a short period of time. In the present work, focus is on the response of paperboard with a moisture ratio within the HMC region where all water is considered bound and it is assumed that the motion of the bound water follows that of the fiber network, i.e. $\mathbf{v}_{l,s} = \mathbf{0}$. Moreover it is assumed that the potentials A_s, A_l^f and A_{g_j} are known as well as the yield surface f.

6.1 Transportation of mass

The transportation of mass in the board is related to the balance of mass equations (11). The intrinsic density of the solid phase is assumed constant and assuming, in addition, the mass of the solid phase to be constant provides a relation between the porosity $1 - n_s$ and the volume change J_s of the board, defined by

$$n_s = n_s^0 J_s^{-1} \tag{74}$$

The remaining balance of mass equations defines the first three governing equations and are provided by

$$\frac{D_s(\bar{\rho}_l)}{Dt} + \bar{\rho}_l \nabla \cdot (\mathbf{v}_s) + \hat{m} = 0 \tag{75a}$$

$$\rho_{g_d} \frac{D_s(n_g)}{Dt} + \frac{\bar{\rho}_{g_d}}{p_{g_d}} \frac{D_s(p_{g_d})}{Dt} - \frac{\bar{\rho}_{g_d}}{\theta} \frac{D_s(\theta)}{Dt} + \nabla \cdot (\mathbf{J}_{g_d}) + \bar{\rho}_{g_d} \nabla \cdot (\mathbf{v}_s) = 0 \tag{75b}$$

$$\rho_{g_v} \frac{D_s(n_g)}{Dt} + \frac{\bar{\rho}_{g_v}}{p_{g_v}} \frac{D_s(p_{g_v})}{Dt} - \frac{\bar{\rho}_{g_v}}{\theta} \frac{D_s(\theta)}{Dt} + \nabla \cdot (\mathbf{J}_{g_v}) + \bar{\rho}_{g_v} \nabla \cdot (\mathbf{v}_s) - \hat{m} = 0 \tag{75c}$$

Equations (75) naturally relates to the primary variables ρ_l, p_{g_d} and p_{g_v} respectively. In addition, using that the thermodynamic pressures and the physical pressures are equal for the gas constituents, pressure and density are related via the ideal gas law $p_{g_j} = R_{g_j} \rho_{g_j} \theta$. The combined mass fluxes $\mathbf{J}_{g_j} = \bar{\rho}_{g_j}(\mathbf{w}_{g_j} + \mathbf{v}_{g,s})$ and the rate of evaporation $\hat{m}$ are defined by

$$\left(1 + \frac{\rho_g \beta_{g,s} k_{g,s}}{\mu_g^D} |\mathbf{v}_{g,s}|\right) \mathbf{R}_{g,s} \cdot \mathbf{v}_{g,s} = -n_g \nabla (p_{g_v} + p_{g_d}) + \bar{\rho}_g \mathbf{b}_g \tag{76a}$$

$$\frac{\mathbf{R}_{g_v}}{\bar{\rho}_{g_v}} \cdot \mathbf{w}_{g_v} = -\nabla(\mu_{g_v} - \mu_{g_d}) - \mathbf{b}_{g_v} + \mathbf{b}_{g_d} \tag{76b}$$

$$\hat{m} = k_{\hat{m}} R_{g_v} \theta \ln\left(\frac{p_{g_v}^{sat} a_w}{p_{g_v}}\right) \tag{76c}$$

where chemical potentials μ_{g_j} are defined in (45). Specific formats for $p_{g_v}^{sat}$ and a_w are discussed in the next section. Furthermore, the evolution law for the volume fraction n_l is given by

$$\frac{D_s(n_l)}{Dt} = r_{n_l} \left(p_l - \sum_{j=d,v} p_{g_j} - p_l^s\right) \tag{77}$$

where the liquid–solid interaction pressure p_l^s is defined in (29). Note that n_s is given by (74) and n_g is obtained from the saturation condition.

6.2 Mechanical response

The balance of linear momentum of the solid phase is used to determine the mechanical response of the paperboard and the linear momentum transfer parameters appearing

in (13a) are therefore replaced via (14). Neglecting all macroscopic fluid inertial terms and making use of definitions (16a), (18c) and (18a) the balance of linear momentum of the solid phase is provided by

$$\bar{\rho}_s \frac{D_s(\mathbf{v}_s)}{Dt} - \nabla \cdot (\boldsymbol{\sigma}) - \rho \mathbf{b} + \hat{m}(\mathbf{v}_{g,s} + \mathbf{w}_{g_v}) = 0 \tag{78}$$

where the total Cauchy stress tensor is defined by

$$\boldsymbol{\sigma} = \bar{\boldsymbol{\sigma}}_s^{eff} - [\sum_{j=d,v} p_{g_j} + n_l k_{n_l} \frac{D_s(n_l)}{Dt}]\mathbf{I} \tag{79}$$

The effective Cauchy stress tensor of the solid phase, $\bar{\boldsymbol{\sigma}}_s^{eff}$, is provided by (33) and to derive the plastic part of the deformation, use is made of the following evolution laws

$$\mathbf{d}_s^p = \dot{\lambda}_p \frac{\partial f}{\partial \bar{\boldsymbol{\tau}}_{eff}}, \qquad \frac{D_s \kappa_s^{(k)}}{Dt} = -\dot{\lambda}_p \frac{\partial f}{\partial \bar{K}_s^{(k)}} \tag{80}$$

The primary variable associated with (78) is the solid displacement vector $\mathbf{u}_s$.

6.3 Transportation of energy

The balance of energy equation presented in (17) is reformulated in B and reduced to

$$\begin{aligned} c^p \frac{D_s(\theta)}{Dt} + \left(p_l^t - \frac{\partial p_l^t}{\partial \theta}\theta\right) \frac{n_l}{\rho_l} \frac{D_s(\rho_l)}{Dt} - n_l k_{n_l} \left(\frac{D_s(n_l)}{Dt}\right)^2 - \rho Q \\ + \rho \mathbf{b} \cdot \mathbf{w}_s + \nabla \cdot (\mathbf{q}) - \sum_j h_{gj} \nabla \cdot (\mathbf{J}_{gj}) + \hat{m} \Delta H_{ads} = 0 \end{aligned} \tag{81}$$

The primary variable associated with (81) is the absolute temperature θ. The thermodynamic pressure, p_l^t, is obtained from (90) and total heat flux $\mathbf{q}$ and the total heat capacity c^p are defined by

$$\mathbf{q} = \sum_{j=d,v} \bar{\rho}_{g_j} h_{g_j} \mathbf{v}_{g,s} - \mathbf{K}_\theta \cdot \nabla(\theta) + \sum_{j=d,v} \bar{\rho}_{g_j} \mu_{g_j} \mathbf{w}_{g_j} \tag{82a}$$

$$c^p = \bar{\rho}_s c_s^p + \bar{\rho}_l c_l^p + \bar{\rho}_{g_v} c_{g_v}^p + \bar{\rho}_{g_d} c_{g_d}^p \tag{82b}$$

where the enthalpies h_{g_j} are defined in (57). The expression for the enthalpy of adsorption ΔH_{ads} is derived in B as

$$\Delta H_{ads} = h_{g_v} - h_l^f + R_{g_v} \theta^2 \frac{\partial(\ln(a_w))}{\partial \theta} \tag{83}$$

where the enthalpy, h_l^f, and the entropy, η_l^f, of the "free" liquid water are given by

$$h_l^f = A_l^f + \eta_l^f \theta + \frac{p_l^t}{\rho_l}, \qquad \eta_l^f = -\frac{\partial A_l^f}{\partial \theta} \tag{84}$$

7 Dynamic mass exchange between liquid water and water vapor

As an illustration of the importance of including a dynamic phase change between bound water and water vapor, and at the same time introduce some of the unknown functions discussed in previous sections, a rapid increase in temperature is considered. A board with the initial moisture ratio W^0 is heated from $\theta^0 = 296^\circ$ K to $\theta^{max} = 438^\circ$ K in 1 s and then held at the elevated temperature for 105 s. In order to single out the effect of the mass exchange, the board is considered to be in a homogeneous state and deformations and mass fluxes are neglected. Further, intrinsic densities of the solid and liquid phases are given by ρ_s =1 500 kg·m^{-3}, ρ_l =1 000 kg·m^{-3}, respectively, and the solid volume fraction is given by $n_s = 0.43$. Both gas constituents are assumed to behave as ideal gases $p_{g_j} = \rho_{g_j} R_{g_j} \theta$ where the specific gas constituents are given by $R_{g_d} = 287.058$ J·kg^{-1}·K^{-1} and $R_{g_v} = 461.5$ J·kg^{-1}·K^{-1}. With these assumptions the system of equations presented in section 6 reduce to three differential equations given by

$$\frac{D_s(n_l)}{Dt} + \frac{\hat{m}}{\rho_l} = 0 \tag{85a}$$

$$\frac{D_s(n_l)}{Dt} - \frac{n_g}{p_{g_d}} \frac{D_s(p_{g_d})}{Dt} + \frac{n_g}{p_{g_d}} \frac{D_s(\theta)}{Dt} = 0 \tag{85b}$$

$$\frac{D_s(n_l)}{Dt} - \frac{n_g}{p_{g_v}} \frac{D_s(p_{g_v})}{Dt} + \frac{n_g}{p_{g_v}} \frac{D_s(\theta)}{Dt} + \frac{\hat{m}}{\rho_{g_v}} = 0 \tag{85c}$$

The dynamic mass exchange is governed by the rate of evaporation, given in (76c) as

$$\hat{m} = k_{\hat{m}} R_{g_v} \theta \ln \left(\frac{p_{g_v}^{sat} a_w}{p_{g_v}} \right) \tag{86}$$

Here $k_{\hat{m}}$ is assumed to be constant $k_{\hat{m}} = 2.7 \times 10^{-7}$ kg·s/m^5, cf. Alexandersson et al. (2016). The water activity, denoted a_w, is an indicator of how tightly water is bound in a medium and $p_{g_v}^{sat}$ denotes the saturation vapor pressure which is assumed to follow the Antoine relation

$$p_{gv}^{sat} = 133.322 \times 10^{(8.07131 - 1730.63/(\theta - 39.574))} \text{[Pa]} \tag{87}$$

The equilibrium vapor pressure inside the board is given by $p_{g_v}^{eq} = a_w p_{g_v}^{sat}$ and (86) implies that depending on whether the vapor pressure is above or below its equilibrium state, adsorption or desorption will occur. The water activity in a porous media is commonly defined by sorption isotherms. Some of the more frequently used isotherms for paperboard are reviewed by Stenström and Petterson Petterson and Stenström (2000). Considering the properties of the isosteric heat of adsorption Stenström and Petterson argue that an isotherm suggested by Heikkilä 1993 is suited for calculations on paper. The isotherm assumed in the present study is similar to the Heikkilä isotherm and given by

$$a_w = 1 - \exp(-84 W^{1.9} - 0.2(\theta - 273.15) W^{1.2}) \tag{88}$$

Experimental adsorption, desorption data and the fitted isotherm are shown in Figure 2(a) and the corresponding difference $\Delta H_{ads} - \Delta H_{vap}$, cf. 102, is shown together with experimental data in Figure 2(b), experimental data are taken from Cleland et al. (2007).

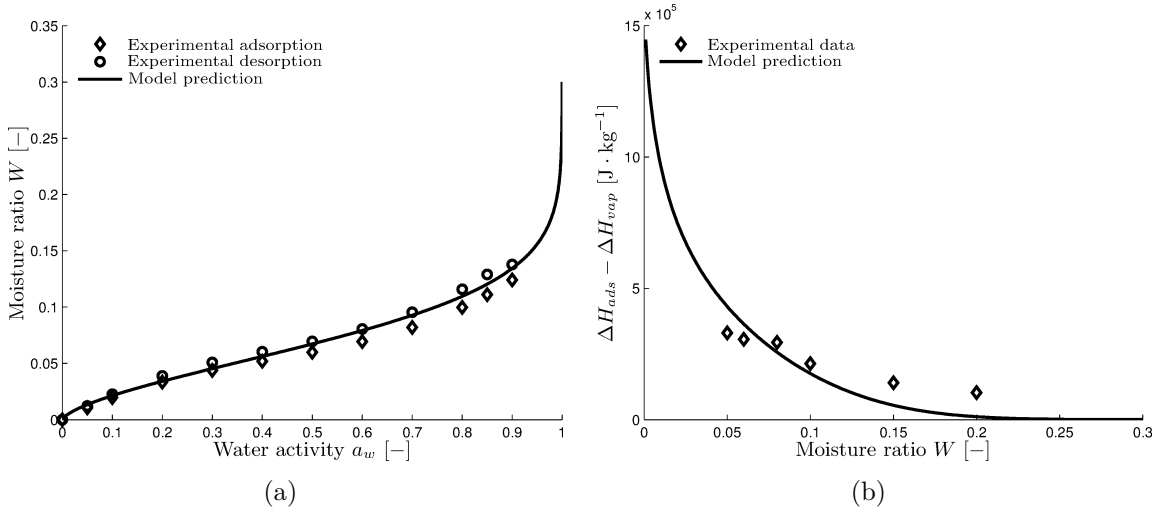

(a) (b)

Figure 2: **a** Sorption isotherm in (88) fitted to experimental adsorption and desorption curves. **b** $\Delta H_{ads} - \Delta H_{vap}$ fitted against experimental data for Kraft linerboard Cleland et al. (2007).

The system of differential equations in (85) are solved using the Matlab `ode15s` solver with the initial conditions: $n_l^0 = W^0 \bar{\rho}_s / \rho_l$, $p_g^0 = 1$ atm, $p_{g_v}^0 = a_w(W^0, \theta^0) p_{g_v}^{sat}(\theta^0)$, $p_{g_d}^0 = p_g^0 - p_{g_v}^0$, $W^0 \in \{0.001, 0.01, 0.1, 0.2, 0.3\}$. In Figure 3(a) the dynamic evolution of the relative humidity $\varphi = p_{g_v}/p_{g_v}^{sat}$ inside the board is illustrated by plotting the difference between the equilibrium relative humidity, $\varphi^{eq} = a_w$, and the current relative humidity φ. It is observed that the difference $a_w - \varphi$ increase while the temperature increases, $t \leq 1$ s, and when the temperature is held constant, φ evolves towards an equilibrium value $a_w(W, \theta^{max})$. From Figure 3(a) it is also noted that the initial moisture ratio has a significant influence on the time it takes to reach an equilibrium state. This property is also seen in Figure 3(b) where the rate of evaporation $\hat{m}$ is shown.

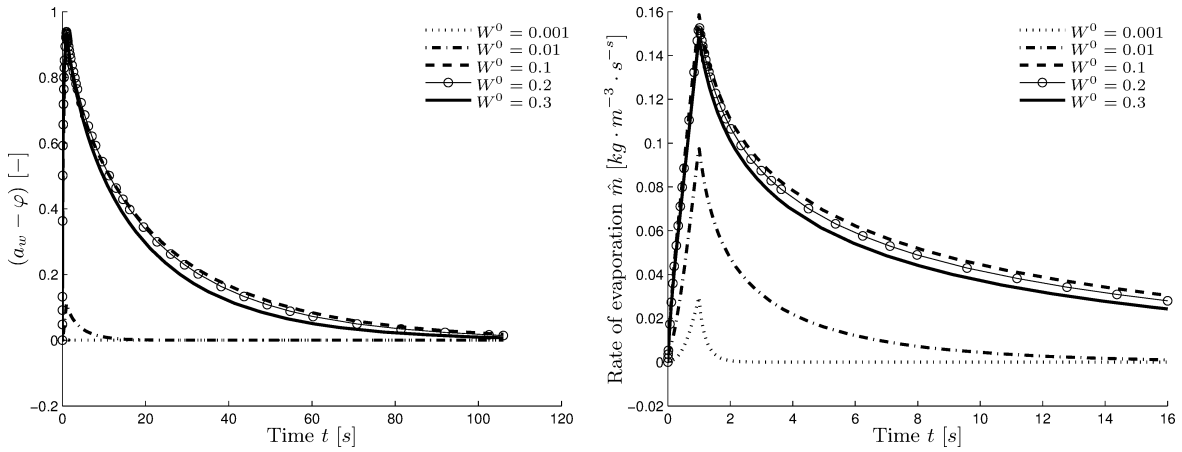

(a) (b)

Figure 3: **a** Evolution of the difference $a_w - \varphi$ over 106 s and **b** evolution of the rate of evaporation $\hat{m}$ over 15 s .

In Figure 4(a) the evolution of the pressure gap $p_g^{gap} = p_g - p_g^{out}$ between the pressure inside the board p_g and the ambient pressure $p_g^{out} = 1$ atm is shown. The initial jump $p_g^{gap}(t = 1s) \approx 0.05$ MPa is caused by the explicit dependence on the absolute temperature in the ideal gas laws. The remaining increase in pressure is due by evaporation which also is visualised in Figure 4(b) where the change in moisture ratio $W^0 - W$ is shown. Considering the higher initial moisture ratios $W^0 \in \{0.1, 0.2, 0.3\}$ the gas pressure reaches a magnitude above 0.36 MPa which is in the range of the out–of–plane failure stress of paperboard, cf. Stenberg (2003).

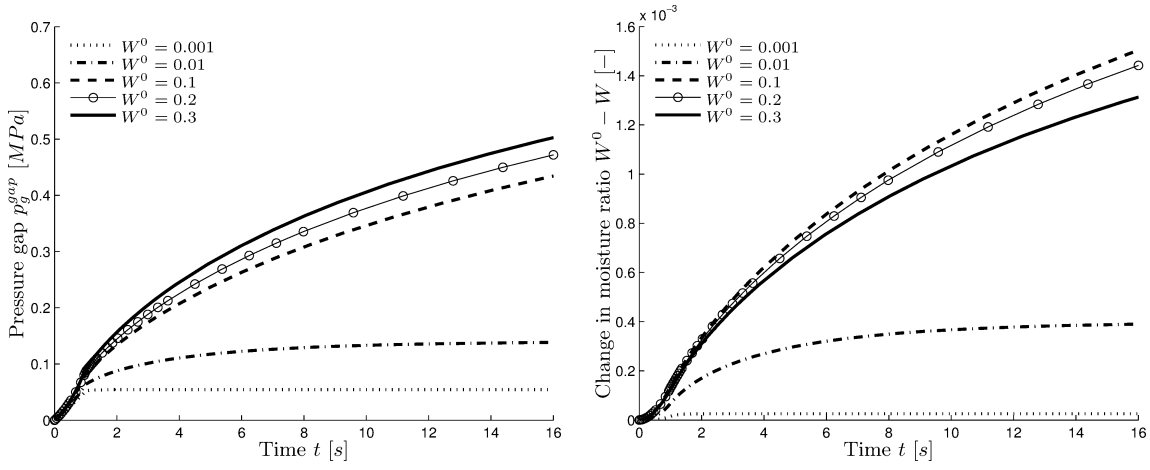

(a) (b)

Figure 4: **a** Simulated gas pressure evolution due to a significant temperature change and **b** simulated drying of the paperboard .

8 Conclusions

A two scale mixture theoretical framework is adopted to derive a model able to describe deformation and complex transportation processes within paperboard. Specific interest is on the response of paperboard in environments where significant temperature and pressure changes are expected during a short period of time. The derived model describes transient heat and moisture transport coupled with the stress–strain response in a large strain setting. Paperboard is viewed as a triphasic medium consisting of a solid phase representing the fiber network, a liquid phase representing bound water and a gas phase representing moist air. The model is derived under the assumption of local thermal equilibrium and that the interfaces do not contain any thermodynamic properties. The model assumes a relatively low moisture ratio, within the HMC region, such that free energy of the liquid water is reduced due to interaction with the fiber network. The dynamic mass exchange between bound water and water vapor is then investigated through a rapid heating of moist paperboard. It is found that the initial moisture ratio may have a significant effect on the response of the board. The effects of changing the initial moisture ratio are seen in e.g. the gas pressure evolution and the time it takes for the board to reach a state of equilibrium. In a forthcoming publication, results related to presence of mass flux and deformations will be reported.

A Thermodynamic quantities

Assuming general expressions for Helmholtz free energies $A_\alpha = A_\alpha(\theta, \rho_{\alpha_j}, x_\alpha^{(l)})$, $A_{\alpha_j} = A_{\alpha_j}(\theta, \rho_{\alpha_j}, x_{\alpha_j}^{(l)})$, the generalized forces, $X_\alpha^{(l)}, X_{\alpha_j}^{(l)}$, energy conjugated with $x_\alpha^{(l)}$ and $x_{\alpha_j}^{(l)}$ are defined as

$$X_\alpha^{(l)} = \left.\frac{\partial A_\alpha}{\partial x_\alpha^{(l)}}\right|_{\theta,\rho_{\alpha_j},x_\alpha^{(k)}(k\neq l)}, \qquad X_{\alpha_j}^{(l)} = \left.\frac{\partial A_{\alpha_j}}{\partial x_{\alpha_j}^{(l)}}\right|_{\theta,\rho_{\alpha_j},x_{\alpha_j}^{(k)}(k\neq l)} \tag{89}$$

In the present work the terminology thermodynamic pressures is used for the thermodynamic quantities defined via

$$p_\alpha^t = \sum_j \rho_\alpha \rho_{\alpha_j} \left.\frac{\partial A_\alpha}{\partial \rho_{\alpha_j}}\right|_{\theta,\rho_{\alpha_k}(k\neq j),x_\alpha^{(l)}}, \qquad p_{\alpha_j}^t = \rho_{\alpha_j}^2 \left.\frac{\partial A_{\alpha_j}}{\partial \rho_{\alpha_j}}\right|_{\theta,x_{\alpha_j}^{(l)}} \tag{90}$$

The term physical pressure will be used to refer to pressures proportional to the trace of the stress tensors,

$$p_\alpha = -\frac{\mathrm{tr}(\boldsymbol{\sigma}_\alpha)}{3}, \qquad p_{\alpha j} = -\frac{\mathrm{tr}(\boldsymbol{\sigma}_{\alpha_j})}{3} \tag{91}$$

Here the chemical potential μ_α of a single species phase is defined as the Gibbs potential and the chemical potential μ_{α_j} of constituent α_j in a multi species phase is defined as the term energy conjugated with the concentration of the constituent, i.e.,

$$\mu_\alpha = \left.\frac{\partial(\rho_\alpha A_\alpha)}{\partial \rho_\alpha}\right|_{\theta,x_\alpha^{(l)}} - \sum_l x_\alpha^{(l)} X_\alpha^{(l)}, \qquad \mu_{\alpha_j} = \left.\frac{\partial(\rho_\alpha A_\alpha)}{\partial \rho_{\alpha_j}}\right|_{\theta,\rho_{\alpha_k}(k\neq j),x_\alpha^{(l)}} \tag{92}$$

With the dependencies of Helmholtz free energies stated in (24) the chemical potentials for the gas constituents and the liquid phase become

$$\mu_{g_j} = \left.\frac{\partial(\rho_g A_g)}{\partial \rho_{g_j}}\right|_{\theta,\rho_{g_k}(k\neq j)}, \qquad \mu_l = A_l + \frac{p_l^t}{\rho_l} + W\left.\frac{\partial A_l}{\partial W}\right|_{\theta,\rho_l} \tag{93}$$

B Derivation of the heat equation

Assuming $\mathbf{v}_{l,s} = \mathbf{0}$, imposing the restricted mass transformations (25), and neglecting second order velocity terms and all macroscopic fluid inertial forces, the balance of energy (17) reduces to

$$\begin{aligned}\bar{\rho}_s \frac{D_s(e_s)}{Dt} + \bar{\rho}_l \frac{D_s(e_l)}{Dt} + \sum_{j=d,v} \bar{\rho}_{g_j} \frac{D_s(e_{g_j})}{Dt} - \boldsymbol{\sigma} : \mathbf{d}_s + \nabla\cdot(\mathbf{q}) - \rho Q \\ + \rho \mathbf{b}\cdot\mathbf{w}_s - \sum_{j=d,v} e_{g_j} \nabla\cdot(\mathbf{J}_{g_j}) + \hat{m}(e_{g_v} - e_l) = 0\end{aligned} \tag{94}$$

Using Legendre transformations $e_{\alpha_j} = A_{\alpha_j} + \eta_{\alpha_j}\theta$, the derived entropy relation, (30a) and the assumed dependencies of Helmholtz free energies (24), the material time derivatives of the internal energies may be expressed by

$$\bar{\rho}_s \frac{D_s(e_s)}{Dt} = \bar{\rho}_s c_s^v \frac{D_s(\theta)}{Dt} + \bar{\boldsymbol{\sigma}}_s^{eff} : \mathbf{d}_s^e + \sum_k \frac{1}{J_s} \bar{K}_s^{(k)} \frac{D_s(\kappa^{(k)})}{Dt} \tag{95a}$$

$$\bar{\rho}_l \frac{D_s(e_l)}{Dt} = \bar{\rho}_l c_l^v \frac{D_s(\theta)}{Dt} + \left(p_l^t - \frac{\partial p_l^t}{\partial \theta}\theta\right) \frac{n_l}{\rho_l} \frac{D_s(\rho_l)}{Dt} + \left(p_l^s - \frac{\partial p_l^s}{\partial \theta}\theta\right) \frac{n_l}{W} \frac{D_s(W)}{Dt} \tag{95b}$$

$$\bar{\rho}_{g_j} \frac{D_s(e_{g_j})}{Dt} = \bar{\rho}_{g_j} c_{g_j}^v \frac{D_s(\theta)}{Dt} \tag{95c}$$

where c^v denotes the specific heat measured at constant volume. The material time derivative of the moisture ratio is rewritten by expanding the derivative into the independent variables n_l, n_s, ρ_l and then replacing the material time derivatives of n_l, n_s with their corresponding mass balances such that

$$\frac{D_s(W)}{Dt} = -\hat{m}\frac{W}{\bar{\rho}_l} \tag{96}$$

Inserting (95) and (96) into (94) allows the energy balance to be rewritten as

$$\begin{aligned}c^v \frac{D_s(\theta)}{Dt} + \Delta_e^p + [n_l p_l^t + (1-n_l)\sum_{j=d,v} p_{g_j}]\nabla\cdot(\mathbf{v}_s) - \rho Q \\ + \rho\mathbf{b}\cdot\mathbf{w}_s + \left(p_l^t - \frac{\partial p_l^t}{\partial\theta}\theta\right)\frac{n_l}{\rho_l}\frac{D_s(\rho_l)}{Dt} + \nabla\cdot(\mathbf{q}) - \sum_{j=d,v} e_{g_j}\nabla\cdot(\mathbf{J}_{g_j}) \\ + \hat{m}\left(e_{g_v} - e_l - \frac{p_l^s}{\rho_l} + \frac{\theta}{\rho_l}\frac{\partial p_l^s}{\partial\theta}\right) = 0\end{aligned} \tag{97}$$

where the total heat capacity was introduced $c^v = \bar{\rho}_s c_s^v + \bar{\rho}_l c_l^v + \sum_j \bar{\rho}_{g_j} c_{g_j}^v$ and (40d) was used to eliminate the $\bar{\boldsymbol{\sigma}}_s^{eff} : \mathbf{d}_s^e$ contribution from (95a). In (97) the heat generated by plastic response is collected in $\Delta_e^p = -\boldsymbol{\sigma} : \mathbf{d}_s^p + \sum_k \frac{1}{J_s} \bar{K}^{(k)} \frac{D_s(\kappa^{(k)})}{Dt}$. In the presented model it is assumed that the contribution from Δ_e^p is sufficiently small and will be neglected. From expression (64c) it follows that

$$\frac{\theta}{\rho_l} \frac{\partial p_l^s}{\partial \theta} - \frac{p_l^s}{\rho_l} = A_l + \eta_l \theta - A_l^f - \eta_l^f \theta + R_{g_v} \theta^2 \frac{\partial(\ln(a_w))}{\partial \theta} \tag{98}$$

where the entropies are defined via (30a). Furthermore the balance of mass equations (74) and (75) are used to replace $n_\alpha \nabla \cdot (\mathbf{v}_s)$ according to

$$\begin{aligned}[n_l p_l^t + (n_s + n_g) \sum_{j=d,v} p_{g_j}] \nabla \cdot (\mathbf{v}_s) = -p_l^t \left(\frac{n_l}{\rho_l} \frac{D_s(\rho_l)}{Dt} - \frac{D_s(n_l)}{Dt} \right) + \hat{m} \left(\frac{p_{g_v}}{\rho_{g_v}} - \frac{p_l^t}{\rho_l} \right) \\ - \sum_{j=d,v} p_{g_j} \left[\frac{D_s(n_s)}{Dt} + \frac{D_s(n_g)}{Dt} - \frac{n_g}{p_{g_j}} \frac{D_s(p_{g_j})}{Dt} - \frac{n_g}{\theta} \frac{D_s(\theta)}{Dt} - \frac{1}{\rho_{g_j}} \nabla \cdot (\mathbf{J}_{g_j}) \right]\end{aligned} \tag{99}$$

The terms including a material time derivative of a volume fraction are rewritten using the saturation condition and the derived relation between the thermodynamic pressures of the fluids (68) as

$$\sum_{j=d,v} p_{g_j} \left[\frac{D_s(n_s)}{Dt} + \frac{D_s(n_g)}{Dt} \right] + p_l^t \frac{D_s(n_l)}{Dt} = -n_l k_{n_l} \left(\frac{D_s(n_l)}{Dt} \right)^2 \tag{100}$$

Inserting (98),(99) and (100) in (97) the heat equation appears in the following format

$$\begin{aligned}c^p \frac{D_s(\theta)}{Dt} + \left(p_l^t - \frac{\partial p_l^t}{\partial \theta} \theta \right) \frac{n_l}{\rho_l} \frac{D_s(\rho_l)}{Dt} - n_l k_{n_l} \left(\frac{D_s(n_l)}{Dt} \right)^2 - \rho Q \\ + \rho \mathbf{b} \cdot \mathbf{w}_s + \nabla \cdot (\mathbf{q}) - \sum_j h_{g_j} \nabla \cdot (\mathbf{J}_{g_j}) + \hat{m} \Delta H_{ads} = 0\end{aligned} \tag{101}$$

where $c^p = c^v + \sum_j \bar{\rho}_{g_j} R_{g_j}$. In this expression the specific enthalpy of adsorption ΔH_{ads} is defined as the term energy conjugated with the rate of evaporation

$$\Delta H_{ads} = \Delta H_{vap} + R_{g_v} \theta^2 \frac{\partial(\ln(a_w))}{\partial \theta} \tag{102}$$

where the specific enthalpy of evaporation $\Delta H_{vap} = h_{g_v} - h_l^f$ is introduced.

References

E. Baggerud, Modelling of Mass and Heat Transport in Paper, Ph.D. thesis, Lund University, 2004.

M. Rigdahl, H. Andersson, L. Salmen, H. Hollmark, The Influence of Moisture on the Stiffness of Paper in Terms of Network Mechanics, Fibre Science and Technology 20 (1984) 1–11.

M. Karlsson, S. Stenström, Static and Dynamic Modeling of Carboard Drying Part 1: Theoretical Model, Drying Technology 23 (2005) 143–163.

E. Linvill, Development of Finite Element Models for 3D Forming Processes of Paper and Paperboard, 2015.

E. Borgqvist, M. Wallin, M. Ristinmaa, J. Tryding, An anisotropic in-plane and out-of-plane elasto-plastic continuum model for paperboard, Composite Structures 126 (2015) 184–195.

Q. S. Xia, M. C. Boyce, D. M. Parks, A constitutive model for the anisotropic elastic-plastic deformation of paper and paperboard, International Journal of Solids and Structures 39 (2002) 4053–4071.

A. Harrysson, M. Ristinmaa, Large strain elasto-plastic model of paper and corrugated board, International Journal of Solid and Structures 45 (2008) 3334–3352.

A. J. M. Spencer, Continuum theory of the mechanics of fiber-reinforced composites, vol. 282, Springer Vienna, 1984.

J. Boehler, Applications of tensor functions in solid mechanics, vol. 292, Springer-Verlag Wien, 1987.

P. A. M. Zapata, M. Fransen, J. T. Boonkkamp, L. Saes, Coupled heat and moisture transport in paper with application to a warm print surface, Applied Mathematical Modelling 37 (2013) 7273–7286.

M. Alexandersson, H. Askfelt, M. Ristinmaa, Triphasic Model of Heat and Moisture Transport with Internal Mass Exchange in Paperboard, Transport in Porous Media 112 (2016) 381–408.

C. Truesdell, R. Toupin, The Classical Field Theories, Springer Berlin Heidelberg, 226–858, 1960.

R. M. Bowen, Part I - Theory of Mixtures, in: A. C. Eringen (Ed.), Continuum Physics, Academic Press, 1–127, 1976.

P. Kelly, A Reacting Continuum, International Journal of Engineering Science 2 (2) (1964) 129–153.

I. Müller, A Thermodynamic Theory of Mixtures of Fluids, Archive for Rational Mechanics and Analysis 28 (1) (1968) 1–39.

A. E. Green, P. M. Naghdi, A theory of mixtures, Archive for Rational Mechanics and Analysis 24 (4) (1967) 243–263.

J. D. Ingram, A. C. Eringen, A continuum theory of chemically reacting media—II Constitutive equations of reacting fluid mixtures, International Journal of Engineering Science 5 (4) (1967) 289–322.

K. R. Rajagopal, L. Tao, Mechanics of mixtures , World Scientific, 1995.

R. J. Atkin, R. E. Crane, Continuum Theories of Mixtures: Basic Theory and Historical Development, The Quarterly Journal of Mechanics and Applied Mathematics 29.

R. de Boer, W. Ehlers, A Historical Review of the Formulation of Porous Media Theories, Acta Mechanica 74 (1988) 1–8.

R. de Boer, Development of Porous Media Theories - A Brief Historical Review, Tranport in Porous Media 94 (1992) 155–164.

R. de Boer, Theory of Porous Media Highlights in Historical Development and Current State, Springer-Verlag Berlin Heidelberg, 2000.

K. R. Rajagopal, A. S. Wineman, M. Gandhi, On Boundary Conditions For a Certain Class of Problems in Mixture Theory, International Journal of Engineering Science 24 (8) (1986) 1453–1463.

L. S. Bennethum, J. H. Cushman, Multiscale, hybrid mixture theory for swelling systems-I: Balance Laws, International Journal of Engineering Science 34 (1996a) 125–145.

S. M. Hassanizadeh, W. G. Gray, Mechanics and thermodynamics of multiphase flow in porous media including interphase boundaries, Advances in Water Resources 13 (4) (1990) 169–186.

M. Hassanizadeh, W. G. Gray, General conservation equations for multi-phase systems: 1. Averaging procedure, Advances in Water Resources 2 (1979) 131–144.

L. S. Bennethum, Multiscale, hybrid mixture theory for swelling systems with interfaces, Ph.D. thesis, Purdue University, 1994.

L. S. Bennethum, J. H. Cushman, Multiscale, hybrid mixture theory for swelling systems-II: Constitutive theory, International Journal of Engineering Science 34 (1996b) 147–169.

M. Ristinmaa, N. S. Ottosen, B. Johannesson, Mixture theory for a thermoelastoplastic porous solid considering fluid flow and internal mass exchange, International Journal of Engineering Science 49 (2011) 1185–1203.

W. Ehlers, Toward finite theories of liquid-saturated elasto-plastic porous media, International Journal of Plasticity 7 (1991) 433–475.

W. Ehlers, An Elastoplasticity Model in Porous Media Theories, Transport in Porous Media 94 (1992) 49–59.

W. G. Gray, C. T. Miller, Consistent thermodynamic formulations for multiscale hydrologic systems: Fluid pressures, Water Resources Research 43.

I. S. Liu, Method of Lagrange multipliers for exploitation of the entropy principle, Archive for Rational Mechanics and Analysis 46 (1972) 131–141.

S. M. Hassanizadeh, W. G. Gray, High Velocity Flow in Porous Media, Transport in Porous Media 2 (1987) 521–531.

L. S. Bennethum, T. Giorgi, Generalized Forchheimer Equation for Two-Phase Flow Based on Hybrid Mixture Theory, Transport in Porous Media 26 (1997) 261–275.

D. D. Joseph, D. A. Nield, G. Papanicolaou, Nonlinear Equation Governing Flow in a Saturated Porous Medium, Water Resources Research 18 (4) (1982) 1049–1052.

S. Srinivasan, K. R. Rajagopal, A thermodynamic basis for the derivation of the Darcy, Forchheimer and Brinkman models for flows through porous media and their generalizations, International Journal of Non-Linear Mechanics 58 (2014) 162–166.

L. S. Bennethum, J. H. Cushman, Clarifying hybrid mixture theory and the macroscale chemical potential for porous media, International Journal of Engineering Science 34 (1996c) 1611–1621.

L. S. Bennethum, M. A. Murad, J. H. Cushman, Modified Darcys Law Terzaghis Effective Stress Principle and Ficks Law for Swelling Clay Soils, Computers and Geotechnics 20 (39) (1997) 245–266.

Z. C. Grasley, K. R. Rajagopal, C. K. Leung, Equilibrium of partially dried porous media influenced by dissolved species and the development of new interfaces, International Journal of Engineering Science 49 (2011) 711–725.

J.C. Bénet, A. Ramirez-Martinez, F. Ouedraogo, F. Cherblanc, Measurment of chemical potential of a liquid in porous media, Journal of Porous Media 15 (2012) 1019–1029.

H. DeVoe, Thermodynamics and Chemistry, Pearson Education, Inc, 2nd edition edn., 2012.

R. M. Bowen, Compressible porous media models by use of the theory of mixtures, International Journal of Engineering Science 20 (6) (1982) 697–735.

L. S. Bennethum, J. H. Cushman, M. A. Murad, Macroscale Thermodynamics and the Chemical potential for Swelling Porous Media, Transport in Porous Media 39 (2000) 187–225.

S. M. Hassanizadeh, Derivation of basic equations of mass transport in porous media, Part 2. Generalized Darcy's and Fick's laws, Advances in Water Resources 94 (1986) 207–222.

M. Petterson, S. Stenström, Experimental evaluation of electric infrared dryers, Tappi Journal 83 (2000) 89–106.

D. J. Cleland, J. E. Bronlund, D. J. Tanner, N. J. Smale, J. F. Wang, A. L. Nevis, T. Elsten, S. B. Mackay, A. J. Mawson, I. Merts, Refrigeration Load Due to Moisture Sorption From Food Packaging Materials (1210-RP), Tech. Rep., Institute of Technology and Engineering, 2007.

N. Stenberg, A model for the through-thickness elastic-plastic behaviour of paper, International Journal of Solids and Structures 40 (2003) 7483–7498.

Paper C

Henrik Askfelt and Matti Ristinmaa

Response of moist paperboard during rapid compression and heating.

Accepted for publication in Applied Mathematical Modelling

Response of moist paperboard during rapid compression and heating.

Henrik Askfelt[a] and Matti Ristinmaa[a]

[a] Division of Solid Mechanics, Lund University

P.O. Box 118, S-221 00 Lund, Sweden

Abstract

The response of moist paperboard exposed to extensive compression and heating in short periods of time is investigated. A generic framework describing this response, in a thermodynamically consistent manner, has been derived previously. The present paper provides explicit formats of the necessary constitutive relations specific to moist paperboard exposed to extensive compression and heating in short periods of time. The transient transports of mass, momentum and energy, as well as specific interaction terms are considered for orthotropic paperboard. The elasto-plastic response is taken into account in a large strain setting. The exchange of mass between the water bound in or to the fibers and the water vapor during the sealing is also considered. Simulations of an idealized sealing of two sheets of paperboard are performed and the predicted distributions of temperature, vapor pressure, out-of-plane stress and Forchheimer number are studied. The discussion related to the results from the simulations provides a deeper insight to how the different transport processes will affect the paperboard and how these are coupled. The closed system of equations, including the explicit formats of constitutive relations, provided in this paper makes it possible to set up suitable experiments for validation of the model.

1 Introduction

Paperboard may be considered as a material composed of a solid phase, defined by a dry fiber network, a liquid phase, defined by both liquid water bound in or to the fiber network and "free" liquid water that does not interact with the fiber network, and a gas phase which may be regarded as a mixture of two miscible constituents, namely water vapor and dry air. The presence of water in paperboard has a great influence on the response of the board. The amount of liquid water in the board is characterized by the moisture ratio, which is defined as the fraction between the mass of the liquid water and the mass of the dry fiber network. Neglecting the mass of the moist air inside the board the moisture ratio is equivalent to the dry basis moisture content. In the present paper, moisture ratios below the maximum hygroscopic moisture content (HMC) are considered and all liquid water is assumed to be bound in or to the fiber network, see reference Baggerud (2004). Due to the manufacturing process, paperboard may be considered to be an orthotropic material, a property that introduces direction-dependent transports of mass, momentum, and energy. The characteristic directions in paperboard are: Machine Direction (MD), Cross machine Direction (CD), and out-of-plane direction (ZD), cf. Figure 1.

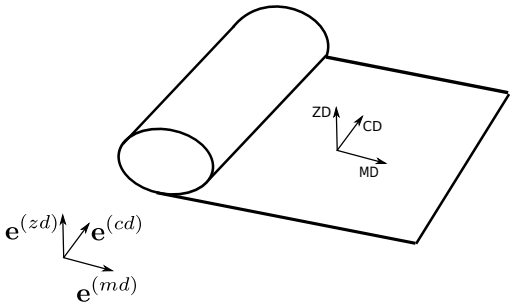

Figure 1: The characteristic directions of paperboard.

The purely mechanical quasi-static stress–strain response of paperboard has been modeled in, e.g., Xia et al. (2002); Harrysson and Ristinmaa (2008), where the invariance properties discussed in Boehler (1987) are adopted and where local characteristic directions are introduced in the form of director vectors which are assumed to evolve with the deformation of the board. The model presented in Xia et al. (2002) describes the in-plane stress response of paperboard as elasto-plastic and the out-of-plane stress response as elastic, limiting the applications of the model to predominant in-plane loading. A more general model of the stress–strain response of paperboard is proposed in Borgqvist et al. (2014) and later extended in Borgqvist et al. (2015) to also include elasto-plastic out-of-plane response. To model the out-of-plane plastic response, the yield surface presented in Xia et al. (2002) is enhanced with six additional sub-surfaces associated with the stress response in the out-of-plane direction. The explicit dependencies of moisture and temperature on the stress–strain response of the fiber network are not considered in the present paper and the model suggested in Borgqvist et al. (2015) is adopted. The reader is referred to the work in Salmén and Back (1980); Linvill and Östlund (2014) for more information on the explicit

dependencies of moisture and temperature on the mechanical response of paperboard.

High velocity gas flow through paper hand sheets has been studied in Modak et al. (2009) by assuming a nonlinear laminar flow described by the Forchheimer equation. The viscous and microscopic inertial resistances of hand sheets are investigated and the microscopic inertial losses are found to contribute more than 50% of the pressure loss. Liquid water transport through paper-like material have been studied in Masoodi and Pillai (2010); Masoodi et al. (2011), where the swelling of the fiber matrix is included via an additional sink term in the balance of mass equation and it is shown that the model is able to predict the wicking experimentally produced in Wiryana and Berg (1991). Intra–fiber and inter–fiber moisture diffusion in bleached kraft board are investigated in Bandyopadhyay et al. (2000) and a model is derived which is able to predict the transient moisture content during a change in the ambient humidity. Transient heat transport in paperboard has been studied in, e.g., Lavrykov and Ramarao (2012), where the out-of-plane thermal conductivity and the specific heat of commercial copy paper sheets are investigated. It is shown that both a series–parallel model and a lumped parameter model may be used to predict the density dependence of the out-of-plane thermal conductivity of copy paper sheets.

The coupled mass and heat transport in paper has been studied in, e.g., Alexandersson et al. (2016), where a hybrid mixture theory (HMT) framework is adopted to derive a model predicting the response of paperboard rolls during a change in the ambient humidity. In Zapata et al. (2013), balance laws, derived in Bachmat and Bear (1986a,b), for transport in porous media are adopted and the evolution of the moisture and temperature distributions in printing and copying paper are analysed during printing. A three phase model describing the moisture, temperature and pressure distributions during a drying phase in the production process of cardboard has been derived in Karlsson and Stenström (2005a), and validated against experimental data in Karlsson and Stenström (2005b).

In order to better understand the response of paperboard to folding and filling processes, a generic framework has been developed in Askfelt et al. (2016) that describes the transient transport of heat and moisture in deforming paperboard. The balance laws presented in Askfelt et al. (2016) are derived from a HMT framework Hassanizadeh and Gray (1979a,b), and considers the balance of mass, the balance of linear momentum, the balance of energy of all components of the paperboard.

In the current paper specific constitutive relations valid for moist paperboard are derived. A brief presentation of the governing balance laws is given in Section 3. After this introduction, it is shown, in Section 4, how the stress–strain response model described in Borgqvist et al. (2015) may be incorporated in the framework. Explicit formats of the constitutive relations specific for paperboard in environments similar to those present during the folding and filling process of a food package are derived in Sections 5, 6 and 7. Having retrieved a complete set of constitutive relations, simulations of an idealised sealing are presented and discussed in Section 8.

2 Preliminaries

A hybrid mixture theory approach is adopted. Each spatial point in the board is viewed as a superposition of phases $()_\alpha$, $\alpha \in \{s, l, g\}$, with the notation $()_s$ for solid, $()_l$ for bound water, and $()_g$ for gas. The gas phase is considered as a mixture of the two miscible constituents, namely dry air $()_{g_d}$ and water vapor $()_{g_v}$. HMT provides possibilities for explicitly including interfaces between the phases, cf. e.g., Bennethum and Cushman (1996); Hassanizadeh and Gray (1990), however, in the present study, these interfaces are only considered implicitly via the constitutive relations describing the interactions between the phases. The motion of a phase is defined by a nonlinear map $\boldsymbol{\chi}_\alpha : \Omega_\alpha^0 \times t \to \Omega \subset \mathbb{R}^3$,

$$\mathbf{x} = \boldsymbol{\chi}_\alpha(\mathbf{X}_\alpha, t) \tag{1}$$

where $\mathbf{X}_\alpha$ denotes the location of phase α in the reference configuration, Ω_α^0, and $\mathbf{x}$ is the position in the deformed configuration, Ω, at time, t, which is simultaneously occupied by all phases and constituents. The deformation gradient, $\mathbf{F}_\alpha$, associated with the motion of each phase is given by

$$\mathbf{F}_\alpha = \frac{\partial \boldsymbol{\chi}_\alpha(\mathbf{X}_\alpha, t)}{\partial \mathbf{X}_\alpha} \tag{2}$$

In order to ensure a continuous bijective mapping, the Jacobian is assumed to be greater than zero, i.e., $J_\alpha = \det(\mathbf{F}_\alpha) > 0$. The spatial velocity gradient $\mathbf{l}_\alpha$ is additively split into the symmetric rate of deformation tensor $\mathbf{d}_\alpha$ and the skew-symmetric spin tensor $\boldsymbol{\omega}_\alpha$ according to

$$\mathbf{l}_\alpha = \frac{D_\alpha(\mathbf{F}_\alpha)}{Dt}\mathbf{F}_\alpha^{-1}, \qquad \mathbf{d}_\alpha = \frac{1}{2}(\mathbf{l}_\alpha + \mathbf{l}_\alpha^T), \qquad \boldsymbol{\omega}_\alpha = \frac{1}{2}(\mathbf{l}_\alpha - \mathbf{l}_\alpha^T) \tag{3}$$

where $D_\alpha(\bullet)/Dt$ denotes the material time derivative with respect to the motion of phase α. Let v and m denote the volume and mass of a representative volume element, (RVE). Then v and m are related to their phase and constituent counterparts via

$$m = \sum_\alpha m_\alpha, \qquad m_\alpha = \sum_j m_{\alpha_j}, \qquad v = \sum_\alpha v_\alpha \tag{4}$$

All constituents are considered miscible, meaning that all constituents α_j within a phase α are associated with the same volume as the phase, i.e., $v_{\alpha_j} = v_\alpha \; \forall \; j$.

The macroscale balance laws assumed in hybrid mixture theory are derived through averaging of microscale balance laws Hassanizadeh and Gray (1979a). During the averaging from micro- to macroscale a new variable, the volume fraction n_α, appears naturally, as

$$n_\alpha = \frac{v_\alpha}{v}, \qquad \sum_\alpha n_\alpha = 1 \tag{5}$$

where (5b) is a consequence of (4c) known as the saturation condition. Throughout the rest of this paper quantities multiplied by volume fractions are denoted with a bar,

i.e., $(\bar{\bullet})_\alpha = n_\alpha(\bullet)$. As an example, the intrinsic densities $\rho_\alpha, \rho_{\alpha_j}$ and bulk densities $\bar{\rho}_\alpha, \bar{\rho}_{\alpha_j}$ are given by

$$\rho_\alpha = \frac{m_\alpha}{v_\alpha}, \qquad \rho_{\alpha_j} = \frac{m_{\alpha_j}}{v_\alpha}, \qquad \bar{\rho}_\alpha = n_\alpha \rho_\alpha, \qquad \bar{\rho}_{\alpha_j} = n_\alpha \rho_{\alpha_j} \tag{6}$$

The mixture density is defined by $\rho = m/v$. The mass averaged velocities $\mathbf{v}$ and $\mathbf{v}_\alpha$ are defined as the weighted summations of the phase velocities $\mathbf{v}_\alpha$ and constituent velocities $\mathbf{v}_{\alpha_j}$, respectively, i.e.,

$$\mathbf{v} = \frac{1}{\rho} \sum_\alpha \bar{\rho}_\alpha \mathbf{v}_\alpha \qquad \mathbf{v}_\alpha = \frac{1}{\bar{\rho}_\alpha} \sum_j \bar{\rho}_{\alpha_j} \mathbf{v}_{\alpha_j} \tag{7}$$

Furthermore, definitions of diffusion velocities $\mathbf{w}_\alpha, \mathbf{w}_{\alpha_j}$ and a relative velocity $\mathbf{v}_{\alpha,\beta}$ are introduced by

$$\mathbf{w}_\alpha = \mathbf{v}_\alpha - \mathbf{v}, \qquad \mathbf{w}_{\alpha_j} = \mathbf{v}_{\alpha_j} - \mathbf{v}_\alpha, \qquad \mathbf{v}_{\alpha,\beta} = \mathbf{v}_\alpha - \mathbf{v}_\beta \tag{8}$$

3 Balance laws

In Askfelt et al. (2016) a framework is derived aimed at predicting the response of moist paperboard in environments where significant temperature and pressure changes are expected in short periods of time. The derivations are made in a thermodynamically consistent manner using a two-scale hybrid mixture theory framework. The interfaces between the phases are not considered explicitly and at a given spatial position, all phases and constituents are assumed to have the same temperature. The solid phase is chosen as a reference phase and balance laws are expressed with respect to the motion of the fiber network. The intrinsic density of the solid phase is assumed constant, for modeling of a varying intrinsic solid density cf. Larsson et al. (2004). The system of equations derived in Askfelt et al. (2016) is summarized below under the assumption that the body forces associated with the gas constituents are negligible and all liquid water is bound in or to the fibers, so that no relative velocity between these two phases is present.

3.1 Balance of mass

The porosity is defined as $\phi = 1 - n_s$ where n_s denotes the solid volume fraction which is given by

$$n_s = \frac{n_s^0}{J_s} \tag{9}$$

The superscript $(\bullet)^0$ indicates the value of a quantity in the undeformed reference configuration, Ω_s^0. Assuming both gas constituents to behave as ideal gases, the

balance of mass equations for the fluids are given by

$$\frac{D_s(\bar{\rho}_l)}{Dt} + \bar{\rho}_l \nabla \cdot (\mathbf{v}_s) + \hat{m} = 0 \tag{10a}$$

$$\rho_{g_d} \frac{D_s(n_g)}{Dt} + \frac{\bar{\rho}_{g_d}}{p_{g_d}} \frac{D_s(p_{g_d})}{Dt} - \frac{\bar{\rho}_{g_d}}{\theta} \frac{D_s(\theta)}{Dt} + \nabla \cdot (\mathbf{J}_{g_d}) + \bar{\rho}_{g_d} \nabla \cdot (\mathbf{v}_s) = 0 \tag{10b}$$

$$\rho_{g_v} \frac{D_s(n_g)}{Dt} + \frac{\bar{\rho}_{g_v}}{p_{g_v}} \frac{D_s(p_{g_v})}{Dt} - \frac{\bar{\rho}_{g_v}}{\theta} \frac{D_s(\theta)}{Dt} + \nabla \cdot (\mathbf{J}_{g_v}) + \bar{\rho}_{g_v} \nabla \cdot (\mathbf{v}_s) - \hat{m} = 0 \tag{10c}$$

where θ denotes the absolute temperature. Moreover p_{g_d} and p_{g_v} denote the gas pressures of dry air and water vapor respectively and $\hat{m}$ the rate of evaporation, all presented in Section 5. The combined mass fluxes are denoted $\mathbf{J}_{g_j} = \bar{\rho}_{g_j}(\mathbf{w}_{g_j} + \mathbf{v}_{g,s})$ and include inter–fiber seepage, $\mathbf{v}_{g,s}$, as well as inter–fiber diffusion, $\mathbf{w}_{g_j}$. Both seepage and diffusive flow are discussed in Section 6.

3.2 Balance of momentum

For the considered application, the macroscopic inertial forces are negligible, and the balance of linear momentum of the solid phase is given by

$$-\nabla \cdot (\boldsymbol{\sigma}) - \rho \mathbf{b} + \hat{m}(\mathbf{v}_{g,s} + \mathbf{w}_{g_v}) = \mathbf{0} \tag{11}$$

where $\mathbf{b}$ denotes the body force tensor and $\boldsymbol{\sigma}$ the total Cauchy stress tensor. Assuming that the rate at which the liquid volume fraction changes has a negligible effect on the total Cauchy stress tensor yields a Terzaghi format of total Cauchy stress tensor, see reference Askfelt et al. (2016), i.e.,

$$\boldsymbol{\sigma} = \bar{\boldsymbol{\sigma}}_s^{eff} - p_g \mathbf{I} \tag{12}$$

where $\mathbf{I}$ denotes the second order identity tensor and the pressure of the moist air p_g is described by Dalton's law, i.e., $p_g = p_{g_d} + p_{g_v}$. The effective Cauchy stress tensor of the solid phase, $\bar{\boldsymbol{\sigma}}_s^{eff}$, characterizes the stress–strain response of the fiber network and will be further elaborated in Section 4 together with plastic deformations.

3.3 Balance of Energy

Assuming no intrinsic heat source is present and the term including the quadratic time derivative of n_l to have a negligible influence on the heat in the board reduces the balance of energy, see reference Askfelt et al. (2016), to

$$c^p \frac{D_s(\theta)}{Dt} + \rho \mathbf{b} \cdot \mathbf{w}_s + \nabla \cdot (\mathbf{q}) - \sum_{j=d,v} h_{g_j} \nabla \cdot (\mathbf{J}_{g_j}) + \hat{m} \Delta H_{ads} = 0 \tag{13}$$

where c^p and $\mathbf{q}$ denote the total heat capacity per unit volume and the total heat flux respectively, which are both discussed in Section 7. Furthermore, h_{g_j} denotes the specific enthalpy of constituent g_j and ΔH_{ads} the enthalpy of adsorption both provided in Section 5.

4 Constitutive relation for the solid fiber

To be able to predict significant inelastic deformations, a multiplicative split of the deformation gradient of the solid phase is performed, i.e., $\mathbf{F}_s = \mathbf{F}_s^e \mathbf{F}_s^p$, where $\mathbf{F}_s^e$ is associated with elastic deformations and $\mathbf{F}_s^p$ with plastic deformations, see also Ristinmaa et al. (2011); Harrysson and Ristinmaa (2008); Borgqvist et al. (2015). Hygro–expansion of the cellulose fibers is not considered in this work, i.e., swelling due to moisture uptake is not included. From the multiplicative split of the deformation gradient there follows an additive split of the spatial velocity gradient $\mathbf{l}_s$ according to

$$\mathbf{l}_s = \mathbf{l}_s^e + \mathbf{l}_s^p, \qquad \mathbf{l}_s^e = \frac{D_s(\mathbf{F}_s^e)}{Dt}(\mathbf{F}_s^e)^{-1}, \qquad \mathbf{l}_s^p = \mathbf{F}_s^e \frac{D_s(\mathbf{F}_s^p)}{Dt}(\mathbf{F}_s^p)^{-1}(\mathbf{F}_s^e)^{-1} \tag{14}$$

Both the elastic and the plastic part of the spatial velocity gradient are further split into symmetric $\mathbf{d}_s^e, \mathbf{d}_s^p$ and skew-symmetric parts $\boldsymbol{\omega}_s^e, \boldsymbol{\omega}_s^p$ according to (3). The purely mechanical model for paperboard described in Borgqvist et al. (2015) is, below, adopted in a hybrid mixture theory setting.

4.1 Anisotropy

Paperboard is viewed as an orthotropic material locally characterized by three director vectors $\boldsymbol{\nu}^{(1)}, \boldsymbol{\nu}^{(2)}, \boldsymbol{\nu}^{(3)}$, cf. Harrysson and Ristinmaa (2008); Borgqvist et al. (2014, 2015). In the material configuration, these director vectors are aligned with the characteristic directions of the paperboard, MD, CD and ZD, and are all of unit length, i.e., $(\boldsymbol{\nu}^{(1)})^0 = \mathbf{e}^{(md)}$, $(\boldsymbol{\nu}^{(2)})^0 = \mathbf{e}^{(cd)}$, $(\boldsymbol{\nu}^{(3)})^0 = \mathbf{e}^{(zd)}$, cf. Figure 1. An isoclinic intermediate configuration is assumed, for more information see Harrysson and Ristinmaa (2007), and the director vectors are assumed to evolve with the elastic part of the deformation gradient according to

$$\boldsymbol{\nu}^{(1)} = \mathbf{F}_s^e(\boldsymbol{\nu}^{(1)})^0, \qquad \boldsymbol{\nu}^{(2)} = \mathbf{F}_s^e(\boldsymbol{\nu}^{(2)})^0, \qquad \boldsymbol{\nu}^{(3)} = J_s^e \mathbf{F}_s^{e-T}(\boldsymbol{\nu}^{(3)})^0 \tag{15}$$

where $J_s^e = \det(\mathbf{F}_s^e)$. Based on the above, three structural tensors, one related to each direction, are defined according to

$$\mathbf{m}^{(1)} = \boldsymbol{\nu}^{(1)} \otimes \boldsymbol{\nu}^{(1)}, \quad \mathbf{m}^{(2)} = \boldsymbol{\nu}^{(2)} \otimes \boldsymbol{\nu}^{(2)}, \quad \mathbf{m}^{(3)} = \boldsymbol{\nu}^{(3)} \otimes \boldsymbol{\nu}^{(3)} \tag{16}$$

4.2 Elastic response

Following Borgqvist et al. (2015), an additive split is assumed for the Helmholtz free energy of the solid phase, i.e.,

$$A_s(\theta, \mathbf{b}_s^e, \mathbf{m}^{(i)}, \kappa_s^{(k)}) = A_s^\theta(\theta) + A_s^{ip}(\mathbf{b}_s^e, \mathbf{m}^{(i)}) + A_s^{op}(\mathbf{b}_s^e, \mathbf{m}^{(i)}) + A_s^p(\kappa_s^{(k)}) \tag{17}$$

where $\mathbf{b}_s^e = \mathbf{F}_s^e \mathbf{F}_s^{eT}$ is the elastic Finger tensor and A_s^{ip} and A_s^{op} describe the in-plane and out-of-plane elastic behaviour respectively. The plastic behaviour is characterized by A_s^p and the accumulation of heat in the fiber network is characterized by A_s^θ, which is provided in (54a). For the specific forms of A_s^{ip}, A_s^{op}, and A_s^p, the reader is referred

to Borgqvist et al. (2015). The elastic part of the deformation gradient relates the effective Cauchy stress tensor to the effective first Piola Kirchhoff stress tensor, $\mathbf{P}_s^{eff}$, via

$$\bar{\boldsymbol{\sigma}}_s^{eff} = J_s^{-1}\mathbf{P}_s^{eff}\mathbf{F}_s^{eT}, \qquad \mathbf{P}_s^{eff} = n_s^0\rho_s^0\frac{\partial A_s}{\partial \mathbf{F}_s^e} \tag{18}$$

Inserting (17) in (18) yields an expression for the effective Cauchy stress tensor given by

$$\bar{\boldsymbol{\sigma}}_s^{eff} = \frac{n_s^0}{n_s^r}\frac{1}{J_s}\left(\mathrm{P}_1\mathbf{m}^{(1)} + \mathrm{P}_2\mathbf{m}^{(2)} + \mathrm{P}_3\mathbf{m}^{(3)} + \mathrm{P}_4\mathbf{I} + \mathrm{P}_5(J_s^e)^{-2}\mathbf{b}_s^e\mathbf{m}^{(3)}\mathbf{b}_s^e\right) \tag{19}$$

where P_i are the invariants provided in Borgqvist et al. (2015). Increasing the initial density of the paperboard increases the stiffness of the board, see reference Alava and Niskanen (2006), and in order to incorporate this, a scaling $\frac{n_s^0}{n_s^r}$ is introduced, where n_s^r indicates a reference value of the initial solid volume fraction from Borgqvist et al. (2015) where $n_s^0 = n_s^r = 0.5253$.

4.3 Plastic response

The plastic behaviour is characterized by a yield function, f, given by

$$f(\bar{\boldsymbol{\tau}}_{eff}, \mathbf{n}_{sub}^{(k)}, \bar{K}_s^{(k)}) = \sum_{\nu=1}^{12} H^{y(\nu)}\left(\frac{\bar{\boldsymbol{\tau}}_{eff} : \mathbf{n}_{sub}^{(\nu)}}{\tau^{(\nu)}}\right)^{2k_y} - 1 \tag{20}$$

where the effective Kirchhoff stress tensor is denoted by $\bar{\boldsymbol{\tau}}_s^{eff} = J_s\bar{\boldsymbol{\sigma}}_s^{eff}$ and $k_y = 3$. The superscript (ν) appearing in (20) refers to the twelve sub-surfaces of the yield function, where six are related to the in-plane and six are related to the out-of-plane plastic response. The normal, $\mathbf{n}_{sub}^{(\nu)}$, to each yield plane is defined by

$$\mathbf{n}_{sub}^{(\nu)} = \sum_{i=1}^{3}\sum_{j=1}^{3} N_{ij}^{(\nu)}\boldsymbol{\nu}^{(i)} \otimes \boldsymbol{\nu}^{(j)}|\boldsymbol{\nu}^{(i)}|^{-1}|\boldsymbol{\nu}^{(j)}|^{-1} \tag{21}$$

where the yield surface coefficients $N_{ij}^{(\nu)}$ are determined via $\sqrt{(\mathbf{n}_{sub}^{(\nu)})^0 : \mathbf{I}} = 1$. The stress quantities $\tau^{(\nu)}$, defining the distance in the stress space from the origin to each yield plane, are given by

$$\tau^{(\nu)} = (\tau^{(\nu)})^0 + \bar{K}_s^{(\nu)} \tag{22}$$

where the hardening functions, $\bar{K}_s^{(\nu)}$, are functions of the the internal variables, $\kappa^{(\nu)}$, and defined by

$$\bar{K}_s^{(\nu)} = \begin{cases} \frac{n_s^0}{n_s^r}a_\nu \ln(b_\nu\kappa_s^{(\nu)} + 1) & \text{for } \nu \in \{1,2,3,6\} \\ \frac{n_s^0}{n_s^r}a_\nu\kappa_s^{(\nu)} & \text{for } \nu = 7 \\ 0 & \text{otherwise.} \end{cases} \tag{23}$$

The initial distances $(\tau^{(\nu)})^0$ and the hardening parameters, a_ν and b_ν as well as $N_{ij}^{(\nu)}$ are provided in Borgqvist et al. (2015). The function $H^{y(\nu)}$, appearing in the yield function, acts as a switch function, indicating whether a yield plane is active, $H^{y(\nu)} = 1$ if $\bar{\boldsymbol{\tau}}_{eff} : \mathbf{n}_{sub}^{(\nu)} > 0$, otherwise $H^{y(\nu)} = 0$ i.e., if the yield plane is inactive. With the yield function defined in (20) the plastic flow rate $\mathbf{d}_s^p$ and the evolution of the plastic internal variables are given by

$$\mathbf{d}_s^p = \dot{\lambda}_p \frac{\partial f}{\partial \bar{\boldsymbol{\tau}}_{eff}} = 2k_y \dot{\lambda}_p \sum_{\nu=1}^{12} H^{y(\nu)} \frac{(\bar{\boldsymbol{\tau}}_{eff} : \mathbf{n}_{sub}^{(\nu)})^{2k_y-1}}{(\tau^\nu)^{2k_y}} \text{sym}(\mathbf{n}_{sub}^{(\nu)}) \tag{24a}$$

$$\frac{D_s(\kappa_s^{(\nu)})}{Dt} = -\dot{\lambda}_p \frac{\partial f}{\partial \bar{K}_s^{(\nu)}} = 2k_y \dot{\lambda}_p H^{y(\nu)} \frac{(\bar{\boldsymbol{\tau}}_{eff} : \mathbf{n}_{sub}^{(\nu)})^{2k_y}}{(\tau^{(\nu)})^{2k_y+1}} \tag{24b}$$

In order to obtain a realistic shear response, an Eulerian plastic spin $\boldsymbol{\omega}^p$ is needed and in Borgqvist et al. (2015) the plastic spin $\boldsymbol{\omega}^p$ is assumed to take the form

$$\boldsymbol{\omega}^p = 2k_y \dot{\lambda}_p \sum_{\nu=1}^{12} H^{y(\nu)} \frac{(\bar{\boldsymbol{\tau}}_{eff} : \mathbf{n}_{sub}^{(\nu)})^{2k_y-1}}{(\tau^\nu)^{2k_y}} \text{skew}(\mathbf{n}_{sub}^{(\nu)}) \tag{25}$$

The mechanical model presented in this section has been calibrated against uniaxial tension and compression tests. The experimental data and model predictions, using the full set of equations provided in Section 4, of the tension in MD, CD and ZD as well as the out-of-plane cyclic compression are shown in Figure 2.

5 Constitutive relations for the gas constituents and the bound water

The considered gas constituents are assumed to behave as ideal gases and the following format of the specific Helmholtz free energy A_{g_j} of gas constituent g_j is used

$$A_{g_j}(\theta, \rho_{g_j}) = A_{g_j}^\theta(\theta) + R_{g_j}\theta \ln(\frac{\rho_{g_j}}{\rho_{g_j}^*}) + h_{g_j}^* - \frac{p_{g_j}^*}{\rho_{g_j}^*} - \eta_{g_j}^* \theta \tag{26}$$

where $A_{g_j}^\theta$ characterizes the ability of the gas constituents to accumulate heat, provided in (54). The specific entropies and enthalpies of the gas constituents are denoted η_{g_j} and h_{g_j} respectively. The superscript $(\bullet)^*$ is used to indicate thermodynamic reference values which are taken from an equilibrium state and provided in Table 1. From (26) it follows that the partial pressures for the dry air and water vapor are given by the ideal gas law, i.e., $p_{g_j} = R_{g_j}\theta\rho_{g_j}$, where R_{g_j} is the specific gas constant. The Helmholtz free energy of the bound water is given by

$$A_l(\theta, \rho_l, W) = A_l^f(\theta, \rho_l) + \frac{R_{g_v}\theta}{W} \int \ln(a_w) dW \tag{27}$$

where A_l^f denotes the specific Helmholtz free energy of the "free" liquid water and the moisture ratio W is defined via

$$W = \bar{\rho}_l / \bar{\rho}_s \tag{28}$$

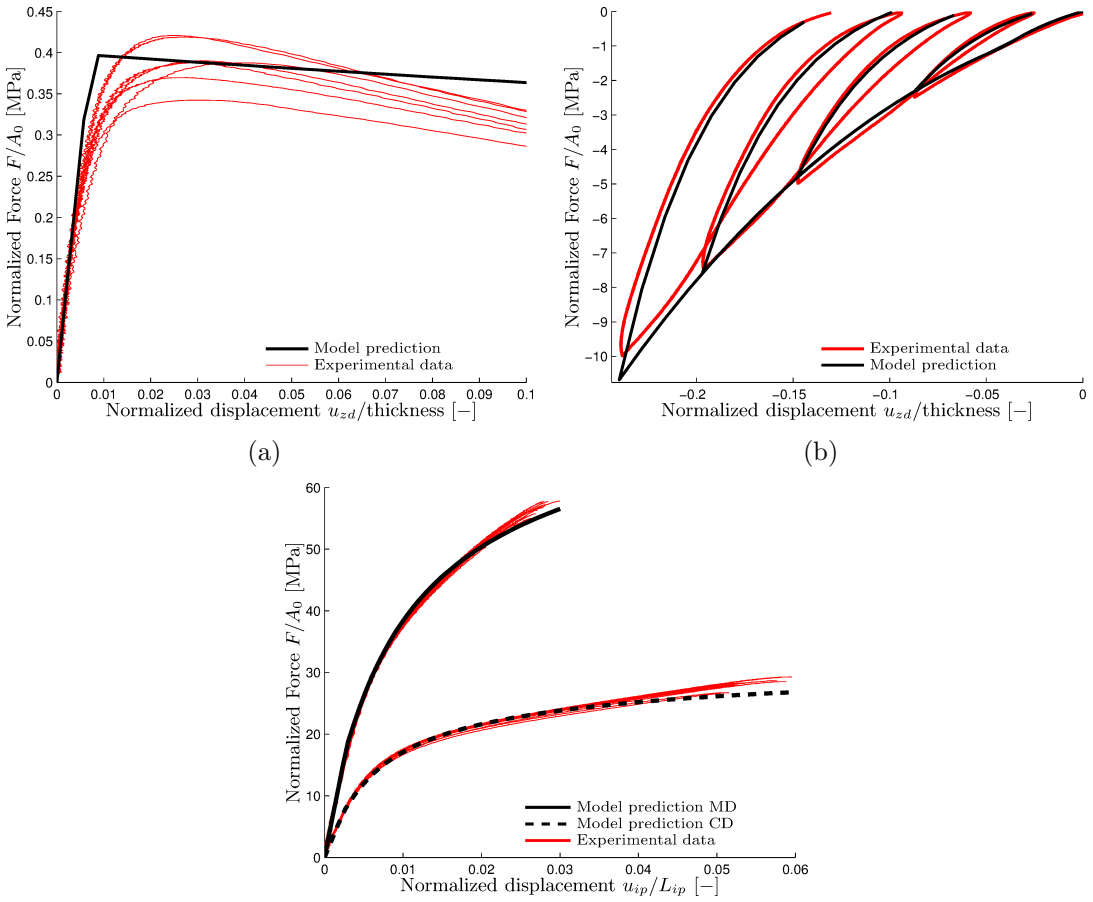

Figure 2: Calibration of the purely mechanical response of paperboard to experimental data provided in Borgqvist et al. (2015) **a**) uniaxial tension in ZD, **b**) uniaxial cyclic compression in ZD, **c**) uniaxial tension in MD and CD. The initial in-plane length in direction ip is denoted L_{ip}

The Helmholtz free energy of the "free" liquid water is described by

$$A_l^f(\theta, \rho_l) = A_l^{f\theta}(\theta) + \int \frac{p_l^t(\theta, \rho_l)}{\rho_l} d\rho_l + (h_l^f)^* - \frac{(p_l^t)^*}{\rho_l^*} - (\eta_l^f)^* \theta \tag{29}$$

where $A_l^{f\theta}$ characterizes the ability of the "free" liquid water to accumulate heat, provided in (54), and p_l^t denotes the thermodynamic pressure of the liquid water, see Askfelt et al. (2016). The specific entropy and enthalpy of the "free" liquid water are denoted by η_l^f and h_l^f respectively. The terminology "free" is here used to indicate a state where the liquid water is not affected by the presence of other phases. Interactions between the fibers and the liquid water reduce the energy of the water, and within the HMC region this is quantified by the water activity a_w and described by the second term in (27). The water activity indicates how tightly bound water is to the solid, and is defined by $a_w = \frac{p_{g_v}^{eq}}{p_{g_v}^{sat}}$, see Bénet et al. (2012), where $p_{g_v}^{eq}$ denotes the equilibrium vapor pressure inside the porous medium and $p_{g_v}^{sat}$ the saturated vapor

pressure. In Askfelt et al. (2016) it is shown that the fraction $p_{g_v}^{eq}/p_{g_v}$ is the driving force for the rate of evaporation $\hat{m}$ which is given by

$$\hat{m} = k_{\hat{m}} R_{g_v} \theta \ln\left(\frac{p_{g_v}^{sat} a_w}{p_{g_v}}\right) \tag{30}$$

where $k_{\hat{m}}$ is the rate coefficient, here taken as $k_{\hat{m}} = 2.7 \times 10^{-7}$ kg·s·m^{-5}. An expression for the water activity a_w is provided in Askfelt et al. (2016) and the saturation vapor pressure $p_{g_v}^{sat}$ is assumed to be described by the Antoine relation,

$$a_w = 1 - e^{(-84W^{1.9} - 0.2(\theta - 273.15)W^{1.2})} \tag{31a}$$

$$p_{g_v}^{sat} = 133.322 \times 10^{(8.07131 - 1730.63/(\theta - 39.574))} \text{[Pa]} \tag{31b}$$

The enthalpy of adsorption is provided as

$$\Delta H_{ads} = h_{g_v} - h_l^f + R_{g_v} \theta^2 \frac{\partial \ln(a_w)}{\partial \theta} \tag{32}$$

Transformations between the Helmholtz free energy and the specific enthalpies and entropies are given by

$$\eta_{g_j} = -\frac{\partial A_{g_j}}{\partial \theta}, \qquad \eta_l^f = -\frac{\partial A_l^f}{\partial \theta} \tag{33a}$$

$$h_{g_j} = A_{g_j} + \eta_{g_j}\theta + \frac{p_{g_j}}{\rho_{g_j}} \qquad h_l^f = A_l^f + \eta_l^f \theta + \frac{p_l^t}{\rho_l} \tag{33b}$$

Table 1: Reference values A.Çengel and Boles (2007)

Notation	Dimension	value
θ^*	K	298.15
$(p_l^t)^*$	Pa	101.3×10^3
$p_{g_v}^*$	Pa	3.1698×10^3
$p_{g_d}^*$	Pa	$(p_l^t)^* - p_{g_v}^*$
$\rho_{g_j}^*$	kg/m^3	$p_{g_j}^*/(R_{g_j}\theta^*)$
$h_{g_v}^*$	kJ/kg	2 546.5
$h_{g_d}^*$	kJ/kg	298.586
$(h_l^f)^*$	kJ/kg	104.83
$\eta_{g_v}^*$	kJ/kg/K	8.5567
$\eta_{g_d}^*$	kJ/kg/K	6.866
$(\eta_l^f)^*$	kJ/kg/K	0.3672

6 Transport of mass

6.1 Inter–fiber gas seepage

Aiming to derive a model applicable to nonlinear anisotropic gas seepage flow, a three-dimensional Forchheimer equation is suggested for the gas–solid seepage,

$$(1 + F_o)\mathbf{R}_{g,s} \cdot \mathbf{v}_{g,s} = -n_g \nabla(p_g) \tag{34}$$

where F_o is the dimensionless Forchheimer number, given by

$$F_o = \frac{\rho_g \beta_{g,s} k_{g,s}}{\mu_g^D} |\mathbf{v}_{g,s}| \tag{35}$$

The intrinsic permeability parameter is given by $k_{g,s} \geq 0$ and the anisotropic gas flow resistivity is defined by a positive definite second order tensor $\mathbf{R}_{g,s}$. Both $\mathbf{R}_{g,s}$ and $k_{g,s}$ are associated with linear laminar gas–solid seepage flow, i.e., Darcy flow, and the Forchheimer correction coefficient $\beta_{g,s}$ compensates for the increased flow resistance appearing at higher pressure heads. The Forchheimer correction coefficient $\beta_{g,s}$ is a property of the porous medium. The reader is referred to Lopez-Hernandez et al. (2004) for a review of some of the more familiar empirical models estimating this correction coefficient. In the present study, the model suggested by Geertsma is adopted, i.e.,

$$\beta_{g,s} = \frac{0.005}{k_{g,s}^{0.5} n_g^{5.5}} \quad [\mathrm{m}^{-1}] \tag{36}$$

The dynamic viscosity of the binary gas is denoted μ_g^D and modeled as a weighted average of the dynamic viscosities of the two gas constituents, see reference Pont et al. (2011),

$$\mu_g^D = \mu_{g_v}^D + (\mu_{g_d}^D - \mu_{g_v}^D)(p_{g_d}/p_g)^{0.608} \tag{37a}$$

$$\mu_{g_v}^D = -7.92 \times 10^{-7} + 3.53 \times 10^{-8}\theta \quad [\mathrm{Pa \cdot s}] \tag{37b}$$

$$\mu_{g_d}^D = 5.91 \times 10^{-6} + 3.52 \times 10^{-8}\theta + 2.22 \times 10^{-11}\theta^2 \quad [\mathrm{Pa \cdot s}] \tag{37c}$$

The resistivity, $\mathbf{R}_{g,s}$, is inversely proportional to the anisotropic intrinsic permeability tensor $\mathbf{K}_{g,s}$ via

$$\mathbf{R}_{g,s}^{-1} = \frac{\mathbf{K}_{g,s}}{\mu_g^D n_g^2} \tag{38}$$

The gas-flow resistivity in paperboard is direction dependent, and changes with the porosity and degree of saturation $S_w = n_l/\phi$. These aspects are considered in the following expression of the intrinsic permeability tensor,

$$\mathbf{K}_{g,s} = k_{g,s} \sum_{id=md,cd,zd} (K_P^{(id)})^r \left(\frac{n_g}{n_g^r}\right)^{a_P^{(id)}} \left(\frac{1 - n_g^r}{1 - n_g}\right) \mathbf{e}^{(id)} \otimes \mathbf{e}^{(id)} \tag{39}$$

A calibration of expression (39) to experimental data is shown in Figure 3. From the calibration, an intrinsic permeability parameter of $k_{g,s} = 33 \times 10^{-14}$ m^2 is retrieved and an anisotropy defined by $K_{g,s}^{(id)} = \mathbf{e}^{(id)} \cdot \mathbf{K}_{g,s} \cdot \mathbf{e}^{(id)}$ is presented in Table 2.

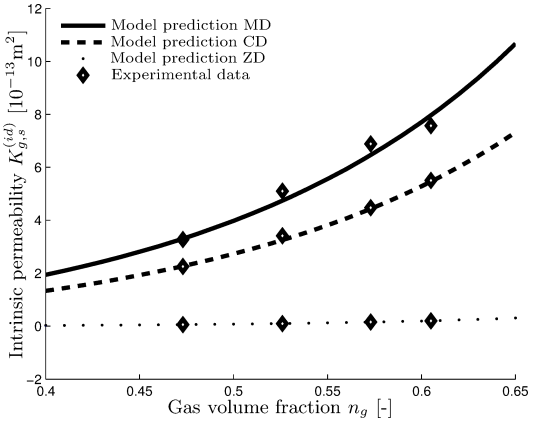

Figure 3: Intrinsic permeability in MD, CD and ZD of paperboard, $K_{g,s}^{(id)} = \mathbf{e}^{(id)} \cdot \mathbf{K}_{g,s} \cdot \mathbf{e}^{(id)}$. Calibrated to experimental data of kraft paperboard.

Table 2: Intrinsic permeability $K_{g,s}^{(id)}$

Direction	Value [m^2]
$K_{g,s}^{(md)}$	$105 \times 10^{-14} n_g^{2.4}/(1-n_g)$
$K_{g,s}^{(cd)}$	$72 \times 10^{-14} n_g^{2.4}/(1-n_g)$
$K_{g,s}^{(zd)}$	$6 \times 10^{-14} n_g^{4}/(1-n_g)$

6.2 Inter–fiber diffusion

Assuming a linear relation between the inter–fiber vapor diffusion and the gradient of the relative chemical potential, $\mu_{g_v} - \mu_{g_d}$, not to be confused with the dynamic viscosities in (37), allows the following expression of the inter–fiber vapor diffusion,

$$(\mathbf{D}_{g_v}^{eff})^{-1} \cdot \mathbf{w}_{g_v} = -\nabla(\mu_{g_v} - \mu_{g_d}) \tag{40}$$

The chemical potential of the gas constituent g_j is defined in Askfelt et al. (2016) as

$$\mu_{g_j} = A_{g_j} + \frac{p_{g_j}}{\rho_{g_j}} \tag{41}$$

where the A_{g_j} are defined in (26). The directional dependency of the effective diffusivity tensor $\mathbf{D}_{g_v}^{eff}$ is modeled via

$$\mathbf{D}_{g_v}^{eff} = \sum_{id=md,cd,zd} (D_{g_v}^{eff})^{(id)} \mathbf{e}^{(id)} \otimes \mathbf{e}^{(id)} \tag{42}$$

A relation between $D_{g_v}^{eff}$ and the diffusion coefficients $D_{g_v}^{F}$ for concentration driven diffusion, Fick's law, has been investigated in Sullivan (2013), where the following relation is provided,

$$(D_{g_v}^{eff})^{(id)} = \frac{1}{R_{g_v}\theta} (D_{g_v}^{F})^{(id)} \tag{43}$$

Furthermore, the effective diffusion coefficient $(D^F_{g_v})^{(id)}$ may be related to the "free space vapor diffusion" coefficient D_{g_v}, see also Akanni and Evans (1987); Massman (1998), via

$$(D^F_{g_v})^{(id)} = \frac{n_g}{\tilde{\tau}^{(id)}} D_{g_v}, \quad \text{where} \quad D_{g_v} = \frac{p^r_g}{p_g} \left(\frac{\theta}{\theta^r} \right)^{5/3} D^r_{g_v} \tag{44}$$

Reference values $p^r_g = 101.325$ kPa, $\theta^r = 298.15$ K and $D^r_{g_v} = 2.58 \times 10^{-5}$ m^2·s^{-1} are given in, Pont et al. (2011). The in-plane and out-of-plane tortuosities $\tilde{\tau}^{(ip)}$ and $\tilde{\tau}^{(zd)}$ are presented in Ramarao and Ramaswamy (2004) as

$$\tilde{\tau}^{(md)} = \tilde{\tau}^{(cd)} = \tilde{\tau}^{(ip)} = 5.2858 \cdot e^{(-2.2837 n_g)}, \qquad \tilde{\tau}^{(zd)} = 30.037 \cdot e^{(-5.2873 n_g)} \tag{45}$$

7 Transport of energy

7.1 Heat flux

The total heat flux vector $\mathbf{q}$ appearing in the energy balance equation is defined as the sum of a convective part $\mathbf{q}^{conv}$ describing the energy transported via inter–fiber gas seepage, a diffusive part $\mathbf{q}^{diff}$ related to the energy transported via inter–fiber diffusion, and a conductive part $\mathbf{q}^{cond}$ related to the energy transport via molecular interaction. The heat fluxes associated with the transport of mass, i.e., $\mathbf{q}^{conv}$ and $\mathbf{q}^{diff}$, are defined as

$$\mathbf{q}^{conv} = \sum_{j=d,v} \bar{\rho}_{g_j} h_{g_j} \mathbf{v}_{g,s}, \qquad \mathbf{q}^{diff} = \sum_{j=d,v} \bar{\rho}_{g_j} \mu_{g_j} \mathbf{w}_{g_j} \tag{46}$$

and the conductive part $\mathbf{q}^{cond}$ is described by Fourier's law:

$$\mathbf{q}^{cond} = -\mathbf{K}_\theta \nabla(\theta) \tag{47}$$

where $\mathbf{K}_\theta$ defines an effective conductivity tensor whose inverse describes the combined resistivity of the conductive energy transport from all phases. The conductive energy flux in paperboard is direction dependent and $\mathbf{K}_\theta$ is modeled as

$$\mathbf{K}_\theta = \sum_{id=md,cd,zd} K^{(id)}_\theta \mathbf{e}^{(id)} \otimes \mathbf{e}^{(id)} \tag{48}$$

The effective thermal conductivity of paperboard is usually modeled by viewing the board as a composite structure. The conductivity $K^{(id)}_\theta$ in each direction is then assumed to be a combination of a series conductivity K^{ser}_θ and a parallel conductivity K^{par}_θ, see also Baggerud (2004); Lavrykov and Ramarao (2012); Karlsson and Stenström (2005a), i.e.,

$$K^{(id)}_\theta = a^{(id)}_\theta K^{ser}_\theta + (1 - a^{(id)}_\theta) K^{par}_\theta, \quad K^{ser}_\theta = \frac{1}{\sum_\alpha n_\alpha (\lambda^\theta_\alpha)^{-1}}, \quad K^{par}_\theta = \sum_\alpha n_\alpha \lambda^\theta_\alpha \tag{49}$$

where $a_\theta^{(id)}$ is a calibration parameter which describes the percentage of series flow in direction (id) and λ_α^θ denotes the thermal conductivity of phase α, which in the present study is assumed to be isotropic for all phases. As argued in, Baggerud (2004); Lavrykov and Ramarao (2012); Lucisano (2002), the thermal conductivity of the fiber network λ_s^θ is assumed to be independent of the temperature and the value of λ_s^θ is taken as that of cellulose, $\lambda^\theta = 0.335$ W·m^{-1}·K^{-1}, Reardon et al. (1999). The thermal conductivity of the gas mixture λ_g^θ is modeled by the format presented in Bird et al. (2007), i.e.,

$$\lambda_g^\theta = \frac{x_{g_d}\lambda_{g_d}^\theta}{x_{g_d} + x_{g_v}\Phi_{vd}} + \frac{x_{g_v}\lambda_{g_v}^\theta}{x_{g_v} + x_{g_d}\Phi_{dv}} \tag{50a}$$

$$\Phi_{ij} = 8^{-1/2}(1 + M_{g_i}M_{g_j}^{-1})^{-1/2}(1 + (\mu_{g_i}^D/\mu_{g_j}^D)^{1/2}(M_{g_j}M_{g_i}^{-1})^{1/4})^2 \tag{50b}$$

$$x_{g_v} = \rho_{g_v}M_{g_v}^{-1}(\rho_{g_v}M_{g_v}^{-1} + \rho_{g_d}M_{g_d}^{-1})^{-1}, \qquad x_{g_d} = 1 - x_{g_v} \tag{50c}$$

where M_{g_j} and x_{g_j} denote the molar weight and the mole fraction of constituent g_j. The dynamic viscosity $\mu_{g_j}^D$ is defined in (37) and Φ_{ij} is a dimensionless quantity. The thermal conductivities of the two gas constituents and the thermal conductivity of the liquid water are modeled by

$$\lambda_{g_j}^\theta = a_{g_j}^\lambda + b_{g_j}^\lambda\theta + c_{g_j}^\lambda\theta^2, \qquad \lambda_l^\theta = a_l^\lambda + b_l^\lambda\theta + c_l^\lambda\theta^2 \tag{51}$$

where the material parameters of the thermal conductivities are provided in Table 3

Table 3: Thermal conductivity parameters

Phase/constituent	a^λ [W·m^{-1}·K^{-1}]	b^λ [W·m^{-1}·K^{-2}]	c^λ [W·m^{-1}·K^{-3}]
Liquid	-0.9	8.39×10^{-3}	-1.12×10^{-5}
Dry air	6.7×10^{-3}	65×10^{-6}	0
Vapor	-9.7×10^{-3}	94.7×10^{-6}	0

The model for the thermal conductivity of the liquid phase is taken from Ramires et al. (1995) and only valid in the interval 274 K $\leq \theta \leq$ 370 K. For temperatures over 370 K, the thermal conductivity of liquid water is modeled as a constant, i.e., $\lambda_l^\theta(\theta >$370 K)=$\lambda_l^\theta$(370 K).

In order to find suitable values for a_θ^{id}, the model is calibrated against the experimental data presented in Punton (1985). From the calibration one finds $a_\theta^{zd} = 0.75$, i.e., 75% of the out-of-plane flow may be assumed to be series flow. Furthermore $a_\theta^{md} = a_\theta^{cd} = 0.05$ is chosen, i.e., 5% of the in-plane flow is modeled as a series flow. With these choices, the thermal conductivity of paperboard is plotted as a function of the sheet density in Figure 4(a) and the thermal conductivity of each phase is plotted as functions of the absolute temperature in Figure 4(b). Figure 4(b) reveals that the gas phase acts as an isolator, reducing the energy transport within the board, which agrees well with Figure 4(a) where it is observed that a higher sheet density results in a higher thermal conductivity. In Figure 4(b) it is also seen that, assuming the solid

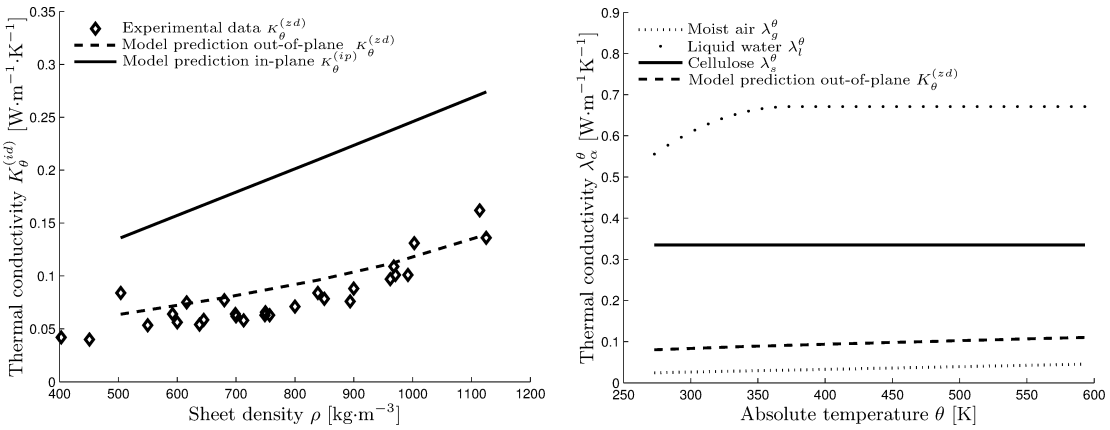

(a) (b)

Figure 4: **a**) Thermal conductivity, $K_\theta^{(id)} = \mathbf{e}^{(id)} \cdot \mathbf{K}_\theta \cdot \mathbf{e}^{(id)}$, of paperboard as a function of the sheet density, **b**) Model prediction of the temperature dependency of the thermal conductivity, λ_α^θ, of each phase compared with the out-of-plane thermal conductivity of paperboard with $n_s = 0.42$ and $W = 0.1$.

volume fraction n_s to be constant, an increased moisture ratio should increase the thermal conductivity of the board since the thermal conductivity of liquid is greater than the thermal conductivity of moist air i.e., $\lambda_l^\theta > \lambda_g^\theta$.

7.2 Heat capacity

The total heat capacity per unit volume, c^p, appearing in the balance of energy, (13), is defined by

$$c^p = \bar{\rho}_s c_s^p + \bar{\rho}_l c_l^p + \bar{\rho}_{g_v} c_{g_v}^p + \bar{\rho}_{g_d} c_{g_d}^p \tag{52}$$

The energy of the bound water is reduced due to interactions with the fibres, which affects c_l^p. In the present article this influence is neglected and c_l^p is assumed to take the same value as the specific heat of "free" water. Furthermore, the term including the integrated thermodynamic pressure of the liquid water in (29) is assumed not to affect the specific heat, and the specific heats are written as

$$c_s^p = -\frac{\partial^2 A_s^\theta}{\partial\theta^2}\theta, \qquad c_l^p = -\frac{\partial^2 A_l^{f\theta}}{\partial\theta^2}\theta, \qquad c_{g_j}^p = -\frac{\partial^2 A_{g_j}^\theta}{\partial\theta^2}\theta + R_{g_j} \tag{53}$$

where the parts of the Helmholtz free energies that characterize the ability to accumulate heat are modeled in the following form:

$$A_s^\theta = -\frac{b_s^c}{2}(\theta-\theta^*)^2 - a_s^c\left[\theta\ln\left(\frac{\theta}{\theta^*}\right) - (\theta-\theta^*)\right] \tag{54a}$$

$$A_l^{f\theta} = -\frac{b_l^c}{2}(\theta-\theta^*)^2 - a_l^c\left[\theta\ln\left(\frac{\theta}{\theta^*}\right) - (\theta-\theta^*)\right] \tag{54b}$$

$$A_{g_j}^\theta = -\frac{b_{g_j}^{c^v}}{2}(\theta-\theta^*)^2 - a_{g_j}^{c^v}\left[\theta\ln\left(\frac{\theta}{\theta^*}\right) - (\theta-\theta^*)\right] \tag{54c}$$

With these free energies, the specific heats are given by

$$c_s^p = a_s^c + b_s^c\theta, \qquad c_l^p = a_l^c + b_l^c\theta, \qquad c_{g_j}^p = a_{g_j}^{c^p} + b_{g_j}^{c^p}\theta \tag{55a}$$

where the material parameters of the specific heats of all phases and constituents are given in Table 4.

Table 4: Specific heat parameters

Phase/constituent	a^{c^p} [J·kg^{-1}·K^{-1}]	b^{c^p} [J·kg^{-1}·K^{-2}]
Solid	-78.5	4.5
Liquid	4 200	0
Dry air	963.735	0.1455
Vapor	1 727	0.48

8 Numerical simulation of an idealized sealing of two sheets of paperboard

Simulations were carried out in order to investigate the response of paperboard in conditions similar to those present during a local sealing of two sheets of paperboard. The setup of the idealized sealing considered is illustrated in Figure 5(a). In the idealized sealing, two sheets of paperboard are pressed together by compression tools, marked with gray boxes, and in order to get the sheets to stick together after the sealing, a polymer is melted between them. The effect of the heat transferred from

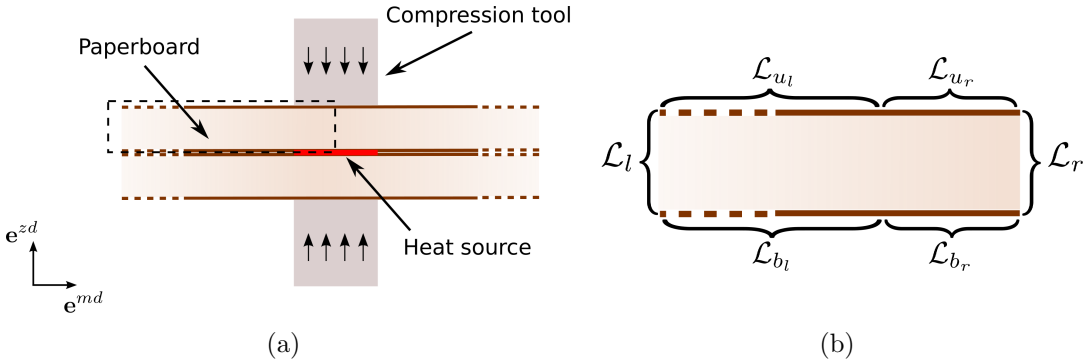

(a) (b)

Figure 5: **a**) Illustration of the problem setup where the dashed lines indicate the computational domain, **b**) boundary conditions, given in Table 5, imposed on the computational domain.

the polymer to the paperboard is simulated by a local heat source stretched over the same md-coordinates as the compression tools act and placed between the sheets. The sheets and the compression tools are wide in CD and the idealized sealing is viewed as a 2D problem (with coordinates denoted md and zd) where plane strain is assumed to prevail. Due to symmetry, the computational domain is reduced to the area enclosed

by the black dashed line in Figure 5(a). The ambient climate is given by the absolute temperature $\theta^{\infty} = 298.15$ K and the binary gas pressure p_g^{∞} =101 325 Pa.

During the sealing, the response of the boards is defined by three balance of mass equations (10), one balance of linear momentum equation (11), and one balance of energy equation (13). For the considered application, the intrinsic density ρ_l of the liquid water is assumed to be constant and the body force $\mathbf{b}$ is considered negligible. The primary variables are chosen as $\mathcal{P} = \{n_l, p_{g_d}, p_{g_v}, \mathbf{u}_s, \theta\}$ which naturally relate to different governing equations. The governing balance equations are multiplied by arbitrary weight functions ω_{n_l}, $\omega_{p_{g_d}}$, $\omega_{p_{g_v}}$, $\boldsymbol{\omega}_{\mathbf{u}_s}$, ω_θ and integrated over the spatial domain spanned by the solid phase, Ω_s. Making use of the Gauss divergence theorem the corresponding weak formulations are obtained, as follows

Balance of mass

$$\int_{\Omega_s} \omega_{n_l} \left(\rho_l \frac{D_s(n_l)}{Dt} + \bar{\rho}_l \nabla \cdot (\mathbf{v}_s) + \hat{m} \right) dA = 0 \tag{56a}$$

$$\int_{\Omega_s} \omega_{p_{g_d}} \left(\rho_{g_d} \frac{D_s(n_g)}{Dt} + \frac{\bar{\rho}_{g_d}}{p_{g_d}} \frac{D_s(p_{g_d})}{Dt} - \frac{\bar{\rho}_{g_d}}{\theta} \frac{D_s(\theta)}{Dt} + \bar{\rho}_{g_d} \nabla \cdot (\mathbf{v}_s) \right) dA - \int_{\Omega_s} \nabla(\omega_{p_{g_d}}) \cdot \mathbf{J}_{g_d} dA + \int_{\partial\Omega_s} \omega_{p_{g_d}} q_{g_d} d\mathcal{L} = 0 \tag{56b}$$

$$\int_{\Omega_s} \omega_{p_{g_v}} \left(\rho_{g_v} \frac{D_s(n_g)}{Dt} + \frac{\bar{\rho}_{g_v}}{p_{g_v}} \frac{D_s(p_{g_v})}{Dt} - \frac{\bar{\rho}_{g_v}}{\theta} \frac{D_s(\theta)}{Dt} + \bar{\rho}_{g_v} \nabla \cdot (\mathbf{v}_s) - \hat{m} \right) dA - \int_{\Omega_s} \nabla(\omega_{p_{g_v}}) \cdot \mathbf{J}_{g_v} dA + \int_{\partial\Omega_s} \omega_{p_{g_v}} q_{g_v} d\mathcal{L} = 0 \tag{56c}$$

Balance of linear momentum

$$\int_{\Omega_s} \boldsymbol{\omega}_{\mathbf{u}_s} \cdot \hat{m}(\mathbf{v}_{g,s} + \mathbf{w}_{g_v}) dA + \int_{\Omega_s} \nabla(\boldsymbol{\omega}_{\mathbf{u}_s}) : \boldsymbol{\sigma} dA - \int_{\partial\Omega_s} (\boldsymbol{\omega}_{\mathbf{u}_s} \cdot \mathbf{t})\, d\mathcal{L} = \mathbf{0} \tag{57}$$

Balance of energy

$$\int_{\Omega_s} \omega_\theta \left(c^p \frac{D_s(\theta)}{Dt} - \sum_j h_{g_j} \nabla \cdot (\mathbf{J}_{g_j}) + \hat{m} \Delta H_{ads} \right) dA - \int_{\Omega_s} \nabla(\omega_\theta) \cdot \mathbf{q} dA + \int_{\partial\Omega_s} \omega_\theta q_\theta d\mathcal{L} = 0 \tag{58}$$

where the mass fluxes $q_{g_j} = \mathbf{J}_{g_j} \cdot \mathbf{n}$, the momentum flux $\mathbf{t} = \boldsymbol{\sigma} \cdot \mathbf{n}$, and the heat flux $q_\theta = \mathbf{q} \cdot \mathbf{n}$ through a boundary with the normal $\mathbf{n}$ have been introduced. The boundary conditions imposed on $\partial\Omega_s$ are decomposed into six parts, $\mathcal{L}_i$, in Figure 5(b). The effect of the heat source and the compression are applied as Dirichlet boundary conditions over $\mathcal{L}_{b_r}$ and $\mathcal{L}_{u_r}$, respectively, which both stretch 0.5 cm in from the right boundary. Both Dirichlet boundary conditions are ramped up over the time t^h, for

temperature $\theta(t) = \theta^0 + \Delta\theta\frac{t}{t^h}$ where $\Delta\theta = 250$ K. In order to reduce local stress concentrations in the transition region between the compressed and non-compressed areas, the displacements are ramped up spatially as well:

$$u_{zd}(t, md) = \begin{cases} [\{1 - (md_{re} - md)/(md_{re} - md_{rs})\}0.9 + 0.1]u_{zd}^{max}\frac{t}{t^h} & x \leq md_{re} \\ u_{zd}^{max}\frac{t}{t^h} \quad \text{where} \quad u_{zd}^{max} = -0.4 \cdot 400\ \mu\text{m} & md > md_{re} \end{cases} \tag{59}$$

The start and end coordinates of the spatial displacement ramp are given by $md_{rs} = md^{max} - 5 \times 10^{-3}$ m and $md_{re} = md^{max} - 3 \times 10^{-3}$ m respectively. Each sheet is 400 μm thick and, in order to avoid dealing with convective boundary conditions within the board, sufficiently long sheets are modeled; here the width of the computational domain is chosen to be 0.2 m, so that u_{md}, p_{g_d}, p_{g_v} and θ are assumed constant on the left boundary $\mathcal{L}_l$. The sheets are assumed to be laminated on the sides in contact with the ambient climate and no mass transport occurs through the boundaries $\mathcal{L}_{u_l}$ or $\mathcal{L}_{u_r}$. As no mass is transported through $\mathcal{L}_{u_l}$ or $\mathcal{L}_{u_r}$, only the conductive part of the heat flux is present through these boundaries. The conductive heat flux through $\mathcal{L}_{u_l}, \mathcal{L}_{u_r}$ is modeled with Newton convection $q_\theta = \alpha_\theta(\theta - \theta^\infty)$ where the heat transfer coefficient $\alpha_\theta = 5$ W·m^{-2}·K^{-1} is assumed. Symmetry boundary conditions are assumed on $\mathcal{L}_{b_l}, \mathcal{L}_{b_r}$ and $\mathcal{L}_r$ and a summary of the boundary conditions is provided in Table 5. During the simulations, the effect of changing the initial moisture ratio W^0 and the

Table 5: Boundary conditions

$\mathcal{L}_l$	$\mathcal{L}_{u_l}$	$\mathcal{L}_{u_r}$	$\mathcal{L}_r,\ \mathcal{L}_{b_l}$	$\mathcal{L}_{b_r}$
$\theta = \theta^0$	$q_\theta = \alpha_\theta(\theta - \theta^\infty)$	$q_\theta = \alpha_\theta(\theta - \theta^\infty)$	$q_\theta = 0$	$\theta = \theta(t)$
$u_{md} = 0$	$\mathbf{t} = [0\ \ -p_g^\infty]^T$	$u_{zd}(t, md)$	$\mathbf{u} \cdot \mathbf{n} = 0$	$u_{zd} = 0$
$p_{g_v} = p_{g_v}^0$	$q_{g_v} = 0$	$q_{g_v} = 0$	$q_{g_v} = 0$	$q_{g_v} = 0$
$p_{g_d} = p_{g_d}^0$	$q_{g_d} = 0$	$q_{g_d} = 0$	$q_{g_d} = 0$	$q_{g_d} = 0$

time of the simulation t^h were investigated. The initial values for all simulations are presented in Table 6.

8.1 Discretization

The coupled problem (56)–(58) is solved by adopting a mixed Finite Element Method (FEM) with discrete approximation spaces for all primary variables. The liquid volume fraction n_l, the absolute temperature θ, and the partial pressures p_{g_d} and p_{g_v} are spatially discretized using bilinear shape functions. The total stress tensor, $\boldsymbol{\sigma}$, is modeled with a Terzaghi format, cf. (12), which suggest that the displacements $\mathbf{u}_s$ should have a higher order interpolation than the pressure interpolations, motivating

Table 6: Initial values

Parameter	Unit	Initial value
ρ_s^0	kg·m^{-3}	1 500
ρ_l^0	kg·m^{-3}	1 000
θ^0	K	298.15
p_g^0	Pa	101 325
$p_{g_v}^0$	Pa	$a_w(W^0, \theta^0) p_{g_v}^{sat}(\theta^0)$
$p_{g_d}^0$	Pa	$p_g^0 - p_{g_v}^0$
n_s^0	-	0.42
n_l^0	-	$n_s^0 \rho_s W^0 / \rho_l$
n_g^0	-	$1 - n_s^0 - n_l^0$

a spatially discretization of $\mathbf{u}$ with quadratic serendipity shape functions. The continuous spatial domain Ω_s is therefore approximated with a discrete domain Ω_s^d defined as a union of quadrilateral Taylor–Hood elements (Q8P4) which satisfy the discrete inf–sup condition LBB, see also Market (2005). The weight functions are discretized via Galerkin's method.

The first order time derivatives are discretized via an implicit Euler scheme:

$$\frac{D_s(\mathcal{P}(md, zd, t))}{Dt} = \frac{\mathcal{P}(md, zd, t) - \mathcal{P}(md, zd, t - dt)}{dt} \tag{60}$$

The resulting nonlinear problem was solved by adopting a monolithic Newton–Raphson method. Simulations are executed in an in–house Fortran code.

8.2 Results

Due to the high width to thickness ratio of the computational domain, the results will be presented for the subdomain defined by $\Omega_{sub}^d = \{(md, zd) \in \Omega_s^d \ : md \geq 0.18 \text{ m}\}$. The predicted 2D distributions of temperature, vapor pressure, out-of-plane stresses, and Forchheimer number, as well as the mass exchange between the bound water and the water vapor are presented in Figure 6, at $t = t^h$, for a reference simulation where $(t^h, W^0) = (0.1 \text{ s}, 0.1)$. Comparisons with simulations where $t^h \in \{0.1 \text{ s}, 1 \text{ s}, 10 \text{ s}\}$, $W^0 \in \{0.01,\ 0.1,\ 0.2\}$ are provided in Figures 7 and 8, where the mean out-of-plane values of the distributions are presented over the md-coordinates of the subdomain, Ω_{sub}^d.

From the distributions provided in Figure 6 it is seen that the board does not reach a stationary state and it is clear that transient transports of mass, momentum and energy are of importance when simulating the sealing of two sheets of paperboard. A distinct local increase in vapor pressure is observed in the area around the applied heat source. The significant increase and its local nature is partly due to the explicit temperature dependence of the vapor pressure and the compression of the binary gas, but also due to secondary effects, such as evaporation and the inter–fiber vapor

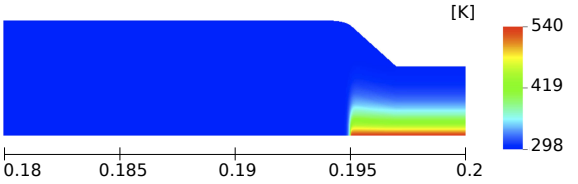

(a) Absolute temperature θ.

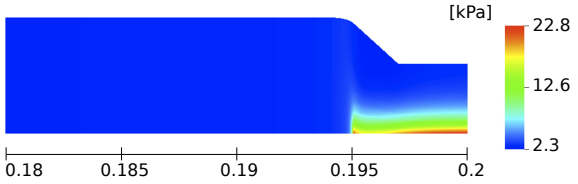

(b) Vapor pressure p_{g_v}.

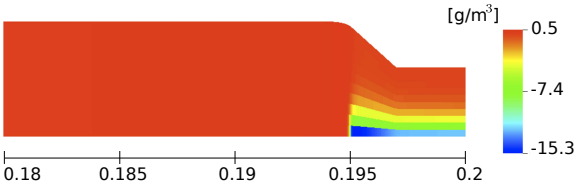

(c) Volume specific change in liquid mass $(\Delta m_l)_e/v_e^0$.

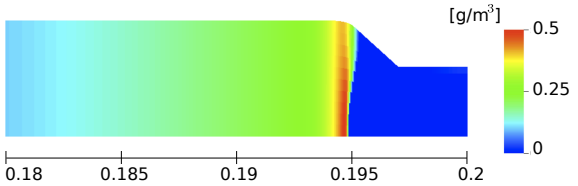

(d) Volume specific change in liquid mass due to condensation $\max((\Delta m_l)_e/v_e^0, 0)$.

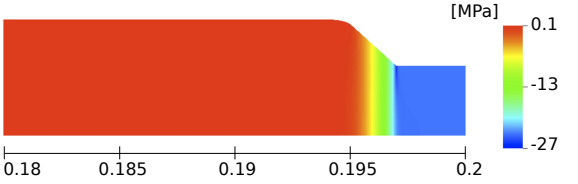

(e) Out-of-plane stresses $\sigma^{(zd)}$.

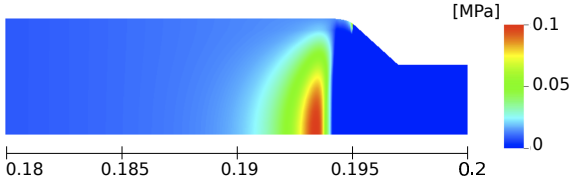

(f) Out-of-plane tension stresses $\max(\sigma^{(zd)}, 0)$.

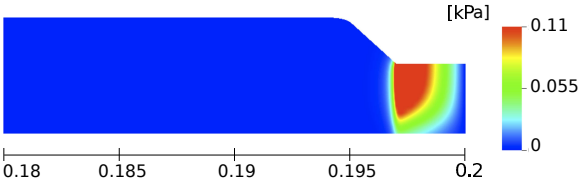

(g) Forchheimer number $\max(F_o, F_o^c)$.

Figure 6: Predicted distributions in a board with the initial moisture ratio $W^0 = 0.1$ after a local compression of 40% and heating of 250 K in 0.1 seconds.

diffusion which drives the vapor towards the heated area. Depending on the relation between the equilibrium vapor pressure $p_{g_v}^{eq} = p_{g_v}^{sat} a_w$ and the vapor pressure p_{g_v}, evaporation or condensation occurs inside the board, cf. (30). The mass exchange between the bound water and the water vapor in the board is presented in Figure 6(c). The mass exchange is here illustrated by the elementwise volume specific change in liquid mass $(\Delta m_l)_e/v_e^0$, where v_e^0 denotes the initial volume of element e and $(\Delta m_l)_e$ the change in liquid mass in element e, which is calculated by

$$(\Delta m_l)_e = (m_l)_e - (m_l^0)_e = -\int_0^t \left[\int_{\Omega_e^d} \hat{m} dv \right] dt \tag{61}$$

From Figure 6(c) it is observed that evaporation has occurred in the area around the heat source, which is due to the equilibrium vapor pressure's being higher than the actual vapor pressure in this area. This is confirmed by estimating the equilibrium vapor pressure in this area as $p_{g_v}^{eq} \approx p_{g_v}^{sat}(\theta = 540 \text{ K}) \approx 5.5$ MPa, which greatly exceeds the partial pressures seen in Figure 6(b). In Figure 6(d), the mass exchange is shown

once more. However, in this figure, the scale is changed so that only areas where the liquid mass has increased are shown. It is observed that the area where bound water has evaporated is followed by a condensation front. This condensation front is a consequence of the vapor pressure front's moving with a higher speed than the heat front, resulting in $p_{g_v} > p_{g_v}^{sat} a_w$.

Extrapolating the out-of-plane compression curve in Figure 2(b) to a compression of 40% gives an out-of-plane stress with a magnitude of -30 MPa, which is within the same range as the predicted value in Figure 6(e), where $\sigma^{(zd)} = \mathbf{e}^{(zd)} \cdot \boldsymbol{\sigma} \cdot \mathbf{e}^{(zd)}$ is shown. The tension stress distribution is presented by changing the scale in Figure 6(e), so that only tension stresses are shown in Figure 6(f). The maximum out-of-plane tension reaches an order of magnitude of approximately 0.1 MPa, which is below the tension failure strength in ZD at $\sigma^{(zd)} \approx 0.36$ MPa, cf. Stenberg (2003), and it is concluded that the pressure does not cause failure in the board for the considered simulation. However, two comments should be made in regard to the stress distribution. First, the adhesion between the board and the laminate has a lower failure strength than the board, and the stress levels in Figure 6(f) should be compared with the failure strength of the adhesion when performing a risk estimation. Second, due to the high levels of stress, the board experiences a plastic response in the compressed region and the plastic responce is determined by the yield surface provided in Borgqvist et al. (2015) which does not include an explicit temperature or moisture dependence. In Wallmeier et al. (2015); Salmen and Back (1977) it is argued that the stress–strain response, including the yield surface, does have explicit temperature and moisture dependences and including such effects could alter the stress distribution provided here.

The inter–fiber gas–solid seepage is described as a nonlinear laminar flow, cf. (34), where the nonlinear part, $F_o \mathbf{R}_{g,s} \mathbf{v}_{g,s}$, corresponds to $F_o/(1 + F_o)\%$ of the pressure gradient. The fraction $F_o/(1 + F_o)$ is the inverse of the friction factor which describes the ratio of the total energy to the kinetic energy loss, see also Modak et al. (2009). Considering a 10% nonlinear effect to be an indication that a nonlinear flow relation is needed gives a critical Forchheimer number of $F_o^c \approx 0.11$. In order to present the areas where a nonlinear flow relation is critical, the Forchheimer number F_o is shown in Figure 6(g) where it should be noted that the scale is changed so that the highest value shown is F_o^c. From the distribution it is seen that the Forchheimer number does exceed the critical value in the compressed area and it is concluded that a nonlinear seepage flow model is needed for an accurate description. The distributions shown in Figure 6 are retrieved from a simulation with a spatial discretization containing 3540 elements, 10 elements in the out–of–plane direction. The same simulation was also performed with a finer mesh, containing 5746 elements. The distributions retrieved from the simulation with the finer mesh matched the distributions in Figure 6. The effect of changing the time t^h and the initial moisture ratio W^0 is illustrated by showing the mean out-of-plane value of $(\Delta m_l)_e / v_e^0$ and p_{g_v} in Figure 7 and $\sigma^{(zd)}$ and F_o in Figure 8. The effect of compressing the board is also shown in these figures by plotting the distributions together with the corresponding distributions from simulations where the board is not compressed (red curves). From Figure 7 it is concluded that the time t^h has a significant influence on the drying of the board. It is also seen that the area

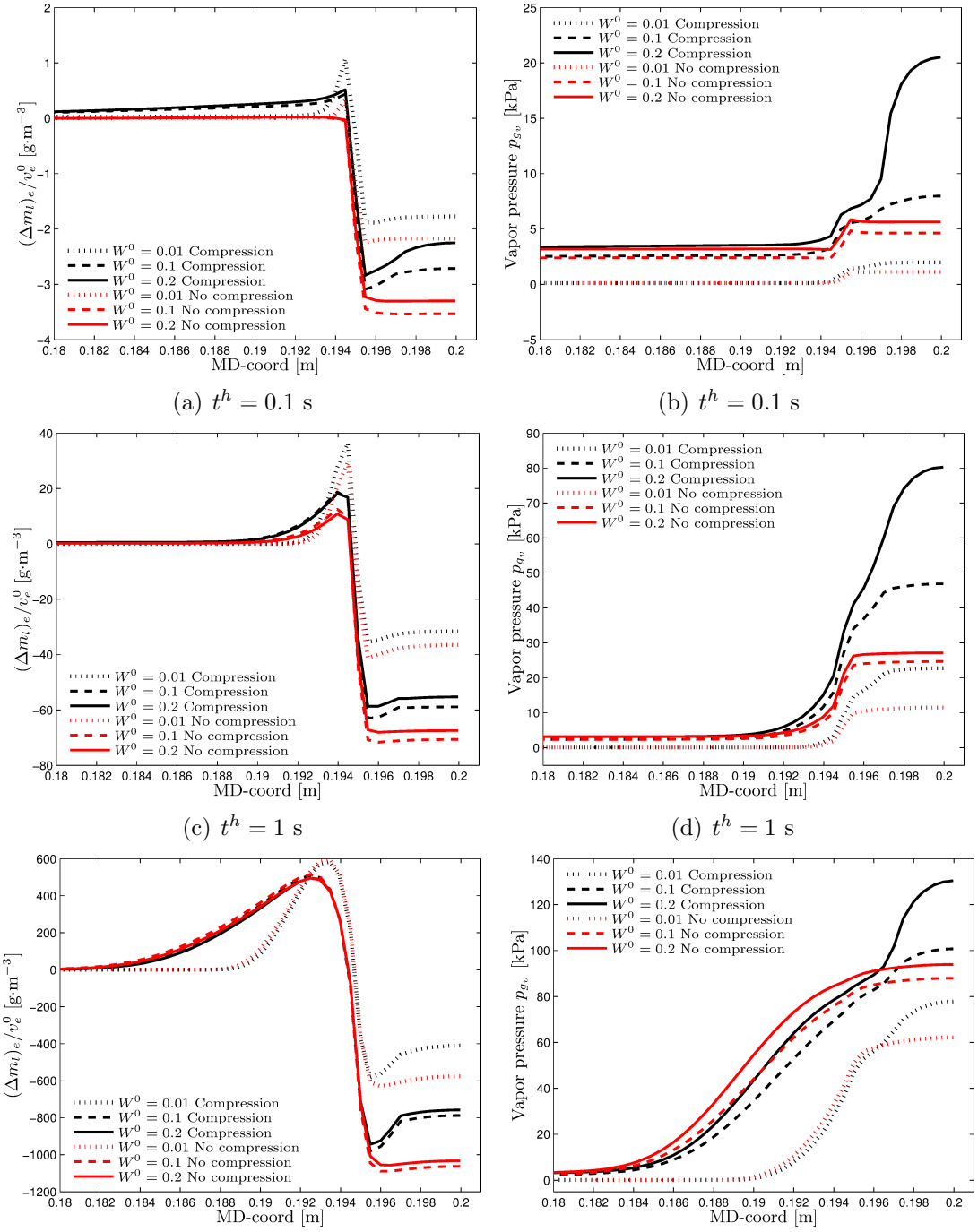

(a) $t^h = 0.1$ s (b) $t^h = 0.1$ s

(c) $t^h = 1$ s (d) $t^h = 1$ s

(e) $t^h = 10$ s (f) $t^h = 10$ s

Figure 7: Mean value in ZD of $(\Delta m_l)_e/v_e^0$, **a**, **c**, **e** and p_{g_v}, **b**, **d**, **f** presented for $W^0 \in \{0.01\ 0.1\ 0.2\}$. In **a**, **b** $t^h = 0.1$ s, **c**, **d** $t^h = 1$ s and **e**, **f** $t^h = 10$ s. Red curves indicates simulations without compression and black curves indicates simulations with compression.

where evaporation appears is followed by a condensation front, which also is visible in Figure 6(d). The energy related to the binding between the bound water and the

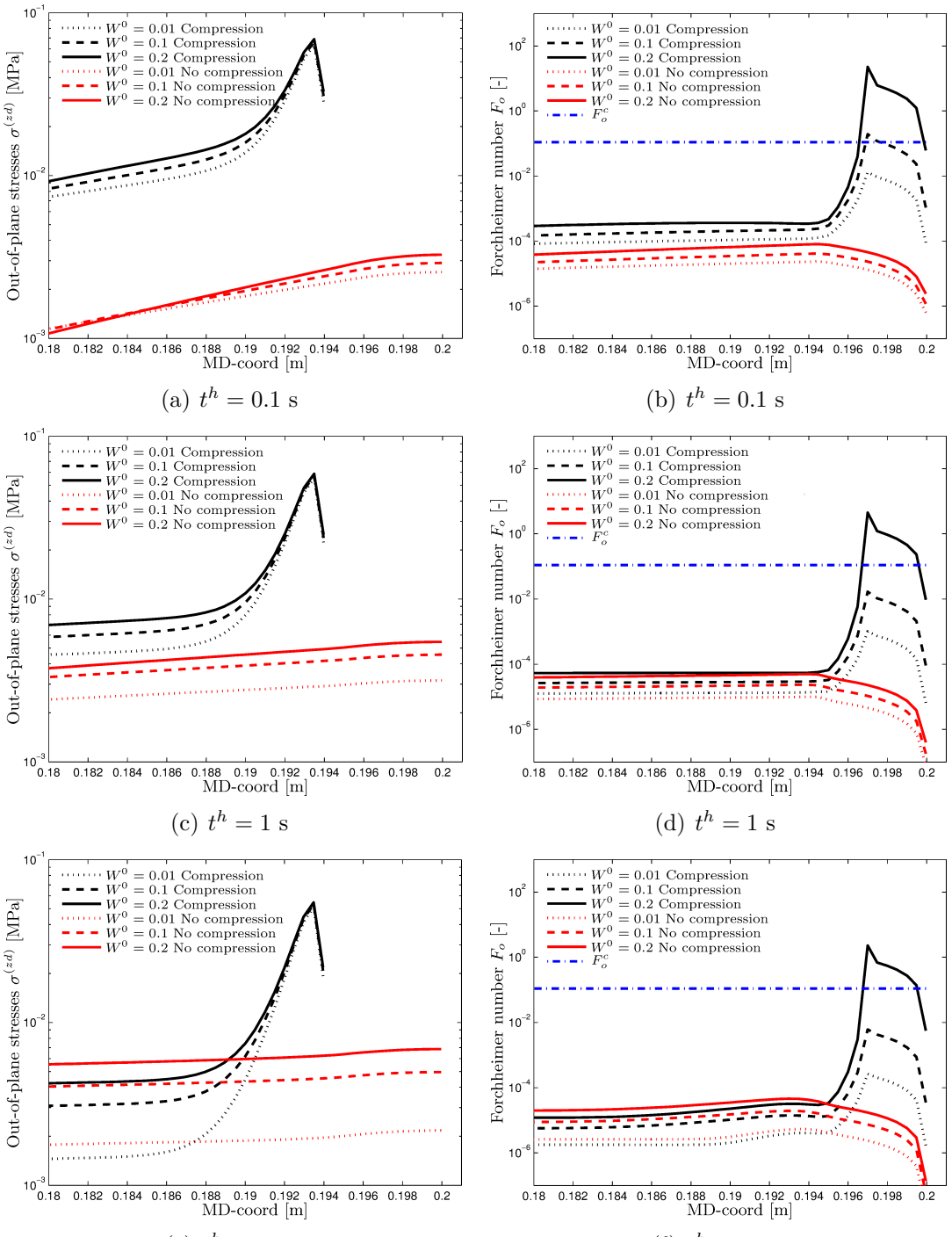

(a) $t^h = 0.1$ s (b) $t^h = 0.1$ s

(c) $t^h = 1$ s (d) $t^h = 1$ s

(e) $t^h = 10$ s (f) $t^h = 10$ s

Figure 8: Mean value in ZD of $\sigma^{(zd)}$, **a**, **c**, **e** and F_o, **b**, **d**, **f** presented for $W^0 \in \{0.01\ 0.1\ 0.2\}$. In **a**, **b** $t^h = 0.1$ s, **c**, **d** $t^h = 1$ s and **e**, **f** $t^h = 10$ s. Red curves indicates simulations without compression and black curves indicates simulations with compression.

fibers increases with a decreasing moisture ratio, implying that more energy is needed for evaporation at lower W. This aspect is seen in Figure 7 where simulations with $W^0 = 0.01$ have more condensation and less evaporation. Focusing on the heated

area, it is, however, seen that $W^0 = 0.1$ results in more evaporation than $W^0 = 0.2$, which is a consequence of the higher vapor pressure for $W^0 = 0.2$ shown in the figures to the right.

It is also observed that simultaneously compressing and heating the paperboard reduces the evaporation and increases the condensation in comparison with a board that is only heated, which is a consequence of the increased vapor pressure caused by the compression. In the right column in Figure 7, the vapor pressure distributions for different W^0 and t^h are shown. From these figures it is observed that boards with a higher initial moisture ratio will experience higher vapor pressures in the inter–fiber pores. Outside the heated area a clear jump in the vapor pressure is visible for different W^0, which is a consequence of the higher degree of saturation's reducing the permeability and the volume the evaporated water may occupy. Comparing the vapor pressure distributions with the change in liquid mass, it is concluded that the wider condensation area for greater t^h is caused by a wider area of elevated vapor pressure. From the vapor pressures distributions for different t^h it is reasoned that the primary cause for the vapor pressure increases for smaller t^h is compression, while for greater t^h the primary cause is evaporation.

Considering the out-of-plane stress distributions in Figure 8 it is observed how, due to the compression of the board, gas is pressed out of the compressed area and the gas pressure outside the compressed area is increased for $t^h = 0.1$ s and $t^h = 1$ s. However, for $t^h = 10$ s the opposite effect is seen. Compared with the mass exchange in Figure 7(e), the compression of the board has reduced the evaporation in the heated area, implying that a lower vapor pressure could be the reason. However, from Figure 7(f), it is observed that the vapor pressure in the area in question is not affected by the compression. The most probable reason for the lower gas pressure in the compressed board is the reduction in the gas volume fraction due to the compression, which decreases the permeability considerably and results in a more local pressure build-up. The reason why this is not seen in the shorter times is that the pressure increases more rapidly for shorter times due to the compression and slower for greater t^h due to evaporation, as discussed previously. In Figure 8(e) the effect of the increased saturation, discussed previously, is seen by the jump in the stress levels further from the compression area.

The distribution of the mean out-of-plane value of the Forchheimer number is shown in Figure 8, right column. In these figures the critical Forchheimer number is marked with a blue striped and dotted line. It is observed that the nonlinear seepage flow description becomes more important for higher W^0. This is a consequence of the reduced permeability due to the reduced gas volume fraction. For simulations without compression, it is seen that the average Forchheimer number has an order of magnitude of $F_o^{av} \approx 10^{-4}$, which would mean a nonlinear effect of approximately $10^{-2}\%$, and it is concluded that the inter–fiber seepage may be considered as a linear laminar flow for these simulations.

9 Conclusions

Paperboard is viewed as a composition of fibers, water bound in or to the fibers, and moist air. The orthotropic elasto-plastic stress–strain model of paperboard has been coupled with a transient moisture and heat transport in hybrid mixture theory framework. The derived model includes e.g., the evolution of the porosity, large plastic deformations, evaporation/condensation, inter–fiber seepage and vapor diffusion, the combined heat flux, and energy losses/gains associated with the mentioned processes. The anisotropic nature of paperboard is taken into account in the transport of mass, momentum, and energy. The derived model is implemented in a finite element setting and the response of moist paperboard during an idealized sealing is predicted. The model is able to capture the transient transport of mass, energy, and momentum as well as interactions between these. For instance, simulations show that due to the nonhomogeneous distributions of vapor pressure and temperature, evaporation as well as condensation occurs within the board. It is also shown how a simultaneous heating and compressing of the board affects the transport of mass such that the inter–fiber gas pressure increases locally which introduces considerable out-of-plane tension stresses in the board. The coupled model is able to represent the nonlinear response during out–of–plane compression. An investigation of the distribution of the Forchheimer number shows that a Forchheimer type of inter–fiber seepage is needed in order to predict an accurate flow for higher initial moisture ratios and shorter heating phases. However, for initial moisture ratios less than $W^0 = 0.1$ a Darcy type of inter–fiber seepage would be sufficient.

Acknowledgements

I would like to thank Stora Enso AB and Tetra Pak AB for providing me with experimental data. The financial support from Tetra Pak AB is gratefully acknowledged.

References

E. Baggerud, Modelling of Mass and Heat Transport in Paper, Ph.D. thesis, Lund University, 2004.

Q. S. Xia, M. C. Boyce, D. M. Parks, A constitutive model for the anisotropic elastic-plastic deformation of paper and paperboard, International Journal of Solids and Structures 39 (2002) 4053–4071.

A. Harrysson, M. Ristinmaa, Large strain elasto-plastic model of paper and corrugated board, International Journal of Solid and Structures 45 (2008) 3334–3352.

J. Boehler, Applications of tensor functions in solid mechanics, vol. 292, Springer-Verlag Wien, 1987.

E. Borgqvist, T. Lindström, J. Tryding, M. Wallin, M. Ristinmaa, Distortional hardening plasticity model for paperboard, International Journal of Solids and Structures 51 (2014) 2411–2423.

E. Borgqvist, M. Wallin, M. Ristinmaa, J. Tryding, An anisotropic in-plane and out-of-plane elasto-plastic continuum model for paperboard, Composite Structures 126 (2015) 184–195.

N. L. Salmén, E. L. Back, Moisture-dependent thermal softening of paper evaluated by its elastic modulus., Tappi Journal 63 (6) (1980) 117–120.

E. Linvill, S. Östlund, The Combined Effects of Moisture and Temperature on the Mechanical Response of Paper, Experimental Mechanics 54 (2014) 1329–1341.

A. Modak, S. S. Takagaki, S. Ramaswamy, Integral Flow Parameters and Material Characteristics Analysis in Through Air Drying: Part I, Drying Technology 27 (2009) 672–684.

R. Masoodi, K. M. Pillai, Darcy's Law-Based Model for Wicking in Paper-Like Swelling Porous Media, AIChE Journal 56 (2010) 2257–2267.

R. Masoodi, H. Tan, K. M. Pillai, Numerical Simulation of Liquid Absorption in Paper-Like Swelling Porous Media, AIChE Journal 58 (8) (2011) 2536–2544.

S. Wiryana, J. Berg, The transport of water in wet-formed networks of cellulose fibers and powdered superabsorbent, Wood and Fiber Science 23 (1991) 457–464.

A. Bandyopadhyay, H. Radhakrishnan, B. V. Ramarao, S. G. Chatterjee, Moisture Sorption Response of Paper Subjected to Ramp Humidity Changes: Modeling and Experiments, Industrial and Engineering Chemistry Research 39 (2000) 219–226.

S. A. Lavrykov, B. V. Ramarao, Thermal Properties of Copy Paper Sheets, Drying Technology 30 (2012) 197–311.

M. Alexandersson, H. Askfelt, M. Ristinmaa, Triphasic Model of Heat and Moisture Transport with Internal Mass Exchange in Paperboard, Transport in Porous Media 112 (2016) 381–408.

P. A. M. Zapata, M. Fransen, J. T. Boonkkamp, L. Saes, Coupled heat and moisture transport in paper with application to a warm print surface, Applied Mathematical Modelling 37 (2013) 7273–7286.

Y. Bachmat, J. Bear, Macroscopic Modelling of Transport Phenomena in Porous Media. 1: The Continuum Approach, Transport in Porous Media 1 (1986a) 213–240.

Y. Bachmat, J. Bear, Macroscopic Modelling of Transport Phenomena in Porous Media. 2: Applications to Mass, Momentum and Energy Transport, Transport in Porous Media 1 (1986b) 241–269.

M. Karlsson, S. Stenström, Static and Dynamic Modeling of Carboard Drying Part 1: Theoretical Model, Drying Technology 23 (2005a) 143–163.

M. Karlsson, S. Stenström, Static and Dynamic Modeling of Carboard Drying Part 2: Simulations and Experimental Results, Drying Technology 23 (2005b) 143–163.

H. Askfelt, M. Alexandersson, M. Ristinmaa, Transient transport of heat, mass and momentum in paperboard including dynamic phase change of water, International Journal of Engineering Science 109 (2016) 131–144.

M. Hassanizadeh, W. G. Gray, General conservation equations for multi-phase systems: 1. Averaging procedure, Advances in Water Resources 2 (1979a) 54–72.

M. Hassanizadeh, W. G. Gray, General conservation equations for multi-phase systems: 2. Mass, momenta, energy, and entropy equations, Advances in Water Resources 2 (1979b) 191–203.

L. S. Bennethum, J. H. Cushman, Multiscale, hybrid mixture theory for swelling systems-I: Balance Laws, International Journal of Engineering Science 34 (1996) 125–145.

S. M. Hassanizadeh, W. G. Gray, Mechanics and thermodynamics of multiphase flow in porous media including interphase boundaries, Advances in Water Resources 13 (4) (1990) 169–186.

R. Larsson, M. Wysocki, S. Toll, Process-modeling of composites using two-phase porous media theory, European Journal of Mechanics A/Solids 23 (2004) 15–36.

M. Ristinmaa, N. S. Ottosen, B. Johannesson, Mixture theory for a thermoelastoplastic porous solid considering fluid flow and internal mass exchange, International Journal of Engineering Science 49 (2011) 1185–1203.

M. Harrysson, M. Ristinmaa, Description of evolving anisotropy at large strains, Mechanics of Materials 39 (2007) 267–282.

M. Alava, K. Niskanen, The physics of paper, Reports on Progress in Physics 69 (3) (2006) 669–723.

J. Bénet, A. Ramirez-Martinez, F. Ouedraogo, F. Cherblanc, Measurment of chemical potential of a liquid in porous media, Journal of porous media 11 (2012) 1019–1029.

Y. A.Çengel, M. A. Boles, Thermodynamics an engineering approach, Elsevier Science, 2nd edition edn., 2007.

H. D. Lopez-Hernandez, P. P. Valko, T. T. Pham, Optimum Fracture Treatment Design Minimizes the Impact of Non-Darcy Flow Effects, Paper SPE 90195 presented at the SPE Annual Technical Conference and Exhibition, 2004.

S. D. Pont, F. Meftah, B. A. Schrefler, Modeling concrete under severe conditions as a multiphase material, Nuclear Engineering and Design 241 (2011) 562–572.

E. R. Sullivan, Heat and moisture transport in unsaturated porous media: a coupled model in terms of chemical potential, Ph.D. thesis, M.S University of Colorado, 2013.

K. A. Akanni, J. W. Evans, Effective transport coefficients in heterogeneous media, Chemical Engineering Science 42 (8) (1987) 1945–1954.

W. J. Massman, A review of the molecular diffusivities of H_2O, CO_2, CH_4, CO,O_3, NH_3, N_2O, NO and NO_2 in air, O_2 and N_2 near STP, Atmospheric Environment 32 (6) (1998) 1111–1127.

B. V. Ramarao, S. Ramaswamy, 3D Characterization of the Structure of Paper and Paperboard and Their Application to Optimize Drying and Water Removal Processes and End-Use Applications, Tech. Rep., 2004.

M. F. C. Lucisano, On Heat and Paper: From Hot Pressing To Impuls Technology, Ph.D. thesis, Royal Institute of Technology Stockholm, 2002.

S. A. Reardon, M. R. Davis, P. E. Doe, Construction of an Analytical Model of Paper Drying , Drying Technology 17 (1999) 655–690.

R. B. Bird, W. E. Stewart, E. N. Lightfoot, Transport Phenomena, JOHN WILEY & SONS, second edition edn., 2007.

M. L. V. Ramires, C. A. N. de Castro, Y. Nagasaka, A. Nagashima, M. J. Assael, W. A. Wakeham, Standard Reference Data for the Thermal Conductivity of Water, Journal of Physical and Chemical Reference Data 24.

V. W. Punton, Papermaking raw materials : their interaction with the production process and their effect on paper properties, Mechanical Engineering Publications Limited London, 381–412, 1985.

B. Market, Porous Media Viscoelasticity with Application to Polymeric Foams, Ph.D. thesis, Universitat Stuttgart, 2005.

N. Stenberg, A model for the through-thickness elastic-plastic behaviour of paper, International Journal of Solids and Structures 40 (2003) 7483–7498.

N. L. Salmen, E. L. Back, Simple stress–strain measurements on dry papers from –25° C to 250° C, Svensk Papperstidning 80 (1977) 178–183.

M. Wallmeier, E. Linvill, M. Hauptmann, J. Majschak, S. Östlund, Explicit FEM analysis of the deep drawing of paperboard, Mechanics of Materials 89 (2015) 202–215.

Paper D

Henrik Askfelt and Matti Ristinmaa

Experimental and numerical analysis of adhesion failure in moist packaging material during excessive heating.

To be submitted for publication

Experimental and numerical analysis of adhesion failure in moist packaging material during excessive heating

Henrik Askfelt[a] and Matti Ristinmaa[a]

[a] Division of Solid Mechanics, Lund University

P.O. Box 118, S-221 00 Lund, Sweden

Abstract

In the presented paper experimental and numerical analyses are made of the failure due to blister formation in moist packaging material when exposed to excessive heating. The basic concept of the experimental analysis is to expose a package material to a hot air jet and measure the time until the material experience internal failure. For the numerical analysis, a triphasic macroscale hybrid mixture theory approach is adopted. The in–plane permeability and the static and dynamic sorption properties of the paperboard are believed to have significant influences on the blister formation. For this reason in–plane permeability experiments and sorption experiments are performed to retrieve proper constitutive coefficients for the numerical simulations. Results from numerical simulations are compared with the experimental tests in order to better understand the physics behind the forming of a blister. The results indicate that the blister formation primarily depends on the in–plane permeability and the sorption properties of the paperboard as well as the properties of the adhesion between the paperboard and the Al-foil.

1 Introduction

Package material used for storing of food products typically has a layered structure in the out–of–plane direction (ZD). Depending on the product the package is meant to protect and the climates that the product will be stored in different layers are included. One class of package material denoted aseptic package material is depicted in Figure 1(a). The main part of the aseptic package material is comprised of paperboard which carries the main stiffness of the package material. On the inside of the paperboard, i.e., on the side of the board that is in contact with the food product, two thin layers; one of polyethylene and one of Al–foil exists. The Al–foil acts as a barrier, protecting the food product from light as well as the transport of gas and liquid from the ambient climate. The Al–foil is attached to the paperboard with an adhesive, for an elaborate description of this adhesive the reader is referred to e.g., Hallbäck et al. (2014). In order to make the outward surface of the package material smoother and improve the printing quality of the package, it is common to add a clay coating on this surface. Outside the clay coating an additional layer of polyethylene exists which protects the paperboard from the ambient climate. With the layers of polyethylene and Al–foil, the out–of–plane direction of the aseptic package material may be considered as impermeable in many applications.

During the filling and folding process, a package material is exposed to excessive heating in a short period of time. As the package material is heated the liquid water bound in and to the fibers will desorb/evaporate and increase the inter–fiber gas pressure. At the same time the increased temperature will reduce the strength of the adhesion between the paperboard and the Al–foil. In a worst case scenario the increased temperature might lead to failure in the adhesion which will have an negative impact on the integrity of the product. As the adhesion fails a bubble will appear between the Al–foil and the paperboard, cf., Figure 1(b), these bubbles are referred to as blisters.

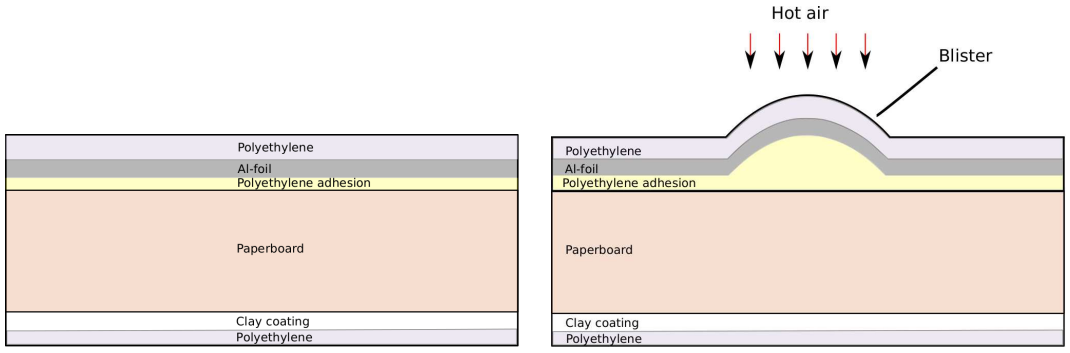

Figure 1: a) Illustration of the layers of the aseptic package material, **b**) Illustration of the blister arising after the package material has been locally exposed to a hot air jet.

Post mortem dissections of the package material, after a blister formation, have shown an accumulation of moisture in the blisters and it is believed that the blisters

are caused primarily due to desorption and evaporation, i.e., mass exchange between water bound in or to the fibers and the inter–fiber water vapor. This hypothesis may also be strengthen by the simulations presented in Askfelt and Ristinmaa (2016) where a significant increase in vapor pressure is seen when a laminated paperboard is heated 250 K in 10 s. The magnitude of the vapor pressure depends on the magnitude of the rate of the mass exchange. A common approach to model the mass exchange between the bound water and the water vapor is to assume chemical equilibrium i.e., an instantaneous phase change governed by the sorption isotherm. However, for the considered application where excessive amounts of heat are added in a short period of time, this assumption is not sufficient.

The dynamic phase change between bound water and water vapor has been modeled in e.g., Zapata et al. (2013); Foss et al. (2003); Bandyopadhyay et al. (2000) as driven by the difference between the current concentration of the bound water and the equilibrium value of the concentration of the bound water, and in Askfelt and Ristinmaa (2016); Benet and Jouanna (1982); Benet et al. (2009); Alexandersson et al. (2016) as driven by the difference in chemical potential between the bound water and the water vapor. For a numerical comparison between the two methods and two additional variants, see e.g., Trautz et al. (2015). In the present work the dynamic mass change is considered to be driven by the difference in chemical potential between the bound water and the water vapor.

In this work a blister test is used to measure the blister times of a package material in different climates. The main idea of the blister test is to expose a sample of moist package material with a hot air jet and measure the time until a blister has developed and grown to a certain size, this time is referred to as the blister time. These measurements are then compared with numerical simulations obtained by use of the model developed in Askfelt and Ristinmaa (2016); Askfelt et al. (2016) which describes the coupled transport of mass, momentum and energy in moist paperboard. This model is derived in a hybrid mixture theory (HMT) framework and a brief summary of the kinematic framework of HMT and of the model developed in Askfelt and Ristinmaa (2016); Askfelt et al. (2016) is provided in Section 2. For a more elaborate description of HMT the reader is referred to Hassanizadeh and Gray (1979a,b, 1980). The in–plane permeability and the static and dynamic sorption properties are believed to have a significant influence of the development of a blister and these properties are evaluated for the considered paperboard in Sections 3.2 and 3.1. The experimental blister test is presented in Section 4 and the numerical analysis is included in Section 5.

2 Preliminaries

2.1 Kinematic framework

In the mixture theory framework each spatial point $\mathbf{x}$, of the body, is viewed as a superposition of N_α immiscible phases α. Each phase α is then viewed as a homogeneous mixture of N_{α_j} miscible constituents α_j. Every phase and every constituent is viewed as a continuum governed by balance laws specific for that component. In addi-

tion each component is allowed to have a separate motion described by the nonlinear mapping $\boldsymbol{\chi}_\alpha : \Omega_\alpha^0 \times t \to \Omega \subset \mathbb{R}^3$

$$\mathbf{x} = \boldsymbol{\chi}_\alpha(\mathbf{X}_\alpha, t) \tag{1}$$

where t denotes the time and $\mathbf{X}_\alpha$ is the position of phase α in the reference configuration of phase α, i.e., Ω_α^0. It may be noted that also the interfaces between the different phases can be treated as separate continuum within HMT, see e.g., Hassanizadeh and Gray (1990); Bennethum and Cushman (1996). In the present work, these interfaces are only considered implicitly via the constitutive relations. The deformation gradient $\mathbf{F}_\alpha$ associated with the motion of phase α is defined by

$$\mathbf{F}_\alpha = \frac{\partial(\boldsymbol{\chi}_\alpha(\mathbf{X}_\alpha, t))}{\partial \mathbf{X}_\alpha} \tag{2}$$

where $D_\alpha(\bullet)/Dt$ denotes the material time derivative following phase α. In order to ensure a continuous bijective mapping, the Jacobian is assumed to be greater than zero, i.e., $J_\alpha = \det(\mathbf{F}_\alpha) > 0$.

The volume and the mass of constituent α_j of a representative volume element, RVE, are denoted v_{α_j} and m_{α_j} respectively. All constituents within a phase are considered miscible implying that they are all associated with the same volume, i.e., $v_{\alpha_j} = v_\alpha$. The volume v and the mass m of the mixture are given by

$$m = \sum_\alpha m_\alpha, \qquad m_\alpha = \sum_j m_{\alpha_j}, \qquad v = \sum_\alpha v_\alpha \tag{3}$$

The macroscale balance laws assumed in hybrid mixture theory are derived through averaging of microscale balance laws, see e.g., Hassanizadeh and Gray (1979a). During the averaging from micro- to macroscale a new variable, the volume fraction n_α, appears naturally, as

$$n_\alpha = \frac{v_\alpha}{v}, \qquad \sum_\alpha n_\alpha = 1 \tag{4}$$

where (4b) is a consequence of (3c) known as the saturation condition. Throughout the rest of this paper, the product between a volume fraction and another quantity will be denoted with a bar, i.e., $(\bar{\bullet})_\alpha = n_\alpha(\bullet)$. The intrinsic densities of the mixture, phase α, and constituent α_j are defined as

$$\rho = \frac{m}{v}, \qquad \rho_\alpha = \frac{m_\alpha}{v_\alpha}, \qquad \rho_{\alpha_j} = \frac{m_{\alpha_j}}{v_\alpha} \tag{5}$$

The mass averaged velocities of the mixture, $\mathbf{v}$, and phase α, $\mathbf{v}_\alpha$, are related to the constituent velocities, $\mathbf{v}_{\alpha_j}$, in the following manner

$$\rho \mathbf{v} = \sum_\alpha n_\alpha \rho_\alpha \mathbf{v}_\alpha, \qquad \rho_\alpha \mathbf{v}_\alpha = \sum_j \rho_{\alpha_j} \mathbf{v}_{\alpha_j} \tag{6}$$

For implementation reasons it is preferable to choose a reference phase which is followed during the simulations and describe the motions of the other components with relative motions. Here, the solid phase is selected as the reference phase and the motion of the other components are described by the diffusion velocities $\mathbf{w}_{\alpha_j} = \mathbf{v}_{\alpha_j} - \mathbf{v}_\alpha$ and the seepage velocities $\mathbf{v}_{\alpha,s} = \mathbf{v}_\alpha - \mathbf{v}_s$. It should be noted that due to (6), the diffusion velocities $\mathbf{w}_{\alpha_j}$ will be constrained via the following summation

$$\sum_j \rho_{\alpha_j} \mathbf{w}_{\alpha_j} = \mathbf{0} \tag{7}$$

The spatial velocity gradient $\mathbf{l}_\alpha$, is additively split into a rate of deformation tensor $\mathbf{d}_\alpha$ and a skew-symmetric spin tensor $\boldsymbol{\omega}_\alpha$ defined by

$$\mathbf{l}_\alpha = \nabla(\mathbf{v}_\alpha), \qquad \mathbf{d}_\alpha = \frac{1}{2}(\mathbf{l}_\alpha + \mathbf{l}_\alpha^T), \qquad \boldsymbol{\omega} = \frac{1}{2}(\mathbf{l}_\alpha - \mathbf{l}_\alpha^T) \tag{8}$$

2.2 Governing equations

A system of equation governing the response of moist paperboard when exposed to extensive compression and heating in a short period of time has been developed in Askfelt and Ristinmaa (2016); Askfelt et al. (2016). A short summary of this model is presented in this subsection.

Paperboard is an orthotropic material with the three material directions denoted by; machine direction (MD), cross machine direction (CD), and out–of–plane directions (ZD). For the considered application, moisture ratios are below the hygroscopic moisture content (HMC) and the paperboard is assumed to be composed three phases: solid $(\bullet)_s$, liquid $(\bullet)_l$, and gas $(\bullet)_g$. The solid phase represents the network of cellulose fibers, the liquid phase represents the liquid water bound in or to the fibers and the gas phase represents moist air which is considered to be a homogeneous mixture of the two miscible gas constituents; dry air $(\bullet)_{g_d}$ and water vapor $(\bullet)_{g_v}$. The intrinsic density and the mass of the solid phase are assumed constant and the balance of mass of the solid phase is reduced to

$$\frac{D_s(n_s)}{Dt} + n_s \nabla \cdot (\mathbf{v}_s) = 0 \Leftrightarrow n_s = n_s^0 / J_s \tag{9}$$

where the superscript $(\bullet)^0$ indicates an initial value, see also Landervik and Larsson (2007). The governing equations are given by three balance of mass equations, one balance of linear momentum, and one balance of energy. The balance of mass for the bound water, the dry air and the water vapor are given by

$$\rho_l \frac{D_s(n_l)}{Dt} + \bar{\rho}_l \nabla \cdot (\mathbf{v}_s) + \hat{m} = 0 \tag{10a}$$

$$\rho_{g_d} \frac{D_s(n_g)}{Dt} + \frac{\bar{\rho}_{g_d}}{p_{g_d}} \frac{D_s(p_{g_d})}{Dt} - \frac{\bar{\rho}_{g_d}}{\theta} \frac{D_s(\theta)}{Dt} + \nabla \cdot (\mathbf{J}_{g_d}) + \bar{\rho}_{g_d} \nabla \cdot (\mathbf{v}_s) = 0 \tag{10b}$$

$$\rho_{g_v} \frac{D_s(n_g)}{Dt} + \frac{\bar{\rho}_{g_v}}{p_{g_v}} \frac{D_s(p_{g_v})}{Dt} - \frac{\bar{\rho}_{g_v}}{\theta} \frac{D_s(\theta)}{Dt} + \nabla \cdot (\mathbf{J}_{g_v}) + \bar{\rho}_{g_v} \nabla \cdot (\mathbf{v}_s) - \hat{m} = 0 \tag{10c}$$

where θ denotes the absolute temperature and the bound water seepage, $\mathbf{v}_{l,s}$, was assumed negligible. The intrinsic density of the bound water is assumed constant $\rho_l = 1000$ kg/m^3 and both gas constituents are assumed to behave as ideal gases, i.e., the pressures of the gas constituents are given by $p_{g_j} = \rho_{g_j} R_{g_j} \theta$ where R_{g_j} denotes the specific gas constant of constituent g_j. The combined mass flux $\mathbf{J}_{g_j} = \bar{\rho}_{g_j}(\mathbf{w}_{g_j} + \mathbf{v}_{g,s})$ includes both the inter–fiber diffusion $\mathbf{w}_{g_j}$ and the inter–fiber gas seepage $\mathbf{v}_{g,s}$. Body forces and macroscopic inertial forces are assumed to be negligible and the relative velocities are given by

$$\mathbf{v}_{g,s} = -\frac{\mathbf{K}_{g,s}}{\mu^D_{g_j} n_g^2} \nabla(p_g), \qquad \mathbf{w}_{g_v} = -\mathbf{D}^{eff}_{g_v} \nabla(\mu_{g_v} - \mu_{g_d}), \qquad \mathbf{w}_{g_d} = -\frac{\rho_{g_v}}{\rho_{g_d}} \mathbf{w}_{g_v} \tag{11}$$

where μ_{g_j} and $\mu^D_{g_j}$ denote the chemical potential and the dynamic viscosity, respectively, of constituent g_j. The gas pressure is given by Dalton's law, i.e., $p_g = p_{g_d} + p_{g_v}$. The intrinsic gas permeability tensor is denoted, $\mathbf{K}_{g,s}$ and the water vapor diffusivity tensor is denoted $\mathbf{D}^{eff}_{g_v}$. Both $\mathbf{K}_{g,s}$ and $\mathbf{D}^{eff}_{g_v}$ are orthotropic tensors with the values $K^{(id)}_{g,s}$ and $(D^{eff}_{g_v})^{(id)}$ in direction $id \in \{md, cd, zd\}$. As mentioned in the introduction, the in–plane permeabilities, $K^{(md)}_{g,s}$ and $K^{(cd)}_{g,s}$, are believed to be of significant influence for the development of a blister and for this reason, these properties are carefully recalibrated in Section 3.2.

The dynamic phase change between the bound water and the water vapor is described by the rate of evaporation $\hat{m}$ which is given by

$$\hat{m} = k_{\hat{m}} R_{g_v} \theta \ln\left(\frac{p^{sat}_{g_v} a_w}{p_{g_v}}\right) \tag{12}$$

where $a_w, k_{\hat{m}}$ and $p^{sat}_{g_v}$ denotes the water activity, the rate of evaporation coefficient, and the saturation vapor pressure, respectively. In the HMC region the mass exchange between bound water and water vapor is caused by both desorption, (mass exchange between intra–fiber pore water and water vapor) and evaporation (mass exchange between inter–fiber pore water and water vapor). In the present work no distinction is made between these two locations of water and the terminology rate of evaporation is used to describe the rate of the total mass exchange between the bound water and the water vapor. The water activity and the rate of evaporation coefficient will be elaborated further in Section 3.1 and the saturation vapor pressure is modeled with an Antoine relation i.e., $p^{sat}_{g_v} = 133.322 \times 10^{(8.07131 - 1730.63/(\theta - 39.574))}$ Pa.

The balance of linear momentum is given by

$$-\nabla \cdot (\boldsymbol{\sigma}) + \hat{m}(\mathbf{v}_{g,s} + \mathbf{w}_{g_v}) = \mathbf{0} \tag{13}$$

where the total Cauchy stress tensor $\boldsymbol{\sigma}$ is described by a Terzaghi format, i.e., $\boldsymbol{\sigma} = \bar{\boldsymbol{\sigma}}^{eff}_s - p_g \mathbf{I}$. The effective Cauchy stress tensor of the solid phase $\bar{\boldsymbol{\sigma}}^{eff}_s$ describes the stress–strain response of the fiber network. Thermal and hygroscopic expansions are neglected in the present analysis and the effective stress tensor is modeled by the theory outlined in Borgqvist et al. (2015). The format of the effective stress tensor is

given by

$$\bar{\boldsymbol{\sigma}}_s^{eff} = \frac{n_s^0}{n_s^r}\frac{1}{J_s}\left(\mathrm{P}_1\mathbf{m}^{(1)} + \mathrm{P}_2\mathbf{m}^{(2)} + \mathrm{P}_3\mathbf{m}^{(3)} + \mathrm{P}_4\mathbf{I} + \mathrm{P}_5(J_s)^{-2}\mathbf{b}_s\mathbf{m}^{(3)}\mathbf{b}_s\right) \tag{14}$$

where $\mathbf{b}_s = \mathbf{F}_s\mathbf{F}_s^T$ is the Finger tensor, $\mathbf{m}^{(\nu)}$ denotes a structure tensor, and P_i are invariants, see Borgqvist et al. (2015). In (14), the effective Cauchy stress tensor is scaled by the ratio between the initial solid volume fraction n_s^0 and the reference solid volume fraction $n_s^r = 0.5253$.

Given a specific spatial point $\mathbf{x}$ all phases and constituents are assumed to have a common absolute temperature θ and the balance of energy governing the evolution of θ is given by

$$c^p\frac{D_s(\theta)}{Dt} + \nabla\cdot(\mathbf{q}) - \sum_{j=d,v} h_{g_j}\nabla\cdot(\mathbf{J}_{g_j}) + \hat{m}\Delta H_{ads} = 0 \tag{15}$$

The heat capacity c^p and the enthalpy of adsorption ΔH_{ads} are defined by

$$\Delta H_{ads} = h_{g_v} - h_l^f + R_{g_v}\theta^2\frac{\partial \ln(a_w)}{\partial\theta} \tag{16}$$

$$c^p = \bar{\rho}_s c_s^p + \bar{\rho}_l c_l^p + \bar{\rho}_{g_v} c_{g_v}^p + \bar{\rho}_{g_d} c_{g_d}^p \tag{17}$$

where h_{g_v} and h_l^f denote the enthalpies of the water vapor and the "free" liquid water. The total heat flux $\mathbf{q} = \mathbf{q}^{cond} + \mathbf{q}^{conv} + \mathbf{q}^{diff}$ describes the net heat flux due to the conductive flux $\mathbf{q}^{cond}$, the convective flux $\mathbf{q}^{conv}$, and the diffusive flux $\mathbf{q}^{diff}$ which are given by

$$\mathbf{q}^{cond} = -\mathbf{K}_\theta\nabla(\theta), \qquad \mathbf{q}^{conv} = \bar{\rho}_g h_g \mathbf{v}_{g,s}, \qquad \mathbf{q}^{diff} = \sum_{j=d,v}\bar{\rho}_{g_j}\mu_{g_j}\mathbf{w}_{g_j} \tag{18a}$$

where the inner part of the enthalpy of the gas phase is defined by $\rho_g h_g = \sum_{j=d,v}\rho_{g_j}h_{g_j}$. Explicit formats of the specific heats, c_α^p, the thermal conductivity tensor $\mathbf{K}_\theta$, and the inter–fiber water vapor diffusivity tensor $\mathbf{D}_{g_v}^{eff}$ as well as the thermodynamic potentials μ_{g_j} and h_{g_j} for the gas constituents and h_l^f for the "free" liquid water are provided in Askfelt and Ristinmaa (2016).

3 Experimental characterizations

Two single–ply boards with different densities were considered. The grammage g (mass per unit square meter) and the thickness $d^{(zd)}$ of each paperboard were determined according to ISO 536:2012 and ISO 534:1988, respectively, see Table 1.

3.1 Static and the dynamic sorption properties

A Q5000 SA dynamic vapor sorption analyser from *TA instruments* was used to determine the static and the dynamic sorption properties of the paperboard. Only one density, $\rho = 786$ kg/m^3 was considered in these tests.

Table 1: Grammage, thickness, and density of the considered paperboards.

Grammage g [kg/m^2]	Thickness $d^{(zd)}$ [μm]	Density ρ [kg/m^3]
0.316	402	786
0.223	265.3	839

Procedure

The static and the dynamic sorption properties of the paperboard were investigated for three different temperatures $\theta \in \{303.15\text{ K}, 323.15\text{ K}, 333.15\text{ K}\}$ and a relative humidity interval of RH=90% $\rightarrow$ 0%. Circular samples with a diameter of 5 mm were punched out and placed in a quartz pan which was inserted to the Q5000 SA dynamic vapor sorption analyser. Before each measurement the sorption analyser was equilibrated at the chosen temperature and RH=0. When the measurement started the samples were first conditioned at RH=90% for 300 min such that the samples reach an equilibrium state with the ambient climate inside the sorption analyser. After 300 min at RH=90%, a jump was made in the relative humidity to RH=70%, were it was kept constant for 200 min. The same procedure was then repeated at RH=50%, RH=30% and RH=0%, with the exception that at RH=0% the time climate was held fixed for 300 min. During the experiments the mass m of the samples were measured every 30 seconds and the final mass, i.e., after 300 min at RH=0%, was assumed to be equal to the dry mass of the sample, m_{dry}.

Results

The water activity a_w describes the energy level of the bound water inside the paperboard and is defined as the ratio between the equilibrium water vapor pressure $p_{g_v}^{eq}$ and the saturation water vapor pressure, i.e.,

$$a_w = \frac{p_{g_v}^{eq}}{p_{g_v}^{sat}} \tag{19}$$

At equilibrium the water activity is equal to the ambient relative humidity φ^∞ and the equilibrium values of the moisture ratio $W = (m - m_{dry})/m_{dry}$ for the different φ^∞ were used to calibrate the water activity $a_w(W, \theta)$ of the bound water. The water activity is commonly also referred to as the sorption isotherm and the form of $a_w(W, \theta)$ should be chosen carefully as it has direct implications on the enthalpy of adsorption, see (16). An extensive review of common formats of the water activity used for paperboard is found in Petterson and Stenström (2000) where the authors argue that an isotherm suggested by Heikkilä 1993 is best suited for calculations on paper. The isotherm assumed in the present study is similar to the Heikkilä isotherm and given by

$$a_w = 1 - \exp(a^a W^{a^b} + a^c(\theta - 273.15)W^{a^d}) \tag{20}$$

This format of a_w was calibrated against the equilibrium values of the moisture ratio for the different RH and the different θ. The calibrated model is shown in Figure 2(a) and the effect on the enthalpy of adsorption is shown in Figure 2(b) where the difference between the enthalpy of adsorption, ΔH_{ads}, and the enthalpy of evaporation, ΔH_{vap}, is shown. The parameters retrieved from the calibration are given by $a^a = -59.72, a^b = 1.7, a^c = -0.237$ 1/K, and $a^d = 1.31$. From the water activity (20) the

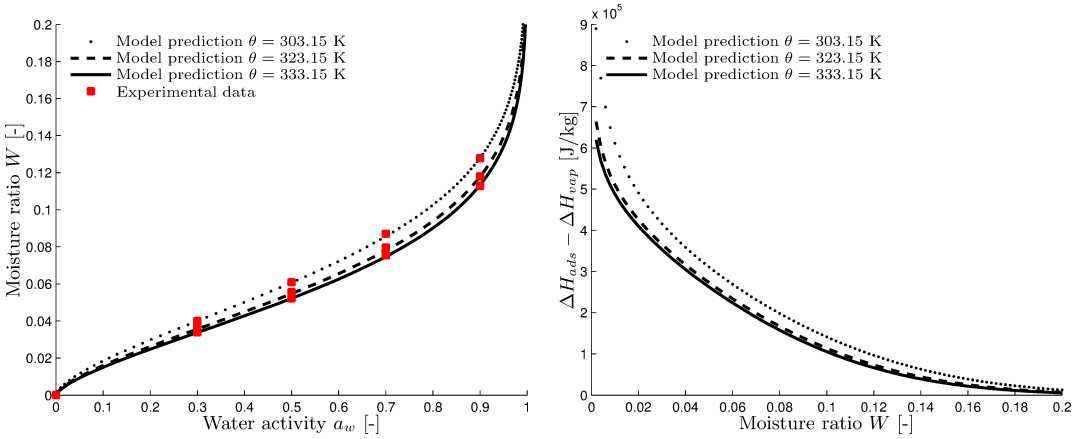

(a) (b)

Figure 2: **a**) Water activity in (20) calibrated to experimental sorption data **b**) Change in enthalpy of adsorption due to the interaction between the fiber network and the liquid water.

equilibrium moisture ratio at $\theta = 296.15$ K and RH=50% is determined as W=0.063. Using this together with the density of the paperboard $\rho = 786$ kg/m^3 the initial volume fractions are estimated

$$n_s^0 = \frac{\rho}{\rho_s(0.063+1)} = 0.493, \quad n_l^0 = \frac{0.063 n_s^0 \rho_s}{\rho_l} = 0.0466, \quad n_g^0 = 1 - n_s^0 - n_l^0 = 0.46 \tag{21}$$

When calculating the initial volume fraction of the liquid water, in (21), it was assumed that the mass of the gas phase is negligible, such that the moisture ratio is given by

$$W = \frac{\bar{\rho}_l}{\bar{\rho}_s} \tag{22}$$

The rate of evaporation coefficient $k_{\hat{m}}$ depend on the moisture ratio, the absolute temperature, and the nature of the porous medium, see Ouedraogo et al. (2013), and will here be calibrated to fit the evolution of the moisture ratio for each step in RH and for each temperature. When calibrating $k_{\hat{m}}(\theta, W)$, two assumptions are made. First, it is assumed that the phase change from the bound water to the water vapor is a much slower process than the combined mass flux $\mathbf{J}_{g_v}$ and the local relative humidity $\varphi^{loc} = p_{g_v}/p_{g_v}^{sat}$ is assumed to be in equilibrium with the ambient relative humidity φ^{∞} instantaneously. Second, it is assumed that the deformation of the paperboard is negligible during these sorption experiments, i.e, $\nabla \cdot (\mathbf{v}_s) \approx 0$. The rate of evaporation

coefficient $k_{\hat{m}}$ is then calibrated against the evolution of the moisture ratio given by

$$\frac{D_s(W)}{Dt} = \frac{W}{n_l\rho_l}\frac{D_s(n_l\rho_l)}{Dt} - \frac{W}{n_s\rho_s}\frac{D_s(n_s\rho_s)}{Dt} = -k_{\hat{m}}(\theta, W)\frac{R_{g_v}\theta}{n_s^0\rho_s^0}\ln\left(\frac{a_w(\theta, W)}{\varphi^\infty}\right) \quad (23)$$

where (9), (10a), and (12) were used.

For a porous medium, the rate of evaporation coefficient $k_{\hat{m}}$ typically has a bell shaped dependence on the moisture ratio, see also Benet et al. (2009); Ouedraogo et al. (2013); Bénet and Jouanna (1982). The reduced rate at higher moisture ratios is explained by the reduced interfacial area between the liquid water and the water vapor, see Ouedraogo et al. (2013). The present paper considers relatively low moisture ratios and the decreasing rate at higher moisture ratios is not included. The temperature dependence of $k_{\hat{m}}$ is assumed to follow a Arrhenius type equation and the following format of $k_{\hat{m}}$ is suggested,

$$k_{\hat{m}} = k^a W^{k^b}\exp(k^c(W + k^d)^{k^e})\exp(k^f/\theta) \quad (24)$$

The calibrated rate of evaporation parameters are given by $k^a = 0.4$ kg·s/m^5, $k^b = 0.3, k^c = -0.0039, k^d = 0.071, k^e = -2.9$, and $k^f = -3500$ K. The predicted moisture ratio evolutions retrieved from (23), (20), and (24) are included in Figure 3 together with the experimental measurements. In Figure 4, the rate of evaporation coefficient in (24) is plotted against the moisture ratio W for three different absolute temperatures $\theta = 303.15$ K, $\theta = 323.15$ K, and $\theta = 333.15$ K.

3.2 Determination of the in–plane gas permeability

The in–plane gas permeability of the paperboard was determined by an *L & W Air Permeance Tester, low range – Code 168.*

Preparation of samples

Sheets of the paperboard were conditioned in the relative humidity RH=50% and the absolute temperature θ =296.15 K according to ISO 187. After conditioning a desktop pouch laminator (*Photonex - 235*) was use to laminate both sides of the sheets with a polymer which, in the in-plane permeability test, may be considered to be impermeable. Twenty samples of the size 10 X 10 cm were punched out. Each sample contained two parallel slits placed symmetrically of a distance $d^{RCK} = 20$ mm apart, see Figure 5(a). The width and length of each slit were $t_{slit}^{RCK} = 2$ mm and $l_{slit}^{RCK} = 50$ mm respectively. Plastic tape was attached over each slit, one piece on each side, in order to prevent air to flow straight through the slits, see Figure 5(b). The intended gas flow direction is indicated with black arrows in both figures and out of the 20 samples that were punched out, 10 samples had a flow direction in MD and 10 samples a flow direction in CD.

Procedure

All test were performed in the same environment as the samples were conditioned, i.e., RH=50% and θ =296.15 K. The *L & W Air Permeance Tester, low range – Code*

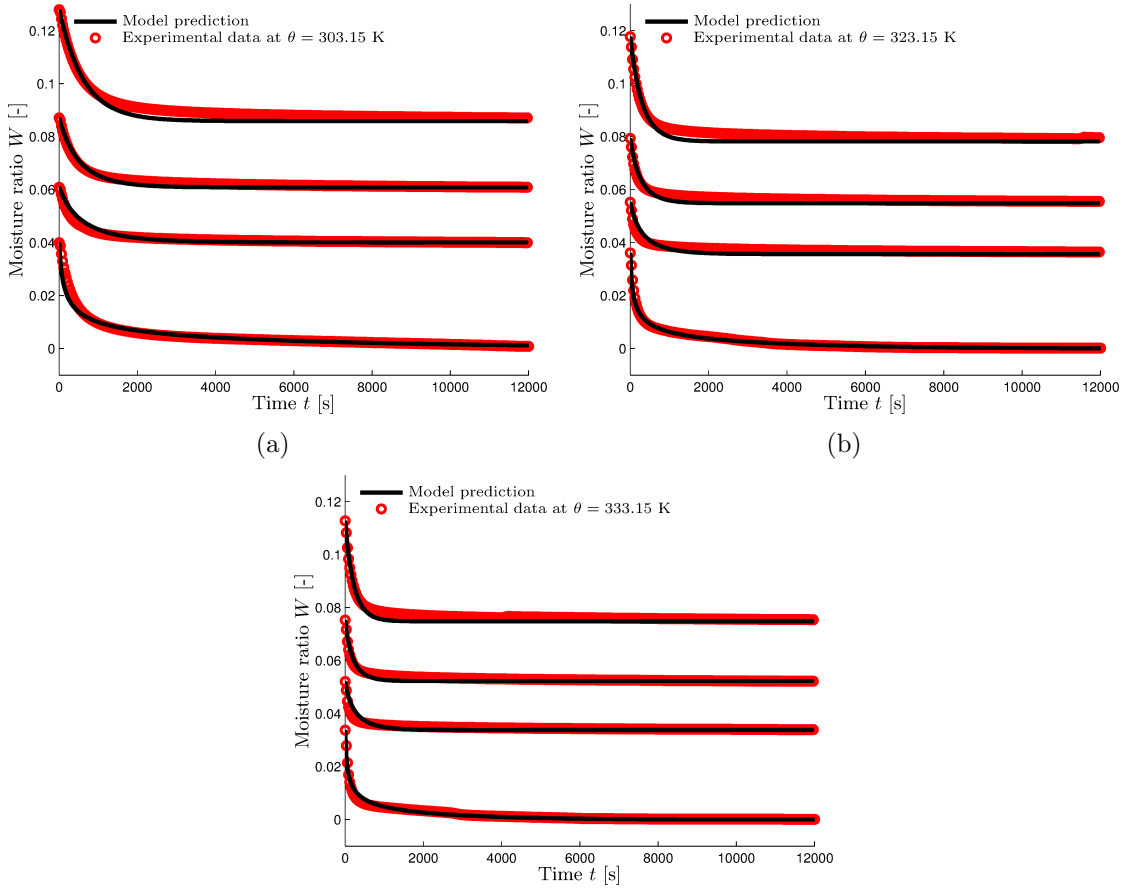

Figure 3: Moisture ratio evolutions resulting from jumps in RH, from top to bottom curves: RH=90% → RH=70%, RH=70% → RH=50%, RH=50% → RH=30%, and RH=30% → RH=0%. **a**) $\theta = 303.15$ K, **b**) $\theta = 323.15$ K, and **c**) $\theta = 333.15$ K.

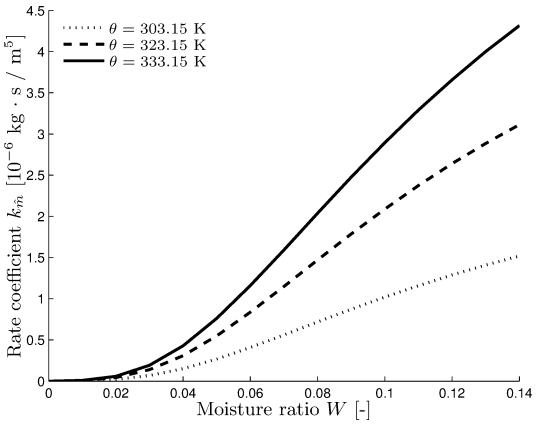

Figure 4: Calibrated rate of evaporation coefficient $k_{\hat{m}}$ plotted against the moisture ratio W for different temperatures.

168 was used to measure the air permeance (mean air flow rate through unit area under unit pressure difference in unit time) through the samples. The air permeance

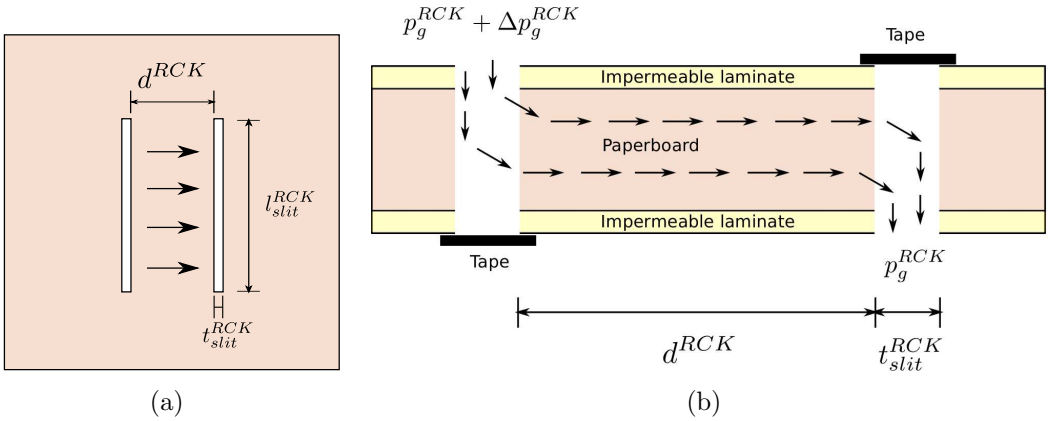

(a) (b)

Figure 5: Illustration of the samples used in the in–plane permeability tests, **a**) seen from above **b**) seen from the side.

tester was adjusted to obtain a pressure difference of $\Delta p_g^{RCK} = 20$ kPa between the two surfaces of the sample. The pressure difference was preserved during the tests and the apparent air–permeance P^{RCK} [m/Pa/s] leaving the sample was registered.

Results

The intrinsic in–plane permeability, $K_{g,s}^{(id)}$, in direction $id \in \{md, cd\}$ is determined via Darcy's law, (11a), i.e.,

$$K_{g,s}^{(id)} = \frac{P^{RCK} A_{lw} d^{RCK}}{l_{slit}^{RCK} d_{zd}} \tag{25}$$

where $A_{lw} = 50$ cm^2 is the measuring area of the air permeance tester. The in–plane permeability tests were made on both paperboards with the different densities, $\rho = 786$ kg/m^3 and $\rho = 839$ kg/m^3, corresponding to $n_g = 0.46$ and $n_g = 0.42$, respectively, following the derivations in (21). In order to fit the experimental data the calibration of the permeability suggested in Askfelt and Ristinmaa (2016) had to be slightly adjusted. The calibration is shown in Figure 6 and given by

$$K^{(md)} = 80 \times 10^{-14} n_g^{1.8}/(1 - n_g) \quad [\text{m}^2] \tag{26a}$$

$$K^{(cd)} = 46 \times 10^{-14} n_g^{1.4}/(1 - n_g) \quad [\text{m}^2] \tag{26b}$$

$$K^{(zd)} = 6 \times 10^{-14} n_g^{4}/(1 - n_g) \quad [\text{m}^2] \tag{26c}$$

No new experimental tests were made on the out–of–plane gas permeability and the intrinsic permeability in ZD is modeled by the format provided in Askfelt and Ristinmaa (2016).

4 Experimental procedure of the blister tester

The essence of the blister test is to locally expose the package material to a hot air jet and measure the time needed for a blister to form and grow to a specific size, this

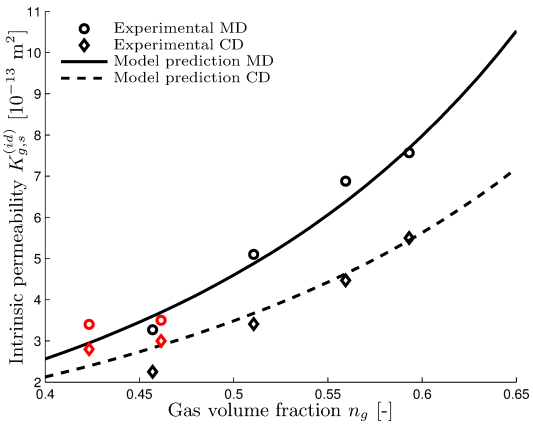

Figure 6: Calibration of the intrinsic permeability, $K_{g,s}^{(id)}$, in MD and CD. Black marking: experimental data provided in Askfelt and Ristinmaa (2016). Red marking: new experimental data.

time is referred to as the blister time. A blister is defined as a local elevation of the surface of the board, see Figure 1(b). As indicated in Figure 1(b), the appearance of a blister is assumed to be due to some local failure in the adhesion between the Al–foil and the paperboard. The package material evaluated in the blister test was made with the single–ply paperboard with the density $\rho = 786$ kg/m^3, see Table 1.

4.1 Preparation of samples

Sixty samples of dimensions 90 mm × 80 mm (MD × CD) were cut out of the package material and conditioned in three different climates, 20 samples in each climate. The considered climates were defined by the absolute temperature θ= 299.15 K and the relative humidities, RH=10%, RH=50%, and RH=80%, respectively, and all blister tests were also performed in the same environment as the samples were conditioned. In order to apply an accurate temperature distribution during the numerical simulations, thermocouples were used to measure the temperature evolution on the surfaces of 12 samples for each climate. Defining origin of the samples in the upper left corner, the positions of the thermocouples were given by, T1=(MD=40 mm, CD = 10 mm), T2=(MD=40 mm, CD = 20 mm), T3=(MD=40 mm, CD = 30 mm), and T4=(MD=40 mm, CD = 40 mm), see Figure 9(a). With these positions, the thermocouple at T4 was positioned right beneath the centre of the hot air jet. For each climate, three samples were prepared with thermocouples on positions T2 and T4 and three samples were prepared with thermocouples on positions T1 and T3 on the aluminium side. In addition three samples were prepared with thermocouples on positions T2 and T4 and three samples were prepared with thermocouples on positions T1 and T3 on the opposite side, i.e., on the clay coating side. Alumel and chromel thermocouples with a diameter of 12.7 μm were used. The thermocouples were attached to the surfaces with a 25.4 μm thick Kapton tape and connected to a logger with the logging rate 10 000 samples per second.

4.2 Procedure

An illustration of the experimental set–up of a blister test is shown in Figure 7. An electronically–controlled hot air gun, (*Steinel HG 2000E*) is used to heat the pressure chamber. On the bottom of the pressure chamber, a small hole exists, see Figure 7(b). During the heating of the pressure chamber, and also in between the blister tests, this hole was closed by an air regulator. The samples, of the aseptic package material, were placed with the aluminium side up, in the test piece holder located beneath the pressure chamber. The blister test started when the air regulator was moved allowing the stream of hot air to locally heat the sample. The air regulator was coupled to a electronic timer (*kübler codix 524*) which started when the air regulator was moved and stopped when a photoelectric sensor detected a blister on the package material. The time registered by the electronic timer is referred to as the blister time and this time was registered for each sample. In addition to the standard blister detection method, i.e., the photoelectric sensor, the samples were also filmed with a high speed camera during the blister tests.

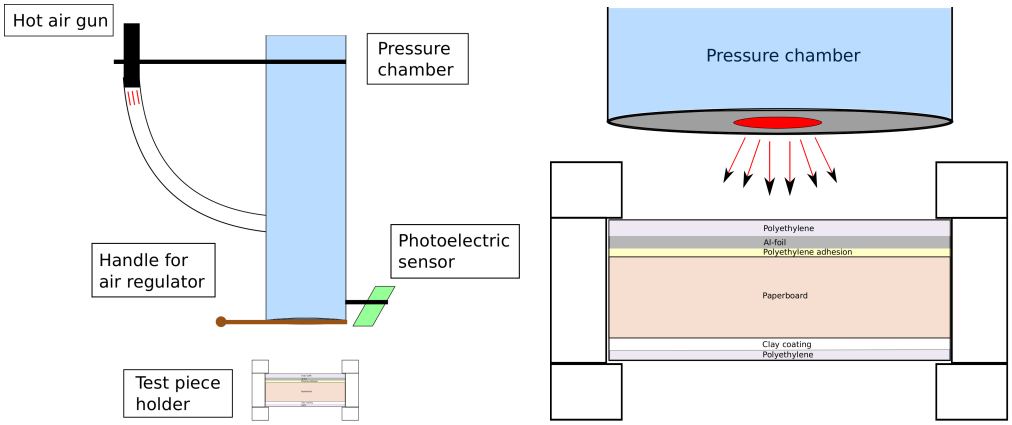

Figure 7: a) Illustration of the experimental blister test setup **b**) Zoom in on the test piece holder.

4.3 Analysis of the experimental results

The mean blister times and the standard deviations of blister times for the climates; RH=50% and RH=80% are shown in Figure 8. Unfortunately the photoelectric sensor did not register the blisters, at the tests performed, at the relative humidity of RH=10%. It is believed that this error is caused by the curving of the samples when conditioned at the low relative humidity. The videos of the blister tests were analysed and the time to the initiation of the blisters were registered for all samples. During the analysis of the videos it was observed that, soon after the air lock was removed, a small irregular elevation appeared in the Al–foil, then the blister initiated from the centre of this elevation. Note that the blister initiation time is here defined as when a bubble starts to appear and not when the irregular elevation appears. The mean blister initiation times as well as the standard deviations of these are also included in

Figure 8. Comparing the blister initiation times and the blister times for the different

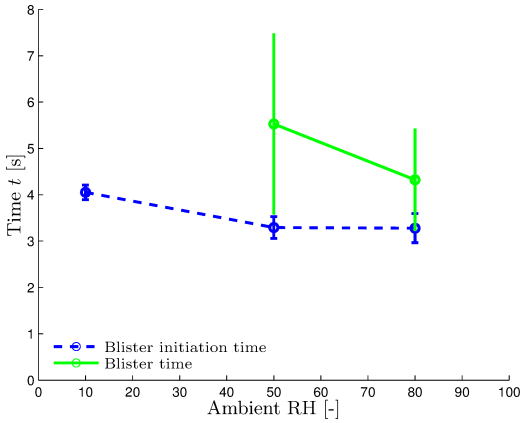

Figure 8: Mean values and standard deviations of the blister initiations times determined from the video analysis and the blister times registered during the blister test.

climates it is seen that the blister initiation times are rather similar for the different climates while the blister times has a more pronounced variation between the different climates. These results indicate that the initiation of a blister is more related to the temperature while the growing of a blister is more related to the moisture ratio of the board. This hypotheses is strengthened by the moisture ratio dependence in the rate of evaporation coefficient, see Equation (24) and Figure 4, indicating that the blisters will grow faster at higher moisture ratios.

The evolutions of the absolute temperature at positions T1, T2, T3, and T4 registered by the thermocouples on the surface closest to the pressure chamber are shown in Figure 9. The adhesive between the Al–foil and the paperboard is assumed to consist of low density polyethylene (LDPE) which has a typical melting point around 376.15 K, dos Santos et al. (2013). In Figure 8 it is observed that the melting temperature of LDPE is reached at $t \approx 1.1$ s for position T4, at $t \approx 3.3$ s for position T3, and for positions T2 and T1 the melting temperature is not reached within the first 7 s of the blister test. Comparing this with the blister initiation time, i.e., t $\approx$ 3.3 s, it is noted that the blister will initiate when the radius of the molten LDPE has reached approximately 1 cm, i.e., the distance between T4 and T3. However, locally the LDPE starts to melt approximately 2 s before the initiation of the blister and this is probably the reason for the irregular elevation observed a priory to the blister initiation in the video analysis.

5 Numerical simulation of the blister test

For simplicity only a two–dimensional segment of the package material is considered in the numerical simulations. The segment is indicated with a green line in Figure 9(a). The computational domain Ω is spanned by the axis $\mathbf{e}^{md}$ and $\mathbf{e}^{zd}$, see Figure 10, and the spatial positions are defined by coordinates md and zd, respectively. The width and thickness of Ω^0 are 4 cm and 400 μm, respectively. In the numerical simulations the failure of the LDPE adhesion is modeled by the void volume fraction ϕ. The

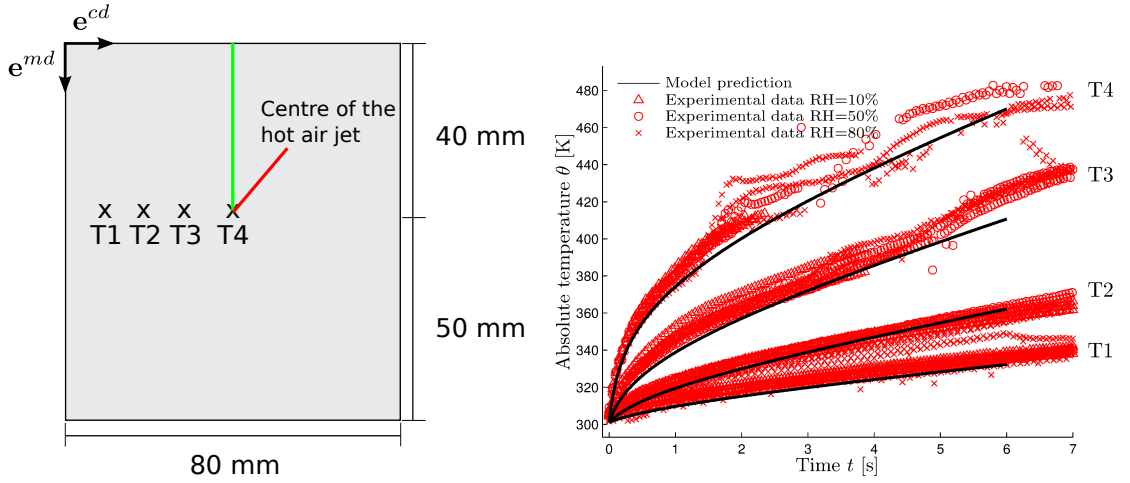

Figure 9: **a**) Illustration of the positions of the thermocouples. **b**) Temperatures retrieved from the thermocouples at positions T1, T2, T3, and T4 at the aluminium side. The black curves show the temperatures, at positions T1, T2, T3, and T4, used as Dirichlet boundary conditions, θ^{hs}, in the numerical simulations, see (32).

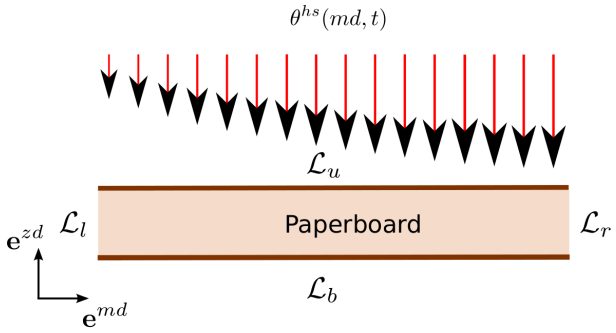

Figure 10: Illustration of the Computational domain Ω.

void space is occupied by moist air and the top three rows of elements are modeled as two phase media, i.e., the model outlined in Section 2 without the bound water. The solid phase, in the top row of elements, is modeled as a mixture of aluminium and LDPE, denoted $()_{mix}$, and the solid phase in the following two rows is modeled as LDPE, denoted $()_{pe}$. The Cauchy stress tensors, the thermal conductivity tensors, the specific heats, the intrinsic permeability tensors, and the tortuosity tensors in the top three layers are given by

$$\boldsymbol{\sigma} = \boldsymbol{\sigma}_x^{eff} - p_g \mathbf{I} \tag{27a}$$

$$\mathbf{K}_\theta = \left((1-\phi)\lambda_{pe}^\theta + \phi\lambda_g^\theta\right)\mathbf{I} \tag{27b}$$

$$c^p = (1-\phi)\rho_{pe}c_{pe}^p + \phi c_g^p \tag{27c}$$

$$\mathbf{K}_{g,x} = (4\times 10^{-18} + \phi \times 10^{-13})\mathbf{I} \ \ \mathrm{m}^2 \tag{27d}$$

$$\tilde{\tau} = 60\exp(-5.5\phi)\mathbf{I} \tag{27e}$$

where $x \in \{mix, pe\}$ and $\rho_{pe} = 950$ kg/m^3. Note that Dirichlet boundary conditions are applied on the aluminium and therefore dictates the temperature in the aluminium. The effective stress tensors of $()_{mix}$ and $()_{pe}$ are modeled with isotropic Neo-Hookean models, i.e.,

$$\boldsymbol{\sigma}_{pe}^{eff} = K_{pe}\ln(J_{pe})\mathbf{I} + 2J_{pe}^{-2/3}G_{pe}\left(\mathbf{b}_{pe} - \frac{(\mathbf{b}_{pe} : \mathbf{I})}{3}\mathbf{I}\right) \tag{28a}$$

$$\boldsymbol{\sigma}_{mix}^{eff} = K_{mix}\ln(J_{mix})\mathbf{I} + 2J_{mix}^{-2/3}G_{mix}\left(\mathbf{b}_{mix} - \frac{(\mathbf{b}_{mix} : \mathbf{I})}{3}\mathbf{I}\right) \tag{28b}$$

where $K_{mix} = S_{al}K_{al} + (1 - S_{al})K_{pe}$, $G_{mix} = S_{al}G_{al} + (1 - S_{al})G_{pe}$, and $S_{al} = 0.1$ denotes the ratio between aluminium and LDPE in the elements connected to the upper boundary. The Poisson's ratios of aluminium and LDPE are given by $\nu_{al} = 0.334$ and $\nu_{pe} = 0.3$, respectively. The Young's modulus of the aluminium is calibrated against the experimental data provided in McLellan and Ishikawa (1987) and modeled by $E_{al} = 7 \times 10^{10} - 4 \times 10^{10}(\theta - 273)$. Furthermore, the shear modulus G_{pe} of the LDPE is a functions of the absolute temperature, see e.g., Korin (2009), and modeled by

$$G_{pe} = \exp(10\exp(-1(\theta/100 - 2.7)^4) + 3 \times 10^{-5}(\theta - 373)^2 - 0.029\theta + 17) + 100 \quad \text{Pa} \tag{29}$$

where the significant stiffness reduction takes place during the melting of the LDPE. The thermal conductivity, λ_{pe}, and the specific heat, c_{pe}^p, of the LDPE are modeled as functions of the absolute temperature and calibrated against the experimental data provided in dos Santos et al. (2013),

$$\begin{aligned}\lambda_{pe}^{\theta} =& -3.63 \cdot 10^{-8}\theta^3 + 5.235 \cdot 10^{-5}\theta^2 - 2.474 \cdot 10^{-2}\theta + 3.99 \\ &+ 0.15\exp\left(-15 \cdot 10^{-4}(\theta - 376.15)^2\right) \quad \text{W/m/K}\end{aligned} \tag{30a}$$

$$\begin{aligned}c_{pe}^{p} =& 3080\exp\left(-0.005(\theta - 376.15)^2\right) - 2600 + 11.6\theta \\ &+ 1600\exp\left(-0.0003(\theta - 340)^2\right) \quad \text{J/kg/K}\end{aligned} \tag{30b}$$

Formats of the specific heat c_g^p and the thermal conductivity λ_g^{θ}, of the gas phase are provided in Askfelt and Ristinmaa (2016). The specific heat in (30b) includes a peak at the melting temperature of LDPE, which describes the enthalpy of fusion, i.e., the energy needed for the phase change from solid to molten LDPE.

5.1 Boundary and initial conditions

The mass fluxes q_{g_j}, the momentum flux $\mathbf{t}$, and the heat flux q_θ through the upper boundary, $\mathcal{L}_u$, the right boundary, $\mathcal{L}_r$, the bottom boundary, $\mathcal{L}_b$, and the left boundary, $\mathcal{L}_l$, are defined by

$$q_{g_j} = \mathbf{J}_{g_j} \cdot \mathbf{n}, \qquad \mathbf{t} = \boldsymbol{\sigma} \cdot \mathbf{n}, \qquad q_\theta = \mathbf{q} \cdot \mathbf{n} \tag{31}$$

where $\mathbf{n}$ denotes the unit normal perpendicular to the surface through which the flux act, see Figure 10. Numerical simulations were run in three different ambient

climates, set to match the climates for the experimental blister tests. When analysing the data from the thermocouples it was noticed that the package material had an initial temperature of 304.15 K which indicate that some heat radiated from the pressure chamber even when the air regulator was closed. For this reason the three climates, assumed in the numerical simulations, were defined by the absolute temperature $\theta^{\infty} =$ 304.15 K, the gas pressure $p_g^{\infty} =$1 atm, and the relative humidities $\varphi^{\infty} \in \{0.1, 0.5, 0.8\}$. The paperboard is assumed to be in equilibrium with the ambient climate at time $t = 0$ s for all simulation, i.e., $\theta^0 = \theta^{\infty}$, $p_{g_v}^0 = \varphi^{\infty} p_{g_v}^{sat}(\theta^{\infty})$, $p_{g_d}^0 = p_g^{\infty} - p_{g_v}^0$. Furthermore, the same initial volume is assumed in all three climates, implying that $n_s^0 = 0.493$ for all simulations. The initial moisture ratios are determined from the water activity (20) and the initial volume fractions n_l^0 and n_g^0 are calculated via (4b) and (22). Initial moisture ratios and volume fractions for the different climates are collected in Table 2.

Table 2: Initial values

RH [-]	W^0 [-]	n_l^0 [-]	n_g^0 [-]
10	0.0197	0.0146	0.4924
50	0.063	0.0466	0.46
80	0.1068	0.079	0.428

The effect of the heat convection from the pressure chamber and the heat conduction in the AL–foil is implemented via Dirichlet boundary conditions on $\mathcal{L}_u$. The temperature function on the upper surface is modeled as

$$\theta^{hs}(md, t) = a^{hs}(md)\ln(b^{hs}(md)t + 1) + c^{hs}(md)t + \theta^{\infty} \tag{32}$$

where explicit formats of $a^{hs}(md), b^{hs}(md)$, and $c^{hs}(md)$ are provided in Table 3. The

Table 3: Dirichlet heat source parameters

Parameter	Unit	Value
$a^{hs}(md)$	K	7exp(42[md–0.01])–3
$b^{hs}(md)$	1/s	0.7exp(100[md–0.01])+2
$c^{hs}(dm)$	K/s	$663md^{5.8}$ exp(–500(md–0.346)^3)+3

predicted temperature, in positions T1, T2, T3, and T4 are shown in Figure 9.

Symmetry conditions are assumed on $\mathcal{L}_r$. Due to the polyethylene and the Al–foil no mass is assumed to flow out from $\mathcal{L}_u$ or $\mathcal{L}_b$. The conductive heat flux through,

$\mathcal{L}_b$, is described by Newton cooling, i.e., $q_\theta = \alpha_\theta(\theta - \theta^\infty)$. Newton convection is also assumed on both the temperature flux q_θ and the mass fluxes q_{g_j} through $\mathcal{L}_l$. For the considered application the contributions from the diffusion on these boundary fluxes are assumed negligible, i.e., the mass flux through $\mathcal{L}_l$ is approximated as $q_{g_j} = \bar{\rho}_{g_j}\mathbf{v}_{g,s} \cdot \mathbf{n} = \bar{\rho}_{g_j}\beta_g(p_g^\infty - p_g)$ and the total heat flux through $\mathcal{L}_l$ is approximated as $q_\theta = \mathbf{q}^{cond} \cdot \mathbf{n} + \mathbf{q}^{conv} \cdot \mathbf{n} \approx \alpha_\theta(\theta - \theta^\infty) + \bar{\rho}_g h_g \beta_g(p_g^\infty - p_g) \approx \gamma_\theta(\theta - \theta^\infty)$. The convection coefficients $\alpha_\theta, \beta_\theta$, and γ_θ are functions of the ambient air flow. In the present work a simplification is made and the convection coefficients are chosen as $\alpha_\theta = 5$ W/m^2/K, $\beta_\theta = 6 \times 10^{-8}$ m/Pa/s, and $\gamma_\theta = 10$ W/m^2/K. A summation of all boundary conditions is presented in Table 4 where the notations $t^{(id)}$ and $u^{(id)}$ defines the traction and the displacement, respectively, in direction id.

Table 4: Boundary conditions applied on the computational domain Ω, shown in Figure 10.

$\mathcal{L}_l$	$\mathcal{L}_u$	$\mathcal{L}_r$	$\mathcal{L}_b$
$q_\theta = \gamma_\theta(\theta - \theta^\infty)$	$\theta = \theta^{hs}(md, t)$	$q_\theta = 0$	$q_\theta = \alpha_\theta(\theta - \theta^\infty)$
$t^{(md)} = p_g^\infty,\ u^{(zd)} = 0$	$t^{(md)} = 0,\ t^{(zd)} = -p_g^\infty$	$u^{(md)} = 0,\ t^{(zd)} = 0$	$t^{(md)} = 0,\ u^{(zd)} = 0$
$q_{g_j} = \bar{\rho}_{g_j}\beta_g(p_g^\infty - p_g)$	$q_{g_j} = 0$	$q_{g_j} = 0$	$q_{g_j} = 0$

5.2 Discretization

The governing equations defined in (10), (13), and (15) constitutes a coupled problem with the primary variables given by; the displacements $\mathbf{u}$, the bound water volume fraction n_l, the absolute temperature θ, and the partial pressures p_{g_d} and p_{g_v}. The coupled set of equations, presented in Section 2, is solved by adopting the Finite Element Method (FEM) with discrete approximation spaces for all primary variables. Galerkin's method is adopted and the spatial discretization is made with Taylor–Hood elements (Q8P4) where the displacements, $\mathbf{u}$ are discretized with quadratic serendipity shape functions whereas the remaining primary variables, θ, p_{g_d}, p_{g_v}, and n_l are discretized with bilinear shape functions. First order time derivatives are discretized via an implicit Euler scheme and the resulting nonlinear problem was solved by adopting a monolithic Newton–Raphson method. Numerical simulations are executed in an in–house Fortran code.

5.3 Results

Evolutions of the predicted out–of–plane stress distributions for the different ambient climates are shown in Figure 11. The LDPE and aluminium layers are included in the simulation with the only purpose of providing more realistic boundary conditions for the paperboard. The predicted stresses levels in these layers are not the focus of this paper and are therefore assigned the value zero in Figure 11.

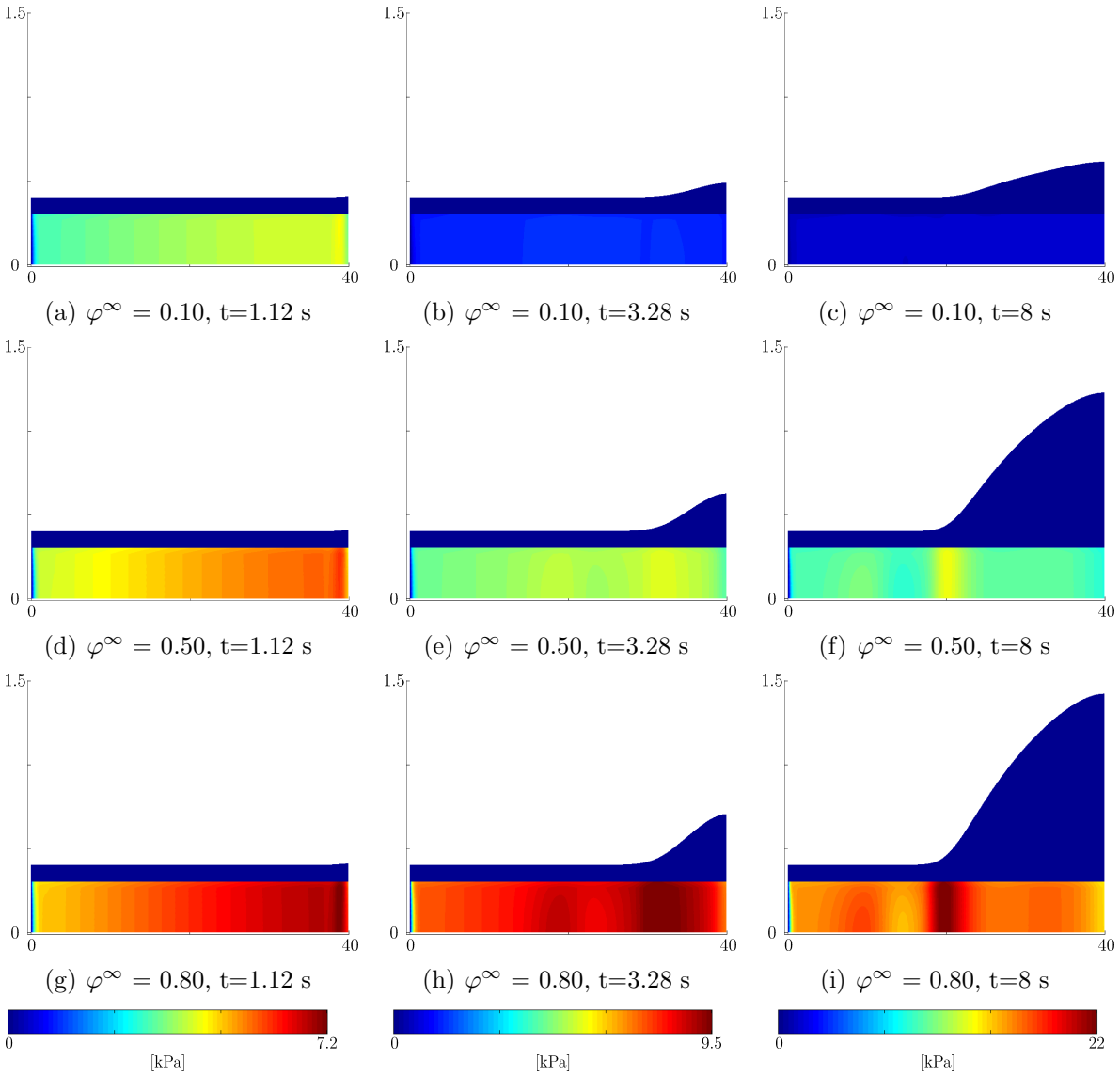

Figure 11: Predicted distributions of the out–of–plane stresses $\sigma^{(zd)} = \mathbf{e}^{(zd)} \cdot \boldsymbol{\sigma} \cdot \mathbf{e}^{(zd)}$ for **a**)-**c**) RH=10%, **d**)-**f**) RH=50%, and **g**)-**i**) RH=80%. The md and zd axis are shown in mm.

In the out–of–plane stress distributions of the paperboard, a moving stress concentration peak is observed. This peak is an indication of the radii of the molten LDPE. It is observed that the radii of the molten LDPE grows as the blister test progress. In Figures 11(a), 11(d), and 11(g) the distributions at time $t = 1.12$ s are shown, i.e., the approximate time when the LDPE was assumed to melt, see Section 4. In these figures the stress peaks are very close to the right boundary meaning that the radii of the molten LDPE is very small and it is concluded that the simulations are able to capture the initial melting of the LDPE fairly well. The out–of–plane stress distributions at the approximate blister initiation time $t \approx 3.3$, (retrieved from the video analysis in Section 4), are shown in Figures 11(b), 11(e), and 11(h). In these figures it is observed that the surfaces has started to elevate, however, for the simulations

in RH=10% a less pronounced elevation is seen. This agrees with the results from the video analysis of the blister tests, where it was found that the initiation of a blister took longer time for RH=10% compared to the blister tests performed in higher RH. In Figures 11(c), 11(f), and 11(i), the out–of–plane stress distributions at time $t = 8$ s are shown. In these figures considerable surface elevations are observed. The stress peaks are located at approximately the same distance from the right boundary, however, there is a significant difference in the elevation of the surfaces.

The out–of–plane tension stresses of paperboard are considered to be elastic up to stress levels around 0.36 MPa, see e.g., Stenberg (2003); Borgqvist et al. (2015). Comparing this value with the magnitudes of the stress peaks in Figure 11 it is concluded that the response of the fiber network is well within the elastic region during a blister test and the development of a blister is not related to out–of–plane failure in the paperboard.

In Figure 12 the predicted evolutions of the inter–fiber water vapor pressure distributions are shown for the three climates. As for the stress distributions, the vapor pressure distributions in the aluminium and LDPE layers are not the focus of this paper and are therefore, in Figure 12, given the value of the initial water vapor pressure. Comparing the difference in the inter–fiber water vapor pressure between the different climates it is observed that the absolute difference is growing during the blister test. At time $t = 8$ the pressure difference between the different climates is very pronounced and it is concluded that there is a clear correlation between the blister expansion and the inter–fiber water vapor pressure. Note that the radii of the blisters are approximately the same and that the correlation between the inter–fiber water vapor pressure and the blister expansion is in reference to the "hight" of the blisters. There is a noticeable vapor pressure gradient in MD and there are at least four reasons for this. First the temperature distribution has a similar sharp gradient and the vapor pressure has an explicit dependence on the absolute temperature, see Section 2. Second, the inter–fiber vapor diffusion drives the vapor towards the heated area. Third, the sorption rates are much higher in the heated area cf. Equations (12) and (24), Figure 4, and Table 2. Fourth, the permeability of the inter–fiber gas seepage is reduced for the higher RH due to the reduced volume fraction, n_g, in the board, cf. Equation (26) and Figure 6.

The drying of the paperboard is, in the presented work, illustrated via the ratio between the current volume of the bound water and the initial volume of the bound water, i.e., v_l/v_l^0. This ratio is retrieved from the following expression

$$\frac{v_l}{v_l^0} = \frac{n_l J_s}{n_l^0} \tag{33}$$

The distributions of v_l/v_l^0 are shown in Figure 13 for the three climates and the times t=1.12 s, t=3.28 s, and t=8 s. From these figures it is concluded that the drying patterns in the different climates are rather similar. The percentage volume decrease is less for the simulation in RH=10% which is expected since the final water during the drying has higher bonding strength.

The evolution of the maximum out–of–plane stress during the blister tests are, for the different climates, shown in Figure 14(a). It is noticed that the different maximum

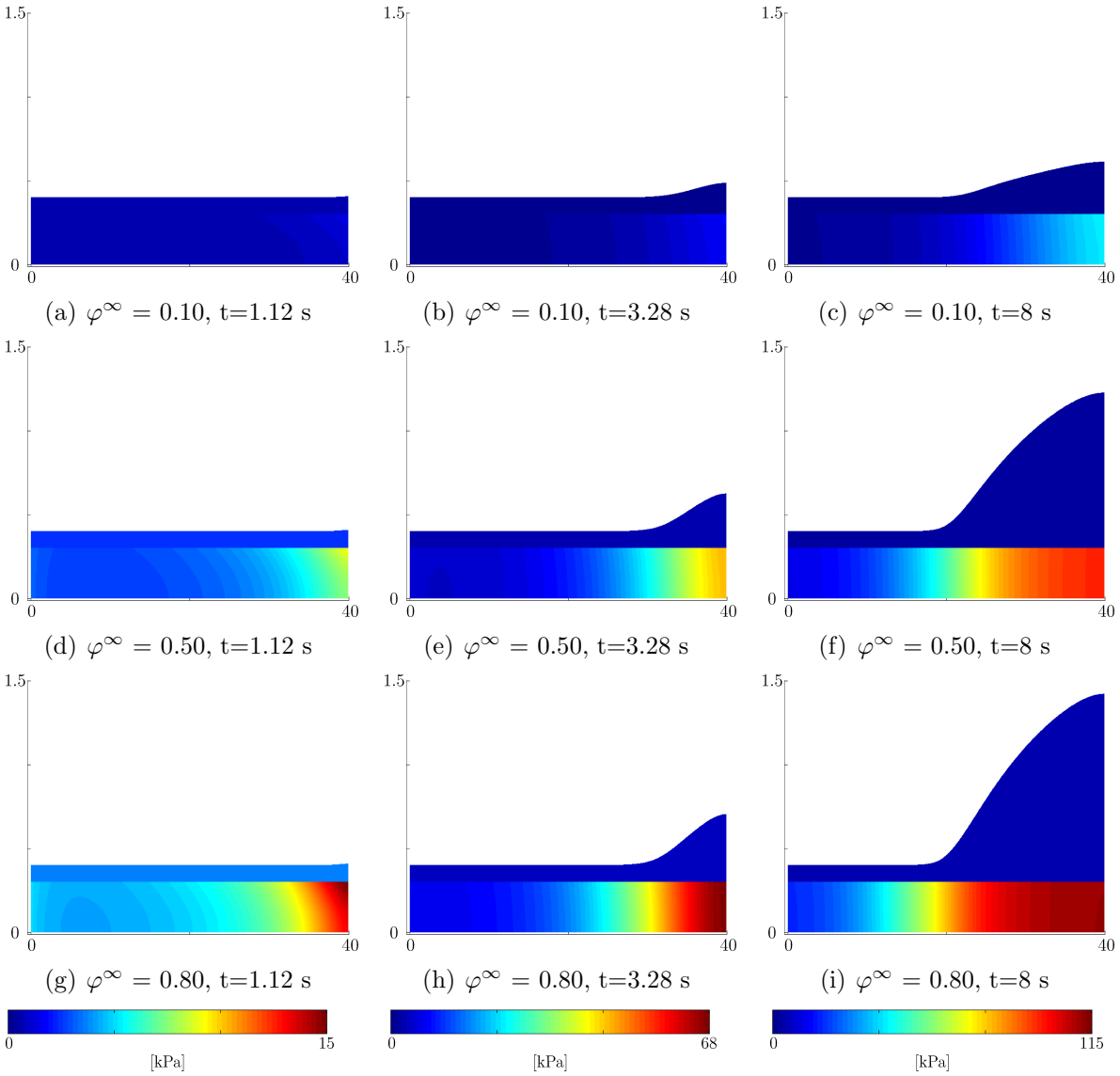

Figure 12: Predicted distributions of the water vapor pressure for **a**)-**c**) RH=10%, **d**)-**f**) RH=50%, and **g**)-**i**) RH=80%. The md and zd axis are shown in mm.

out–of–plane stresses are rather similar up to $t \approx 1.1$ s where the LDPE starts to melt. It is also observed that for all tree climates a out–of–plane stress relaxation takes place as the LDPE melts. For the climates with higher RH the maximum out–of–plane stress then increase again. However, for the simulation in RH=10% the stress level does not reach the same stress level after the LDPE has molten. In Figure 14(b) the evolution of the maximum water vapor pressure is shown. From this figure it is clear that inter–fiber water vapor pressure is not affected in the same distinct manner as the out–of–plane stresses by the melting of the LDPE.

An additional illustration of the evolution of the blisters is given in Figure 15(a) where the out–of–plane displacements of the paperboard are shown for all three climates at the times $t = 1.12$ s, $t = 3.28$ s, and $t = 8$ s. From this figure the different

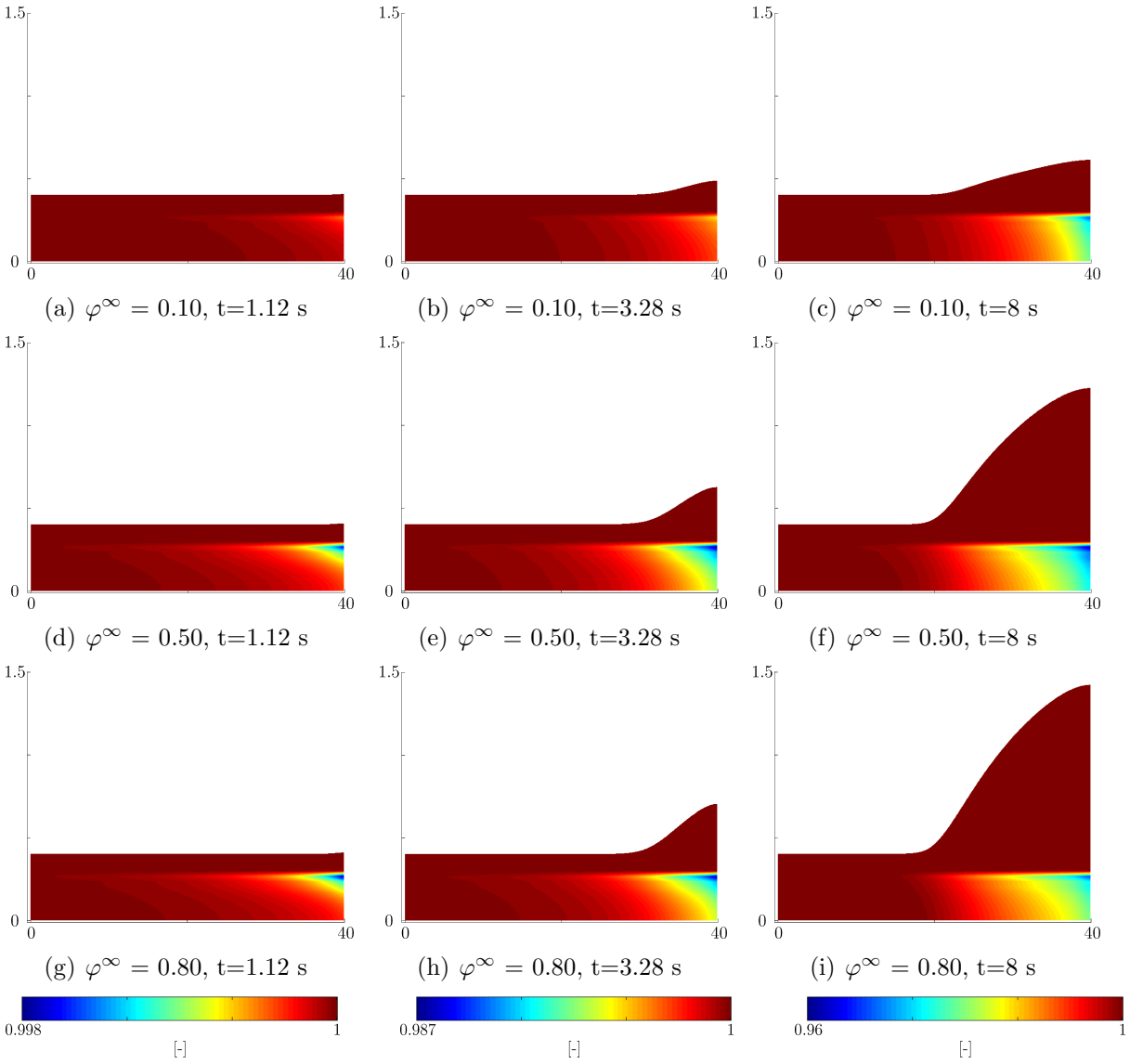

Figure 13: Predicted distributions of the ratio v_l/v_l^0 for **a**)-**c**) RH=10%, **d**)-**f**) RH=50%, and **g**)-**i**) RH=80%. The md and zd axis are shown in mm.

expansion rates of the blisters are visible. Figure 15(a) also indicate that the radii of the blisters in the different climates are the same and that it is only the elevation of the blisters that differ. In Figure 15(a) the blisters at time $t = 1.12$ s are zoomed in. In this figure it is seen that the sizes of the blisters are quite similar at $t = 1.12$ s, i.e., at the approximate blister initiation time.

Finally a comparison between the experimental and the numerical temperature evolutions at positions T1, T2, T3, and T4 on the clay coating side is made in Figure 16. It is observed that the numerical simulations are able to capture the temperature evolutions fairly well. Comparing the temperature evolutions between the different climates it is found that more heat has transported through the package material for the lower RH which might seam counter intuitive since the wet paperboard should

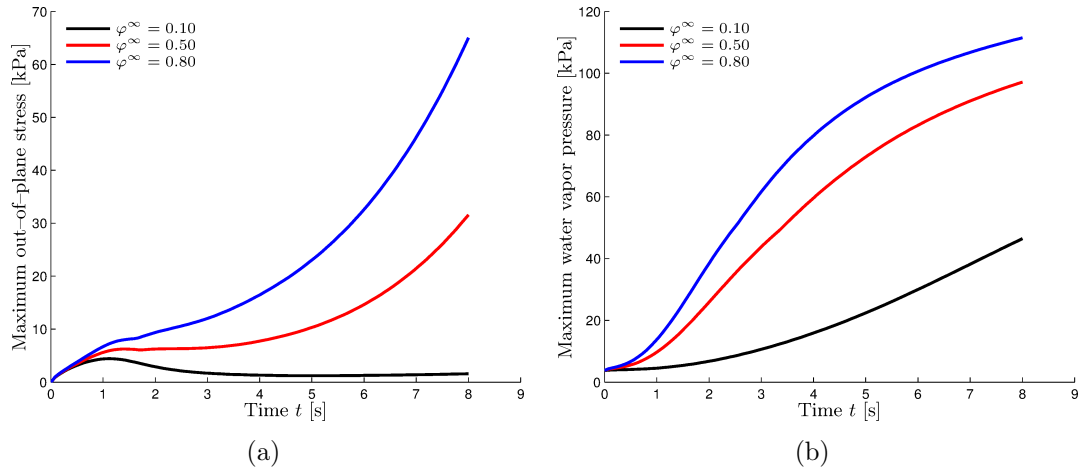

Figure 14: **a**) Evolution of the maximum out–of–plane stress during the blister test, **b**) evolution of the maximum inter–fiber water vapor pressure during the blister test.

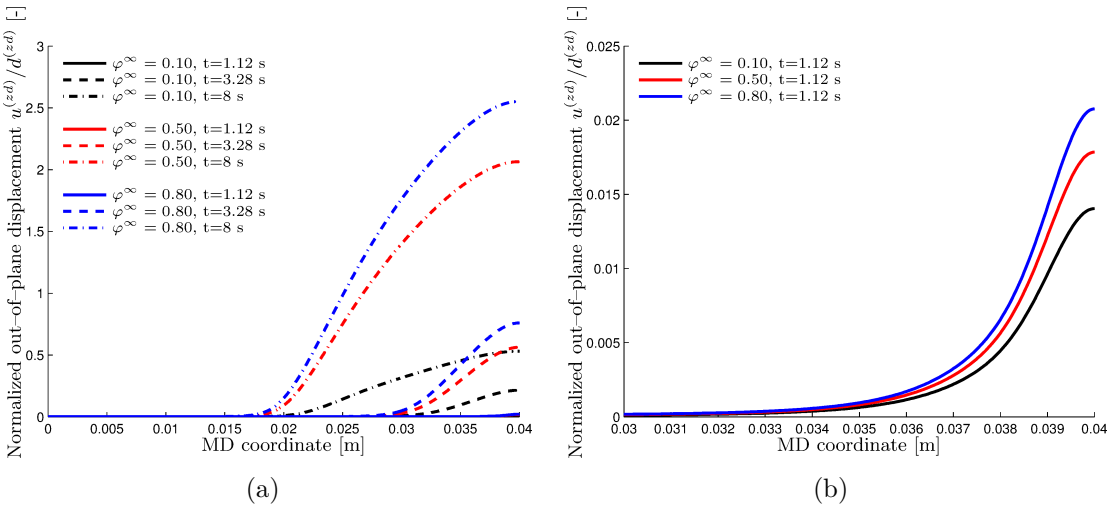

Figure 15: **a**) Development of the normalized out–of–plane displacements for the different climates during the blister tests **b**) normalized out–of–plane displacements for the different climates at $t = 1.12$ s.

transport heat better than the dry paperboard, see also Askfelt and Ristinmaa (2016). The reason for the reduced heat transport for the higher RH is the formation of the blister. As the blister grows the specific heat and the thermal conductivity of the two phase medium, in the top three layers, approaches those of moist air, see also (27), and the moist air acts as an isolator. In Figure 16(a) it is observed that the temperature at T4 is overestimated in the numerical simulation. This indicates that the blister has not grown enough and that the two phase medium describing the LDPE and AL–foil layers is too stiff.

To conclude this section, the numerical simulations indicate that the development of a blister is primarily caused by two processes. The initiation of a blister is mostly related to the melting of the LDPE adhesion, while the speed and magnitude of the elevation of the blister is mainly a consequence of the sorption properties. These

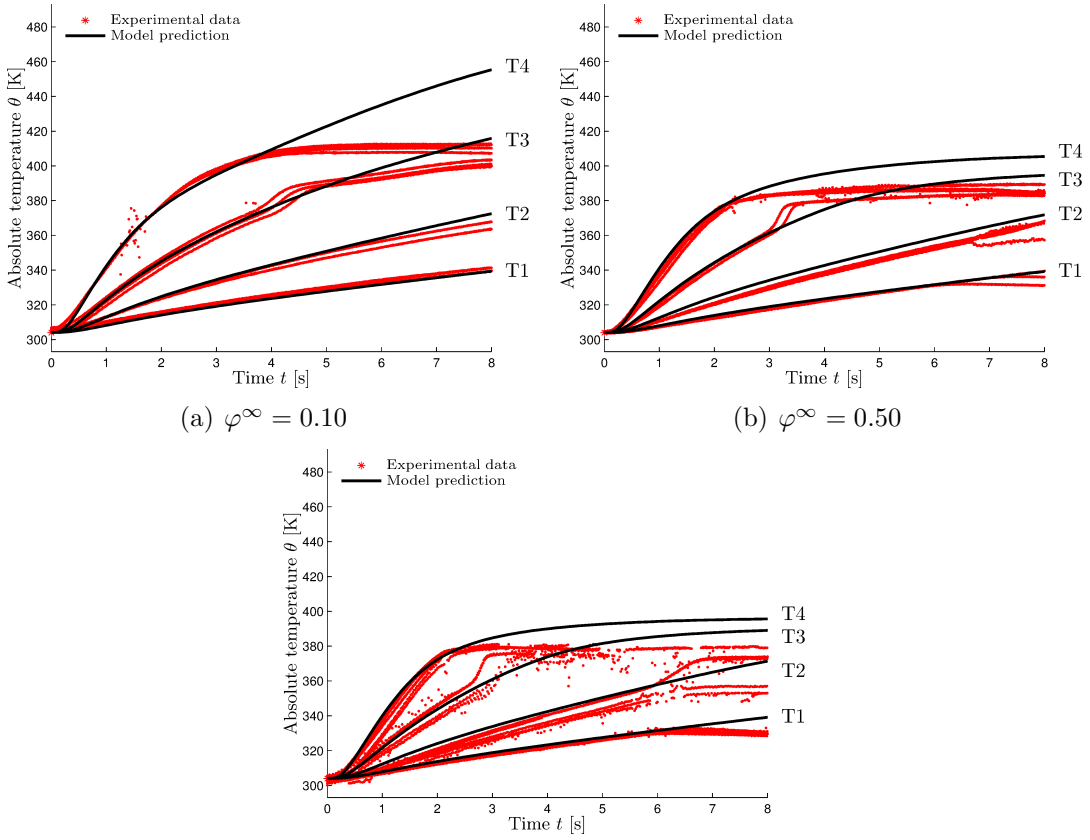

(a) $\varphi^{\infty} = 0.10$

(b) $\varphi^{\infty} = 0.50$

(c) $\varphi^{\infty} = 0.80$

Figure 16: Temperature evolutions at positions T1, T2, T3, and T4 on the clay coating side obtained from the experiments (*) and from the numerical simulations (—) in the climates **a**) RH=10%, **b**) RH=50%, and **b**) RH=80%.

findings agrees well with those found from the experimental analyses in Section 4 where similar conclusions were drawn.

6 Conclusions

In this paper, experimental and numerical analyses of blister formation in moist packaging material exposed to excessive heating are performed. Both the experimental and the numerical analyses indicate that the development of a blister is primarily caused by two processes. The first one being the melting of the LDPE adhesion, which will depend on the applied heat. The second one being the increase in the inter–fiber gas pressure which will depend on the temperature, the in–plane permeability, and the dynamic mass exchange from liquid water bound in or to the fibers to the inter–fiber water vapor. Via an experimental investigation, it is also shown that both the static and dynamic sorption processes are functions of the temperature and the moisture ratio of the board. Furthermore, it is shown that numerical simulations are able to capture the decreased transport of heat which arises due to the formation of the blister.

7 Acknowledgements

The access to the blister test equipment developed by Stora Enso AB in Karlstad and Tetra Pak AB as well as the guidance from Stora Enso in Karlstad in relation to the experimental blister tests are gratefully acknowledged. The assistance with the static and dynamic desorption tests from Innventia AB is highly appreciated. The financial support from Tetra Pak AB and guidance of the in-plane permeability measurements from Tetra Pak AB greatly acknowledged.

References

N. Hallbäck, C. Korin, C. Barbier, M. Nygårds, Finite Element Analysis of Hot Melt Adhesive Joints in Carton Board, Packaging Technology and Science 27 (2014) 701–712.

H. Askfelt, M. Ristinmaa, Response of moist paperboard during rapid compression and heating, Submitted for publication .

P. A. M. Zapata, M. Fransen, J. T. Boonkkamp, L. Saes, Coupled heat and moisture transport in paper with application to a warm print surface, Applied Mathematical Modelling 37 (2013) 7273–7286.

W. R. Foss, C. A. Bronkhorst, K. A. Bennett, Simultaneous heat and mass transport in paper sheets during moisture sorption from humid air, International Journal of Heat and Mass Transfer 46 (2003) 2875–2886.

A. Bandyopadhyay, H. Radhakrishnan, B. V. Ramarao, S. G. Chatterjee, Moisture Sorption Response of Paper Subjected to Ramp Humidity Changes: Modeling and Experiments, Industrial and Engineering Chemistry Research 39 (2000) 219–226.

J. C. Benet, P. Jouanna, Phenomenological relation of phase change of water in porous medium: experimental verification and measurement of the phenomenological coefficient, International Journal of Heat and Mass Transfer 25 (11) (1982) 1747–1754.

J.-C. Benet, A.-L. Lozano, F. Cherblanc, B. Cousin, Phase change of water in a hygroscopic porous medium. Phenomenological relation and experimental analysis for water in soil., Journal of Non-Equilibrium Thermodynamics 34 (2009) 133–153.

M. Alexandersson, H. Askfelt, M. Ristinmaa, Triphasic Model of Heat and Moisture Transport with Internal Mass Exchange in Paperboard, Transport in Porous Media 112 (2) (2016) 381–408.

A. C. Trautz, K. M. Smits, A. Chian, Continuum-scale investigation of evaporation from bare soil under different boundary and initial conditions: An evaluation of nonequilibrium phase change, Water Resources Research 51 (2015) 7630–7648.

E. Baggerud, Modelling of Mass and Heat Transport in Paper, Ph.D. thesis, Lund University, 2004.

H. Askfelt, M. Alexandersson, M. Ristinmaa, Transient transport of heat, mass and momentum in paperboard including dynamic phase change of water, International Journal of Engineering Science 109 (2016) 54–72.

M. Hassanizadeh, W. G. Gray, General conservation equations for multi-phase systems: 1. Averaging procedure, Advances in Water Resources 2 (1979a) 131–144.

M. Hassanizadeh, W. G. Gray, General conservation equations for multi-phase systems: 2. Mass, momenta, energy, and entropy equations, Advances in Water Resources 2 (1979b) 191–203.

M. Hassanizadeh, W. G. Gray, General conservation equations for multi-phase systems: 3. Constitutive theory for porous media flow, Advances in Water Resources 32 (1980) 25–40.

S. M. Hassanizadeh, W. G. Gray, Mechanics and thermodynamics of multiphase flow in porous media including interphase boundaries, Advances in Water Resources 13 (4) (1990) 169–186.

L. S. Bennethum, J. H. Cushman, Multiscale, hybrid mixture theory for swelling systems-I: Balance Laws, International Journal of Engineering Science 34 (1996) 125–145.

M. Landervik, R. Larsson, Pore-gas interaction in foams at finite deformation using staggered solution techniques, Computer methods in applied mechanics and engineering 197 (2007) 148–159.

E. Borgqvist, M. Wallin, M. Ristinmaa, J. Tryding, An anisotropic in-plane and out-of-plane elasto-plastic continuum model for paperboard, Composite Structures 126 (2015) 184–195.

M. Petterson, S. Stenström, Experimental evaluation of electric infrared dryers, Tappi Journal 83 (8) (2000) 89–106.

F. Ouedraogo, F. Cherblanc, B. Naon, J. C. Bénet, Water transfer in soil at low water content. Is the local equilibrium assumption still appropriate?, Journal of Hydrology 492 (2013) 117–127.

J. C. Bénet, P. Jouanna, Phenomenological relation of phase change of water in porous medium: experimental verification and measurment of the phenomenological coefficient, International Journal of Heat and Mass Transfer 25 (1982) 1747–1754.

W. N. dos Santos, J. A. de Sousa, R. G. Jr., Thermal conductivity behaviour of polymers around glass transition and crystalline melting temperatures, Polymer Testing 32 (2013) 987–994.

R. B. McLellan, T. Ishikawa, The elastic properties of aluminium at high temperatures, Journal of Physics and Chemistry of Solids 48 (1987) 603–606.

C. Korin, Mechanical Behaviour of Adhesive Joints in Cartonboard for Packaging, Ph.D. thesis, Karlstad University, 2009.

N. Stenberg, A model for the through-thickness elastic-plastic behaviour of paper, International Journal of Solids and Structures 40 (2003) 7483–7498.